# Numerical Modelling and Simulation of Cavitating Marine Propeller Flows

Vom Promotionsausschuss der
Technischen Universität Hamburg-Harburg
zur Erlangung des akademischen Grades

Doktor-Ingenieurin (Dr.-Ing.)

genehmigte Dissertation

von
Maria Gaschler geb. Bauer

aus
Bischkek

2017

**Vorsitzender des Prüfungsausschusses**

Prof. Dr.-Ing. J. Grabe

**Gutachter**

1. Gutachter: Prof. Dr.-Ing. M. Abdel-Maksoud
2. Gutachter: Prof. Dr.-Ing. S. Krüger

**Datum der mündlichen Prüfung**

30. März 2017

# Abstract

The thesis presents the development of a three-dimensional inviscid boundary element method for the simulation of steady and unsteady partial sheet cavitation on marine propellers. The target application of the method focuses on the calculation of hydrodynamic loads generated by the flow field around and behind a cavitating propeller on the surrounding structures such as the ship hull and harbour bed. The governing equations of the potential flow problem with non-linear boundary conditions on the cavity surfaces are formulated for the steady and unsteady case. The numerical approach is based on the three-dimensional low-order panel method with quadrilateral panels and a constant distribution of source and dipole strengths. Sheet cavitation is modelled by the partially non-linear approach without re-meshing of the cavity surface grid. The steady sheet cavitation model is tested on two hydrofoils and a propeller. The results are validated against measured data and the impact of the grid discretisation level on the cavity shape is investigated. The unsteady sheet cavitation model is verified and validated for a hydrofoil and two propellers. Several unsteady flow characteristics are calculated and the influence of the inhomogeneous inflow on the cavitation behaviour is studied. Subsequently, the hull pressure fluctuations induced by a propeller subject to a uniform and non-uniform inflow are simulated and validated for different cavitation conditions. The impact of the unsteady sheet cavitation patterns and the non-uniform inflow on the hull pressure fluctuations is discussed. The numerical method is further applied to the prediction of hydrodynamic loads induced by a marine propeller flow during the manoeuvring process of a ship in the port area. The propeller flow is simulated for the non-cavitating and cavitating case. On the harbour bottom the propeller-induced pressures and velocities are evaluated and the maximal axial and tangential velocities are identified. The investigated examples demonstrate that the developed method is fast and usable for a wide range of hydrodynamic applications. The three-dimensional sheet cavitation model is found to be stable and the numerical results for the steady and unsteady cavitating flow agree well with the experimental data for a large number of examples.

*Die vorliegende Arbeit stellt die Entwicklung eines reibungsfreien Randelement-Verfahrens zur Simulation der stationären und instationären partiellen Schichtkavitation an Schiffspropellern vor. Die Anwendung der Methode richtet sich an die Berechnung der hydrodynamischen Belastungen, die durch das Strömungsfeld um und hinter einem kavitierenden Propeller auf die umgebenden Sturkturen, wie z.B. Schiffsaußenhaut und Gewässersohle, erzeugt werden. Die Grundgleichungen des Potentialströmungsproblems mit nichtlinearen Randbedingungen an den Kavitationsoberflächen werden für den stationären und instationären Fall formuliert. Der numerische Ansatz basiert auf einem dreidimensionalen Paneel-Verfahren niedriger Ordnung mit viereckigen Paneelen und einer konstanten Verteilung der Dipol- und Quellstärken. Schichtkavitation wird anhand des teilweise nicht-linearen Ansatzes modelliert und das Gitter der Kavitationfläche nicht verändert. Das stationäre Schichtkavitations-Modell wird an zwei Tragflügeln und einem Propeller getestet. Die Resultate werden mit Hilfe von Messdaten validiert und der*

*Einfluss des Gitter-Diskretisierungsgrades auf die Form der Schichtkavitation untersucht. Das instationäre Schichtkavitations-Modell wird an einem Tragflügel und zwei Propellern verifiziert und validiert. Mehrere instationäre Strömungseigenschaften werden berechnet und der Einfluss der inhomogenen Anströmung auf das Kavitationsverhalten analysiert. Darauf folgend werden die Druckschwankungen berechnet, die von einem Propeller in homogener und inhomogener Anströmung auf die Schiffsaußenhaut bei unterschiedlichen Kavitationsbedingungen induziert werden. Es wird untersucht, welche Einflüsse die instationäre Kavitation und die inhomogene Anströmung auf die Druckschwankungen an der Schiffsaußenhaut haben. Das numerische Verfahren wird ferner angewendet auf die Bestimmung von hydrodynamischen Belastungen, die durch eine Propellerströmung beim Manövriervorgang eines Schiffes im Hafenbereich auftreten. Die Propellerströmung wird für den nichtkavitierenden und kavitierenden Fall simuliert. Auf der Gewässersohle werden die induzierten Drücke und Geschwindigkeiten ausgewertet und die maximalen axialen und tangentialen Geschwindigkeiten ermittelt. Die untersuchten Beispiele zeigen, dass das entwickelte Verfahren schnell und für eine Vielzahl von hydrodynamischen Anwendungen geeignet ist. Das dreidimensionale Schichtkavitations-Modell ist stabil und die numerischen Ergebnisse für die stationäre und instationäre kavitierende Strömung zeigen ausgeprägte Übereinstimmungen mit den experimentellen Daten für eine Reihe von Beispielen.*

# Acknowledgements

The present work was developed during my employment as a Research Associate at the Institute of Fluid Dynamics and Ship Theory and within the research training group "Ports for Container Ships of Future Generations" at the Hamburg University of Technology.

First and foremost I would like to deeply acknowledge Prof. Dr.-Ing. Abdel-Maksoud for his support. He always showed a great interest in my work and enriched it with discussions and contributions. I would also like to thank my reviewer Prof. Dr.-Ing. Krüger and the chair of the examination board Prof. Dr.-Ing. Grabe for their participation in the examining board and their strong interest on my work.

I want to thank my colleagues at the Institute of Fluid Dynamics and Ship Theory who always supported me during my project. The teamwork and the conversations with them were at all times motivating and enriching. Stephan Berger, Anne Gerdes and Marzia Leonardi contributed to my motivation thanks to the friendly working environment. I would also like to thank Martin Greve and Markus Druckenbrod for the productive scientific teamwork and the inspiring discussions.

Special thanks go to the 'Deutsche Forschungsgemeinschaft' (DFG) for funding the project and giving me the opportunity to be part of an interdisciplinary group of researchers within the research training group. Thanks to the interdisciplinary character of the research group I had so many interesting conversations and gained an insight in several research areas.

Last of all, I appreciate the support of my family and friends who always gave me the greatest possible support and motivated me during all phases of the thesis.

# List of Figures

# List of Tables

# Nomenclature

## Abbreviations

| Symbol | Description |
|---|---|
| KCS | KRISO container ship |
| RANSE | Reynolds Averaged Navier Stokes Equations |
| SVA | Potsdam Model Basin |

## Numerical symbols

| Symbol | Description |
|---|---|
| $A_{i,j}$ | Influence function describing the dipole influence of the panel $i$ on the panel $j$ |
| $A_j$ | Area of the panel $j$ |
| $B_{i,j}$ | Influence function describing the source influence of the panel $i$ on the panel $j$ |
| $\eta_{(l,k)}^{cav}$ | Steady cavity thickness on a point related to the indices $(l,k)$ |
| $\eta_{(l,k)}^{cav,n}$ | Unsteady cavity thickness on a point related to the indices $(l,k)$ |
| $M$ | Number of body surfaces in the fluid domain |
| $\mu_i^{cav}$ | Dipole strength on the cavitating panel $i$ |
| $\mu_i^n$ | Dipole strength on the body panel $i$ |
| $\mu_{W,i}^n$ | Dipole strength on the wake panel $i$ |
| $N$ | Number of panels on the body surface |
| $N^{cav}$ | Number of cavitating panels on the body surface |
| $N_k$ | Number of panels on the body or wake surface in the radial direction |
| $N_l$ | Number of panels on the body surface in the circumferential direction |
| $N^m$ | Number of panels on the body surface $m$ |
| $N^{noncav}$ | Number of non-cavitating panels on the body surface |
| $N_{total}$ | Total number of panels |
| $N_W$ | Number of panels on the wake surface |
| $N_{W,l}$ | Number of panels on the wake surface in the circumferential direction |
| $N_W^m$ | Number of panels on the wake surface $m$ |
| $\phi_i^{cav}$ | Dipole on the cavitating panel $i$ |

| | |
|---|---|
| $\sigma_i^{cav}$ | Source strength on the cavitating panel $i$ |
| $\sigma_i^n$ | Source strength on the body panel $i$ |
| $t_n$ | Discrete time |
| $\mathbf{x}_i$ | Panel centre point |
| $\mathbf{x}_j^{col}$ | Collocation point |

### Physical symbols

| Symbol | Description |
|---|---|
| $a$ | Mean camber line distribution |
| $A_0$ | Propeller area |
| $A^{cav}$ | Cavity area |
| $A_E$ | Projected area |
| $\alpha$ | Angle of attack |
| $\alpha_0$ | Zero-lift angle of attack |
| $A_{ref}$ | Reference area |
| $b$ | Span width |
| $\mathbf{c}_0$ | Midpoint of a quad/panel |
| $C_d$ | Drag coefficient; $C_d = \frac{Drag}{1/2\rho\lvert\mathbf{V}_{ship}\rvert^2 A_{ref}}$ |
| $c_F$ | Friction resistance coefficient |
| $c$ | Chord length |
| $\mathbf{c}$ | Chord line |
| $\mathbf{c}_i$ | $i$-th corner point of a quad/panel, $i = 1, \ldots, 4$ |
| $C_l$ | Lift coefficient |
| $c_l$ | Lift coefficient per unit span |
| $C_{p,n}$ | Pressure coefficient based on the rotational speed; $C_{p,n} = \frac{p-p_{ref}}{1/2\rho(nD)^2}$ |
| $C_{p,nx}$ | Pressure coefficient at local radius $xR$, $x \in [0,1]$, based on the rotational speed; $C_{p,nx} = \frac{p-p_{ref}+\rho gxR}{1/2\rho(nD)^2}$ |
| $C_{p,v}$ | Pressure coefficient based on the ship speed; $C_{p,v} = \frac{p-p_{ref}}{1/2\rho\lvert\mathbf{V}_{ship}\rvert^2}$ |
| $D$ | Propeller diameter |
| $D_{hub}$ | Propeller hub diameter |
| $D$ | Drag |
| $\mathbf{e}_i$ | Base unit vector of the global coordinate system, $i = 1, 2, 3$ |
| $\eta$ | Camber height |
| $\eta^{cav}$ | Cavity thickness |
| $\eta$ | Propeller efficiency |
| $\eta_{max}$ | Maximal camber height |
| $\mathbf{F}$ | Force vector |
| $\Gamma$ | Circulation |

| | |
|---|---|
| $g$ | Gravity constant; $g = 9.81\text{m/s}^2$ |
| $\mathbf{I}$ | Identity matrix |
| $\mathbf{J}$ | Jacobian matrix |
| $J$ | Advance coefficient; $J = \frac{V_{ship,x}}{nD}$ |
| $k_q$ | Propeller torque coefficient |
| $k_t$ | Propeller thrust coefficient |
| $\Lambda$ | Aspect ratio |
| $\lambda$ | Scale factor |
| $L$ | Lift |
| $\mathbf{M}$ | Moment vector |
| $\mu$ | Dipole strength on the body surface; $\mu = -\phi$ |
| $\mu_W$ | Dipole strength on the wake surface; $\mu_W = -(\phi^+ - \phi^-)$ |
| $\mathbf{n}$ | Normal vector |
| $n$ | Propeller rotational speed |
| $\nu$ | Kinematic viscosity |
| $\Omega$ | Flow domain |
| $\omega$ | Angular velocity |
| $P$ | Pitch |
| $p$ | Pressure |
| $\Phi$ | Total potential |
| $\phi$ | Perturbation potential |
| $\phi_{\xi_d}$ | Potential at the detachment point of cavitation |
| $\Phi_\infty$ | Undisturbed potential |
| $\Phi^{inner}$ | Total inner potential |
| $\phi^{inner}$ | Disturbed inner potential |
| $\phi_{\xi_r}$ | Potential at the reattachment point of cavitation |
| $p^{[i]}$ | The $i$th harmonic of the pressure fluctuations |
| $p_\infty$ | Pressure at the free surface height $z_\infty$ |
| $P_{0.5}/D$ | Mean pitch ratio at relative radius $r/R = 0.5$ |
| $p_{ref}$ | Reference pressure; $p_{ref} = p_\infty + \rho g z_\infty$ |
| $P_{0.7}/D$ | Pitch ratio at relative radius $r/R = 0.7$ |
| $\psi$ | Pitch angle |
| $p_v$ | Vapour pressure of water |
| $R$ | Propeller radius |
| $r$ | Local radius; $r = xR$, $x \in [0, 1]$ |
| $Re$ | Reynolds number |
| $\rho$ | Fluid density |
| $S$ | Boundary of the flow domain $\Omega$; $S = \partial\Omega$ |
| $\mathbf{s} = (s_1, s_2, s_3)$ | Point defined in the local non-orthogonal coordinate system |
| $S_B$ | Body surface |
| $S_{B_C}$ | Reference sheet cavity surface on the body |

| | |
|---|---|
| $S_C$ | Sheet cavity surface |
| $s_d$ | Detachment point in the local non-orthogonal coordinate system |
| $\sigma$ | Source strength on the body surface; $\sigma = -\frac{\partial \phi}{\partial n}$ |
| $\sigma_n$ | Cavitation number based on the rotational speed; $\sigma_n = \frac{p_{ref} - p_v}{1/2\rho(nD)^2}$ |
| $\sigma_{nx}$ | Cavitation number at local radius $xR$, $x \in [0, 1]$, based on the rotational speed; $\sigma_{nx} = \frac{p_{ref} - p_v - \rho g x R}{1/2\rho(nD)^2}$. |
| $\sigma_v$ | Cavitation number based on the homogeneous inflow velocity; $\sigma_v = \frac{p_{ref} - p_v}{1/2\rho\lvert\mathbf{V}_{ship}\rvert^2}$ |
| $\sigma_W$ | Source strength on the wake surface; $\sigma_W = -(\frac{\partial \phi^+}{\partial n} - \frac{\partial \phi^-}{\partial n})$ |
| $S_\infty$ | Boundary at infinity |
| $s_r$ | Reattachment point in the local non-orthogonal coordinate system |
| $S_W$ | Wake surface |
| $S_{W_C}$ | Reference sheet cavity surface on the wake |
| $\mathbf{t}_i$ | Base covariant vector of the local non-orthogonal coordinate system, $i = 1, 2, 3$ |
| $\mathbf{t}^i$ | Base contra-variant vector of the local non-orthogonal coordinate system, $i = 1, 2, 3$ |
| $\tau_i$ | Base covariant vector of the local orthogonal coordinate system, $i = 1, 2, 3$ |
| $\tau^i$ | Base contra-variant vector of the local orthogonal coordinate system, $i = 1, 2, 3$ |
| $\theta$ | Skew angle |
| $t$ | Foil profile thickness |
| $T$ | Propeller thrust |
| $t$ | Time variable |
| $t_{max}$ | Maximal foil profile thickness |
| $Q$ | Propeller torque |
| $\mathbf{V}$ | Total velocity; $\mathbf{V} = \mathbf{v} + \mathbf{V}_\infty$ |
| $\mathbf{V}_A$ | Advance velocity |
| $V^{cav}$ | Cavity volume |
| $\mathbf{v}$ | Induced velocity |
| $\mathbf{V}_\infty$ | Reference velocity; $\mathbf{V}_\infty = -\mathbf{V}_{inflow} - \mathbf{V}_{rot}$ |
| $\mathbf{V}_{inflow}$ | Translational velocity; $\mathbf{V}_{inflow} = \mathbf{V}_{ship} - \mathbf{V}_{wake}$ |
| $\mathbf{V}_{rot}$ | Rotational velocity; $\mathbf{V}_{rot} = \omega \times \mathbf{x}$ |
| $(V_{s_1}, V_{s_2}, V_{s_3})$ | Total velocity in the local non-orthogonal coordinate system |
| $(v_{s_1}, v_{s_2}, v_{s_3})$ | Induced velocity in the local non-orthogonal coordinate system |
| $\mathbf{V}_{ship}$ | Ship speed |
| $\mathbf{V}_{wake}$ | Ship wake field |
| $(V_\xi, V_\eta, V_\zeta)$ | Total velocity in the local orthogonal coordinate system |
| $(v_\xi, v_\eta, v_\zeta)$ | Induced velocity in the local orthogonal coordinate system |
| $w$ | Wake fraction |

| | |
|---|---|
| $\mathbf{X} = (X, Y, Z)$ | Point defined in the space-fixed global coordinate system |
| $\mathbf{x} = (x, y, z)$ | Point defined in the body-fixed global coordinate system |
| $\xi = (\xi, \eta, \zeta)$ | Point defined in the local orthogonal coordinate system |
| $\xi_d$ | Detachment point in the local orthogonal coordinate system |
| $\xi_r$ | Reattachment point in the local orthogonal coordinate system |
| $z$ | Number of propeller blades |
| $z_\infty$ | Free surface height |

## Subscripts and superscripts

| **Symbol** | **Description** |
|---|---|
| $back$ | Suction side of a profile |
| $cav$ | Cavitating |
| $face$ | Pressure side of a profile |
| $i, j, k, m, n$ | Discretisation indices |
| $l_d$ | Index of the detachment point in the cross-wise direction |
| $l.e.$ | Leading edge |
| $l_r$ | Index of the reattachment point in the cross-wise direction |
| $model$ | Model scale |
| $noncav$ | Non-cavitating |
| $n$ | Index related to the time step |
| $PS$ | Pressure side |
| $SS$ | Suction side |
| $t.e.$ | Trailing edge |

# Contents

# Chapter 1
# Introduction

The chapter introduces the scientific background and the objectives of the present work. In the first section, 1.1, the motivation of the thesis is presented. The second section, 1.2, discusses the current state of research on numerical modelling of sheet cavitation by means of inviscid methods. The goals of the present work are formulated in Section 1.3 and the structure of the thesis is outlined in Section 1.4.

## 1.1 Motivation

The present work was developed within the research training group "Seaports for container ships of future generations: Interaction of ship, fluid, structure and soil". This research training group deals with the new challenges on harbour facilities for container ships of future generations. In recent years, container handling and container ship dimensions increased considerably and the requirements for the quay constructions, the soil, cranes etc. have changed (s. Grabe, 2011, p. VII). In order to meet the requirements of the future developments in modern harbour constructions, there is a need for extensive research in the fields of geotechnics, fluid dynamics, mechanics, naval architecture, control engineering and concrete structures. The present research work studies the fluid dynamical aspect of the problem. In particular, the work deals with flows over ship propellers in presence of sheet cavitation and the resulting oscillating hydrodynamic forces generated by the flow field around and behind the cavitating propeller on the surrounding structures, such as the ship hull or the harbour bed during the manoeuvring of a ship. During the manoeuvring of a ship the rotating propeller generates a slipstream. This slipstream can radiate an immense force on the harbour bottom and lead to soil erosion and scour developing. Due to the increasing container ship dimensions, the ship propellers operate in heavily loaded conditions and the associated propeller-induced unsteady forces are expected to become more problematic.

From the physical point of view there are four major aspects that are responsible for the development of propeller-induced periodic hydrodynamic forces: the rotating vortex sheets induced by the circulation on the propeller blades, the displacement effect due to the blade thickness, the displacement effect due to the cavity thickness and the unsteady variation of the cavity volume (s. ITTC, 1999, p. 7). The present work analyses to what extent sheet cavitation influences the characteristics of a propeller flow and the magnitude of the induced hydrodynamic forces. Cavitation in general is a physical phenomenon that is commonly observed in marine propeller flows, especially in case of high-speed vessels. It occurs in a liquid flow when the pressure in the flow falls below the vapour pressure of the liquid such that gas and vapour bubbles emerge in the liquid. In contrast to the physical phenomenon of boiling, the phase change from liquid to vapour is driven by a decrease of the static pressure while the temperature of the liquid remains constant (s. Carlton, 2007, p. 207f.). Cavitation can cause several undesirable effects, e.g. reduction of the propeller performance, increase of propeller-induced hull pressure fluctuations, noise, vibrations and erosion on propeller blades (s. Young, 2002, p. 2f.). There are different types of cavitation in a propeller flow: bubble cavitation, tip and hub vortex cavitation, cloud cavitation and sheet cavitation. Apart from tip vortex cavitation, sheet cavitation is the most common type of cavitation that occurs in a marine propeller flow. Sheet cavitation appears in the shape of an attached vapour region on the propeller blades (s. Figure 1.1). The vapour region usually begins at the leading edge of the blade profiles and either closes at the blade surface (partial sheet cavitation) or extends beyond the trailing edge of the blade profiles (supercavitation). This work exclusively investigates partial sheet cavitation that is allowed to occur on both sides of the propeller blade surface. Sheet cavitation appearing at the suction side is called back cavitation, while sheet cavitation appearing on the pressure side is called face cavitation (s. Young, 2002, p. 42). Sheet cavitation and in particular the time-dependent volume variations of sheet cavitation were found to be the most significant factor in the prediction of hull pressure fluctuations. Indeed, sheet cavitation can have a considerable volume and the dynamic behaviour of the vapour volume can generate pressure fluctuations at frequencies of first order, which are five to fifteen times greater than in the case of a non-cavitating propeller flow (s. ITTC, 1999, p. 2).

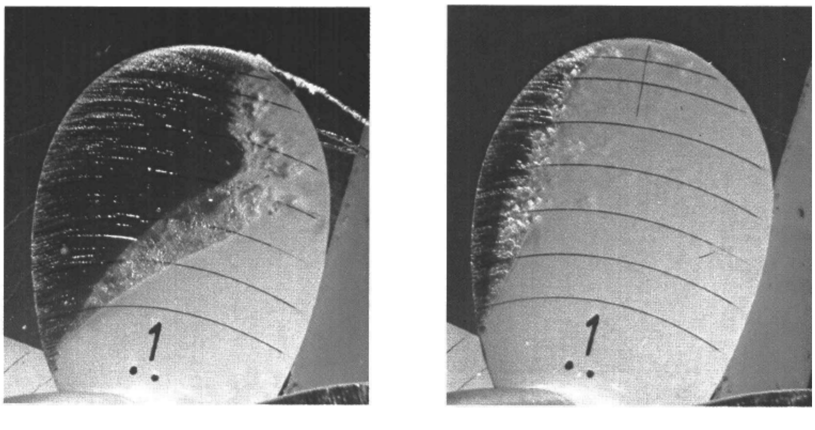

Figure 1.1: Sheet cavitation on MARIN S-Propeller blade (taken from Kuiper (1981, p. XVI))

For the simulation of sheet cavitation on marine propellers a three-dimensional numerical method is used in the present work. The advantage of numerical methods is their time and cost efficiency, but it has to be analysed whether the error rate of these methods is acceptable or not. Model tests serve the purpose of validating numerical tools and increase their accuracy and reliability. Due to the huge developments in computer sciences in recent years, a substantial progress in the field of numerical propeller hydrodynamics and design was achieved. Nowadays, three kinds of methods are mainly represented in propeller design: propeller series based methods, viscous flow solvers and potential flow solvers. The propeller series based methods are based on empirical data evaluated for various propeller series by varying propeller parameters like the number of blades, pitch ratio, area ratio etc. An example of such series are the Wageningen B-Series (s. Carlton, 2007, p. 103f.). The disadvantage of these methods is their limitation concerning cavitation estimation and prediction of unsteady characteristics of propeller flows, such as propeller-induced hull forces or transient cavity volume variations. Viscous and potential flow solvers play an important role in applied ship and propeller research and design. They are an adequate alternative to model tests, which usually are very time- and cost-consuming. Viscous flow solvers such as the Reynolds Averaged Navier Stokes Equations (RANSE) based methods include the viscous character of the flow and are found to deliver more accurate results than potential flow solvers. At the same time these methods are very time-consuming. Potential flow solvers are based on the assumption that the fluid is incompressible and the flow is non-viscous and irrotational. These assumptions reduce the complexity of the flow calculations and lead to fast computational methods. Nowadays, the most commonly used methods based on potential flow theory for the prediction of propeller hydrodynamics in presence of sheet cavitation are the inviscid boundary element methods, which are also called panel methods. Panel methods describe the lifting and displacement effects of a solid body by distributing dipole, source and sink strengths over the body's surface. The main reason for the popularity of panel methods in propeller design is their flexibility and short computation time. The short CPU time enables parameter studies during the propeller design process and an accurate determination of unsteady sheet cavitation and propeller-induced pressure fluctuations in an acceptable time frame. These advantages were essential for the decision to use a panel method in the present work. The applied panel method is able to simulate the flow around arbitrary propeller blade and hydrofoil geometries, to use different motion models for several bodies in the fluid domain and to calculate the unsteady hydrodynamic blade forces and moments.

For the mathematical description of the sheet cavitation phenomenon panel methods provide three different approaches. The approaches differ in their application of the boundary conditions for sheet cavitation and the treatment of the panel grid. The boundary conditions can be applied directly on the cavity surface or on an auxiliary surface beneath the cavity sheet. Furthermore, the surface grid where the boundary conditions are applied can be re-meshed or it can be kept the same during the iteration procedure. In the present work the partially non-linear approach without the re-meshing of the surface grid is applied. The boundary conditions are defined not directly on the cavity surface but on an auxiliary surface underneath the cavity sheet and the pressure within the cavity sheet is assumed to be equal to the vapour pressure of water. The use of this model delivers a fast and flexible numerical method, which can easily be extended with regards to other common types of cavitation like tip and hub vortex cavitation.

## 1.2 Current state of research

In the past years a considerable amount of research work has been devoted to the numerical modelling of sheet cavitation by means of potential flow theory based methods. There are three different numerical approaches based on potential flow theory: lifting-line methods, lifting-surface methods and boundary element methods (s. Carlton, 2007, p. 163). Lifting-line methods neglect the thickness of the blade profiles and only consider the lifting problem (s. Carlton, 2007, p. 163). In order to model the lifting effect of the body, vortices are distributed on a lifting line, which starts at the propeller hub and ends at the propeller tip. Lifting-surface methods also neglect the thickness of the body but use a lifting surface for the distribution of the vortices instead of a lifting line, i.e. the vortex strengths are allowed to vary along the circumferential direction of the propeller profiles (s. Carlton, 2007, p. 163). A detailed description of the lifting-line and -surface methods can be found in Carlton (2007). The third type of methods are the inviscid boundary element methods, which are also called panel methods. They describe not only the lifting effect of a body but also its displacement effect, which arises from the thickness of the body. The displacement effect is described by distributing source and sink strengths over the body's surface. A detailed description of the theory and numerics of panel methods is published by Katz and Plotkin (2001).

The first developments of numerical cavitation models by means of lifting-surface methods go back to the 1970s and 80s. Kerwin and Lee (1978) developed a lifting-surface method for the determination of steady and unsteady marine propeller performance. This method was first applied by Lee (1979) on the calculation of sheet cavitation. Breslin et al. (1982) used the lifting-surface method to study the pressure fluctuations induced by blade cavitation on the ship hull. Kerwin et al. (1986) modified the method of Lee (1979) by including the non-linear effect of the leading edge radius on the cavity solution. A similar lifting-surface method was applied by Gent (1994) for the prediction of pressure fluctuations induced by a propeller flow under consideration of unsteady sheet cavitation. Similarly, Szantyr (1994) used a lifting-surface method to investigate cavitating marine propeller flows in a non-uniform inflow.

In the 1980s and 90s the development of sheet cavitation models by means of inviscid boundary element methods gained in importance. Lee (1987) and Hsin (1990) developed a panel method for the analysis of steady and unsteady propeller flows. Fine (1992) extended this method for the non-linear analysis of unsteady cavitating flows around marine propellers. Kinnas and Fine (1992) and Kinnas and Fine (1993) applied the method of Fine (1992) to investigate steady and unsteady sheet cavitation on hydrofoils and propellers. Kinnas (1992) modified the panel method for the simulation of supercavitation on hydrofoils. Since then an extensive research has been conducted on the modelling of cavitating propeller flows with the help of panel methods by Kinnas and his group at the University of Texas at Austin. Mueller and Kinnas (1999) predicted the time-dependent cavitation on propellers subject to non-uniform inflow and modified the panel method in order to be able to predict mid-chord cavitation detachment. Young and Kinnas (2001) investigated unsteady mid-chord face and back propeller cavitation and Young (2002), Young and Kinnas (2003a) and Kinnas and Young (2003) applied the panel method to the simulation of supercaviting and surface-piercing propeller flows. Young and Kinnas (2003b) studied the hydro-elastic effects by coupling the boundary element method with a transient finite element method. The effect of a free water surface on sheet cavitation patterns was investigated by Bal and Kinnas (2002). Natarajan (2003) calculated rudder cavitation by means of the panel method and studied the interaction between rudder and propeller. Furthermore, Lee and Kinnas (2004) used the boundary element method to predict unsteady blade sheet and tip vortex cavitation, while Lee and Kinnas (2005) simulated unsteady sheet cavitation on propellers with the complete tunnel wall effect. Sun and Kinnas (2006) developed a Viscous/Inviscid Interactive method for the simulation of cavitating flows around a marine propeller. Pan (2009) applied the viscous/inviscid interactive approach on the study of cavitating hydrofoils and propellers with non-zero trailing edge thickness.

Parallel to the developments at the University of Texas at Austin, extensive research has been conducted by several researchers around the world. Gans (1994) derived a higher-order panel method for the prediction of time-dependent sheet cavitation. Krishnaswamy (2000) developed a low-order panel method for partially cavitating two-dimensional hydrofoils with focus on the modelling of the cavity closure. Achkanadze and Krasilnikov (2001) developed a velocity-based boundary element method for the calculation of partial cavities on wing and propeller geometries. Dang (2001) investigated unsteady partial sheet cavitation on propellers. Salvatore and Esposito (2001) and Salvatore et al. (2003) employed a boundary element method with a non-linear partial sheet cavitation model and included viscosity effects via a viscous/inviscid coupling approach. The hydrodynamical/hydro-acoustical analysis of cavitation on marine propellers was investigated by Salvatore and Ianniello (2002). Salvatore et al. (2011) presented results computed by the boundary element method based on the approach of Salvatore and Esposito (2001) for a cavitating propeller in uniform inflow. Noticeable effort was made by Vaz et al. (2003) and Vaz (2005) in employing different numerical modelling concepts for sheet cavitation prediction on hydrofoils and propellers. Vaz (2005) provided an in-depth analysis of three types of models for partial sheet cavitation as well as supercavitation and presented several validation studies and examples. Based on the developments of Vaz (2005), Falcão de Campos et al. (2006) performed an analysis on the influence of reduced frequency on the two-dimensional partial sheet cavitation behaviour for a foil in a gust. Additionally, Phoemsapthawee et al. (2009) presented a partial sheet cavitation model and its implementation in a boundary element approach and applied their numerical method to the calculation of hydrodynamical forces and the performance of a propeller or rudder working in an unsteady flow field. An alternative panel method for the prediction of sheet cavitation on marine propeller flows was proposed by Ando and Nakatake (2001). Their method uses source distributions on the blade surface and discrete vortex distributions arranged on the camber surface according to a quasi-continuous vortex lattice method. Based on the approach of Ando and Nakatake (2001), Kanemaru and Ando (2009) analysed numerically steady and unsteady sheet cavitation on marine propellers. The same method was also applied by Kanemaru and Ando (2011) in order to investigate the influence of sheet cavitation on propeller-induced loads on a ship hull.

## 1.3 Objectives

As the previous section shows, an extensive amount of work has been devoted to the development of cavitation models by means of inviscid boundary element methods. Although boundary element methods have been expanded and validated by experimental data for many years, there is still room for improvement concerning the reliable prediction of unsteady sheet cavitation. There are diverse publications investigating and validating the unsteady sheet cavitation patterns, but there are only limited studies focusing on the validation of the time-dependent sheet cavitation volume variations. This fact can be traced back to the complexity of comparing the measured and computed cavity volume variations. Alternatively, the comparison of calculated and measured hull pressure fluctuations induced by a cavitation propeller flow can serve as validation (s. ITTC, 1999, p. 9). The time-dependent volume variations of sheet cavitation and in particular the second derivative of the cavity volume is found to be proportional to the magnitude of the hull pressure fluctuations (s. Kanemaru and Ando, 2011, p. 372). The current status of computational methods for the prediction of propeller-induced pressure fluctuations is still in the developing stage and there is need for further research.

The major objective of the present work is to develop a computationally efficient, robust and accurate numerical method for the simulation of steady and unsteady partial sheet cavitation in marine propeller flows. The target application of the employed method is the prediction of the sheet cavitation extent on propeller blades and the determination of the impact of unsteady sheet cavitation on the propeller flow characteristics and propeller-induced hydrodynamic loads. For the development of a numerical sheet cavitation model an existent boundary element method called *pan*MARE is used and the sheet cavitation model is build upon it. The simulation tool *pan*MARE was originally developed by Hundemer (2013) and is constantly extended by the research group of the Institute of Fluid Dynamics and Ship Theory (FDS) at the Hamburg University of Technology. It is based on a three-dimensional panel method with quadrilateral panel elements and a constant source and dipole distribution over the panels. The sheet cavitation model is integrated in the panel method *pan*MARE in three main steps. In the first step different modelling approaches are discussed and the model that promises to be the most efficient computationally and the most suitable for the target application is chosen. The employed sheet cavitation model must be able to predict the extent of sheet cavitation, to calculate the pressure distribution and cavity thickness within the cavity sheet and to reproduce the lifting and displacement effect of the cavity volume. In the second step, the mathematical model for steady and unsteady sheet cavitation is implemented in the overall numerical algorithm. The goal of this step is to derive a computationally stable numerical procedure. In the third step, the robustness and accurateness of the numerical method are proven. The development of an accurate and robust unsteady sheet cavitation model is crucial for the prediction of the time variation of the cavity shape and cavity volume and the resulting pressure fluctuations. The robustness is proven by studying the numerical behaviour of the model for different geometries (hydrofoils and propellers) and by analysing the influence of the surface grid resolution on the calculated sheet cavitation shape. The accuracy of the sheet cavitation model is tested in two steps. First, the computed sheet cavitation shapes are verified and validated by several examples in steady and unsteady flow conditions. Second, the ability of the numerical method to accurately predict the time-dependent cavitation volume variations is proven by comparing computed and measured propeller-induced hull pressure fluctuations in the presence of sheet cavitation.

## 1.4 Overview

The present work consists of eight chapters. Chapter 1 presents the motivation, literature review and objectives of the thesis. In Chapter 2 different coordinate systems and motion models are introduced and the governing equations for an inviscid propeller flow are formulated. Chapter 3 describes the numerical approach based on the three-dimensional panel method. In Chapter 4 the governing equations of the steady and unsteady sheet cavitation model are formulated and their implementation in the overall numerical algorithm is outlined. The numerical sheet cavitation model is validated and verified on several hydrofoil and propeller geometries in steady and unsteady flow conditions in Chapter 5. Chapter 6 focuses on the numerical calculation and validation of propeller-induced hull pressure fluctuations. In Chapter 7 an application example is studied where the flow around a propeller is simulated during the manoeuvring process of a ship and the induced loads on the harbour bed are analysed. Chapter 8 concludes the present work and its findings and presents perspectives for future research.

# Chapter 2
# Governing equations

The goal of this chapter is to describe the underlying mathematical and physical problem of the present work and to derive the governing equations used for the modelling of marine propeller flows. In the first section, different coordinate systems and motion models of a propeller are described. In the second and third section, the mathematical model based on potential flow theory is introduced and the boundary value problem is formulated. In the fourth section, the determination of flow characteristics is presented.

## 2.1 Coordinate systems and motion models

The description of a mathematical problem can often be simplified by choosing a suitable coordinate system. In this work two global Cartesian and two local curvilinear coordinate systems are used for the modelling purposes. They are presented in the first part of this section, Chapter 2.1.1. The second part, Chapter 2.1.2, deals with different types of propeller motion and their mathematical description.

### 2.1.1 Reference coordinate systems

In the present work, the flow past a single body or multiple bodies with an individual rotational and/or translational speed is considered. For that purpose two different reference frames are defined: a Cartesian reference frame that is fixed in space and a Cartesian reference frame moving in unison with the considered body. Both Cartesian systems are defined by the base unit vectors $\mathbf{e}_i$, $i = 1, 2, 3$. The reference frame fixed in space is described by the coordinates $\mathbf{X} = (X, Y, Z)$, whereas the body-fixed Cartesian reference frame is identified by the coordinates $\mathbf{x} = (x, y, z)$ and the $z$-axis is positive upwards (s. Figure 2.1).

For different applications, for example for the treatment of the sheet cavitation model, to be introduced later, it is more convenient to use a local surface-fitted curvilinear coordinate system. Thus, two additional local body-fixed coordinate systems are introduced. The first one consists of orthogonal base unit vectors $\tau_i$, $i = 1, 2, 3$ and local coordinates $\xi = (\xi, \eta, \zeta)$. The second one is composed of non-orthogonal base unit vectors $\mathbf{t}_i$, $i = 1, 2, 3$ and the local coordinates are described by the vector $\mathbf{s} = (s_1, s_2, s_3)$. In a

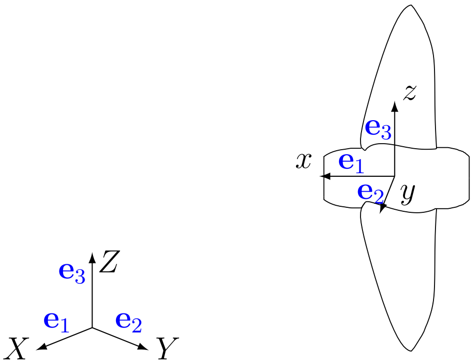

Figure 2.1: Space and body fixed coordinate systems

local orthogonal coordinate system, all unit vectors are aligned perpendicular as shown in Figure 2.2a on an example grid. In a local non-orthogonal coordinate system, the tangential vectors are perpendicular to the normal vector but the tangential vectors are not orthogonal amongst each other, as shown in Figure 2.2b.

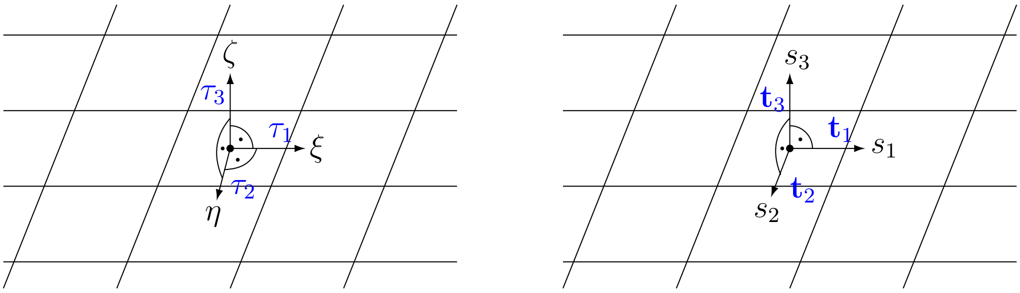

(a) Local orthogonal coordinate system

(b) Local non-orthogonal coordinate system

Figure 2.2: Local surface-fitted coordinate systems

For the construction of a local coordinate system, a quadrilateral with the edge points $\mathbf{c}_i$, $i = 1, \ldots, 4$ and the centroid $\mathbf{c}_0$ is considered (s. Figure 2.3). For both systems it is assumed that the origin of the system lies at the centroid of the quadrilateral. The orthogonal system is then defined by the following unit vectors:

$$\tau_1 = \frac{(\mathbf{c}_1 - \mathbf{c}_4) + (\mathbf{c}_2 - \mathbf{c}_3)}{|(\mathbf{c}_1 - \mathbf{c}_4 + \mathbf{c}_2 - \mathbf{c}_3)|}, \quad \tau_3 = \frac{(\mathbf{c}_4 - \mathbf{c}_2) \times (\mathbf{c}_1 - \mathbf{c}_3)}{|(\mathbf{c}_4 - \mathbf{c}_2) \times (\mathbf{c}_1 - \mathbf{c}_3)|}, \quad \tau_2 = \frac{\tau_3 \times \tau_1}{|\tau_3 \times \tau_1|}. \tag{2.1}$$

The local non-orthogonal coordinate system is defined in the way that the tangential vectors $\mathbf{t}_1$ and $\mathbf{t}_2$ pass through the midpoints of the quad edges $c_1\bar{}c_2$ and $c_4\bar{}c_1$, respectively. The normal vector is the vector that is perpendicular to both tangential vectors:

$$\mathbf{t}_1 = \frac{(\mathbf{c}_1 - \mathbf{c}_4) + (\mathbf{c}_2 - \mathbf{c}_3)}{|(\mathbf{c}_1 - \mathbf{c}_4 + \mathbf{c}_2 - \mathbf{c}_3)|}, \quad \mathbf{t}_2 = \frac{(\mathbf{c}_4 - \mathbf{c}_3) + (\mathbf{c}_1 - \mathbf{c}_2)}{|(\mathbf{c}_4 - \mathbf{c}_3 + \mathbf{c}_1 - \mathbf{c}_2)|}, \quad \mathbf{t}_3 = \frac{\mathbf{t}_1 \times \mathbf{t}_2}{|\mathbf{t}_1 \times \mathbf{t}_2|}. \tag{2.2}$$

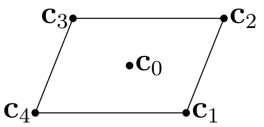

Figure 2.3: Edge points and the midpoint of a quad

The transformations from a global to a local system and vice versa are described in detail in Appendix B.

### 2.1.2 Motion models of a propeller

There are three different types of motion of a fluid element: translation, rotation and deformation. In this work, no deformation of the fluid particles is considered, the body is assumed to be rigid. Thus, for each considered body its translational velocity and/or its angular velocity and the axis about which it rotates must be defined. The translation of fluid particles is described by the vector:

$$\mathbf{V}_{inflow} = (U, V, W), \tag{2.3}$$

where $U, V$ and $W$ are constant velocity components in the $x, y$ and $z$ direction, respectively. For a propeller, the body-fixed reference system translates with an inflow velocity $\mathbf{V}_{inflow}$ =$\mathbf{V}_{ship}$ - $\mathbf{V}_{wake}$, where $\mathbf{V}_{ship} = (V_{ship}, 0, 0)$ is the ship speed and $\mathbf{V}_{wake}$ is the ship wake field. The wake describes the velocity field at the aft-ship and is the result of the interaction between several effects. There is a potential induced part, a viscous part and a part which is induced through the waves. Since the ship propeller operates in the wake of a ship, the actual inflow velocity seen by the propeller is lower than the ship speed. The percentage of the ship speed seen by the propeller in the axial direction is described by the wake fraction: $w$= $1 - {}^{V_{A,x}}/_{V_{ship}}$, where $\mathbf{V}_A$ is the advance velocity. In ship theory there are two different definitions of the wake: the effective wake and the nominal wake. The nominal wake is the wake field that can be observed without the existence of a propeller. In contrast, the effective wake is the wake field that develops due to the interaction between the propeller inflow velocity field and the propeller presence (s. Carlton, 2007, p. 68ff.).

For a non-uniform inflow, i.e. $\mathbf{V}_{wake} \not\equiv \mathbf{0}$, the velocity vector $\mathbf{V}_{wake}$ is defined as follows:

$$\mathbf{V}_{wake} = \mathbf{V}_{ship} - \mathbf{V}_A. \tag{2.4}$$

In case of a uniform inflow to the body, the fluid particle's motion does not depend on time in the body-fixed Cartesian reference frame, i.e. the flow is time-independent. Since the inflow velocity of the propeller is not uniform in general, an unsteady flow is considered in this work.

In addition to the translational velocity, the rotation of a propeller plays an important role. The rotation velocity of a propeller is described by the vector:

$$\mathbf{V}_{rot}(\mathbf{x}) = \omega \times \mathbf{x}, \tag{2.5}$$

where $\mathbf{x}$ is the position vector and $\omega$ is the angular velocity. The overall undisturbed velocity relative to the propeller is then given by (s. Figure 2.4):

$$\mathbf{V}_{\infty}(\mathbf{x}) = -\mathbf{V}_{inflow}(\mathbf{x}) - \mathbf{V}_{rot}(\mathbf{x}). \tag{2.6}$$

In addition, the flow of a propeller can be subject to a pitch, heave, surge, yaw, roll or sway motion. Heave, surge and sway motions are three aspects of translation, whereas the components of the rotational motion are pitch, yaw and roll. In order to model this motion, the propeller is allowed to move according to a prescribed periodical linear or rotational ship motion along the $x, y$ and $z$-axis, respectively. The resulting translational and rotational velocities are then defined as functions of time:

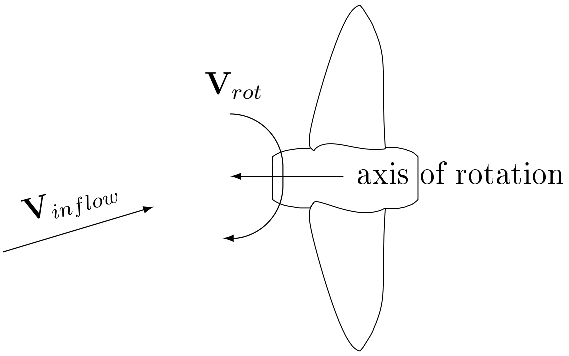

Figure 2.4: Motion model of a marine propeller

$$\mathbf{V}_{inflow}(t) = (U(t), V(t), W(t)), \quad \mathbf{V}_{rot}(\mathbf{x}, t) = \omega(t) \times \mathbf{x}. \tag{2.7}$$

For example, in heaving, a ship is accelerated upwards and downwards along the vertical axis, such that for the parallel velocity of the propeller it holds:

$$\mathbf{V}_{inflow}(t) = (U, 0, W(t)), \tag{2.8}$$

where $U$ is constant and $W(t)$ describes the time-dependant periodical heave motion of the ship in the $z$ direction.

## 2.2 Governing equations for a potential flow

This section describes the modelling approach used in this work to simulate propeller flows. The approach is based on potential flow theory where the following assumptions about the fluid and flow characteristics are made:

- The fluid is incompressible.
- The flow is irrotational and non-viscous. Irrotational means that the fluid particles do not rotate about their own axis, they keep their orientation when following a streamline of the flow.

Incompressible and non-viscous fluids are denoted as ideal fluids and their flow is usually called potential flow. Additionally, the assumption is made that the bodies contained in the flow domain are rigid, i.e. deformation of the bodies is not considered. Based on these assumptions, the governing equations for a propeller flow are derived and introduced below.

Consider a flow of interest which lies in a region $\Omega \in \mathbf{R}^3$ (s. Figure 2.5). For a potential flow, the Navier-Stokes equations for mass and momentum simplify to the three-dimensional Laplace's equation $(2.9)$ and unsteady Bernoulli equation $(2.10)$ (s. Katz and Plotkin, 2001, p. 27f.):

$$\nabla^2\Phi = \frac{\partial^2\Phi}{\partial^2 x} + \frac{\partial^2\Phi}{\partial^2 y} + \frac{\partial^2\Phi}{\partial^2 z} = 0, \tag{2.9}$$

$$p = p_\infty + \frac{\rho}{2}\Big(|\nabla\Phi_\infty|^2 - |\nabla\Phi|^2\Big) - \rho\frac{\partial\phi}{\partial t} + \rho g(z_\infty - z), \tag{2.10}$$

where $\Phi = \Phi(\mathbf{x}, t) = \phi(\mathbf{x}, t) + \Phi_\infty(\mathbf{x}, t)$ is the total velocity potential, which is composed of the disturbed potential $\phi$ and the undisturbed free stream potential $\Phi_\infty$, $p = p(\mathbf{x}, t)$ is the local pressure and $\mathbf{x} \in \Omega$ and $t$ are the space and time variables, respectively. The constants $p_\infty$, $\rho$, $g$ and $z_\infty$ are the atmospheric pressure, water density, gravity constant and the distance to the free water surface, respectively. The velocity potential $\Phi_\infty$ determines the motion of the body and the dynamical behaviour of the flow.

The boundary of the flow domain is denoted by $S = \partial\Omega$. Consider now one or more bodies that are submerged in a potential flow. Then there are three types of boundaries in the flow domain (s. Figure 2.5):

- the solid body surface $S_B$,
- the wake sheet of a lifting body $S_W$ and
- the boundary at infinity $S_\infty$.

The overall boundary $S$ is then defined as the union of the single boundaries: $S = S_B \cup S_W \cup S_\infty$.

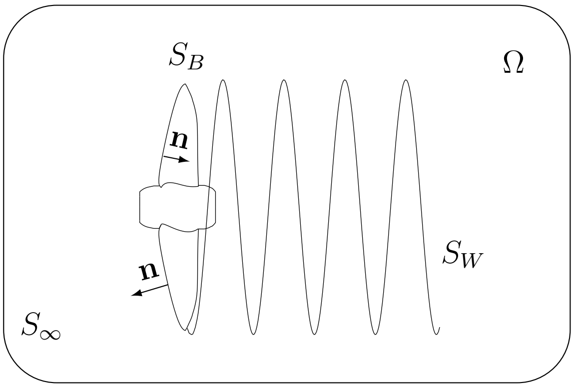

Figure 2.5: Potential flow domain and boundaries

### 2.2.1 General solution of the Laplace's equation

The Laplace's equation is an elliptic linear equation. Each solution of the Laplace equation is a harmonic function or potential function and can be derived from the divergence theorem (s. Katz and Plotkin, 2001, p. 8):

$$\int_\Omega \nabla \cdot \mathbf{F} dV = \int_S \mathbf{F} \cdot \mathbf{n} dS, \tag{2.11}$$

where $\mathbf{n}$ is the normal vector which points outwards the body (s. Figure 2.5) and $\mathbf{F}$ is a continuously differentiable vector field. According to Katz and Plotkin (2001, p. 44f.), the function $\mathbf{F}$ can be replaced by $\Phi_1 \nabla \Phi_2 - \Phi_2 \nabla \Phi_1$ such that one obtains:

$$\int_\Omega \nabla \cdot (\Phi_1 \nabla \Phi_2 - \Phi_2 \nabla \Phi_1) dV = \int_S (\Phi_1 \nabla \Phi_2 - \Phi_2 \nabla \Phi_1) \cdot \mathbf{n} dS. \tag{2.12}$$

From this relation, it follows:

$$\int_\Omega (\Phi_1 \nabla^2 \Phi_2 - \Phi_2 \nabla^2 \Phi_1) dV = \int_S (\Phi_1 \nabla \Phi_2 - \Phi_2 \nabla \Phi_1) \cdot \mathbf{n} dS. \tag{2.13}$$

Referred to Katz and Plotkin (2001, p. 45), the functions $\Phi_1$ and $\Phi_2$ can be defined as follows:

$$\Phi_1(\mathbf{x}, t) = \frac{1}{\|\mathbf{x} - \mathbf{P}\|} = \frac{1}{r(\mathbf{x}, \mathbf{P})}, \quad \Phi_2(\mathbf{x}, t) = \Phi(\mathbf{x}, t), \quad \forall \mathbf{x}, \mathbf{P} \in \Omega, \tag{2.14}$$

where $\mathbf{x}$ and $\mathbf{P}$ are points in the flow domain and $r$ is the distance from $\mathbf{P}$ to $\mathbf{x}$. The function $\Phi_2$ fulfils the Laplace equation for all $\mathbf{P} \in \Omega$ and it holds $\nabla^2 \Phi_2 = 0$. From this observation, Equation (2.13) results in:

$$-\int_{\Omega}\Phi_2\nabla^2\Phi_1 dV=\int_{\in S}(\Phi_1\nabla\Phi_2-\Phi_2\nabla\Phi_1)\cdot\mathbf{n}dS. \tag{2.15}$$

The function $\Phi_1$ shows a singularity as $\mathbf{P}$ is approached, i.e. $\mathbf{x}\to\mathbf{P}$. For this reason a case distinction is made for the term on the left hand side of the Equation (2.15). The following cases are investigated:

- Point $\mathbf{P}$ lies inside the flow domain $\Omega$, but not on or inside the body boundary $S_B$. In this case, point $\mathbf{P}$ must be excluded from the integration volume (s. Katz and Plotkin, 2001, p. 45). By excluding a small sphere around the point with radius $\varepsilon$, one obtains an additional boundary, namely the boundary of the sphere with radius $\varepsilon$ (s. Figure 2.6a):

$$\begin{aligned}\underbrace{-\int\limits_{\Omega/\mathbf{P}}\Phi_2\nabla^2\Phi_1 dV}_{=0\text{ (since }\nabla^2\Phi_1=0)}&=\int\limits_{S+S_{sphere}}(\Phi_1\nabla\Phi_2-\Phi_2\nabla\Phi_1)\cdot\mathbf{n}dS\\&=\int\limits_{S}(\Phi_1\nabla\Phi_2-\Phi_2\nabla\Phi_1)\cdot\mathbf{n}dS+\int\limits_{S_{sphere}}(\Phi_1\nabla\Phi_2-\Phi_2\nabla\Phi_1)\cdot\mathbf{n}dS.\end{aligned} \tag{2.16}$$

- Point $\mathbf{P}$ lies inside $\Omega$ and on the body boundary $S_B$. In this case, point $\mathbf{P}$ must also be excluded from the integration volume (s. Katz and Plotkin, 2001, p. 46). By excluding a small hemisphere around the point that lies outside the body, one obtains an additional boundary, namely the boundary of the hemisphere with radius $\varepsilon$ (s. Figure 2.6b):

$$\begin{aligned}0&=\int\limits_{S+S_{hemisphere}}(\Phi_1\nabla\Phi_2-\Phi_2\nabla\Phi_1)\cdot\mathbf{n}dS\\&=\int\limits_{S}(\Phi_1\nabla\Phi_2-\Phi_2\nabla\Phi_1)\cdot\mathbf{n}dS+\int\limits_{S_{hemisphere}}(\Phi_1\nabla\Phi_2-\Phi_2\nabla\Phi_1)\cdot\mathbf{n}dS.\end{aligned} \tag{2.17}$$

- Point $\mathbf{P}$ lies inside the body with boundary $S_B$. In this case, the inner potential of the flow inside the body is considered and denoted by $\Phi^{inner}$. Since the distance function $\Phi_1$ is not singular for this case ($\mathbf{x}$ is not inside $S_B$), it follows from Equation (2.15):

$$0=-\int_{S_B}(\Phi_1\nabla\Phi_2^{inner}-\Phi_2^{inner}\nabla\Phi_1)\cdot\mathbf{n}dS. \tag{2.18}$$

  The minus sign in front of the equation appears since the normal vector inside the body shows in the opposite direction to the normal vector outside the body (s. Figure 2.5).

For the integrals over the sphere and hemisphere there exists an analytical solution for $\varepsilon \rightarrow 0$ (s. Katz and Plotkin, 2001, p. 46):

$$\begin{aligned}\int_{S_{sphere}} (\Phi_1 \nabla \Phi_2 - \Phi_2 \nabla \Phi_1) \cdot \mathbf{n} dS &= -4\pi \Phi_2(\mathbf{P}, t) = -4\pi \Phi(\mathbf{P}, t), \\ \int_{S_{hemisphere}} (\Phi_1 \nabla \Phi_2 - \Phi_2 \nabla \Phi_1) \cdot \mathbf{n} dS &= -2\pi \Phi_2(\mathbf{P}, t) = -2\pi \Phi(\mathbf{P}, t).\end{aligned} \tag{2.19}$$

In order to include the influence of the inner potential, Equation $(2.18)$ is added to $(2.16)$ and $(2.17)$ such that one obtains:

$$\begin{aligned}\epsilon \Phi(\mathbf{P}, t) = \int_{S_B} & (\Phi_1 \nabla (\Phi - \Phi^{inner}) - (\Phi - \Phi^{inner}) \nabla \Phi_1) \cdot \mathbf{n} dS \\ & + \int_{S/S_B} (\Phi_1 \nabla \Phi - \Phi \nabla \Phi_1) \cdot \mathbf{n} dS,\end{aligned} \tag{2.20}$$

where $\epsilon$ is defined by:

$$\epsilon = \begin{cases} 4\pi & \text{if point } \mathbf{P} \text{ lies outside the body,} \\ 2\pi & \text{if point } \mathbf{P} \text{ lies on the body boundary } S_B. \end{cases} \tag{2.21}$$

The boundary $S/S_B$ consists of the boundary at infinity $S_\infty$ and the wake surface $S_W$. The disturbed potential at infinity can be defined as:

$$\epsilon \Phi_\infty(\mathbf{P}, t) = \int_{S_\infty} (\Phi_1 \nabla \Phi - \Phi \nabla \Phi_2) \cdot \mathbf{n} dS. \tag{2.22}$$

The wake surface is a thin surface, which is composed of an upper and a lower surface. Instead of considering the value of the potentials at both surfaces, the difference $\Delta\Phi = \Phi^+ - \Phi^- = \phi^+ - \phi^- = \Delta\phi$ can be considered, where the superscript $+$ denotes the upper side and $-$ the lower side of the surface. From the above considerations, the final solution of the Laplace's equation reads as:

$$\begin{aligned}\epsilon(\Phi(\mathbf{P}, t) - \Phi_\infty(\mathbf{P}, t)) = \int_{S_B} & (\Phi_1 \nabla (\Phi - \Phi^{inner}) - (\Phi - \Phi^{inner}) \nabla \Phi_1) \cdot \mathbf{n} dS \\ + \int_{S_W} & (\Phi_1 \nabla (\Delta\phi) - \Delta\phi \nabla \Phi_1) \cdot \mathbf{n} dS,\end{aligned} \tag{2.23}$$

There is no physical meaning in an inner potential, so it can be chosen arbitrarily. The choice of its value defines different boundary value problems. In the present work the value is chosen to be equal to the undisturbed potential $\Phi^{inner} \equiv \Phi_\infty$ such that one obtains:

$$\begin{aligned}\epsilon\phi(\mathbf{P},t) &= \int_{S_B}\left[\frac{1}{r(\mathbf{x},\mathbf{P})}\nabla\phi - \phi\nabla\frac{1}{r(\mathbf{x},\mathbf{P})}\right]\cdot\mathbf{n}dS\\ &+ \int_{S_W}\left[\frac{1}{r(\mathbf{x},\mathbf{P})}\nabla(\Delta\phi) - \Delta\phi\nabla\frac{1}{r(\mathbf{x},\mathbf{P})}\right]\cdot\mathbf{n}dS\\ &= -\int_{S_B}\left[\frac{1}{r(\mathbf{x},\mathbf{P})}\sigma - \mu\Big(\nabla\frac{1}{r(\mathbf{x},\mathbf{P})}\cdot\mathbf{n}\Big)\right]dS\\ &- \int_{S_W}\left[\frac{1}{r(\mathbf{x},\mathbf{P})}\sigma_W - \mu_W\Big(\nabla\frac{1}{r(\mathbf{x},\mathbf{P})}\cdot\mathbf{n}\Big)\right]dS\end{aligned} \tag{2.24}$$

where $\mu := -\phi$ is the body dipole strength, $\sigma := -\nabla\phi\cdot\mathbf{n} = -\frac{\partial\phi}{\partial n}$ is the body source/sink strength, $\mu_W := -\Delta\phi = -(\phi^+ - \phi^-)$ is the wake dipole strength and $\sigma_W := -\frac{\partial\Delta\phi}{\partial n} = -(\frac{\partial\phi^+}{\partial n} - \frac{\partial\phi^-}{\partial n})$ is the wake source/sink strength.

Equation (2.24) indicates that the value of the potential in an arbitrary point of the flow field can be determined by the knowledge of the potentials at the boundary. That means that the problem of calculating the potential in a three-dimensional space was reduced to a two-dimensional problem.

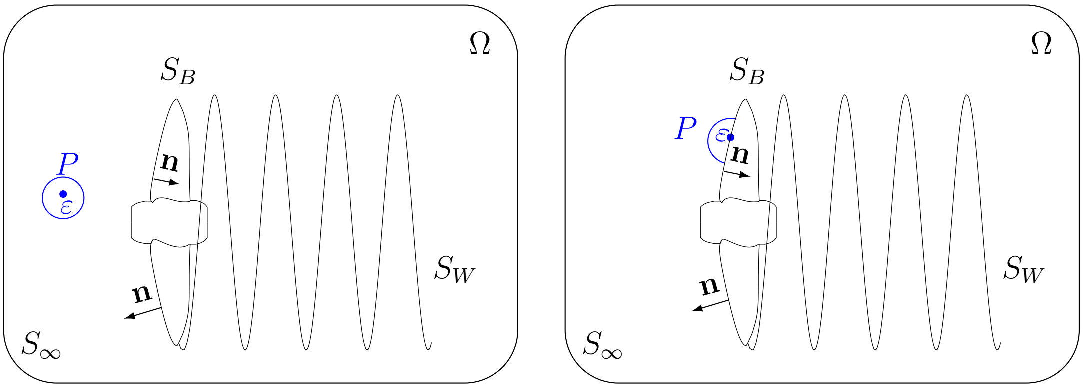

(a) (b)

Figure 2.6: Location of the collocation points in the potential flow domain

### 2.2.2 Boundary conditions

Equation (2.24) contains unknown dipole and source strengths. Thus, for the unique solution of this equation additional boundary conditions must be introduced. There are three types of boundaries: the body surface, the wake sheet and the boundary at infinity. According to the type of boundary, different conditions are applied.

### Neumann boundary condition on the wetted part of the body surface

The Neumann boundary condition is defined on the solid body surface. This condition states that the velocity component normal to the body surface must vanish, i.e. the following equation must hold (s. Katz and Plotkin, 2001, p. 27f.):

$$\nabla\Phi \cdot \mathbf{n} = 0, \, \forall \mathbf{x} \in S_B, \tag{2.25}$$

where $\mathbf{n}$ is the normal vector directed upwards to the body. It follows:

$$\nabla\Phi \cdot \mathbf{n} = \frac{\partial \Phi}{\partial n} = \frac{\partial}{\partial n}(\phi + \Phi_\infty) = 0 \Rightarrow \frac{\partial \phi}{\partial n} = -\frac{\partial \Phi_\infty}{\partial n} = -\mathbf{V}_\infty \cdot \mathbf{n}, \tag{2.26}$$

where $\mathbf{V}_\infty = \nabla\Phi_\infty$ is the inflow velocity vector. Using the definition $\sigma = -\frac{\partial \phi}{\partial n}$, Equation $(2.26)$ leads to the following relation for the source strength:

$$\sigma = \mathbf{V}_\infty \cdot \mathbf{n}. \tag{2.27}$$

This consideration includes that in case of a lifting body, only the dipole strengths are unknown and the source strengths are known values that can be determined by Equation $(2.27)$. In case of a non-lifting body, there are no dipoles and the source strengths are unknown quantities.

### Kutta condition (Vortex theorem)

The circulation generated by a propulsion organ is shed as a sheet of dipoles into the trailing flow, i.e. there are additional dipoles on the wake sheet with unknown dipole strengths. On the wake surface the jump of the normal velocity component as well as the force difference between the lower and upper side of the wake sheet must vanish (s. Katz and Plotkin, 2001, p. 88f.). This observation can be formulated mathematically as follows:

$$p^+ - p^- = 0 \quad \text{and} \quad \mathbf{V}^+ \cdot \mathbf{n} - \mathbf{V}^- \cdot \mathbf{n} = 0, \quad \forall \mathbf{x} \in S_W, \tag{2.28}$$

where $\mathbf{V}$ is the total velocity. The first condition in Equation $(2.28)$ yields:

$$\begin{gathered} \frac{\partial \mu_W}{\partial t} - \frac{1}{2}(|\nabla\Phi^+|^2 - |\nabla\Phi^-|^2) = 0, \quad \text{(unsteady case)} \\ |\nabla\Phi^+| = |\nabla\Phi^-|. \quad \text{(steady case)} \end{gathered} \tag{2.29}$$

The second condition in Equation $(2.28)$ determines the source strength on the wake surface:

$$\sigma_W = -(\frac{\partial \phi^+}{\partial n} - \frac{\partial \phi^-}{\partial n}) = 0. \tag{2.30}$$

The force-free condition at the trailing edge of the lifting surface is also known as the Kutta condition (s. Katz and Plotkin, 2001, p. 88). This condition is intended for bodies with sharp edges like the trailing edge of a foil profile. The Kutta condition is an alternative method of incorporating some aspects of viscous effects in potential theory. It constitutes that there cannot be an infinite change in velocity at the trailing edge. Although an inviscid fluid can mathematically have abrupt changes in velocity, in reality viscosity smooths out sharp velocity changes. If the trailing edge has a non-zero angle, the flow velocity there must be zero. At a cusped trailing edge, the velocity can be non-zero although it still must be identical above and below the foil (s. Katz and Plotkin, 2001, p. 211f.).

### Boundary condition at infinity

At infinity, the disturbed potential should vanish (s. Katz and Plotkin, 2001, p. 28), i.e.:

$$|\nabla\phi| \underset{\mathbf{x}\to\infty}{\to} 0. \tag{2.31}$$

## 2.3 Formulation of the boundary value problem

There are different possibilities of defining the boundary value problem. In the literature, panel methods are grouped according to the following characteristics (s. Kerwin et al., 1987, p. 109):

- Singularity type: source, dipole, vortex, combination of several singularity types.
- Order of the singularities: constant, linear and higher.
- Velocity-based or potential-based boundary integral equations. The velocity-based boundary value problem is an indirect formulation of the boundary value problem, since the potential is determined indirectly. In contrast, the potential-based boundary value problem is called the direct formulation.

The use of the indirect formulation of the boundary value problem leads to a solution where the potential velocity is determined uniquely but the potential itself is determined up to an additive constant. The use of the direct formulation leads to a solution where the potential as well as the velocity are determined uniquely.

In this work, both the indirect as well as the direct formulations are presented. In both approaches dipoles and sources of zero order (constant distribution) are used as singularities. For the sheet cavitation model, to be introduced in Chapter 4, only the Dirichlet type of the boundary value problem is used.

It is also possible to use a mixed formulation of the boundary conditions, i.e. on one part of the problem the indirect formulation is applied, while on the other part of the boundary the direct formulation is applied. For example, in case of a problem where a non-lifting and a lifting body are submerged in the flow field, it is useful to combine the velocity-based and the potential-based boundary integral equations.

### 2.3.1 Indirect formulation

In the indirect formulation of the boundary value problem, the Neumann boundary condition is used to set up the governing integral equations. Assume that the fixed point $\mathbf{P}$ is located on $S_B$, then it holds:

$$\begin{aligned}\nabla\Phi(\mathbf{P},t)\cdot\mathbf{n} = \frac{1}{2\pi}\Big(\int_{S_B}\nabla(\mu\frac{\partial}{\partial n}(\frac{1}{r}))dS - \int_{S_B}\nabla(\sigma(\frac{1}{r}))dS \\ + \int_{S_W}\nabla(\mu_W\frac{\partial}{\partial n}(\frac{1}{r}))dS\Big)\cdot\mathbf{n} + \nabla\Phi_\infty(\mathbf{P},t)\cdot\mathbf{n} \overset{(2.25)}{=} 0.\end{aligned}$$

Then it follows:

$$\begin{aligned}\frac{1}{2\pi}\Big(\int_{S_B}\nabla(\mu\frac{\partial}{\partial n}(\frac{1}{r}))dS - \int_{S_B}\nabla(\sigma(\frac{1}{r}))dS + \int_{S_W}\nabla(\mu_W\frac{\partial}{\partial n}(\frac{1}{r}))dS\Big)\cdot\mathbf{n} \\ = -\mathbf{V}_\infty(\mathbf{P},t)\cdot\mathbf{n}.\end{aligned} \tag{2.32}$$

In Equation (2.32), the source strengths can be determined by using relation (2.27). The dipole strengths on the wake are obtained by applying the Equation (2.29) and the only unknowns are the dipole strengths on the body.

Since no condition for the potential itself was used in order to derive Equation (2.32), only the absolute value of the potential's gradient will be determined uniquely. The value of the potential will be predicted up to an additive constant, i.e. $\phi = -\mu + constant$.

In case of a non-lifting body, for example a flat plate or ship hull, the boundary value problem reads as:

$$\frac{1}{2\pi}\int_{S_B}\nabla(\sigma(\frac{1}{r}))dS = \mathbf{V}_\infty(\mathbf{P},t)\cdot\mathbf{n}. \tag{2.33}$$

### 2.3.2 Direct formulation

There are two different approaches to the direct formulation. In the first one, the fixed point $\mathbf{P}$, also called collocation point, is put outside the body with the surface $S_B$. In the second approach, the fixed point $\mathbf{P}$ is put inside the body. This results in two different formulations of the boundary integral equations.

**Direct formulation type 1:** Considering a collocation point $\mathbf{P}$ that lies outside the body and using Equation (2.24), one obtains:

$$\phi(\mathbf{P},t) = \frac{1}{4\pi}\Big(\int_{S_B}(\mu\frac{\partial}{\partial n}(\frac{1}{r}) - \sigma\frac{1}{r})dS + \int_{S_W}\mu_W\frac{\partial}{\partial n}(\frac{1}{r})dS\Big). \tag{2.34}$$

**Direct formulation type 2:** Considering a collocation point $\mathbf{P}$ that lies inside the body and using Equation (2.24), one obtains:

$$\begin{aligned}\phi(\mathbf{P},t) = \phi^{inner}(\mathbf{P},t) &= \frac{1}{4\pi}\Big(\int_{S_B}(\mu\frac{\partial}{\partial n}(\frac{1}{r}) - \sigma\frac{1}{r})dS + \int_{S_W}\mu_W\frac{\partial}{\partial n}(\frac{1}{r})dS\Big)\\ &\overset{(\Phi^{inner}=\Phi_\infty)}{=} 0.\end{aligned} \tag{2.35}$$

For both types of direct formulation, a condition for the potential's gradient as well as a condition for the potential itself are formulated, such that their absolute values are determined uniquely. In case of a non-lifting body, the direct formulation cannot be used since it cannot be guaranteed that the Neumann boundary condition will be fulfilled.

## 2.4 Flow characteristics

The solution of the boundary value problem provides a dipole and source/sink distribution on the solid body boundaries and a dipole distribution on the wake surfaces. By means of these values, velocities and pressures on the bodies as well as in an arbitrary point of the flow domain can be determined.

### 2.4.1 Determination of velocities and pressures

For a collocation point $\mathbf{x}$ where the dipole and source strength are known, the induced velocity distribution $\mathbf{v}$ can be calculated from the induced potential $\phi$ and its normal derivative. In the local orthogonal coordinate system it holds:

$$v_\xi = \frac{\partial\phi}{\partial\xi} = -\frac{\partial\mu}{\partial\xi}, \quad v_\eta = \frac{\partial\phi}{\partial\eta} = -\frac{\partial\mu}{\partial\eta}, \quad v_\zeta = \frac{\partial\phi}{\partial\zeta} = -\sigma. \tag{2.36}$$

Then, the total velocity $\mathbf{V} = \mathbf{v} + \mathbf{V}_\infty$ reads in the local coordinate system as:

$$V_\xi = -\frac{\partial\mu}{\partial\xi} + V_{\infty,\xi}, \quad V_\eta = -\frac{\partial\mu}{\partial\eta} + V_{\infty,\eta}, \quad V_\zeta = -\sigma + V_{\infty,\zeta}. \tag{2.37}$$

The local velocities are transformed to the global coordinate system by means of the formulas derived in Appendix B.

For a collocation point $\mathbf{x}$ where the dipole and source strength are unknown, the value of the induced velocity is obtained from Equation (2.24):

$$\mathbf{v}(\mathbf{x},t) = \nabla\phi(\mathbf{x},t) = \frac{1}{4\pi}\Big[\int_{S_B} \nabla(\mu\frac{\partial}{\partial n}(\frac{1}{r}) - \sigma\frac{1}{r})dS + \int_{S_W} \nabla\mu_W\Big(\frac{\partial}{\partial n}(\frac{1}{r})\Big)dS\Big]. \quad (2.38)$$

The pressure in a point $\mathbf{x} \in \Omega$ is computed from Bernoulli equation (2.10):

$$p(\mathbf{x},t) = p_\infty + \frac{\rho}{2}\Big(|\mathbf{V}_\infty(\mathbf{x},t)|^2 - |\mathbf{V}(\mathbf{x},t)|^2\Big) - \rho\frac{\partial\phi}{\partial t}(\mathbf{x},t) + \rho g(z_\infty - z). \quad (2.39)$$

The pressure coefficient can then be calculated from the following definitions:

$$C_{p,v} = \frac{p - p_{ref}}{1/2\rho V_{ref}^2},\ C_{p,n} = \frac{p - p_{ref}}{1/2\rho(nD)^2},\ C_{p,nx} = \frac{p - p_{ref} + \rho g x R}{1/2\rho(nD)^2}, \quad (2.40)$$

where $p_{ref} = p_\infty + \rho g z_\infty$ is the reference pressure, $V_{ref}$ the reference velocity, $r = xR$, $x \in [0:1]$ the local radius and $R$ the propeller radius. For a propeller flow the reference velocity is usually set to $|\mathbf{V}_{ship}|$.

## 2.4.2 Determination of forces, moments and dimensionless propeller characteristics

In the post-processing the propeller characteristics can be determined. The potential induced forces and moments are calculated by the formulas (s. Katz and Plotkin, 2001, p. 85ff.):

$$\mathbf{F}_{pot} = -\int\limits_{S_B} p\mathbf{n}dS, \quad \mathbf{M}_{pot} = -\int\limits_{S_B} p(\mathbf{n}\times\mathbf{x})dS = -\int\limits_{S_B} p\begin{pmatrix} n_y z - n_z y \\ n_z x - n_x z \\ n_x y - n_y x \end{pmatrix} dS.$$

The viscous and leading edge suction forces cannot be captured by the potential theory and must be included via semi-empirical formulas. According to Nakamura (1985, p. 101f.), the leading edge suction force results from the generation of a vortex in the vicinity of the leading edge on thin foil sections. This effect occurs due to the detachment of the flow and directly influences the pressure distribution on the blade. The direct modelling of the leading edge vortex is very difficult and an alternative concept is mentioned in the literature: the leading edge suction force analogy (s. e.g. Polhamus, 1968). A leading edge suction force correction is not implemented in *pan*MARE, yet.

The viscous forces, which arise due to the friction effects in the flow, cannot be calculated by a potential flow solver directly. The semi-empirical formula, which is implemented in *pan*MARE, is based on measurements and theoretical approaches. It is assumed that the friction force acts in the direction of the velocity vector and is approximated by the following relation (s. Hundemer and Abdel-Maksoud, 2009, p. 4):

$$\mathbf{F}_D = c_F \frac{\rho}{2} |\mathbf{V}|^2, \tag{2.41}$$

where $c_F$ is the friction resistance coefficient that relates the local Reynolds number to a frictional force. The local Reynolds number is defined as (s. Hundemer and Abdel-Maksoud, 2009, p. 4):

$$Re = \frac{v_{rel} d_{l.e.}}{\nu}, \tag{2.42}$$

where $v_{rel}$ is the relative velocity between the body and fluid, $d_{l.e.}$ is the distance from the considered point on the foil surface to the leading edge of the foil profile and $\nu$ is the kinematic viscosity. The friction coefficient is defined according to the Prandtl-von Karman theory:

$$c_F = c_{F,\text{factor}} Re^{c_{F,\text{exponent}}}. \tag{2.43}$$

The constants $c_{F,\text{factor}}$ and $c_{F,\text{exponent}}$ are the factor and exponent of the friction resistance coefficient. The values used in *pan*MARE are $c_{F,\text{factor}} = 0.059$ and $c_{F,\text{exponent}} = -0.2$ (s Hundemer and Abdel-Maksoud, 2009, p. 4).

By means of the forces and moments, the thrust and torque of a propeller can be computed:

$$T = \mathbf{F} \cdot \frac{\mathbf{V}_{ship}}{|\mathbf{V}_{ship}|}, \quad Q = \mathbf{M} \cdot \frac{\mathbf{V}_{ship}}{|\mathbf{V}_{ship}|}. \tag{2.44}$$

For a propeller flow the dimensionless characteristics such as propeller thrust and torque coefficients as well as the propeller efficiency are useful. They are defined by:

$$k_t = \frac{T}{\rho n^2 D^4}, \; k_q = \frac{Q}{\rho n^2 D^5}, \; \eta = \frac{k_t}{k_q} \frac{J}{2\pi}, \tag{2.45}$$

where $n$ is the rotational speed, $D$ the diameter and $J = {}^{V_{ship}}/_{nD}$ the advance coefficient of the propeller.

The lift coefficient per unit span, denoted by $c_l(r)$, is calculated by the following formula:

$$c_l(r) = \frac{dL(r)}{0.5 \rho V_{ref}^2 c(r)}, \tag{2.46}$$

where $c(r)$ is the chord length at radius $r$ and $dL$ is the lift per unit span. The three-dimensional lift coefficient $C_l$ is then obtained by:

$$C_l = \frac{L}{0.5 \rho V_{ref}^2 A_{ref}}, \tag{2.47}$$

where $L$ is the overall lift and $A_{ref}$ is the projected area.

# Chapter 3

# Numerical approach

In this chapter all parts of the solution process that are used to find the numerical solution of the potential flow problem are discussed. The process of finding a numerical solution to the underlying mathematical problem consists of three main parts (s. Figure 3.1):

1. Pre-processing: This part of the numerical process implies the import or generation of a geometry file, the generation of a numerical grid (mathematical description of the domain) and inclusion of periodicity or symmetry of the geometry. In this part of the process it is important to have a grid refinement strategy and to perform a grid convergence study in order to guarantee a grid independence of the calculation results.

2. Main calculation process: In this part of the process all parameters must be defined and the physical conditions must be incorporated. This can be done via an input file imported into and read by the program. Next, the calculation process is started, parallel or sequentially. During the calculations, the convergence of the numerical model should be monitored.

3. Post-processing: The aim in this stage of the process is the calculation of forces, moments and other post-processing variables that are not calculated by the main solution process. Subsequently, a result output file is generated and the results are evaluated, illustrated and analysed.

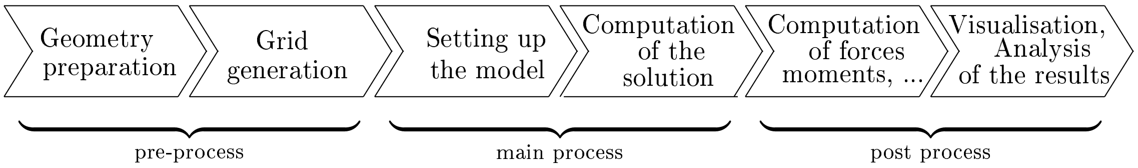

Figure 3.1: Numerical solution procedure

In the first section of this chapter, 3.1, general information about the grid generation and configuration of the body and wake grid elements are presented. In the second section, 3.2, the discrete boundary value problem is derived. The third section, 3.3, deals with the wake alignment procedure. In the last section, 3.4, the numerical calculation of velocities, pressures and propeller flow characteristics is outlined.

## 3.1 Grid generation

The method used to discretise the continuous boundary value problem which was defined in Section 2.3, is the three-dimensional low-order panel method. The main idea behind this method is to discretise the body and wake surfaces of a body into small two-dimensional elements called panels. Panels can be triangular or quadrilateral, and their shape can be approximated by polynomials of first, second and higher order (s. Katz and Plotkin, 2001, p. 218). Depending on the order of approximation, the panel method is called low-order (first order) or higher-order (second and higher order) method. The method applied in this work uses a first order approximation and quadrilateral elements. These quadrilateral elements have four edge points $\mathbf{c}_1, \ldots, \mathbf{c}_4$ and four straight edges $\bar{c_1 c_2}$, $\bar{c_2 c_3}$, $\bar{c_3 c_4}$, $\bar{c_4 c_1}$ (s. Figure 3.2). The centre of a panel is calculated according to Section 2.1 and is denoted by $\mathbf{c}_0$.

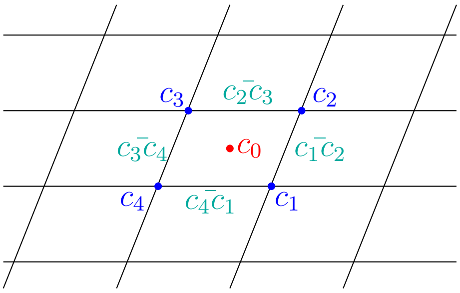

Figure 3.2: Declaration of edge points, midpoint and edges on a panel

The geometry and grid are generated by an in-house design tool developed by Hundemer (2013). The grid is generated for the body and wake surfaces and is constructed according to the cosine spacing technique (s. Kornev, 2009, p. 45). A grid based on the cosine spacing is called conventional grid. A conventional grid uses grid lines that coincide with the blade sections at constant radius. This kind of grid can cause issues at the blade tip since the chord at the tip goes to zero and the last two sequent grid lines become almost parallel. On the other hand, a conventional grid has the advantage that its radial grid lines coincide better with the streamlines of the flow. Besides, the use of a conventional grid simplifies the implementation of a sheet cavitation model. For the numerical sheet cavitation model used in this work it is required that the grid is structured. However, when no sheet cavitation calculations need to be performed, the implemented numerical method generally allows for the use of an unstructured grid as well.

### 3.1.1 Nomenclature

For the discretisation of the geometry the following notation is used (s. Figure 3.3):

| | |
|---|---|
| $N_k$ | Number of panels on the body or wake surface in the radial direction. |
| $k = 1, \dots, N_k$ | Index describing the radial stripe on a body or wake surface grid. |
| $N_l$ | Number of panels on the body surface in the circumferential direction. |
| $N_{W,l}$ | Number of panels on the wake surface in the circumferential direction. |
| $l = 1, \dots, N_l$ / $N_{W,l}$ | Index describing the circumferential stripe on a body or wake surface grid. |
| $N= N_k N_l$ | Overall number of panels on the body surface. |
| $N_W= N_k N_{W,l}$ | Overall number of panels on the wake surface. |
| $N_{total}= N + N_W$ | Total number of panels. |
| $i = l + (k-1)N_l$ | Index describing the location of a panel by the index pair $l$ and $k$. |
| $\mathbf{x}_j^{col}, \forall\, j = 1, \dots, N$ | Collocation point on the body surface. |
| $\mathbf{x}_i, \forall\, i = 1, \dots, N + N_W$ | Centre of a panel on the body or wake surface. |
| $\Delta t$ | Time step. |
| $t_n= n\Delta t$ | Discrete time. |
| $n= 0, 1, \dots, n_{max}$ | Index describing the discrete time. |
| $n_{max}$ | Maximum number of time steps. |
| $\Delta\theta$ | Angular step. |
| $\mu_i^n= \mu_{(l,k)}^n := \mu(\mathbf{x}_\mathbf{i}, t_n)$ | Dipole strength on the body panel centre $\mathbf{x}_i$ for the discrete time step $t_n$. |
| $\sigma_i^n= \sigma_{(l,k)}^n := \sigma(\mathbf{x}_\mathbf{i}, t_n)$ | Source strength on the body panel centre $\mathbf{x}_i$ for the discrete time step $t_n$. |
| $\mu_{W,i}^n= \mu_{W,(l,k)}^n := \mu_W(\mathbf{x}_\mathbf{i}, t_n)$ | Dipole strength on the wake panel centre $\mathbf{x}_i$ for the discrete time step $t_n$. |

The body and wake surfaces are discretised by radial and cross-wise grid lines. The number of span-wise panels is denoted by $N_k$ and the number of cross-wise panels by $N_l$. The overall number of body panels is $N = N_k N_l$. The number of wake panels in the span-wise direction must be equal to that of the body. In the in-house grid generation program only the first row of panels on the wake surface is generated, the shape and the number of the remaining wake panels depends on the time step size and is generated in the main numerical procedure. The number of wake panels in the cross-wise direction is denoted by $N_{W,l}$, such that the overall number of wake panels is $N_W = N_k N_{W,l}$.

The displacement and the lift force of each body panel is described by a source and a dipole. The source strengths and the dipole strengths of the $i$th panel are denoted by $\sigma_i^n$ and $\mu_i^n$ for all $i = 1, \dots, N$. The lift force of each wake panel is displayed by a dipole that is denoted by $\mu_{W,i}^n$ for all $i = 1, \dots, N_W$. For the dipole and source strengths a zero-order approximation is used, i.e. the dipole and source distribution on each element is constant. In unsteady calculations additional notations are required. The time and angular steps are denoted by $\Delta t$ and $\Delta\theta$, respectively. In order to simulate $x$ number of propeller revolutions, the required number of iterations (equivalent to the number of time steps) is $n = {}^{360\,x}\!/_{\Delta\theta}$.

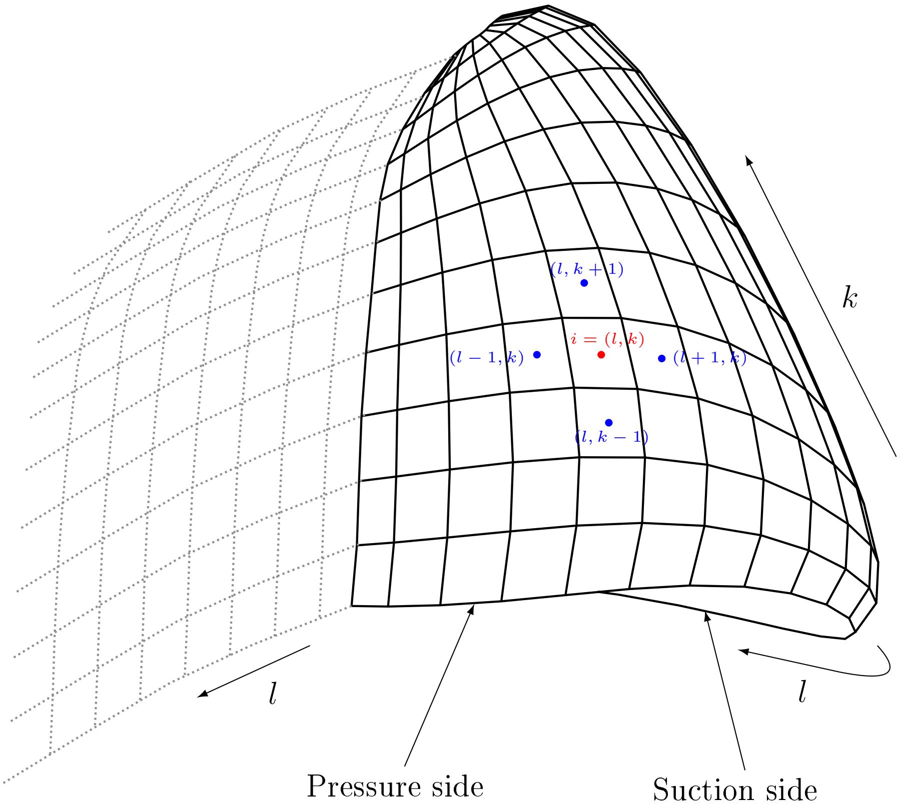

Figure 3.3: Grid structure on a blade and wake surface

### 3.1.2 Wake grid initialisation

In order to reproduce the lifting effect of a body, its slipstream must be modelled. The slipstream is modelled as a thin wake sheet attached to the trailing edge of the solid body surface (s. Figure 3.4). The shape of the wake sheet is not known a priori and its determination is part of the solution process. At the beginning of this process the shape is initialised by the following procedure:

- Firstly, the first row of the wake panels is generated according to the geometrical pitch of the last two trailing edge panels (at the lower and upper side). The slope of the wake panels at the first row corresponds to the slope of the bisecting line $\mathbf{a}$ between the upper and lower trailing edge panel. The wake panel edges are numbered in the clockwise direction starting from the lower point at the trailing edge as illustrated in Figure 3.4. At the first wake row the edge points $\mathbf{c}_1$ and $\mathbf{c}_2$ are not moved, only the points $\mathbf{c}_3$ and $\mathbf{c}_4$ are moved according to the geometrical pitch.
- Secondly, the second and following rows of the wake sheet are modelled depending on the motion model of the considered body. In case of a propeller flow, the trailing wake is modelled as a helix and the edge points $\mathbf{c}_3$ and $\mathbf{c}_4$ are moved according to a certain pitch. The length of each wake panel in the chord-wise direction depends on the time step $\Delta t$. The wake length in the span-wise direction depends on the radial grid resolution of the solid body.

There are two different approaches to the construction of the wake helix. The first one exclusively uses the undisturbed inflow velocity for the adjustment of the wake panels and is called "Aligned to inflow model". The second model is called "Aligned to inflow and pitch model" and uses the inflow velocity as well as the geometrical pitch of each circular blade section for the adjustment of the wake panels. In the following, both models are introduced briefly.

**Aligned to inflow model:** This model exclusively uses the undisturbed inflow velocity for the adjustment of the wake panels. The edge points $\mathbf{c}_3$ and $\mathbf{c}_4$ of each radial section are displaced by the following procedure:

$$\mathbf{c}_3 = \mathbf{c}_2 + \mathbf{V}_\infty(\mathbf{c}_2)\Delta t, \quad \mathbf{c}_4 = \mathbf{c}_1 + \mathbf{V}_\infty(\mathbf{c}_1)\Delta t. \tag{3.1}$$

**Aligned to inflow and pitch model:** In this model the pitch of the wake sheet helix is a function of the hydrodynamical and geometrical pitch of the trailing edge. The edge points $\mathbf{c}_3$ and $\mathbf{c}_4$ are adjusted at each radial section as follows:

$$\begin{aligned}
\mathbf{c}_3 &= \mathbf{c}_2 + \Big(\mathbf{V}_\infty(\mathbf{c}_2) - f\frac{\mathbf{b}_{cor}}{|\mathbf{b}_{cor}|}\Big)\Delta t,\ \mathbf{b}_{cor} = (\mathbf{c}_3^{old} - \mathbf{c}_2) - \omega \times \mathbf{c}_2 - \mathbf{V}_{ship}(\mathbf{c}_2),\\
\mathbf{c}_4 &= \mathbf{c}_1 + \Big(\mathbf{V}_\infty(\mathbf{c}_1) - f\frac{\mathbf{b}_{cor}}{|\mathbf{b}_{cor}|}\Big)\Delta t,\ \mathbf{b}_{cor} = (\mathbf{c}_4^{old} - \mathbf{c}_1) - \omega \times \mathbf{c}_1 - \mathbf{V}_{ship}(\mathbf{c}_1)
\end{aligned} \tag{3.2}$$

where $f = 0.95\min(r/R + 0.5, 1)$ is a function that reduces the correction at the hub of the propeller.

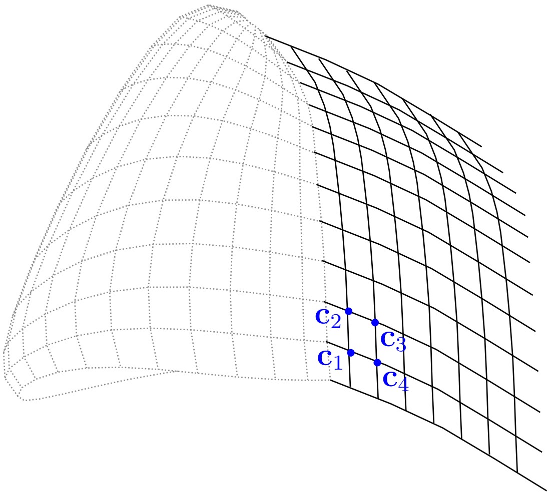

Figure 3.4: Declaration of the panel edges on the wake sheet

## 3.2 Discrete boundary value problem

In this section a discretisation procedure for the boundary value problem (2.35) is employed.

### 3.2.1 Discretisation of the integral equations

For the derivation of a numerical solution of the boundary value problem, one defines $N$ collocation points $x_j^{col}, j = 1, \dots, N$, where the integral equations are applied. A collocation point $x_j^{col}$ is defined to be the centre of the panel $j$ which is slightly displaced inside the body. For these collocation points the integral equation (2.35) can be used and the boundary value problem reads as:

$$\begin{aligned} \frac{1}{4\pi}\sum_{i=1}^{N}\mu_i^n \int\limits_{Panel_i} \frac{\partial}{\partial n}\frac{1}{r(\mathbf{x_j^{col}},\mathbf{x_i})} dS(\mathbf{x_i}) + \frac{1}{4\pi}\sum_{i=1}^{N_W}\mu_{W,i}^n \int\limits_{Panel_i} \frac{\partial}{\partial n}\frac{1}{r(\mathbf{x_j^{col}},\mathbf{x_i})} dS(\mathbf{x_i}) \\ - \frac{1}{4\pi}\sum_{i=1}^{N}\sigma_i^n \int\limits_{Panel_i} \frac{1}{r(\mathbf{x_j^{col}},\mathbf{x_i})} dS(\mathbf{x_i}) = 0. \end{aligned} \tag{3.3}$$

From the above relation one obtains:

$$\sum_{i=1}^{N}\mu_i^n A_{i,j} + \sum_{i=1}^{N_W}\mu_{W,i}^n A_{i,j} - \sum_{i=1}^{N}\sigma_i^n B_{i,j} = 0, \quad \text{for all} \quad x_j^{col}, j = 1, \dots, N, \tag{3.4}$$

where

$$\begin{aligned} A_{i,j} &:= A(\mathbf{x_i}, \mathbf{x_j^{col}}) = \frac{1}{4\pi} \int\limits_{Panel_i} \frac{\partial}{\partial n} \frac{1}{r(\mathbf{x_j^{col}}, \mathbf{x_i})} dS(\mathbf{x_i}), \quad \forall\, i = 1, \dots, N + N_W, \\ B_{i,j} &:= B(\mathbf{x_i}, \mathbf{x_j^{col}}) = \frac{1}{4\pi} \int\limits_{Panel_i} \frac{1}{r(\mathbf{x_j^{col}}, \mathbf{x_i})} dS(\mathbf{x_i}), \quad \forall\, i = 1, \dots, N, \end{aligned} \tag{3.5}$$

are the influence functions that describe the dipole or source influence of the panel $i$ on the point $\mathbf{x}_j^{col}$. The influence coefficients in Equation (3.5) only depend on the geometry and the choice of the collocation points. In case of flat quadrilateral panels, they can be calculated analytically (s. Appendix C).

Applying Equation (3.4) on $N$ collocation points leads to a linear system of equations that consist of $N + N_W$ columns and $N$ rows:

$$\begin{pmatrix} A_{1,1} & \dots & A_{N_W,1} \\ \vdots & \vdots & \vdots \\ A_{1,N} & \cdots & A_{N_W,N} \end{pmatrix} \cdot \begin{pmatrix} \mu_1^n \\ \vdots \\ \mu_N^n \\ \mu_{W,1}^n \\ \vdots \\ \mu_{W,N_W}^n \end{pmatrix} = \begin{pmatrix} B_{1,1} & \dots & B_{N,1} \\ \vdots & \vdots & \vdots \\ B_{1,N} & \cdots & B_{N,N} \end{pmatrix} \cdot \begin{pmatrix} \sigma_1^n \\ \vdots \\ \sigma_N^n \end{pmatrix}. \tag{3.6}$$

The discrete source strengths are known from the discrete form of Equation (2.27):

$$\sigma_i^n = \mathbf{V}_{\infty,i}^n \cdot \mathbf{n}_i, \quad \forall\, i = 1, \dots, N. \tag{3.7}$$

It follows that there are $N + N_W$ unknowns and only $N$ equations. The unknowns are the body and wake dipole strengths. The determination of the wake dipole strengths differs in steady and unsteady computations:

- In steady computations the value of the dipoles on the discrete wake sheet is calculated as follows:

    1. On the first row of the trailing wake the value of the dipole strengths $\mu_{W,(1,k)}$, $\forall\, k = 1, \dots, N_k$ is obtained by using the Kutta condition.
    2. At the following rows of the trailing wake the dipole values are set to the same value as the dipoles at the leading panel: $\mu_{W,(l,k)} = \mu_{W,(1,k)}$, $\forall\, l = 2, \dots, N_{W,l}$, $\forall\, k = 1, \dots, N_k$ (s. Figure 3.5).

- In unsteady computations the value of the dipole strengths at the wake panels changes for each time step and each radial stripe. In the first time step the values from the steady computations are used. In the following steps the procedure goes as follows:

1. On the first row of the trailing wake the value of the dipole strengths $\mu^n_{W,(1,k)}$, $\forall\, k = 1, \ldots, N_k$ is obtained by using the Kutta condition.
2. The dipole values for the remaining wake panels are set to the value from the previous time step: $\mu^n_{W,(l,k)} = \mu^{n-1}_{W,(l-1,k)}$, $n = 1, \ldots, \forall\, l = 2, \ldots, N_{W,l}$, $\forall\, k = 1, \ldots, N_k$.

The number of unknown dipole strengths is the same in the steady and unsteady case, namely $N_k$. The numerical implementation of the Kutta condition used in the steady and unsteady computations for the determination of the dipole strengths on the trailing wake is introduced below.

## 3.2.2 Implementation of the Kutta condition

The aim of the Kutta condition is the determination of unknown wake dipole strengths $\mu^n_{W,(1,k)}$ for each radial stripe $k$ such that the force-free condition $\Delta p = p^+ - p^- = 0$ is fulfilled on the wake sheet. The potential jump $\Delta p$ is a non-linear function of the dipole strengths and cannot be solved directly. In order to solve this equation numerically, either a linear approximation or the Kutta condition can be used or the non-linear condition must be solved by an iterative procedure. The linear condition is easier to implement, but is less accurate than the non-linear form of the condition. The iterative solution of the non-linear equation, e.g. by means of Newton's method, complicates the implementation and increases the computational effort. In *pan*MARE both solution approaches are implemented.

### Linear form of the Kutta condition

The linear form of the Kutta condition reads as:

$$\mu^n_{W,(1,k)} = \mu^n_{(N_l,k)} - \mu^n_{(1,k)}, \tag{3.8}$$

where $\mu^n_{(N_l,k)}$ and $\mu^n_{(1,k)}$ are the dipole strengths on the upper and on the lower side of the trailing edge of the solid body, respectively. This condition means that a body panel will be influenced by the wake panels when it is located at the trailing edge. Now, the following substitution is made:

$$\begin{aligned} A^*_{i,j} &= A_{i,j} \text{ if the panel } i \text{ does not lie at the trailing edge, i.e. } i = l + (k-1)N_l \\ &\quad \text{and} \quad l \neq N_l \text{ and } l \neq 1, \\ A^*_{i,j} &= A_{i,j} \pm \sum_{h=1+(k-1)N_{W,l}}^{kN_{W,l}} A_{h,j} \text{ if the panel } i \text{ lies at the trailing edge of the} \\ &\quad \text{radial stripe } k, \text{ i.e. } i = N_l + (k-1)N_l \text{ or } i = 1 + (k-1)N_l, \end{aligned} \tag{3.9}$$

where the sign ± stands for the suction and the pressure side, respectively. By means of this substitution, one obtains a linear system of equations of dimension $N \times N$ for the unknown body dipole strengths $\mu_i$, $\forall i = 1, \dots N$:

$$\begin{pmatrix} A^*_{1,1} & \dots & A^*_{N,1} \\ \vdots & \vdots & \vdots \\ A^*_{1,N} & \cdots & A^*_{N,N} \end{pmatrix} \cdot \begin{pmatrix} \mu^n_1 \\ \vdots \\ \mu^n_N \end{pmatrix} = \begin{pmatrix} B_{1,1} & \dots & B_{N,1} \\ \vdots & \vdots & \vdots \\ B_{1,N} & \cdots & B_{N,N} \end{pmatrix} \cdot \begin{pmatrix} \sigma^n_1 \\ \vdots \\ \sigma^n_N \end{pmatrix}. \tag{3.10}$$

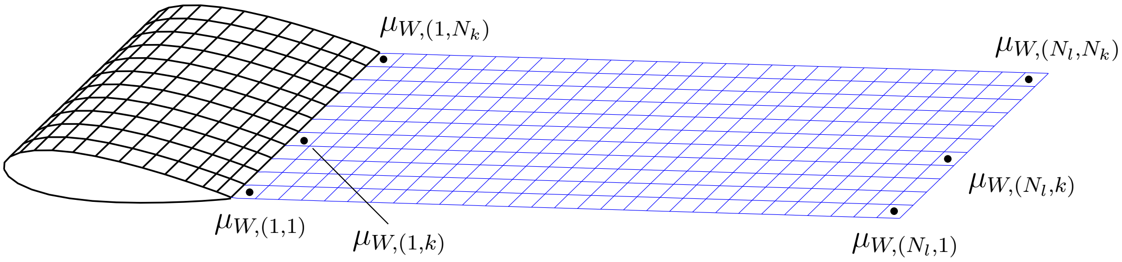

Figure 3.5: Declaration of the dipole strengths on the wake sheet

### Non-linear form of the Kutta condition

The non-linear form of the Kutta condition at each radial stripe of the lifting body reads as:

$$\Delta p_{(1,k)} = p^+_{(1,k)} - p^-_{(1,k)} = 0, \quad \forall\, k = 1, \dots, N_k, \tag{3.11}$$

where $p^\pm$ is the pressure value at the upper and lower side of the wake sheet, respectively. This non-linear system of equations can be solved iteratively by Newton's method (s. Kerwin et al., 1987, p. 111f.). The method computes from a starting solution, a new solution that is the root of the non-linear system and solves the linear system of equations:

$$\mathbf{J} \cdot \mathbf{x}^{(m+1)} = -\mathbf{f}^{(m)},\ m = 0, 1, 2 \dots. \tag{3.12}$$

where $\mathbf{J}$ is the Jacobian matrix and the vector functions $\mathbf{x}$ and $\mathbf{f}$ are defined by:

$$\mathbf{x}^{(m+1)} = \underbrace{\begin{pmatrix} \mu^{(m+1)}_{W,(1,1)} \\ \mu^{(m+1)}_{W,(1,2)} \\ \vdots \\ \mu^{(m+1)}_{W,(1,N_k)} \end{pmatrix}}_{\mu^{(m+1)}_W} - \underbrace{\begin{pmatrix} \mu^{(m)}_{W,(1,1)} \\ \mu^{(m)}_{W,(1,2)} \\ \vdots \\ \mu^{(m)}_{W,(1,N_k)} \end{pmatrix}}_{\mu^{(m)}_W}, \quad \mathbf{f}^{(m)} = \begin{pmatrix} \Delta p^{(m)}_{(1,1)} \\ \Delta p^{(m)}_{(1,2)} \\ \vdots \\ \Delta p^{(m)}_{(1,N_k)} \end{pmatrix}. \tag{3.13}$$

The solution algorithm reads as:

(1) The solution from the linear Kutta condition is used to have an initial guess for the potential jump at the trailing edge. The initial guess is denoted by $\mathbf{x}^0 = (\mu^0_{W,(1,1)}, \ldots, \mu^0_{W,(1,N_k)})$. For this initial guess the pressure jump $\Delta p^0_{(1,k)}$ is calculated for all $k = 1, \ldots, N_k$.

(2) The previous approximation is corrected by $\mu_W^{(m+1)} = \mu_W^{(m)} - \mathbf{J}^{-1} \cdot \mathbf{f}^{(m)}$. The Jacobian matrix $\mathbf{J}$ is given by:

$$J_{jk} = \frac{\Delta p^{\beta}_{(1,k)} - \Delta p^0_{(1,k)}}{\mu^{\beta}_{W,(1,j)} - \mu^0_{W,(1,j)}}, \quad j, k = 1, \ldots, N_k, \tag{3.14}$$

where $\mu^{\beta}_{W,(1,j)} = (1-\beta)\mu^0_{W,(1,j)}$ for $j = k$ and, $\mu^{\beta}_{W,(1,j)} = \mu^0_{W,(1,j)}$ for $j \neq k$. The constant $\beta$ is usually set to $0.01$ (see Kerwin et al., 1987, p. 111). In order to avoid the inversion of the Jacobian matrix, the linear system of equations $(3.12)$ is first solved to obtain $\mathbf{x}^{(m+1)}$. Then, the following relation is used:

$$\mu_W^{(m+1)} = \mu_W^{(m)} + \mathbf{x}^{(m+1)}. \tag{3.15}$$

(3) The iteration procedure is repeated as long as for one iteration step $m = 0, 1, 2, \ldots$ the relation $\max\limits_{k=1}^{N_k}(|\Delta p^{(m)}_{(1,k)}|) < \varepsilon$ for a given threshold $\varepsilon$ is satisfied.

Newton's method is based on the assumption that the initial guess is not too far off from the exact solution. The starting point is very important since it determines which root is found by Newton's method, which it is not always the closest root. If the initial solution found by the linear Kutta condition is too far off from the actual solution, Newton's method can diverge.

### 3.2.3 Initial condition for the unsteady problem

In the unsteady case, an initial condition for the first time step must be specified. An initial condition is required because of the dependency of the governing equations on the time-variable $t$. As the initial condition the solution from the steady computation is used, i.e. the problem is solved for the steady case first. The solution achieved by the steady computation is then used as the initial value for the unsteady computations.

### 3.2.4 Boundary value problem for multiple bodies in the flow domain

It is possible to compute several bodies submerged in the flow domain $\Omega$. Such a case is given for example when calculating propeller-induced pressure pulses on a ship hull. In this case, two bodies, namely the propeller and the ship hull, are contained in the flow domain $\Omega$. In order to adapt the linear system of equations $(3.6)$ for several bodies, the following additional notation is introduced:

| | |
|---|---|
| $M$ | Number of body surfaces in the fluid domain $\Omega$. |
| $N^m$ | Number of panels on the body surface $m = 1, \dots, M$. |
| $N_W^m$ | Number of panels on the wake surface $m = 1, \dots, M$. |
| $N = \sum_{m=1}^{M} N^m$ | Overall number of body panels. |
| $N_W = \sum_{m=1}^{M} N_W^m$ | Overall number of wake panels. |

Based on the Equation $(3.4)$, the modified boundary integral equations for $M$ bodies in the fluid domain read as:

$$\sum_{m=1}^{M} \Big[ \sum_{i=1}^{N^m} \mu_i^n A_{i,j} + \sum_{i=1}^{N_W^m} \mu_{W,i}^n A_{i,j} - \sum_{i=1}^{N^m} \sigma_i^n B_{i,j} \Big] = 0, \quad \text{for all} \quad \mathbf{x}_j^{col}, j = 1, \dots, N, \tag{3.16}$$

where the influence functions are defined in the same way as in Equation $(3.5)$ for $\forall\, i = 1, \dots, N + N_W$.

## 3.3 Wake alignment modelling

In Section 3.1.2 the initialisation of the wake sheet was discussed. In order to fulfil Kelvin's theorem (s. Katz and Plotkin, 2001, p. 25f.), the wake shape must be adjusted according to the latest flow conditions. There are different possibilities to model the wake sheet of a lifting body. The methodology introduced here was employed by Hundemer (2013, p. 32ff.). The wake shape is not known a priori and has to be determined in an iterative manner. The iterative procedure differs in the steady and unsteady calculations.

- In the steady calculations the wake panels are adjusted starting from the last panel row at the wake sheet. The new wake shape is calculated by moving the edge points $\mathbf{c}_3$ according to the following formula:

$$\mathbf{c}_3 = \mathbf{c}_2 + \Big( \frac{\mathbf{v}_k + \mathbf{v}_{k+1}}{2} + \mathbf{V}_\infty \Big) \Delta t, \tag{3.17}$$

where $\Delta t$ corresponds to the wake panel length and $\mathbf{v}_k$ and $\mathbf{v}_{k+1}$ are the induced velocities at the collocation points of the neighbouring panels along the radial direction (s. Figure 3.6).

- In the unsteady calculations the solution from the steady calculations is used as the initial wake shape. The wake sheet is not moved with the unsteady motion, but the body is moved according to the unsteady motion model and a new row of wake panels is inserted between the body trailing edge of the old wake sheet. The wake panels are then adjusted starting from the first panel row on the wake sheet. For the displacement of the panel edges only the induced velocities are used and the location of the edge points $\mathbf{c}_3$ is determined by:

$$\mathbf{c}_3 = \mathbf{c}_2 + \left(\frac{\mathbf{v}_k + \mathbf{v}_{k+1}}{2}\right)\Delta t. \tag{3.18}$$

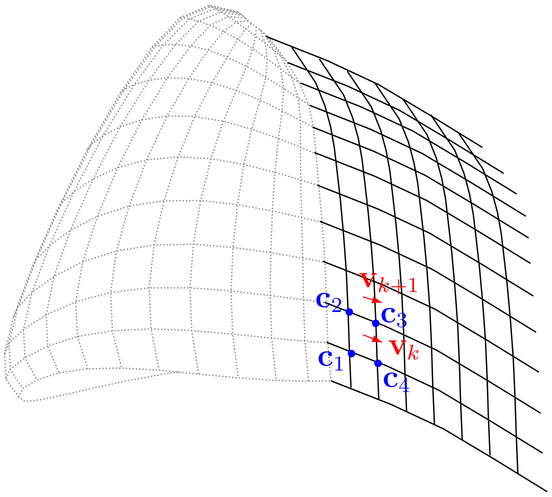

Figure 3.6: Wake alignment in steady computations

In both steady and unsteady calculations the velocity distribution on the wake sheet must be calculated first. For each wake panel it holds:

$$\mathbf{V}(\mathbf{x}_i) = \mathbf{v}(\mathbf{x}_i) + \mathbf{V}_\infty(\mathbf{x}_i),\ \forall\, i = 1, \dots, N_W. \tag{3.19}$$

Then, depending on the type of wake alignment model being applied, certain velocity components might be suppressed. There are four different types of models, which are implemented in *pan*MARE:

1. No wake alignment model: In this model the wake is not aligned at all, i.e. all velocity components are suppressed. After the initialisation of the wake it remains the same for all steady and unsteady steps.

2. Free wake alignment model: In this model the wake is aligned according to the local velocities and all velocity components are used for the adjustment of the wake edge points.
3. Radially fixed wake alignment: This model suppresses the radial component of the velocity and the wake edges are adjusted according to the tangential and axial velocity components.
4. Tangentially and radially fixed wake alignment: This model suppresses the radial as well as the tangential component of the velocity and the wake edges are adjusted according to the axial velocity components.

On Figures 3.7 and 3.8 the four wake models described above are illustrated on an example propeller for its operational point $J = 0.719$ and for the advance coefficient $J = 0.35$. The figures show that for the operational point the difference between the models (b)-(d) is negligible. In contrast, the shape of the free aligned wake for $J = 0.35$ differs considerably compared to models (c) and (d). The models with a suppressed radial component are numerically more stable and cause less problems in the computations. The model with a free aligned wake corresponds more accurately to the real wake sheet but can lead to unstable results for the propeller's thrust and torque, especially for low advance coefficients.

**Remarks:** The induced velocities on the wake are usually smoothed such that their values do not exceed $0.7$ times of the inflow velocity $\mathbf{V}_\infty$. Additionally, in unsteady calculations the induced velocities are smoothed by the value from the previous time step in order to avoid major changes of the wake shape between two subsequent time steps.

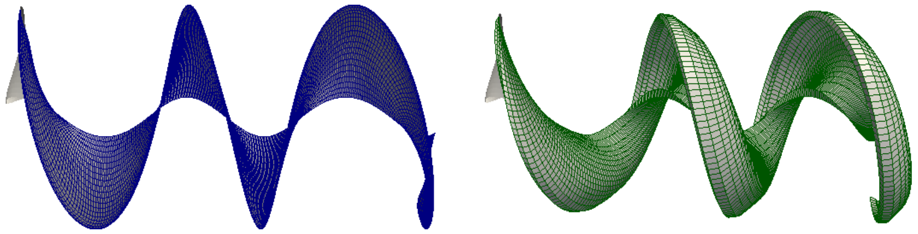

(a) No wake alignment model

(b) Free wake alignment model

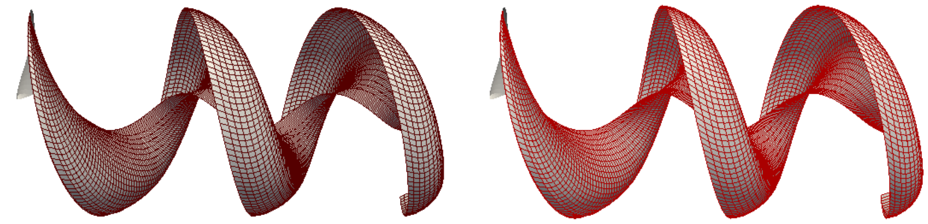

(c) Radially fixed wake alignment model

(d) Tangentially and radially fixed wake alignment model

Figure 3.7: Different wake alignment models applied on an example propeller P1356 (s. Section 5.1.3) at its operational point $J = 0.719$

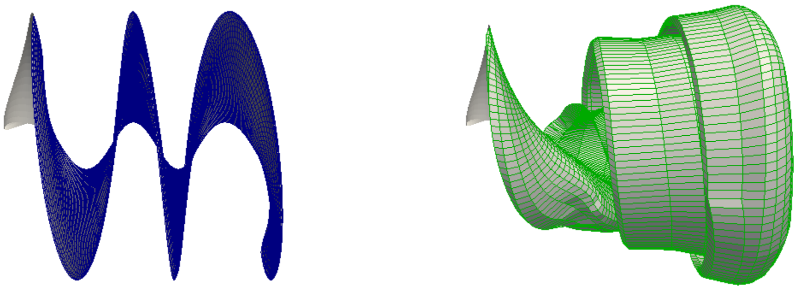

(a) No wake alignment model

(b) Free wake alignment model

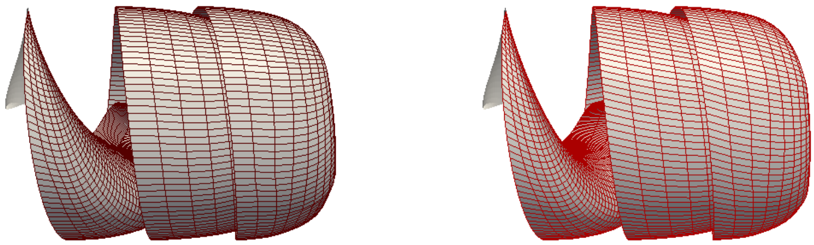

(c) Radially fixed wake alignment model

(d) Tangentially and radially fixed wake alignment model

Figure 3.8: Different wake alignment models applied on an example propeller P1356 (s. Section 5.1.3) for the advance coefficient $J = 0.35$

## 3.4 Flow characteristics

This section deals with the numerical calculation of velocities, pressures and propeller characteristics.

### 3.4.1 Numerical determination of velocity distribution

On the solid body surface, the local induced velocity components can be computed from the dipole and source strengths by the following relations:

$$v_{\xi,j} = \frac{\partial \phi_j}{\partial \xi} = -\frac{\partial \mu_j}{\partial \xi},\ v_{\eta,j} = \frac{\partial \phi_j}{\partial \eta} = -\frac{\partial \mu_j}{\partial \eta},\ v_{\zeta,j} = \frac{\partial \phi_j}{\partial \zeta} = -\sigma_j,\ \forall j = 1,\dots,N. \quad (3.20)$$

The potential gradients in Equation (3.20) are not known and must be approximated numerically. There are several possibilities for their approximation. In *pan*MARE the approximation is done by interpolating the potential's distribution over four neighbouring panels by a bilinear function. Afterwards, the potential distribution is differentiated in order to obtain the required gradients of the potentials. In the following this procedure is described in detail. Consider a panel $j$ with the collocation point $\mathbf{x}_j^{col}$. In the local orthogonal coordinate system of the panel the collocation point is defined as: $\mathbf{x}_j^{col,loc} = (\xi_0, \eta_0, 0) = (0, 0, 0)$. The panel $j$ has four neighbouring panels: above, underneath and on the left and right side (s. Figure 3.9). The collocation points of these four neighbouring panels are defined in the local orthogonal coordinate system of the panel $j$ as $\mathbf{x}_i^{col,loc} = (\xi_i, \eta_i, 0)$, $i = 1, 2, 3, 4$. The dipole strength of the panel $j$ is described by $\mu_j$ and the dipole strengths of the four neighbouring panels are denoted by $\mu_i$ for $i = 1, \dots, 4$.

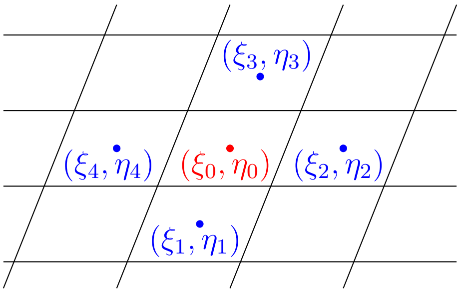

Figure 3.9: Bilinear interpolation of the dipole distribution

Then, a bilinear distribution of the dipoles over the four neighbouring panels is assumed:

$$\mu(\xi, \eta) = a + b\xi + c\eta + d\xi\eta. \quad (3.21)$$

This function is now evaluated on four collocation points $\mathbf{x}_i^{col,loc}$, $i = 1, \ldots, 4$ such that one obtains:

$$\underbrace{\begin{pmatrix} 1 & \xi_1 & \eta_1 & \xi_1\eta_1 \\ \vdots & \vdots & \vdots & \\ 1 & \xi_4 & \eta_4 & \xi_4\eta_4 \end{pmatrix}}_{A} \cdot \underbrace{\begin{pmatrix} a \\ b \\ c \\ d \end{pmatrix}}_{\mathbf{x}} = \underbrace{\begin{pmatrix} \mu_1 \\ \vdots \\ \mu_4 \end{pmatrix}}_{\mathbf{b}} . \tag{3.22}$$

The linear system of equations $\mathbf{A} \cdot \mathbf{x} = \mathbf{b}$ can easily be solved by the Gauss-method. The gradient of the distribution $\mu(\xi, \eta)$ in the centre point $(\xi_0, \eta_0) = (0, 0)$ is given by:

$$\nabla\mu|_{(0,0)} = (\frac{\partial\mu}{\partial\xi}, \frac{\partial\mu}{\partial\eta})|_{(0,0)} = (b, c). \tag{3.23}$$

Now, the tangential components of the induced velocities can be obtained:

$$\begin{aligned} v_\xi &= -\frac{\partial\mu}{\partial\xi} = -b \\ v_\eta &= -\frac{\partial\mu}{\partial\eta} = -c. \end{aligned} \tag{3.24}$$

Afterwards, the velocity components are transformed to the global coordinate system (s. Section B).

On those points of the flow domain that are not located on the solid body surface, the induced velocities are obtained from the discrete form of Equation (2.38):

$$\mathbf{v}(\mathbf{x_j}, t^n) = \sum_{i=1}^{N} \mu_i^n \nabla A_{i,j} + \sum_{i=1}^{N_W} \mu_{W,i}^n \nabla A_{i,j} - \sum_{i=1}^{N} \sigma_i^n \nabla B_{i,j}, \quad \forall \mathbf{x_j} \in \Omega/S_B. \tag{3.25}$$

### 3.4.2 Determination of pressures, forces and moments

The local pressures are computed from the discretised form of the Bernoulli equation. For a panel $j$ it holds:

$$p_j^n = p_\infty + \frac{\rho}{2}\Big(|\mathbf{V}_{\infty,j}^n|^2 - |\mathbf{V}_j^n|^2\Big) - \rho\frac{\partial\phi_j^n}{\partial t} + \rho g(z_\infty - z_j), \tag{3.26}$$

where the potential gradient with respect to time ${\partial\phi_j^n}/{\partial t}$ is approximated by the backwards difference scheme of first order.

From the known pressure values, the potential induced forces and moments can be calculated numerically by:

$$\mathbf{F}_{pot}^n = -\sum_{j=1}^{N} p_j^n \mathbf{n}_j A_j, \quad \mathbf{M}_{pot}^n = -\sum_{j=1}^{N} p_j^n (\mathbf{n}_j \times \mathbf{x}_j) A_j,$$

where

$$A_j = \int\limits_{\text{Panel}_j} dS(\mathbf{x})$$

is the area of the panel $j$.

# Chapter 4
# Sheet cavitation model

The goal of this chapter is to employ a numerical sheet cavitation model. In the first section, 4.1, the physical fundamentals and different types of cavitation are presented. In the second section, 4.2, the mathematical model for partial sheet cavitation is derived. The third and fourth sections, 4.3 and 4.4, are dedicated to the discretisation of the boundary value problem for the steady and unsteady cavitating flow. In 4.5 the chapter concludes with the numerical computation of the cavitation characteristics.

## 4.1 Physical fundamentals of cavitation

Cavitation can occur in different kinds of machines that operate in liquid, e.g. pumps, turbines and propellers (s. Carlton, 2007, p. 207). In general, cavitation develops in a liquid flow when the pressure in the flow falls below the vapour pressure of the liquid while the temperature of the fluid remains constant (s. Carlton, 2007, p. 207). The pressure decrease is mostly caused by high local fluid velocities in the vicinity of a submerged body. According to Carlton (2007, p. 212) there are two main phases of fluid in a cavitating flow, namely the vapour-phase and the liquid-phase. Additionally, also gas, such as air, can be contained in the cavitating water flow. Consequently, Carlton (2007, p. 212) characterises cavitation as a "two-phase, three-component flow regime".

In a propeller flow different types of cavitation occur. Their definition depends on their physical appearance. Cavitation can appear as bubble, tip and hub vortex, cloud and sheet cavitation. A detailed description of these types of cavitation is published in Carlton (2007, p. 212ff.). The present work focuses on the modelling of sheet cavitation that occurs in form of a vapour sheet that is attached to the solid body surface. This type of cavitation is very common on marine propulsion organs (s. Young, 2002, p. 4). It starts near the leading edge of a blade profile and ends either at the propeller surface or at the trailing wake. If the cavity sheet leaves the solid blade surface and closes at the trailing wake, it is called supercavitation (s. Young, 2002, p. 4). Otherwise, it is denoted as partial sheet cavitation (s. Young, 2002, p. 4). Both types are schematically illustrated in Figures 4.1a and 4.1b. Sheet cavitation can be located on the suction or on the pressure side of the blade. When the blade sections are working at positive angles of attack, sheet cavitation appears at the suction side of the blade and is called back cavitation; when the blade sections are working at negative angles of attack, sheet cavitation appears on the pressure side of the blade and is called face cavitation.

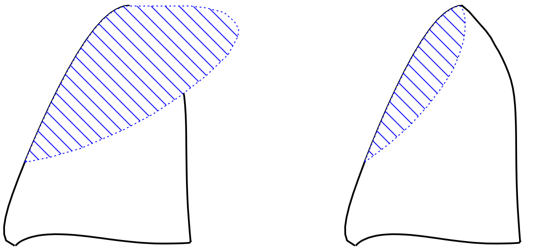

(a) Supercavitation (b) Partial sheet cavitation

Figure 4.1: Schematic illustration of different types of sheet cavitation

Sheet cavitation can influence the performance of a propeller, cause high pressure pulses on the ship hull, which can lead to noise and vibrations, and can cause erosion on the propeller blades (s. Young, 2002, p. 2f.). On this account, the prediction of the amount of sheet cavitation on propeller blades and the estimation of its effects on the propeller's performance and the surrounding boundaries is one of the most interesting aspects in the propeller design process. A small amount of partial sheet cavitation will have a negligible effect on the thrust of a propeller, it may even increase the thrust since the camber of the blade sections may be increased. However, when the blade is covered with a high amount of cavitation, the propeller's thrust and torque will be reduced. Additionally, sheet cavitation on a blade can have a considerable volume. The unsteady variations of this large volume can induce high pressure fluctuations on the ship hull.
In propeller design the main cavitation parameter is the cavitation number. This is defined by Carlton (2007, p. 219) as:

$$\text{cavitation number} = \frac{\text{static pressure head}}{\text{dynamic pressure head}}, \tag{4.1}$$

where the static pressure head may relate to the shaft centre line immersion or to a local section immersion. The dynamic head may be based on the undisturbed free stream velocity or on the rotational speed of the propeller. In the present work three different definitions are used:

$$\sigma_v = \frac{p_{ref} - p_v}{\rho/2|\mathbf{V}_{ship}|^2}, \; \sigma_n = \frac{p_{ref} - p_v}{\rho/2(nD)^2}, \; \sigma_{nx} = \frac{p_{ref} - p_v - \rho g x R}{\rho/2(nD)^2}, \tag{4.2}$$

where $\sigma_v$ is the free stream-based cavitation number and $\sigma_n$ and $\sigma_{nx}$ are the rotational speed-based cavitation numbers. The number $\sigma_n$ relates to the shaft center line and $\sigma_{nx}$ relates the local section immersion. The smaller the cavitation number is, the higher amount of cavitation is expected on the body's surface.

## 4.2 Governing equations for a cavitating potential flow

The goal of the present work is to derive a model for partial sheet cavitation, including both face and back cavitation. The modelling of supercavitation can be added in the future as an extension to the current modelling approach. The aim of the mathematical model is to predict the area of the cavity sheet, to calculate the pressure distribution inside the cavity sheet and to determine the cavity volume. Additionally, it is aimed at being able to simulate the sheet cavity volume patterns in unsteady calculations and to reproduce the displacement effect of sheet cavitation on the propeller induced pressure pulses. Acoustic aspects of cavitation are not described by the present potential based cavitation model.

With regards to the requirements described above, potential flow theory provides three different relevant approaches to modelling sheet cavitation. The approaches differ in their application of the boundary conditions for sheet cavitation and in the treatment of the panel grid. The first model is called the "fully non-linear model" and is based on the approach in which the boundary conditions are applied directly on the cavity surface, denoted by $S_C$ (s. Vaz, 2005, p. 32f.). The second and third model are called "partially non-linear model" with and without re-meshing of the panel grid, respectively. In the partially non-linear model the boundary conditions are not applied directly on the cavity surface but on an auxiliary surface underneath the cavity sheet (s. Vaz, 2005, p. 33f.). In case of partial cavitation, the body surface is used as the reference surface. This reference surface is denoted by $S_{B_C}$ as illustrated in Figure 4.2a. In case of supercavitation, the body as well as the wake surface are used as reference surfaces. In this case the reference surfaces are denoted by $S_{B_C}$ and $S_{W_C}$, respectively (s. Figure 4.2b). The reference grid in the partially non-linear model can be re-meshed or can be kept as is for all iteration steps. The grid re-meshing is only performed on the reference surfaces such that the remaining grid stays as is. This approach guarantees the grid convergence of the results. However, it is also associated with a higher CPU time since the influence coefficients must be re-computed in each iteration step.

All three models are non-linear since the cavity surface is not known a priori and its determination is a part of the solution process. Firstly, a guess for the cavity shape is made and the boundary conditions are applied on this approximate cavity surface or on the reference surfaces. Secondly, the cavity shape is adjusted based on the solution of the current step and the boundary conditions are applied on the modified surface. The iterative procedure is repeated until the results converge.

In the present work the partially non-linear sheet cavitation model without re-meshing of the grid is applied. The advantages of this model are its easier implementation and shorter

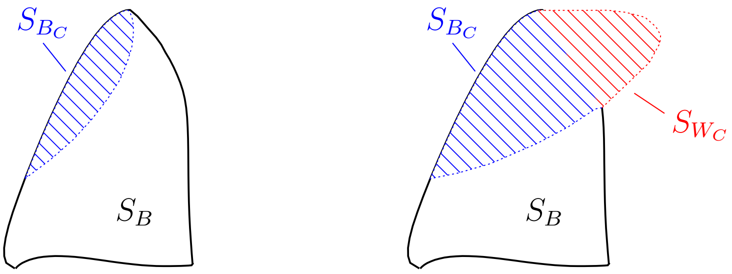

(a) Reference surface of partial sheet cavitation

(b) Reference surfaces of super-cavitation

Figure 4.2: Reference surfaces of the partially non-linear sheet cavitation model

computation time since no re-computation of the influence coefficients and no re-meshing of the grid are required. The fully non-linear model is supposed to be the most physically correct model of the three aforementioned ones, but Vaz (2005, p. 142) found it to be numerically the most demanding. A significant assumption of the partially non-linear model is that the cavity thickness keeps small, whereas the cavity induced velocities are allowed to be high (s. Vaz, 2005, p. 33). The non-re-meshing of the grid simplifies the implementation of the model, but it also involves difficulties concerning the choice of the body surface grid. On the one hand, the grid must be fine enough to deliver grid-independent and accurate results for sheet cavitation. On the other hand, it must not be too fine since instabilities can occur and the computation time can increase. Hence, the choice of a suitable grid is part of the solution process of the partially non-linear model without grid re-meshing.

In addition to the choice of the overall model, there are three main physical phenomenon that must be determined by the numerical partial sheet cavitation model:

- **Sheet cavitation inception:** The region where sheet cavitation begins is called cavitation inception. According to Carlton (2007, p. 228), a necessary condition for the inception of cavitation is the presence of nuclei (tiny gas bubbles) in the sea water. When the pressure in the water is reduced to the vapour pressure, the nuclei reach a critical size and grow explosively. At this point cavitation takes place. Carlton (2007, p. 228) concludes that cavitation inception depends on three main parameters: the nuclei content of water, the growth of the boundary layer over the propeller sections and the type of cavitation. This indicates that not only the flow environment has an influence on the cavitation inception but also the geometry of the propeller and the wake field (s. Carlton, 2007, p. 228). Hence, the numerical determination of cavitation inception is a complex matter.

- **Cavity closure:** The region where the cavity sheet ends is called cavity closure. The flow conditions at the cavity closure are complicated and dominated by viscous effects. Carlton (2007, p. 212) states that a re-entrant jet is formed at the cavity trailing edge between the underside of the cavity and the propeller blade surface. That means that some fluid re-enters the cavity and the flow streamlines do not attach smoothly to the blade surface.

- **Boundary conditions on the cavity sheet:** In the region between the sheet cavitation inception and the cavity closure (in the so-called cavity sheet) the pressure must be equal or less than the vapour pressure.

The implementation of these three aspects in the partially non-linear model is described in detail below.

### 4.2.1 Determination of sheet cavitation inception

The inception point of cavitation is denoted in the numerical model as detachment point and is defined in the local coordinate system by the coordinate along the chord-wise direction. In the local orthogonal coordinate system this point is denoted by $\xi_d$, in the local non-orthogonal coordinate system by $s_d$. Since the region of cavitation inception is dominated by viscous effects and is physically a very complex phenomenon, the determination of its location in potential flow theory requires simplification. In the relevant literature there are three prevailing approaches:

- Villat-Brillouin criterion: This criterion, also called the smooth detachment condition, demands that the cavity has a non-negative thickness at the leading edge and the pressure upstream of the cavitation surface should be greater than the vapour pressure (s. Young, 2002, p. 39).

- Sheet cavitation starts at the blade's leading edge: In this approach, the detachment point is located at a fixed point, namely at the leading edge of the blade profile or hydrofoil (s. Vaz, 2005, p. 36).

- Sheet cavitation starts at the point of minimum pressure. The point of minimum pressure is usually a point that lies downstream of the leading edge and downstream of the point determined by the Villat-Brillouin criterion (s. Vaz, 2005, p. 36).

In *pan*MARE the first and second approach are implemented. The disadvantage of the third approach is that it does not deliver accurate results for thick foils (s. Vaz, 2005, p. 36). The location of the detachment at the leading edge has the advantage that the point is usually independent of the discretisation of the body surface. According to Vaz (2005,

p. 36f.) all of the above approaches tend to the same point for blade profiles with a small thickness.

### 4.2.2 Determination of cavity closure

In order to numerically define a cavity shape, the region where sheet cavitation ends must be detected and its surface must be modelled. It is a challenging point to model the cavity closure in potential flow theory because this region is highly influenced by viscous effects. There are two basic modelling approaches (s. Vaz, 2005, p. 37ff.):

- Open models: The cavity is left open at the end and a wake with a certain length is modelled behind the cavity sheet.
- Closed models: The cavity closes at a certain point with the solid body surface.

Although open models coincide better with measured results, their implementation is more difficult in potential flow theory (s. Vaz, 2005, p. 37). The choice of a suitable cavity closure approach depends mainly on the underlying sheet cavitation model. In the present work the partially non-linear model is used where the boundary conditions are applied not on the exact cavity surface but on the reference surface on the body. The use of a closed model is more suitable in this case and is implemented in *pan*MARE. In the closed model the cavity closure is defined as a point where the cavity thickness reaches zero and is non-negative. This point is called the reattachment point. In the orthogonal local coordinate system its coordinate is denoted by $\xi_r$, in the non-orthogonal local coordinate system by $s_r$.

### 4.2.3 Boundary conditions on the cavity sheet

In the region between the sheet cavitation inception and the cavity closure, in the so-called cavity sheet, certain physical conditions must be fulfilled. These conditions are (s. Vaz, 2005, p. 12):

- Dynamic boundary condition: This condition states that the pressure inside the cavity sheet must be equal to or smaller than the vapour pressure. Pressure outside the cavity sheet must be higher than the vapour pressure.
- Kinematic boundary condition: This condition requires that there is no flux through the cavity sheet, i.e. velocity normal to the cavity sheet must vanish.

In the following, the mathematical application of both conditions on the current boundary value problem is described.

### Dynamic boundary condition

The first boundary condition used to model sheet cavitation is the dynamic boundary condition:

$$p = p_v \Leftrightarrow C_{p,v} = -\sigma_v,\ \forall\, \mathbf{x} \in S_{B_C}. \tag{4.3}$$

This condition requires the pressure in the cavity region to be equal to the vapour pressure. Actually, this criterion represents a simplification of the real physical condition, since the pressure can be lower than the vapour pressure. However, in the numerical model the real physical condition is hardly applicable. The combination of condition $(4.3)$ with the Bernoulli equation $(2.10)$ results in:

$$\frac{\rho}{2}\Big(|\mathbf{V}|^2 - |\mathbf{V}_\infty|^2\Big) - g\rho(z_\infty - z) + \rho\frac{\partial \phi}{\partial t} = p_\infty - p_v, \quad \text{on} \quad S_{B_C}.$$

This condition is now transformed to the curvilinear orthogonal coordinate system with coordinates $(\xi, \eta, \zeta)$ where $\zeta$ is directed outwards (s. Section 2.1). In the orthogonal local coordinate system it holds:

$$|\mathbf{V}|^2 = V_\xi^2 + V_\eta^2 + V_\zeta^2.$$

From this relation one obtains:

$$V_\xi^2 + V_\eta^2 + V_\zeta^2 = |\mathbf{V}_\infty|^2 + \frac{2}{\rho}(p_\infty - p_v) + 2g(\zeta_\infty - \zeta) - 2\frac{\partial \phi}{\partial t}. \tag{4.4}$$

The dynamic boundary condition is not linear in $\phi$ because of the quadratic terms $V_\xi^2 = \left(\frac{\partial \phi}{\partial \xi}\right)^2$, ... . But it can be transformed in a Dirichlet-like boundary condition for the unknown $\phi$ (s. Vaz, 2005, p. 16). For this purpose Equation $(4.4)$ is solved for $V_\xi$ and relation $V_\xi = \frac{\partial \phi}{\partial \xi} + V_{\infty,\xi}$ is used. It follows:

$$\frac{\partial \phi}{\partial \xi} = v_\xi = \sqrt{|\mathbf{V}_\infty|^2 + \frac{2}{\rho}(p_\infty - p_v) + 2g(\zeta_\infty - \zeta) - 2\frac{\partial \phi}{\partial t} - V_\eta^2 - V_\zeta^2} - V_{\infty,\xi}.$$

Integration along $\xi$ leads to:

$$\begin{aligned}\phi = \phi\,|_{\xi_d} + \int_\xi \Bigg[&\sqrt{|\mathbf{V}_\infty|^2 + \frac{2}{\rho}(p_\infty - p_v) + 2g(\zeta_\infty - \zeta) - 2\frac{\partial \phi}{\partial t} - V_\eta^2 - V_\zeta^2} \\ &- V_{\infty,\xi}\Bigg] d\xi \quad \text{on} \quad S_{B_C}.\end{aligned} \tag{4.5}$$

In the partially non-linear model the normal velocity component $V_\zeta$ is neglected in Equation $(4.5)$ to increase the robustness of the model (s. Vaz, 2005, p. 17). With this simplification the dynamic boundary conditions for back and face cavitation read as follows:

$$\begin{aligned}\phi = \phi^{back}\,|_{\xi_d} + \int_{\xi}\Big[\sqrt{|\mathbf{V}_\infty|^2 + (p_\infty - p_v)\frac{2}{\rho} + 2g(\zeta_\infty - \zeta) - 2\frac{\partial\phi}{\partial t} - V_\eta^2} \\ - V_{\infty,\xi}\Big]d\xi \quad \text{on} \quad S_{B_C}, \quad \text{(Back cavitation)}\end{aligned} \tag{4.6}$$

$$\begin{aligned}\phi = \phi^{face}\,|_{\xi_d} + \int_{\xi}\Big[\sqrt{|\mathbf{V}_\infty|^2 + (p_\infty - p_v)\frac{2}{\rho} + 2g(\zeta_\infty - \zeta) - 2\frac{\partial\phi}{\partial t} - V_\eta^2} \\ - V_{\infty,\xi}\Big]d\xi \quad \text{on} \quad S_{B_C}, \quad \text{(Face cavitation)}\end{aligned} \tag{4.7}$$

where $\phi^{back}_{\xi_d}$ is the potential at the detachment point on the suction side of the profile and $\phi^{face}_{\xi_d}$ is the potential at the detachment point on the pressure side of the profile. The potential at the detachment point is calculated via extrapolation. The extrapolation formulas for face and back cavitation are derived in Section 4.3.4.

### Kinematic boundary condition

The second physical condition that must be valid on the cavity sheet is the kinematic boundary condition. It postulates that the normal component of the velocity on the cavity sheet must vanish:

$$\frac{D}{Dt}F(s_1, s_2, s_3, t) = (\frac{\partial}{\partial t} + \mathbf{V}\cdot\nabla)(s_3 - \eta^{cav}(s_1, s_2, t)) = 0, \quad \text{on} \quad S_{B_C}. \tag{4.8}$$

The function $F = s_3 - \eta^{cav}(s_1, s_2, t)$ represents the cavity surface, where $\eta^{cav}$ is the cavity thickness (s. Vaz, 2005, p. 12). The kinematic boundary condition is described in the curvilinear non-orthogonal coordinate system with coordinates $(s_1, s_2, s_3)$, where $s_3$ is directed outwards (s. Section 2.1).

The vector $\mathbf{V}$ and the nabla operator in Equation (4.8) must be formulated in the coordinates of the local non-orthogonal coordinate system. The term $\mathbf{V}\cdot\nabla$ can be written in terms of the local non-orthogonal coordinates as:

$$\mathbf{V}\cdot\nabla = \frac{(V_{s_1} - (\mathbf{t}_1\cdot\mathbf{t}_2)V_{s_2})}{\|\mathbf{t}_1\times\mathbf{t}_2\|^2}\frac{\partial}{\partial s_1} + \frac{(V_{s_2} - (\mathbf{t}_1\cdot\mathbf{t}_2)V_{s_1})}{\|\mathbf{t}_1\times\mathbf{t}_2\|^2}\frac{\partial}{\partial s_2} + V_{s_3}\frac{\partial}{\partial s_3} \tag{4.9}$$

and the velocity components read as:

$$V_{s_1} = \underbrace{\frac{\partial\phi}{\partial s_1}}_{=v_{s_1}} + \mathbf{V}_\infty\cdot\mathbf{t}_1, \quad V_{s_2} = \underbrace{\frac{\partial\phi}{\partial s_2}}_{=v_{s_2}} + \mathbf{V}_\infty\cdot\mathbf{t}_2, \quad V_{s_3} = \underbrace{\frac{\partial\phi}{\partial s_3}}_{=v_{s_3}} + \mathbf{V}_\infty\cdot\underbrace{\mathbf{t}_3}_{=\mathbf{n}}. \tag{4.10}$$

Equation $(4.8)$ combined with Equation $(4.9)$ leads to the following relation:

$$\frac{D}{Dt}F = -\frac{\partial \eta^{cav}}{\partial t} + V_{s_3} - \frac{(V_{s_1} - (\mathbf{t}_1 \cdot \mathbf{t}_2)V_{s_2})}{\|\mathbf{t}_1 \times \mathbf{t}_2\|^2}\frac{\partial \eta^{cav}}{\partial s_1} - \frac{(V_{s_2} - (\mathbf{t}_1 \cdot \mathbf{t}_2)V_{s_1})}{\|\mathbf{t}_1 \times \mathbf{t}_2\|^2}\frac{\partial \eta^{cav}}{\partial s_2} = 0.$$

The kinematic boundary condition can now be rewritten and one obtains:

$$\frac{\partial \eta^{cav}}{\partial s_1}(V_{s_1} - (\mathbf{t}_1 \cdot \mathbf{t}_2)V_{s_2}) + \frac{\partial \eta^{cav}}{\partial s_2}(V_{s_2} - (\mathbf{t}_1 \cdot \mathbf{t}_2)V_{s_1}) = \|\mathbf{t}_1 \times \mathbf{t}_2\|^2\Big(V_{s_3} - \frac{\partial \eta^{cav}}{\partial t}\Big) \quad (4.11)$$

on $S_{B_C}$. The mathematical formulation of the kinematic boundary condition is the same for face and back cavitation.

## 4.3 Numerical model for steady sheet cavitation

This section describes the discretisation of the governing equations for a steady cavitating flow around a fully submerged body.

### 4.3.1 Nomenclature

The nomenclature used in the numerical algorithm for sheet cavitation calculation is summarised below.

| | |
|---|---|
| $l_d$ | Index of the detachment point in the cross-wise direction. |
| $l_r$ | Index of the reattachment point in the cross-wise direction. |
| $N_k^{cav} = l_r - l_d + 1$ | Number of cavitating panels at the radial stripe $k$. |
| $N_k^{noncav} = N_k - N_k^{cav}$ | Number of non-cavitating panels at the radial stripe $k$. |
| $N^{cav} = \sum_{k=1}^{N_k} N_k^{cav}$ | Number of cavitating panels on the body surface. |
| $N^{noncav} = N - N^{cav}$ | Number of non-cavitating panels on the body surface. |
| $\sigma_i^{cav} = \sigma_{(l,k)}^{cav}$ | Source strength on the cavitating panel $i = (l,k)$, where $l$ is the circular stripe and $k$ is the radial stripe. |
| $\mu_i^{cav} = \mu_{(l,k)}^{cav}$ | Dipole strength on the cavitating panel $i = (l,k)$. |

The value of the indices $l_d$ and $l_r$ can vary in each iteration step. Consequently, the number of cavitating and non-cavitating panels, $N_k^{cav}$ and $N_k^{noncav}$, can also vary during the iteration procedure. The number of collocation points for partial sheet cavitation calculations is the same as in the non-cavitating case, namely $N_{total} = N^{noncav} + N^{cav} = N_k N_l$ where $N_k$ is the number of panels in the span-wise direction and $N_l$ is the number of panels in the cross-wise direction.

### 4.3.2 Discretised form of the boundary value problem

In the following, the discretisation of the boundary value problem for a propeller flow with partial cavitation model is introduced. The approach being used here for the boundary equations is the potential-based formulation of type 2 (s. Equation (2.35)). In continuous form, the boundary value problem reads as:

$$\frac{1}{4\pi}\Big[\int\limits_{S_B/S_{B_C}}(\mu\frac{\partial}{\partial n}(\frac{1}{r})-\sigma\frac{1}{r})dS+\int\limits_{S_{B_C}}(\mu^{cav}\frac{\partial}{\partial n}(\frac{1}{r})-\sigma^{cav}\frac{1}{r})dS + \int\limits_{S_W}\mu_W\frac{\partial}{\partial n}(\frac{1}{r})dS\Big]=0. \tag{4.12}$$

The discretisation of the body and wake geometry into panels results in the following equation:

$$\frac{1}{4\pi}\Big[\sum_{i=1}^{N^{noncav}}\mu_i\int\limits_{Panel_i}\frac{\partial}{\partial n}(\frac{1}{r})dS+\sum_{i=1}^{N^{cav}}\mu_i^{cav}\int\limits_{Panel_i}\frac{\partial}{\partial n}(\frac{1}{r})dS - \sum_{i=1}^{N^{noncav}}\sigma_i\int\limits_{Panel_i}\frac{1}{r}dS-\sum_{i=1}^{N^{cav}}\sigma_i^{cav}\int\limits_{Panel_i}\frac{1}{r}dS+\sum_{i=1}^{N_W}\mu_{W,i}\int\limits_{Panel_i}\frac{\partial}{\partial n}(\frac{1}{r})dS\Big]=0. \tag{4.13}$$

From the above equation one obtains:

$$\sum_{i=1}^{N^{noncav}}A_{i,j}\mu_i+\sum_{i=1}^{N^{cav}}A_{i,j}\mu_i^{cav}+\sum_{i=1}^{N_W}A_{i,j}\mu_{W,i}-\sum_{i=1}^{N^{noncav}}B_{i,j}\sigma_i-\sum_{i=1}^{N^{cav}}B_{i,j}\sigma_i^{cav}=0, \tag{4.14}$$

for all collocation points $x_j^{col}$, $j=1,\dots,N=N^{noncav}+N^{cav}$, where the influence functions are defined in the same way as in Equation (3.5). By using the linear Kutta condition (3.8), the influence function $A_{i,j}$ can be rewritten (s. Section 3.2.2) and one obtains:

$$\sum_{i=1}^{N^{noncav}}A^*_{i,j}\mu_i+\sum_{i=1}^{N^{cav}}A^*_{i,j}\mu_i^{cav}-\sum_{i=1}^{N^{noncav}}B_{i,j}\sigma_i-\sum_{i=1}^{N^{cav}}B_{i,j}\sigma_i^{cav}=0. \tag{4.15}$$

The cavitating panels are treated differently than the non-cavitating panels. For each type of panel adequate boundary conditions are applied to obtain a linear system of equations for the unknown strengths. The known and unknown strengths are:

- $N^{noncav}$ known source strengths $\sigma$ calculated from the Neumann boundary condition (2.25) on the body surface,

- $N^{cav}$ known dipole strengths $\mu^{cav}$ computed from the dynamic boundary condition $(4.6)$ or $(4.7)$ on the reference body surface $S_{B_C}$,
- $N^{noncav}$ unknown dipole strengths $\mu$ on the non-cavitating part of the surface,
- $N^{cav}$ unknown source strengths $\sigma^{cav}$ on the reference body surface $S_{B_C}$,
- $N_W$ known dipole strengths $\mu_W$ on the wake which are determined by the linear form of the Kutta condition $(3.8)$.

The total number of unknown strengths is $N^{noncav} + N^{cav} = N$.
The numerical determination of the potential at the body reference surface $S_{B_C}$ is discussed in Section 4.3.4. It is shown there that the following relation holds:

$$\mu^{cav}_{(l,k)} = \mu^{back/face}_{(l_d,k)} + \tilde{\mu}^{cav}_{(l,k)} = -\phi^{cav}_{(l,k)} = -\phi^{back/face}_{(l_d,k)} - \tilde{\phi}^{cav}_{(l,k)}, \tag{4.16}$$

$\forall\, l = 1, \ldots, N_l, k = 1, \ldots, N_k$. The dipole strength $\mu^{back/face}_{(l_d,k)}$ depends on the dipole strengths upstream (in case of back cavitation) or downstream (in case of face cavitation) of the cavitation detachment point. Using Equation $(4.24)$ or $(4.25)$ for the potential at the detachment point, the influence coefficients $A_{i,j}$ can again be re-written and one obtains:

$$\begin{aligned}
A^{**}_{i,j} &= A_{i,j} + \alpha_1\Big(\sum_{w=0}^{N^{cav}_k} A_{w,j}\Big), \quad \text{if} \quad i = (l_d \mp 1, k),\\
A^{**}_{i,j} &= A_{i,j} + \alpha_2\Big(\sum_{w=0}^{N^{cav}_k} A_{w,j}\Big), \quad \text{if} \quad i = (l_d \mp 2, k),\\
A^{**}_{i,j} &= A_{i,j} + \alpha_3\Big(\sum_{w=0}^{N^{cav}_k} A_{w,j}\Big), \quad \text{if} \quad i = (l_d \mp 3, k),\\
A^{**}_{i,j} &= A^{*}_{i,j}, \quad \text{else.}
\end{aligned} \tag{4.17}$$

The sign $\mp$ stands for back and face cavitation, respectively. Now the final linear system of equations reads as:

$$\sum_{i=1}^{N^{noncav}} A^{**}_{i,j}\mu_i - \sum_{i=1}^{N^{cav}} B_{i,j}\sigma^{cav}_i = -\sum_{i=1}^{N^{cav}} A^{*}_{i,j}\tilde{\mu}^{cav}_i + \sum_{i=1}^{N^{noncav}} B_{i,j}\sigma_i, \; \forall\, j = 1, \ldots, N, \tag{4.18}$$

where the known parts are put on the right-hand side and the unknown parts on the left-hand side of the system. Once this linear system of equations is solved, the local velocities and pressures can be computed and the shape of the cavity surface can be calculated by solving the kinematic boundary condition for the cavity thickness.

### 4.3.3 Boundary value problem for multiple bodies in the domain

Analogous to the non-cavitating case (s. Section 3.2.4), the case of multiple bodies in the fluid domain is now considered. By assuming that on the body $m$ there are $N^{cav,m}$ cavitating and $N^{noncav,m} = (N^m - N^{cav,m})$ non-cavitating panels, the linear system of equations reads as:

$$\begin{aligned} &\sum_{m=1}^{M}\Big[\sum_{i=1}^{N^{noncav,m}} A^{**}_{i,j}\mu_i - \sum_{i=1}^{N^{cav,m}} B_{i,j}\sigma_i^{cav}\Big] = \\ &-\sum_{m=1}^{M}\Big[\sum_{i=1}^{N^{cav,m}} A^{*}_{i,j}\tilde{\mu}_i^{cav} - \sum_{i=1}^{N^{noncav,m}} B_{i,j}\sigma_i\Big], \quad \forall j = 1,\dots,N. \end{aligned} \tag{4.19}$$

### 4.3.4 Numerical determination of the potential on the cavity surface

In steady calculations the potential at the cavity surface is determined by means of the steady dynamic boundary condition:

$$\phi^{cav} = \phi^{back/face}\mid_{\xi_d} + \int_{\xi}\Big[\sqrt{|\mathbf{V}_\infty|^2 + (p_\infty - p_v)\frac{2}{\rho} + 2g(\zeta_\infty - \zeta) - V_\eta^2} - V_{\infty,\xi}\Big]d\xi. \tag{4.20}$$

The discrete form of this condition reads as:

$$\phi^{cav}_{(l,k)} = \phi^{back/face}_{(l_d,k)} + \tilde{\phi}^{cav}_{(l,k)}. \tag{4.21}$$

In order to calculate the function $\tilde{\phi}^{cav}_{(l,k)}$, the value of this function is computed at two auxiliary points of the panel, namely at the midpoints of the panel edges along the cross-wise coordinate $\xi$, denoted by the subscripts $(l+\frac{1}{2},k)$ and $(l-\frac{1}{2},k)$ (s. Figure 4.3). The values $\tilde{\phi}^{cav}_{(l\pm\frac{1}{2},k)}$ are determined numerically by means of the trapezoidal rule:

$$\begin{aligned} \tilde{\phi}^{cav}_{(l+\frac{1}{2},k)} &= \sum_{w=l_d+1}^{w=l}\Big[\Big(\sqrt{|V_\infty|^2 + \sigma_v|V_{ship}|^2 - 2g\zeta - V_\eta^2} - V_{\infty,\xi}\Big)|_{(w,k)} \\ &\qquad \cdot\Big(\xi_{(w+\frac{1}{2},k)} - \xi_{(w-\frac{1}{2},k)}\Big)\Big], \\ \tilde{\phi}^{cav}_{(l-\frac{1}{2},k)} &= \sum_{w=l_d+1}^{w=l-1}\Big[\Big(\sqrt{|V_\infty|^2 + \sigma_v|V_{ship}|^2 - 2g\zeta - V_\eta^2} - V_{\infty,\xi}\Big)|_{(w,k)} \\ &\qquad \cdot\Big(\xi_{(w+\frac{1}{2},k)} - \xi_{(w-\frac{1}{2},k)}\Big)\Big], \end{aligned} \tag{4.22}$$

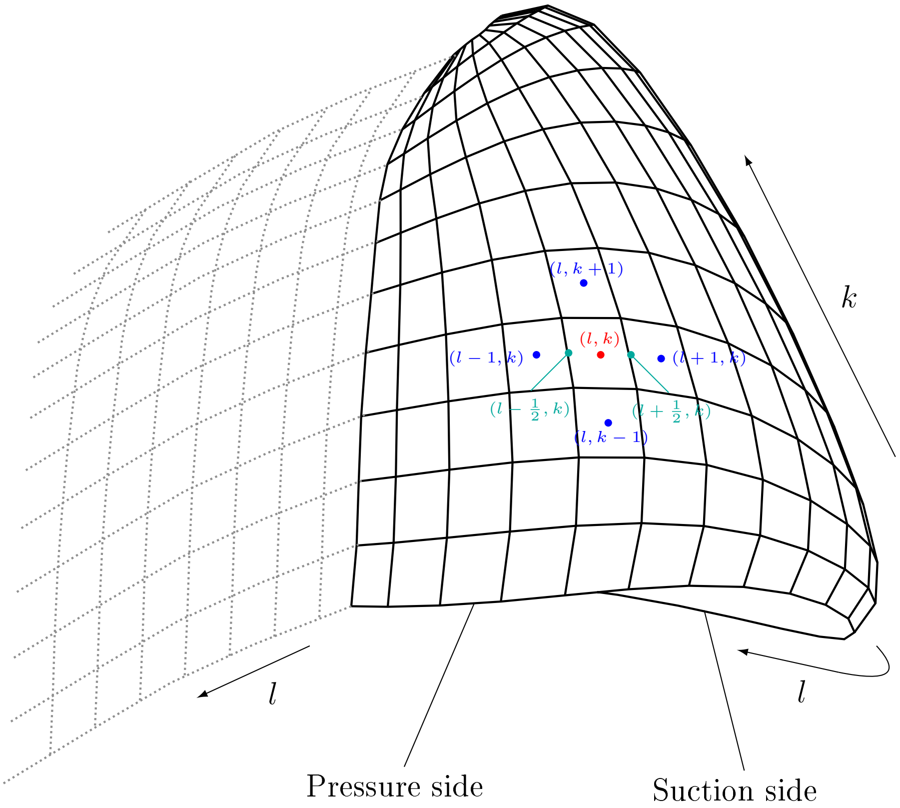

Figure 4.3: Auxiliary points on the blade grid

where $l = l_d + 2, \ldots, l_r$ and $k = 1, \ldots, N_k$. Afterwards the potential at the midpoint of a panel is obtained by using linear interpolation:

$$\tilde{\phi}^{cav}_{(l,k)} = \frac{\tilde{\phi}^{cav}_{(l+\frac{1}{2},k)} + \tilde{\phi}^{cav}_{(l-\frac{1}{2},k)}}{2}. \tag{4.23}$$

In the numerical model the detachment point is identified by the index pair $(l_d, k)$ and the discrete potential at the detachment point is denoted by $\phi_{(l_d,k)}$. The potential $\phi_{(l_d,k)}$ is calculated by an extrapolation of the second order as suggested by Vaz (s. 2005, p. 90). For each radial stripe $k$ it holds:

$$\phi^{back}_{(l_d,k)} = \alpha_1\phi^{back}_1 + \alpha_2\phi^{back}_2 + \alpha_3\phi^{back}_3, \tag{4.24}$$

$$\phi^{face}_{(l_d,k)} = \beta_1\phi^{face}_1 + \beta_2\phi^{face}_2 + \beta_3\phi^{face}_3, \tag{4.25}$$

where

$$\phi^{back}_1 = \phi_{(l_d-1,k)}, \quad \phi^{back}_2 = \phi_{(l_d-2,k)}, \quad \phi^{back}_3 = \phi_{(l_d-3,k)},$$

$$\alpha_1 = \frac{bc}{(a-b)(a-c)}, \quad \alpha_2 = \frac{ac}{(b-a)(b-c)}, \quad \alpha_3 = \frac{ab}{(c-a)(c-b)},$$
$$a = \xi_{(l_d,k)} - \xi_{(l_d-1,k)},\ b = \xi_{(l_d,k)} - \xi_{(l_d-2,k)},\ c = \xi_{(l_d,k)} - \xi_{(l_d-3,k)}$$

and

$$\phi_1^{face} = \phi_{(l_d+1,k)}, \quad \phi_2^{face} = \phi_{(l_d+2,k)}, \quad \phi_3^{face} = \phi_{(l_d+3,k)},$$
$$\beta_1 = \frac{ef}{(d-e)(d-f)}, \quad \beta_2 = \frac{df}{(e-d)(e-f)}, \quad \beta_3 = \frac{de}{(f-d)(f-e)},$$
$$d = \xi_{(l_d,k)} - \xi_{(l_d+1,k)},\ e = \xi_{(l_d,k)} - \xi_{(l_d+2,k)},\ f = \xi_{(l_d,k)} - \xi_{(l_d+3,k)}.$$

In case both face and back side cavitation occur on the blade, the distance between the detachment point location on the suction side and that on the pressure side must be at least three panels. Otherwise, the above extrapolation method cannot be applied.

### 4.3.5 Calculation of the cavity thickness

The determination of the cavity thickness is important for the estimation of the sheet cavity shape and cavity volume. Equation $(4.11)$ for the cavity thickness is a linear partial differential equation that contains spacial and time derivatives of the cavity thickness. The spacial derivatives $\frac{\partial}{\partial s_1}$ and $\frac{\partial}{\partial s_2}$ are discretised by a central difference scheme of first order:

$$\frac{\partial \eta^{cav}}{\partial s_1}|_{(l,k)} \approx \frac{\eta^{cav}_{(l+\frac{1}{2},k)} - \eta^{cav}_{(l-\frac{1}{2},k)}}{s_{1_{(l+\frac{1}{2},k)}} - s_{1_{(l-\frac{1}{2},k)}}}, \quad \frac{\partial \eta^{cav}}{\partial s_2}|_{(l,k)} \approx \frac{\eta^{cav}_{(l,k+1)} - \eta^{cav}_{(l,k-1)}}{s_{2_{(l,k+1)}} - s_{2_{(l,k-1)}}}. \tag{4.26}$$

In the numerical procedure the auxiliary points defined in Figure 4.3 are used as nodes at which the cavity thickness is evaluated. For this purpose a linear interpolation of the values $\eta^{cav}_{(l,k+1)}$ and $\eta^{cav}_{(l,k-1)}$ is assumed:

$$\eta^{cav}_{(l,k+1)} \approx \frac{\eta^{cav}_{(l+\frac{1}{2},k+1)} + \eta^{cav}_{(l-\frac{1}{2},k+1)}}{2}, \quad \eta^{cav}_{(l,k-1)} \approx \frac{\eta^{cav}_{(l+\frac{1}{2},k-1)} + \eta^{cav}_{(l-\frac{1}{2},k-1)}}{2}. \tag{4.27}$$

With these interpolation formulas the derivative of the cavity thickness with respect to the coordinate $s_2$ is approximated by:

$$\frac{\partial \eta^{cav}}{\partial s_2}|_{(l,k)} \approx \frac{1}{2}\Big(\frac{\eta^{cav}_{(l+\frac{1}{2},k+1)} + \eta^{cav}_{(l-\frac{1}{2},k+1)} - \eta^{cav}_{(l+\frac{1}{2},k-1)} - \eta^{cav}_{(l-\frac{1}{2},k-1)}}{s_{2_{(l,k+1)}} - s_{2_{(l,k-1)}}}\Big). \tag{4.28}$$

By means of these approximations, a recursive formula for the cavity thickness at the auxiliary points is now defined:

$$\begin{aligned}
&A_{(l,k)}\Big[\frac{\eta^{cav}_{(l+\frac{1}{2},k)}-\eta^{cav}_{(l-\frac{1}{2},k)}}{s_{1_{(l+\frac{1}{2},k)}}-s_{1_{(l-\frac{1}{2},k)}}}\Big]+\frac{B_{(l,k)}}{2}\Big[\frac{\eta^{cav}_{(l+\frac{1}{2},k+1)}+\eta^{cav}_{(l-\frac{1}{2},k+1)}}{s_{2_{(l,k+1)}}-s_{2_{(l,k-1)}}}\Big]=C_{(l,k)},\ \text{for } k=1,\\
&A_{(l,k)}\Big[\frac{\eta^{cav}_{(l+\frac{1}{2},k)}-\eta^{cav}_{(l-\frac{1}{2},k)}}{s_{1_{(l+\frac{1}{2},k)}}-s_{1_{(l-\frac{1}{2},k)}}}\Big]+\frac{B_{(l,k)}}{2}\Big[\frac{\eta^{cav}_{(l+\frac{1}{2},k+1)}+\eta^{cav}_{(l-\frac{1}{2},k+1)}}{s_{2_{(l,k+1)}}-s_{2_{(l,k-1)}}}-\frac{\eta^{cav}_{(l+\frac{1}{2},k-1)}+\eta^{cav}_{(l-\frac{1}{2},k-1)}}{s_{2_{(l,k+1)}}-s_{2_{(l,k-1)}}}\Big]\\
&\qquad\qquad=C_{(l,k)},\ \text{for } k=2,\dots,N_k-1,\\
&A_{(l,k)}\Big[\frac{\eta^{cav}_{(l+\frac{1}{2},k)}-\eta^{cav}_{(l-\frac{1}{2},k)}}{s_{1_{(l+\frac{1}{2},k)}}-s_{1_{(l-\frac{1}{2},k)}}}\Big]-\frac{B_{(l,k)}}{2}\Big[\frac{\eta^{cav}_{(l+\frac{1}{2},k-1)}+\eta^{cav}_{(l-\frac{1}{2},k-1)}}{s_{2_{(l,k+1)}}-s_{2_{(l,k-1)}}}\Big]=C_{(l,k)},\ \text{for } k=N_k,
\end{aligned}\tag{4.29}$$

where $A_{(l,k)} = V_{s_1,(l,k)} - (\mathbf{t}_1\cdot\mathbf{t}_2)V_{s_2,(l,k)}$, $B_{(l,k)} = V_{s_2,(l,k)} - (\mathbf{t}_1\cdot\mathbf{t}_2)V_{s_1,(l,k)}$ and $C_{(l,k)} = \|\mathbf{t}_1\times\mathbf{t}_2\|^2 V_{s_3,(l,k)}$ for all $l = 1,\dots,N_l$. Equations 4.29 lead to the following linear system of equations:

$$\mathbf{M}\cdot\eta^{cav} = \mathbf{f}, \tag{4.30}$$

where the vectors $\eta^{cav}\in\mathbf{R}^{(N_lN_k)}$ and $\mathbf{f}\in\mathbf{R}^{(N_lN_k)}$ are defined by:

$$\eta^{cav}=\begin{pmatrix}\eta^{cav}_{(\frac{3}{2},1)}\\ \vdots\\ \eta^{cav}_{(N_l+\frac{1}{2},1)}\\ \eta^{cav}_{(\frac{3}{2},2)}\\ \vdots\\ \eta^{cav}_{(N_l+\frac{1}{2},2)}\\ \vdots\\ \eta^{cav}_{(\frac{3}{2},N_k)}\\ \vdots\\ \eta^{cav}_{(N_l+\frac{1}{2},N_k)}\end{pmatrix},\quad \mathbf{f}=\begin{pmatrix}\Delta s_1\frac{C}{A}|_{(\frac{3}{2},1)}\\ \vdots\\ \Delta s_1\frac{C}{A}|_{(N_l+\frac{1}{2},1)}\\ \Delta s_1\frac{C}{A}|_{(\frac{3}{2},2)}\\ \vdots\\ \Delta s_1\frac{C}{A}|_{(N_l+\frac{1}{2},2)}\\ \vdots\\ \Delta s_1\frac{C}{A}|_{(\frac{3}{2},N_k)}\\ \vdots\\ \Delta s_1\frac{C}{A}|_{(N_l+\frac{1}{2},N_k)}\end{pmatrix},$$

where $\Delta s_1|_{(l,k)} = s_{1_{(l+\frac{1}{2},k)}} - s_{1_{(l-\frac{1}{2},k)}}$ for $l = 1,\dots,N_l$ and $k = 1,\dots,N_k$. The values $\eta^{cav}_{(\frac{1}{2},k)}$ are assumed to be zero for all $k = 1,\dots,N_k$. The matrix $\mathbf{M}\in\mathbf{R}^{(N_lN_k)\times(N_lN_k)}$ consists of partial matrices:

$$\mathbf{M}=\begin{pmatrix}
\mathbf{M}_1 & \mathbf{M}_{2,1} & 0 & 0 & \dots & 0\\
\mathbf{M}_{3,2} & \mathbf{M}_1 & \mathbf{M}_{2,2} & 0 & \dots & 0\\
0 & \mathbf{M}_{3,3} & \mathbf{M}_1 & \mathbf{M}_{2,3} & \ddots & \vdots\\
0 & 0 & \mathbf{M}_{3,4} & \mathbf{M}_1 & \ddots & 0\\
\vdots & \vdots & \ddots & \ddots & \ddots & \mathbf{M}_{2,N_k-1}\\
0 & 0 & \dots & 0 & \mathbf{M}_{3,N_k} & \mathbf{M}_1
\end{pmatrix},$$

where the matrices $\mathbf{M}_1 \in \mathbf{R}^{(N_l \times N_l)}$, $\mathbf{M}_{2,k} \in \mathbf{R}^{(N_l \times N_l)}$ and $\mathbf{M}_{3,k} \in \mathbf{R}^{(N_l \times N_l)}$ are defined as follows:

$$\mathbf{M}_1 = \begin{pmatrix} 1 & 0 & 0 & 0 & \dots & 0 \\ -1 & 1 & 0 & 0 & \dots & 0 \\ 0 & -1 & 1 & 0 & \dots & \vdots \\ 0 & 0 & -1 & 1 & \ddots & 0 \\ \vdots & \vdots & \ddots & \ddots & \ddots & 0 \\ 0 & 0 & \dots & 0 & -1 & 1 \end{pmatrix},$$

$$\mathbf{M}_{2,k} = \begin{pmatrix} m_{(1,k)} & 0 & 0 & 0 & \dots & 0 \\ m_{(2,k)} & m_{(2,k)} & 0 & 0 & \dots & 0 \\ 0 & m_{(3,k)} & m_{(3,k)} & 0 & \dots & \vdots \\ 0 & 0 & m_{(4,k)} & m_{(4,k)} & \ddots & 0 \\ \vdots & \vdots & \ddots & \ddots & \ddots & 0 \\ 0 & 0 & \dots & 0 & m_{(N_l,k)} & m_{(N_l,k)} \end{pmatrix},$$

$$\mathbf{M}_{3,k} = \begin{pmatrix} -m_{(1,k)} & 0 & 0 & 0 & \dots & 0 \\ -m_{(2,k)} & -m_{(2,k)} & 0 & 0 & \dots & 0 \\ 0 & -m_{(3,k)} & -m_{(3,k)} & 0 & \dots & \vdots \\ 0 & 0 & -m_{(4,k)} & -m_{(4,k)} & \ddots & 0 \\ \vdots & \vdots & \ddots & \ddots & \ddots & 0 \\ 0 & 0 & \dots & 0 & -m_{(N_l,k)} & -m_{(N_l,k)} \end{pmatrix},$$

where

$$m_{(l,k)} = \frac{1}{2}\frac{B}{A}\frac{\Delta s_1}{\Delta s_2}|_{(l,k)}, \quad \text{and} \quad \Delta s_2|_{(l,k)} = s_{2_{(l,k+1)}} - s_{2_{(l,k-1)}},$$

for all $k = 1, \dots, N_k$ and $l = 1, \dots, N_l$.

### 4.3.6 Algorithm for the determination of the sheet cavity shape

In this section the numerical procedure for the determination of the sheet cavity shape based on the partially non-linear model is introduced. There are two boundary conditions that are to be fulfilled on the cavity surface: the kinematic and the dynamic boundary condition. Additionally, the cavitation inception must be detected and the cavity closure must be modelled. The approach used here at the cavity closure is based on a closed model. For this approach, the geometry grid is not being re-meshed and a point must be found downstream (or upstream, in case of face cavitation) of the cavitation inception with the smallest possible cavity thickness value.

The overall solution algorithm for the steady cavitating flow consists of the following main steps:

(1) In the first steady step the linear system of equations $(3.16)$ is solved once without the sheet cavitation model in order to compute the pressure distribution on the bodies submerged in the flow domain.

(2) Now the criterion $C_{p,v} \leq -\sigma_v$ is applied so that a first guess can be made concerning the cavity length at each radial stripe of the body. For this, a detachment and a reattachment point are defined on each radial stripe according to the following iterative procedure:

  - Detachment point: There are two approaches that are implemented for the detection of the detachment point. In the first approach, the midpoint of the leading edge panel is defined as the detachment point. The second approach is based on the Villat-Brilloin condition. Starting at the midpoint of the leading edge panel the point on the pressure side (back cavitation) or suction side (face cavitation) has to be found where the pressure is less than or equal to the vapour pressure (i.e. $C_{p,v} \leq -\sigma_v$). For the points upstream (back cavitation) or downstream (face cavitation) of this point, the pressure should be greater than the vapour pressure, i.e. $C_{p,v} > -\sigma_v$.
  - Reattachment point: Starting from the estimated detachment point, one searches for the first point on the suction (back cavitation) or pressure side (face cavitation) where the pressure exceeds the vapour pressure, i.e. $C_{p,v} > -\sigma_v$. The point upstream (back cavitation) or downstream (face cavitation) of this point where the condition $C_{p,v} \leq -\sigma_v$ holds is then defined as the reattachment point.

(3) After the first guess of the cavity length, the linear system of equations $(4.19)$ with cavitating panels is set up and solved and new velocity and pressure distributions are calculated. Additionally, the cavity thickness is computed on each cavitating panel of the body by solving the linear system of equations $(4.30)$.

(4) Based on the cavity thickness distribution at the detachment and reattachment points, a new guess for the cavity shape is made. For this, the detachment and reattachment points for each radial stripe are adjusted according to a prescribed scheme.

  - Detachment point: If the detachment point is defined as a fixed point that is located at the leading edge, its location is not modified. If the Villat-Brilloin criterion is used (which demands that cavitation has a non-negative thickness at the detachment point and that the pressure on the non-cavitating part of the body is greater than the vapour pressure $p_v$), the detachment point is adjusted according to the following case distinctions:

(i) If the cavity thickness at the detachment point is positive, but the pressure on the non-cavitating part upstream (back cavitation) or downstream (face cavitation) of the detachment point is less than or equal to the vapour pressure, then the detachment point is moved upstream (back cavitation) or downstream (face cavitation), respectively.

(ii) If the cavity thickness at the detachment point is negative, then the detachment point is moved downstream (back cavitation) or upstream (face cavitation), respectively.

(iii) Else, the detachment point location is not modified.

– Reattachment point: The procedure used for the estimation of the reattachment point reads as follows. Firstly, calculate the sum of the cavity thickness at the reattachment points for all radial stripes:

$$\sum_{k=1}^{N_k} |\eta^{cav}_{(l_r,k)}|. \tag{4.31}$$

If the sum $(4.31)$ is smaller than a given tolerance threshold $\epsilon_1$, i.e when it holds:

$$\sum_{k=1}^{N_k} |\eta^{cav}_{(l_r,k)}| \leq \epsilon_1, \tag{4.32}$$

then the reattachment points are not displaced. The tolerance threshold is defined in *pan*MARE as $\epsilon_1 = \frac{1}{10} \sum\limits_{k=1}^{N_k} \min_{i=1}^{4}(d_i|_{Panel_{(l_r,k)}})$, where $d_i$ is the length of the edge $i$ on the reattachment panel,

If the sum $(4.31)$ is greater than the given tolerance threshold $\epsilon_1$, then the reattachment points are adjusted according to the following procedure:

(i) If the cavity thickness at the reattachment point at stripe $k$ is positive and greater than a given bound $\epsilon_2 = 2\epsilon_1/N_k$, then the reattachment point is moved one panel downstream in case of back cavitation or upstream in case of face cavitation.

(ii) If the cavity thickness at the reattachment point at stripe $k$ is negative and smaller than the given bound $-\epsilon_2$, then the reattachment point is moved one panel upstream in case of back cavitation or downstream in case of face cavitation.

(iii) If the cavity thickness at the reattachment point at stripe $k$ is within the bound $[-\epsilon_2, \epsilon_2]$, the reattachment point is not changed.

Subsequently, the linear system of equations (4.19) is solved again to modify the unknown value of the strengths $\mu$ on $S_B$ and $\sigma^{cav}$ on $S_{B_C}$. Supplementary, the cavity thickness is calculated again from the linear system of equations (4.30) with the new locations of the detachment and reattachment point.

The procedure above is repeated until the criterion for the reattachment and detachment point location are fulfilled.

(5) After the determination of the new cavity shape propeller characteristics are calculated.

(6) For the next steady iteration steps, the solution obtained from the previous steady iteration step is used as an initial guess for the cavity length and the steps (3)-(5) are repeated.

## 4.4 Numerical model for unsteady sheet cavitation

Analogous to the steady model, there are two boundary conditions that have to be satisfied on the sheet cavity surface in the case of the unsteady flow. The difference to the steady model is that both the dynamic and the kinematic boundary conditions include unsteady terms. Furthermore, the dynamic and kinematic boundary conditions must be satisfied for each blade angular position and the shape of the cavity must be adjusted for each time step. For a uniform inflow to the propeller a steady solution will be reached after a certain number of propeller revolutions. In the case of a non-uniform inflow to the propeller, the cavity shape will vary for each blade angular position and the previous shape of the cavity will influence the present cavity sheet geometry. The transient behaviour of the flow is accounted for in the free vortex surfaces with time-dependent dipole intensities and in the cavity patterns on the blades.

The boundary value problem formulation for the unsteady flow is the same as in the steady case (s. Equation (4.19)). This section deals with the special features of the unsteady boundary conditions.

### 4.4.1 Numerical determination of the unsteady potential on the cavity surface

In continuous form the unsteady dynamic boundary condition reads as:

$$\phi = \phi^{back/face}|_{\xi_d} + \int_{\xi} \Big[\sqrt{|\mathbf{V}_\infty|^2 + \sigma_v|\mathbf{V}_{ship}|^2 - 2g\zeta - 2\frac{\partial \phi}{\partial t} - V_\eta^2} - V_{\infty,\xi}\Big] d\xi \quad (4.33)$$

on $S_{B_C}$. The dynamic boundary condition is discretised in the same manner as in the steady case and it holds:

$$\phi^{cav,n}_{(l,k)} = \phi^{back/face,n}_{(l_d,k)} + \tilde{\phi}^{cav,n}_{(l,k)}, \tag{4.34}$$

where $n \in \mathbf{N}$ is the index for the discrete time step. The potential at the detachment point is calculated in the same manner as in the steady model (s. Section 4.3.4). The function $\tilde{\phi}^{cav,n}_{(l,k)}$ is interpolated by:

$$\tilde{\phi}^{cav,n}_{(l,k)} \approx \frac{\tilde{\phi}^{cav,n}_{(l+\frac{1}{2},k)} + \tilde{\phi}^{cav,n}_{(l-\frac{1}{2},k)}}{2},$$

where

$$\begin{aligned}\tilde{\phi}^{cav,n}_{(l+\frac{1}{2},k)} = \sum_{w=l_d+1}^{w=l} \Bigg[ \Bigg( \sqrt{|V^n_\infty|^2 + \sigma_v |V_{ship}|^2 - 2g\zeta - 2\frac{\partial \phi^n}{\partial t} - (V^n_\eta)^2} - V^n_{\infty,\xi} \Bigg)|_{wk} \\ \cdot \Big( \xi_{(w+\frac{1}{2},k)} - \xi_{(w-\frac{1}{2},k)} \Big) \Bigg], \; \forall\, l = l_d + 2, \ldots, l_r,\; k = 1, \ldots, N_k.\end{aligned} \tag{4.35}$$

The time derivative of the potential $\phi^n$ and the value of the velocity component in the tangential direction $V^n_\eta$ are not known a priori. For their estimation a predictor-corrector method is applied.

(1) Calculate $\phi^n$ by using Equations (4.34) and (4.35) and setting $\frac{\partial \phi^n}{\partial t} \approx 0$ and $V^n_\eta \approx V^{n-1}_\eta$.

(2) Solve the linear system of equations (4.19) to determine the unknown strengths. Calculate the modified velocity $\mathbf{V}^{n,new}$ and compute the new pressure by the unsteady Bernoulli equation.

(3) Calculate the potential $\phi^n$ once more by Equations (4.34) and (4.35). Hereby, $V^n_\eta$ is estimated by $V^n_\eta \approx V^{n,new}_\eta$ and $\frac{\partial \phi^n}{\partial t}$ is approximated by using a transformed version of the Equation (4.33):

$$\frac{\partial \phi^n_{(l,k)}}{\partial t} = \frac{1}{2}|\mathbf{V}^n_{\infty,(l,k)}|^2 + \frac{1}{2}|\mathbf{V}_{ship,(l,k)}|^2 \sigma_v - \frac{1}{2}|\mathbf{V}^{n,new}_{(l,k)}|^2 - g\zeta_{(l,k)}. \tag{4.36}$$

(4) Finally, solve the linear system of equations (4.19) again and modify the value of the strengths, velocities and pressures. In the calculation of the unsteady pressure values a case distinction for the approximation of the potential's time derivative is made. On the reference surface $S_{B_C}$ the potential's time derivative is calculated according to the formula (4.36). On the surface $S_B/S_{B_C}$ the potential's time derivative

is approximated by the backwards difference scheme of first order:

$$\frac{\partial \phi^n_{(l,k)}}{\partial t} \approx \frac{\phi^n_{(l,k)} - \phi^{n-1}_{(l,k)}}{\Delta t}. \tag{4.37}$$

### 4.4.2 Calculation of the unsteady cavity thickness

In continuous form the unsteady equation for the cavity thickness reads as:

$$\begin{aligned} &\frac{\partial \eta^{cav}}{\partial s_1}(V_{s_1} - (\mathbf{t}_1 \cdot \mathbf{t}_2)V_{s_2}) + \frac{\partial \eta^{cav}}{\partial s_2}(V_{s_2} - (\mathbf{t}_1 \cdot \mathbf{t}_2)V_{s_1}) \\ &\qquad\qquad = \|\mathbf{t}_1 \times \mathbf{t}_2\|^2 \Big( V_{s_3} - \frac{\partial \eta^{cav}}{\partial t} \Big), \text{ on } S_{B_C}. \end{aligned} \tag{4.38}$$

For the approximation of the spacial derivatives $\frac{\partial}{\partial s_1}$ and $\frac{\partial}{\partial s_2}$ a central difference scheme is used:

$$\frac{\partial \eta^{cav}}{\partial s_1}|_{(l,k)} \approx \frac{\eta^{cav,n}_{(l+\frac{1}{2},k)} - \eta^{cav,n}_{(l-\frac{1}{2},k)}}{s_{1_{(l+\frac{1}{2},k)}} - s_{1_{(l-\frac{1}{2},k)}}}, \quad \frac{\partial \eta^{cav}}{\partial s_2}|_{(l,k)} \approx \frac{\eta^{cav,n}_{(l,k+1)} - \eta^{cav,n}_{(l,k-1)}}{s_{2_{(l,k+1)}} - s_{2_{(l,k-1)}}}. \tag{4.39}$$

Similarly to the steady case, the values $\eta^{cav,n}_{(l,k+1)}$ and $\eta^{cav,n}_{(l,k-1)}$ are approximated by linear interpolation and it holds:

$$\frac{\partial \eta^{cav}}{\partial s_2}|_{(l,k)} \approx \frac{1}{2}\Big( \frac{\eta^{cav,n}_{(l+\frac{1}{2},k+1)} + \eta^{cav,n}_{(l-\frac{1}{2},k+1)} - \eta^{cav,n}_{(l+\frac{1}{2},k-1)} - \eta^{cav,n}_{(l-\frac{1}{2},k-1)}}{s_{2_{(l,k+1)}} - s_{2_{(l,k-1)}}} \Big). \tag{4.40}$$

For the approximation of the time derivative a backwards difference scheme of first order is used:

$$\frac{\partial \eta^{cav}}{\partial t}|_{(l,k)} \approx \frac{\eta^{cav,n}_{(l,k)} - \eta^{cav,n-1}_{(l,k)}}{\Delta t}. \tag{4.41}$$

From the above approximations a discrete form of the unsteady kinematic boundary condition is obtained:

$$\begin{aligned} &\frac{A^n_{(l,k)}}{\Delta s_1}(\eta^{cav,n}_{(l+\frac{1}{2},k)} - \eta^{cav,n}_{(l-\frac{1}{2},k)}) + \frac{B^n_{(l,k)}}{2\Delta s_2}\Big[\eta^{cav,n}_{(l+\frac{1}{2},k+1)} + \eta^{cav,n}_{(l-\frac{1}{2},k+1)} - \eta^{cav,n}_{(l+\frac{1}{2},k-1)} - \eta^{cav,n}_{(l-\frac{1}{2},k-1)}\Big] \\ &\qquad = C^n_{(l,k)} - \frac{\|\mathbf{t}_1 \times \mathbf{t}_2\|^2}{\Delta t}(\eta^{cav,n}_{(l,k)} - \eta^{cav,n-1}_{(l,k)}) \\ &\qquad \approx C^n_{(l,k)} - \frac{\|\mathbf{t}_1 \times \mathbf{t}_2\|^2}{2\Delta t}(\eta^{cav,n}_{(l+\frac{1}{2},k)} + \eta^{cav,n}_{(l-\frac{1}{2},k)} - 2\eta^{cav,n-1}_{(l,k)}), \end{aligned}$$

where $\Delta s_1$ and $\Delta s_2$ are defined in the same way as in Section 4.3.5. The coefficients $A^n_{(l,k)}$, $B^n_{(l,k)}$ and $C^n_{(l,k)}$ are defined as follows:

$$\begin{aligned} &A^n_{(l,k)} = V^n_{s_1,(l,k)} - (\mathbf{t}_1 \cdot \mathbf{t}_2)V^n_{s_2,(l,k)}, \quad B^n_{(l,k)} = V^n_{s_2,(l,k)} - (\mathbf{t}_1 \cdot \mathbf{t}_2)V^n_{s_1,(l,k)}, \\ &C^n_{(l,k)} = \|\mathbf{t}_1 \times \mathbf{t}_2\|^2 V^n_{s_3,(l,k)}, \quad \text{for all} \quad l = 1, \dots, N_l. \end{aligned}$$

Now a recursive scheme for the determination of the cavity thickness at the auxiliary points $(l+\frac{1}{2},k)$ and $(l-\frac{1}{2},k)$ can be defined:

$$\begin{aligned}
&\Big[\frac{A^n_{(l,k)}}{\Delta s_1}+\frac{\|\mathbf{t}_1\times\mathbf{t}_2\|^2}{2\Delta t}\Big]\eta^{cav,n}_{(l+\frac{1}{2},k)}-\Big[\frac{A^n_{(l,k)}}{\Delta s_1}-\frac{\|\mathbf{t}_1\times\mathbf{t}_2\|^2}{2\Delta t}\Big]\eta^{cav,n}_{(l-\frac{1}{2},k)}\\
&\qquad+\frac{B^n_{(l,k)}}{2\Delta s_2}\Big[\eta^{cav,n}_{(l+\frac{1}{2},k+1)}+\eta^{cav,n}_{(l-\frac{1}{2},k+1)}\Big]=C^n_{(l,k)}+\frac{\|\mathbf{t}_1\times\mathbf{t}_2\|^2}{\Delta t}\eta^{cav,n-1}_{(l,k)},\ \text{for } k=1,\\
&\Big[\frac{A^n_{(l,k)}}{\Delta s_1}+\frac{\|\mathbf{t}_1\times\mathbf{t}_2\|^2}{2\Delta t}\Big]\eta^{cav,n}_{(l+\frac{1}{2},k)}-\Big[\frac{A^n_{(l,k)}}{\Delta s_1}-\frac{\|\mathbf{t}_1\times\mathbf{t}_2\|^2}{2\Delta t}\Big]\eta^{cav,n}_{(l-\frac{1}{2},k)}\\
&\qquad+\frac{B^n_{(l,k)}}{2\Delta s_2}\Big[\eta^{cav,n}_{(l+\frac{1}{2},k+1)}+\eta^{cav,n}_{(l-\frac{1}{2},k+1)}\Big]-\frac{B^n_{(l,k)}}{2\Delta s_2}\Big[\eta^{cav,n}_{(l+\frac{1}{2},k-1)}-\eta^{cav,n}_{(l-\frac{1}{2},k-1)}\Big]\\
&\qquad=C^n_{(l,k)}+\frac{\|\mathbf{t}_1\times\mathbf{t}_2\|^2}{\Delta t}\eta^{cav,n-1}_{(l,k)},\ \text{for } k=2,\dots N_k-1,\\
&\Big[\frac{A^n_{(l,k)}}{\Delta s_1}+\frac{\|\mathbf{t}_1\times\mathbf{t}_2\|^2}{2\Delta t}\Big]\eta^{cav,n}_{(l+\frac{1}{2},k)}-\Big[\frac{A^n_{(l,k)}}{\Delta s_1}-\frac{\|\mathbf{t}_1\times\mathbf{t}_2\|^2}{2\Delta t}\Big]\eta^{cav,n}_{(l-\frac{1}{2},k)}\\
&\qquad-\frac{B^n_{(l,k)}}{2\Delta s_2}\Big[\eta^{cav,n}_{(l+\frac{1}{2},k-1)}-\eta^{cav,n}_{(l-\frac{1}{2},k-1)}\Big]=C^n_{(l,k)}+\frac{\|\mathbf{t}_1\times\mathbf{t}_2\|^2}{\Delta t}\eta^{cav,n-1}_{(l,k)},\ \text{for } k=N_k.
\end{aligned}$$

The equations above lead to the following linear system of equations:

$$\mathbf{M}^n\cdot\eta^{cav,n}=\mathbf{f}^n, \tag{4.42}$$

where the vectors $\eta^{cav,n}\in\mathbf{R}^{N_lN_k}$ and $\mathbf{f}^n\in\mathbf{R}^{N_lN_k}$ are defined by:

$$\eta^{cav,n}=\begin{pmatrix}\eta^{cav,n}_{\frac{3}{2},1}\\ \vdots\\ \eta^{cav,n}_{N_l+\frac{1}{2},1}\\ \eta^{cav,n}_{\frac{3}{2},1}\\ \vdots\\ \eta^{cav,n}_{N_l+\frac{1}{2},2}\\ \vdots\\ \eta^{cav,n}_{\frac{3}{2},N_k}\\ \dots\\ \eta^{cav,n}_{N_l+\frac{1}{2},N_k}\end{pmatrix},\quad \mathbf{f}^n=\begin{pmatrix}\Delta s_1\frac{C^n}{A^n}\big|_{(\frac{3}{2},1)}+\frac{\Delta s_1\|\mathbf{t}_1\times\mathbf{t}_2\|^2}{\Delta tA^n}\eta^{cav,n-1}_{(1,1)}\\ \vdots\\ \Delta s_1\frac{C^n}{A^n}\big|_{(N_l+\frac{1}{2},1)}+\frac{\Delta s_1\|\mathbf{t}_1\times\mathbf{t}_2\|^2}{\Delta tA^n}\eta^{cav,n-1}_{(N_l,1)}\\ \Delta s_1\frac{C^n}{A^n}\big|_{(\frac{3}{2},2)}+\frac{\Delta s_1\|\mathbf{t}_1\times\mathbf{t}_2\|^2}{\Delta tA^n}\eta^{cav,n-1}_{(1,2)}\\ \vdots\\ \Delta s_1\frac{C^n}{A^n}\big|_{(N_l+\frac{1}{2},2)}+\frac{\Delta s_1\|\mathbf{t}_1\times\mathbf{t}_2\|^2}{\Delta tA^n}\eta^{cav,n-1}_{(N_l,2)}\\ \vdots\\ \Delta s_1\frac{C^n}{A^n}\big|_{(\frac{3}{2},N_k)}+\frac{\Delta s_1\|\mathbf{t}_1\times\mathbf{t}_2\|^2}{\Delta tA^n}\eta^{cav,n-1}_{(1,N_k)}\\ \vdots\\ \Delta s_1\frac{C^n}{A^n}\big|_{(N_l+\frac{1}{2},N_k)}+\frac{\Delta s_1\|\mathbf{t}_1\times\mathbf{t}_2\|^2}{\Delta tA^n}\eta^{cav,n-1}_{(N_l,N_k)}\end{pmatrix},$$

and the matrix $\mathbf{M}^n\in\mathbf{R}^{(N_lN_k)\times(N_lN_k)}$ consists of partial matrices:

$$\mathbf{M} = \begin{pmatrix} \mathbf{M}_1^n & \mathbf{M}_{2,1}^n & 0 & 0 & \dots & 0 \\ \mathbf{M}_{3,2}^n & \mathbf{M}_1^n & \mathbf{M}_{2,2}^n & 0 & \dots & 0 \\ 0 & \mathbf{M}_{3,3}^n & \mathbf{M}_1^n & \mathbf{M}_{2,3}^n & \dots & \vdots \\ 0 & 0 & \mathbf{M}_{3,4}^n & \mathbf{M}_1^n & \ddots & 0 \\ \vdots & \vdots & \ddots & \ddots & \ddots & \mathbf{M}_{2,N_k-1}^n \\ 0 & 0 & \dots & 0 & \mathbf{M}_{3,N_k}^n & \mathbf{M}_1^n \end{pmatrix},$$

The partial matrices $\mathbf{M}_{1,k}^n \in \mathbf{R}^{(N_l \times N_l)}$, $\mathbf{M}_{2,k}^n \in \mathbf{R}^{(N_l \times N_l)}$ and $\mathbf{M}_{3,k}^n \in \mathbf{R}^{(N_l \times N_l)}$ are defined by:

$$\mathbf{M}_{1,k}^n = \begin{pmatrix} a_{(1,k)} & 0 & 0 & 0 & \dots & 0 \\ b_{(2,k)} & a_{(2,k)} & 0 & 0 & \dots & 0 \\ 0 & b_{(3,k)} & a_{(3,k)} & 0 & \dots & \vdots \\ 0 & 0 & b_{(4,k)} & a_{(4,k)} & \ddots & 0 \\ \vdots & \vdots & \ddots & \ddots & \ddots & 0 \\ 0 & 0 & \dots & 0 & b_{(N_l,k)} & a_{(N_l,k)} \end{pmatrix},$$

$$\mathbf{M}_2^n = \begin{pmatrix} m_{(1,k)} & 0 & 0 & 0 & \dots & 0 \\ m_{(2,k)} & m_{(2,k)} & 0 & 0 & \dots & 0 \\ 0 & m_{(3,k)} & m_{(3,k)} & 0 & \dots & \vdots \\ 0 & 0 & m_{(4,k)} & m_{(4,k)} & \ddots & 0 \\ \vdots & \vdots & \ddots & \ddots & \ddots & 0 \\ 0 & 0 & \dots & 0 & m_{(N_l,k)} & m_{(N_l,k)} \end{pmatrix},$$

$$\mathbf{M}_3^n = \begin{pmatrix} -m_{(1,k)} & 0 & 0 & 0 & \dots & 0 \\ -m_{(2,k)} & -m_{(2,k)} & 0 & 0 & \dots & 0 \\ 0 & -m_{(3,k)} & -m_{(3,k)} & 0 & \dots & \vdots \\ 0 & 0 & -m_{(4,k)} & -m_{(4,k)} & \ddots & 0 \\ \vdots & \vdots & \ddots & \ddots & \ddots & 0 \\ 0 & 0 & \dots & 0 & -m_{(N_l,k)} & -m_{(N_l,k)} \end{pmatrix},$$

where

$$\begin{aligned} a_{(l,k)} &= 1 - \frac{\Delta s_1 \|\mathbf{t}_1 \times \mathbf{t}_2\|^2}{2\Delta t A^n}|_{(l,k)}, \quad b_{(l,k)} = -1 + \frac{\Delta s_1 \|\mathbf{t}_1 \times \mathbf{t}_2\|^2}{2\Delta t A^n}|_{(l,k)}, \\ m_{(l,k)} &= \frac{1}{2}\frac{B^n}{A^n}\frac{\Delta s_1}{\Delta s_2}|_{(l,k)}, \quad \text{for all} \quad l = 1, \dots, N_l \text{ and } k = 1, \dots, N_k. \end{aligned}$$

### 4.4.3 Algorithm for the determination of the unsteady sheet cavity shape

In the following, the solution algorithm for the computation of unsteady sheet cavitation patterns is summarised:

(1) In the first few unsteady time steps the boundary value problem is solved without cavitation to obtain the unsteady pressure distribution on the body surface. For the calculation of the pressure distribution, the unsteady Bernoulli equation is used:

$$p(\mathbf{x},t) = \frac{\rho}{2}\Big(|V_\infty(\mathbf{x},t)|^2 - |V(\mathbf{x},t)|^2\Big) - \rho\frac{\partial\phi(\mathbf{x},t)}{\partial t} + \rho g(z_\infty - z) + p_\infty. \quad (4.43)$$

(2) In the next time step, the unsteady wetted problem (3.4) is solved and the cavity length is estimated in the same manner as in the steady case, i.e. the area where the condition $C_{p,v} + \sigma_v \leq 0$ holds is defined as the first approximation for the cavity surface.

(3) For the same time step as in (2) the dipole strengths on the cavitating part of the body are calculated by using the unsteady dynamic boundary condition (4.34).

(4) The linear system of equations (4.19) with cavitating panels is set up and the boundary value problem is solved to obtain a new unsteady pressure distribution. The cavity thickness is computed by solving the unsteady linear system of equations (4.42). The procedure for the determination of the cavity shape is repeated in the same way as in the steady model until the cavity length is found with the smallest possible cavity thickness at the cavity closure.

(5) The values for the cavity potential and cavity thickness are stored for the present time step $n$. For the following time steps the steps (2)-(4) are repeated until the maximum time step is achieved.

## 4.5 Numerical determination of sheet cavity characteristics

The sheet cavity area and volume on a body with $N^{cav}$ cavitating panels are numerically computed by:

$$A^{cav} \approx \sum_{i=1}^{N^{cav}} \int_{Panel_i} dS(\mathbf{x}), \quad V^{cav} \approx \sum_{i=1}^{N^{cav}} \eta_i^{cav} \int_{Panel_i} dS(\mathbf{x}).$$

Furthermore, the time derivative of the cavity volume can be of interest, e.g. for the pressure pulses calculations. The first and second derivatives of the cavity volume are approximated by the central difference scheme:

$$\frac{\partial V^{cav}}{\partial t} \approx \frac{V^{cav,n+1} - V^{cav,n-1}}{2\Delta t}, \quad \frac{\partial^2 V^{cav}}{\partial^2 t} \approx \frac{V^{cav,n+1} - 2V^{cav,n} + V^{cav,n-1}}{\Delta t^2}, \tag{4.44}$$

for all $n = 2, 3, \ldots$.

# Chapter 5

# Verification and validation of the sheet cavitation model

This chapter is dedicated to the verification and validation of the developed partially non-linear sheet cavitation model. In the first section, Chapter 5.1, the steady model is verified and validated with the help of two different hydrofoils and a propeller geometry. The hydrofoils are the NACA$66_2$-415 and NACA0010 profiles. The propeller is the well-investigated propeller P1356. In the second section, Chapter 5.2, the unsteady sheet cavitation model is verified on the NACA0010 hydrofoil in an oscillating inflow velocity field. For validation the flow around the two propellers P1356 and P1380 subject to inhomogeneous inflow is analysed and the calculated results are compared with measured data.

## 5.1 Steady sheet cavitation model

The focus of the present study is the verification and validation of the steady sheet cavitation model. For this purpose the flows around the NACA$66_2$-415 and NACA0010 hydrofoil and around the P1356 propeller are investigated. In order to verify the steady sheet cavitation model, the calculated scaled pressure distributions on the hydrofoil and propeller surfaces are evaluated. According to the applied sheet cavitation model, the scaled pressure must be equal to the minus of the cavitation number in the area where sheet cavitation occurs. The validation of the steady sheet cavitation model is provided by comparing the sheet cavity extents calculated by *pan*MARE with those obtained in experiments.

Additionally, for the NACA$66_2$-415 hydrofoil and the P1356 propeller flow the influence of the sheet cavitation amount on the calculated flow characteristics is outlined and a grid convergence study is performed. Since no re-meshing of the surface grid is applied in the employed sheet cavitation model, the computed results will strongly depend on the resolution of the grid. In order to guarantee grid-independent results, the impact of the grid resolution on the non-cavitating and cavitating flow is examined. The grids are generated automatically by an in-house grid generation tool embedded in the software program *pan*MARE. In the default configuration this tool uses a cosine spacing technique for the mesh generation, that creates an equal number of panels at the back and face side of the section profiles.

### 5.1.1 NACA66$_2$-415 hydrofoil

This section investigates the flow around the NACA66$_2$-415 hydrofoil. The flow around the NACA66$_2$-415 foil was studied in detail by the Potsdam Model Basin (SVA) and their results were summed up in the report by Richter (2011). The geometry data of this hydrofoil is listed in Table 5.1 and its shape is illustrated in Figure 5.1. The foil has a chord length of 0.2025m and a span width of 0.6m.

| **Characteristics** | **Notation** | **Value** | **Unit** |
|---|---|---|---|
| Span length | $b$ | 0.6 | m |
| Chord length | $c$ | 0.2025 | m |
| Foil area | $A_{ref}$ | 0.1215 | $m^2$ |
| Maximum thickness | $t_{max}$ | 0.0304 | m |
| Aspect ratio | $\Lambda = b^2/A$ | 2.963 | - |
| Scale factor | $\lambda$ | 2.5 | - |

Table 5.1: NACA66$_2$-415 geometry data (in model scale)

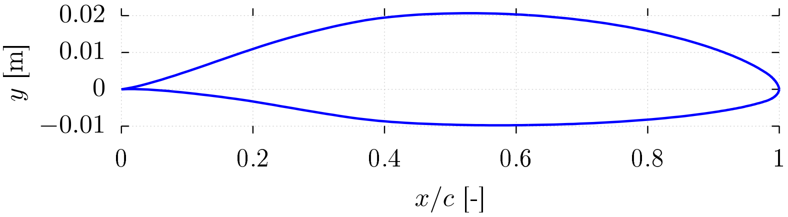

Figure 5.1: Scaled geometry of the NACA66$_2$-415 hydrofoil profile

In the first part of this section the non-cavitating flow around the NACA66$_2$-415 foil with different grid resolutions of the hydrofoil's surface is simulated. The aim of this study is to detect grid resolutions that provide convergent and grid-independent results for the lift coefficients of the hydrofoil flow. For this purpose the lift coefficients calculated by *pan*MARE with different grid discretisation levels are evaluated and validated against measured data from the report by Richter (2011).

The second part of this section focuses on the simulation of the cavitating flow around the NACA66$_2$-415 foil. Analogous to the non-cavitating case, different grid resolutions are used in this study to analyse their influence on the calculated sheet cavity shapes. For the verification and validation of the results obtained by the numerical sheet cavitation model, the scaled pressure distributions and sheet cavity extents are examined and the latter ones are compared with the measurements by Richter (2011). Additionally, the lift and drag coefficients are computed for several cavitation numbers and the influence of the cavitation amount on the hydrofoil's flow characteristics is emphasised.

### Non-cavitating NACA66$_2$-415 hydrofoil flow

In the present study the non-cavitating flow around the NACA66$_2$-415 foil is simulated for the angles of attack $\alpha + \alpha_0 = -5°$-$10°$, where $\alpha$ is the geometrical angle of attack and $\alpha_0$ is the zero-lift angle of attack. The zero-lift angle of attack calculated by *pan*MARE is $\alpha_0 = -3.34°$. All relevant input data of the simulations is summarised in Table 5.2. As mentioned above, different grid resolutions are used in the calculations (s. Table 5.3). The surface is discretised in the circumferential and in the span-wise direction. Figure 5.2 shows two example grid resolutions: a coarse grid (s. Figure 5.2a) and a fine grid (s. Figure 5.2b).

| **Characteristics** | **Notation** | **Value** | **Unit** |
|---|---|---|---|
| Angle of attack | $\alpha$ | $-5$ - 10 | ° |
| Inflow velocity | $V_{inflow}$ | 5.5 | m/s |
| Water density | $\rho$ | 997.46 | kg/$m^3$ |

Table 5.2: Input data for the non-cavitating case study (NACA66$_2$-415 hydrofoil)

| **Characteristics** | **Notation** | **Value** |
|---|---|---|
| Number of panels in span-wise direction | $N_k$ | 4/7/10/13/16 |
| Number of panels in circumferential direction | $N_l$ | 10/18/26/34 |

Table 5.3: Grid resolutions for the non-cavitating case study (NACA66$_2$-415 hydrofoil)

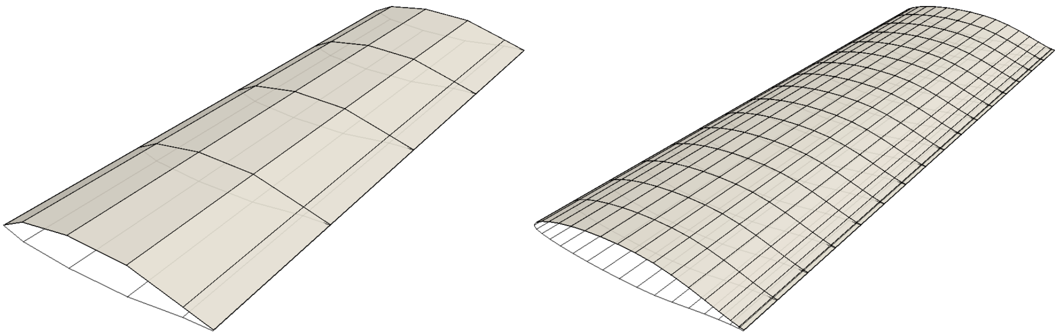
(a) $N_k \times N_l = 4 \times 10$
(b) $N_k \times N_l = 16 \times 34$

Figure 5.2: Grid resolution examples

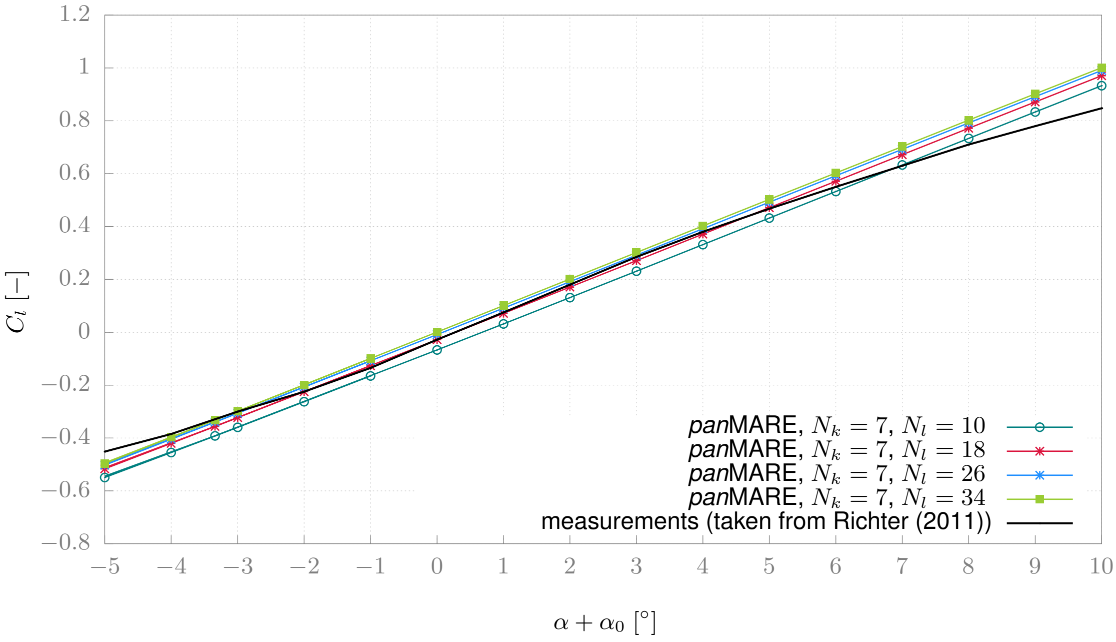

Figure 5.3: Influence of the grid resolution in the circumferential direction on the calculated lift coefficients of the NACA66$_2$-415 hydrofoil

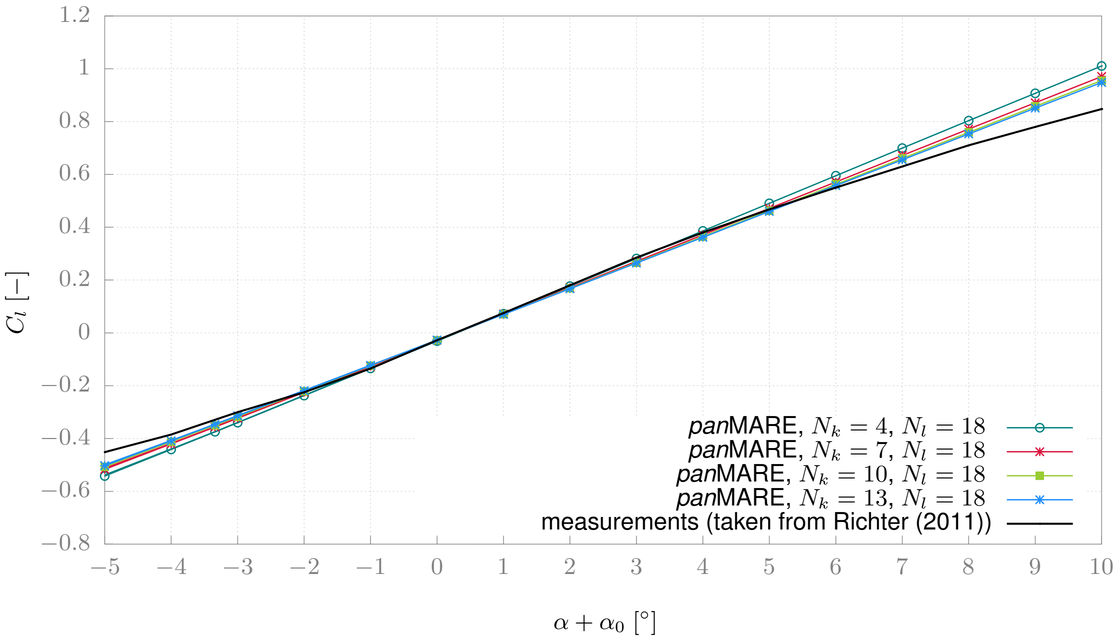

Figure 5.4: Influence of the grid resolution in the span-wise direction on the calculated lift coefficients of the NACA66$_2$-415 hydrofoil

Figures 5.3-5.4 and D.1-D.6 show the measured and simulated results for the dimensionless lift coefficient $C_l$ as functions of the angle of attack. The lift coefficients calculated by *pan*MARE coincide very well with the measured results for the angles of attack $\alpha + \alpha_0 \in [-5° : 6°]$. For the angles within the range $\alpha + \alpha_0 \in [7° : 10°]$ the calculated values are overestimated compared to the measured ones. This deviation can be explained by the friction effects that play an important role for high or low angles of attack. Friction effects cannot be captured by a potential flow solver in an accurate manner and must be included in the numerical method via semi-empirical formulas.

The following section concerns the discussion of the influence of the grid discretisation level on the calculated lift coefficients. Figures 5.3 and D.1-D.3 emphasise the influence of the grid refinement in the circumferential direction and Figures 5.4 and D.4-D.6 illustrate the impact of the mesh refinement in the span-wise direction. The grid resolution has a relatively small influence on the calculated lift coefficients. Only the results calculated with very coarse grids, i.e. $N_l = 10$ and $N_k = 4$, deviate from the results obtained with the finer grids. By increasing the number of panels, the calculated lift coefficients converge to the measurements for $\alpha + \alpha_0 \in [-5° : 6°]$.

### Cavitating NACA66$_2$-415 hydrofoil flow

In the present study the cavitating flow around the NACA66$_2$-415 foil is simulated for different inflow and cavitation conditions. The input data of the simulations is summarised in Table 5.4. Altogether two simulation cases with different angles of attack are investigated. In the simulations the angles of attack are adjusted in such way that they are equal to the lift coefficients measured in experiments under non-cavitating conditions. The analysed grids are presented in Table 5.5. Equivalent to the non-cavitating case study, the grid resolution is varied in the circumferential and span-wise direction. For sheet cavitation calculations a finer grid resolution is used than in the non-cavitating case since an accurate pressure distribution is important for the detection of sheet cavitation.

| **Characteristics** | **Notation** | **Case 1** | **Case 2** | **Unit** |
|---|---|---|---|---|
| Lift coefficient | $C_l^{noncav}$ | 0.84 | 1.04 | - |
| Angle of attack | $\alpha + \alpha_0$ | 14.4 | 18 | ° |
| Inflow velocity | $V_{inflow}$ | 5.5 | 5.5 | m/s |
| Water density | $\rho$ | 997.46 | 997.46 | kg/$m^3$ |
| Cavitation number | $\sigma_v$ | 1.5/ 2.0 | 3.0 | - |

Table 5.4: Input data for the cavitating case study (NACA66$_2$-415 hydrofoil)

| **Characteristics** | **Notation** | **Value** |
|---|---|---|
| Number of panels in span-wise direction | $N_k$ | 10/13/16 |
| Number of panels in circumferential direction | $N_l$ | 24/30/36/42/48/54/60/66 |

Table 5.5: Grid resolutions for the cavitating case study (NACA66$_2$-415 hydrofoil)

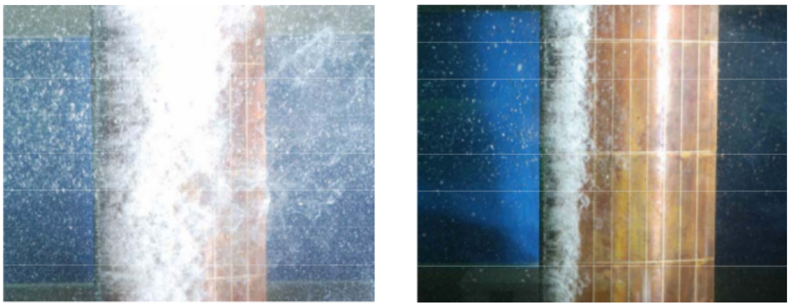

(a) $\sigma_v = 1.5$ (b) $\sigma_v = 2.0$

Figure 5.5: Sheet cavitation extents measured in experiment for the simulation case 1 with air content of 80% (taken from Richter (2011, p. 4.9))

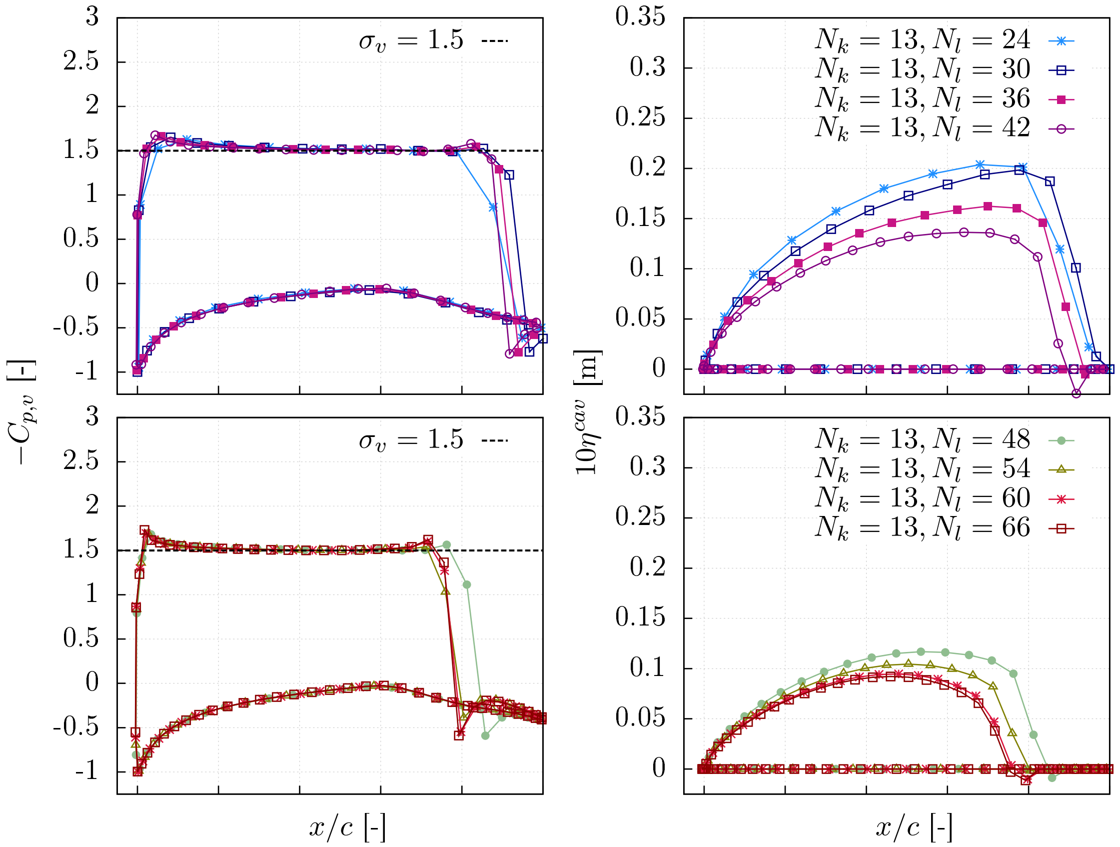

Figure 5.6: Scaled pressure coefficients and sheet cavitation extents calculated by *pan*MARE with different grid resolutions for the simulation case 1 with $\sigma_v = 1.5$

Firstly, the results of the simulation case 1 are discussed. The flow around the hydrofoil is simulated at the angle of attack $\alpha + \alpha_0 = 14.4°$ (corresponds to $\alpha + \alpha_0 = 10°$ in experiments) for two different cavitation numbers, namely $\sigma_v = 1.5$ and $\sigma_v = 2.0$. Figures 5.5a and 5.5b illustrate the sheet cavity extents measured by Richter (2011, p. 4.9) in experiments with the air content in water of 80%. According to the photographs, sheet cavitation extends until approximately 70% of the chord length for the cavitation number

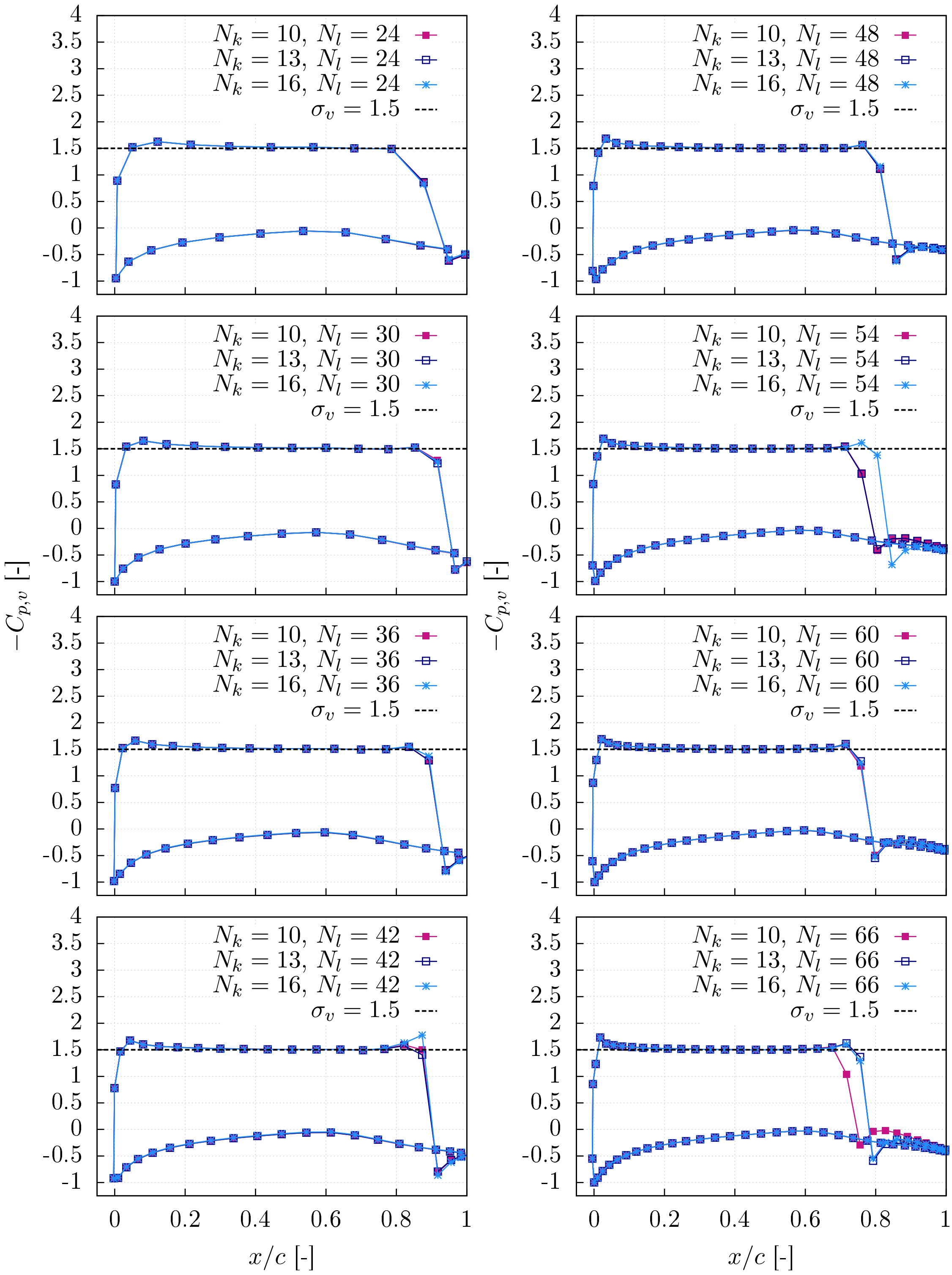

Figure 5.7: Comparison of the scaled pressure coefficients calculated by *pan*MARE with different grid resolutions for the simulation case 1 with $\sigma_v = 1.5$

$\sigma_v = 1.5$. For the cavitation number $\sigma_v = 2.0$ sheet cavitation extends until approximately 30% of the chord length.

Figures 5.6-5.7 and D.7 visualise the results calculated by *pan*MARE for the cavitation

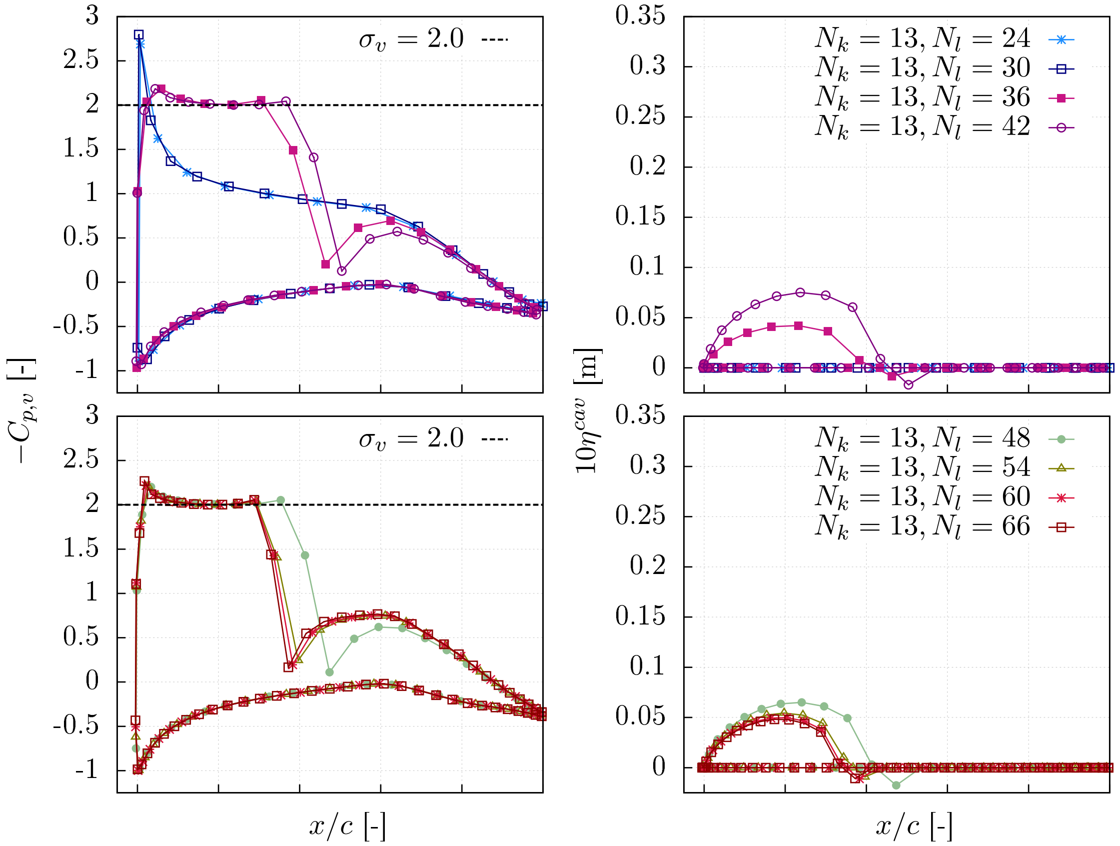

Figure 5.8: Scaled pressure coefficients and sheet cavitation extents calculated by *pan*MARE with different grid resolutions for the simulation case 1 with $\sigma_v = 2.0$

number $\sigma_v = 1.5$. The evaluations present the scaled pressure distributions $-C_{p,v}$ and sheet cavity thickness $10\eta^{cav}$ obtained with different grid resolutions. Independent of the grid refinement, the scaled pressure within the cavity sheet is equal to the cavitation number, i.e. the physics of the implemented sheet cavitation model are reproduced correctly. Furthermore, the constant part of the scaled pressure distribution identifies the length of the cavity sheet. The sheet cavitation length and thickness calculated by *pan*MARE strongly depend on the discretisation of the foil's surface. The impact of the grid refinement in the circumferential direction is significant (s. Figures 5.6). For example, the cavity thickness calculated with the grid $13 \times 24$ is twice as big as the cavity thickness obtained with the grid $13 \times 66$. Compared to the measured cavity length, the computed results are overestimated when the number of panels is $N_l \leq 48$. The results calculated with the grid resolutions $N_l = 54/60/66$ converge to the measured length, namely $0.7c$ where $c$ is the foil chord length. The refinement of the grid in the span-wise direction shows almost no influence on the calculated pressure distributions and corresponding sheet cavity extents.

Figures 5.8-5.9 and D.8 illustrate the calculated results obtained for the cavitation num-

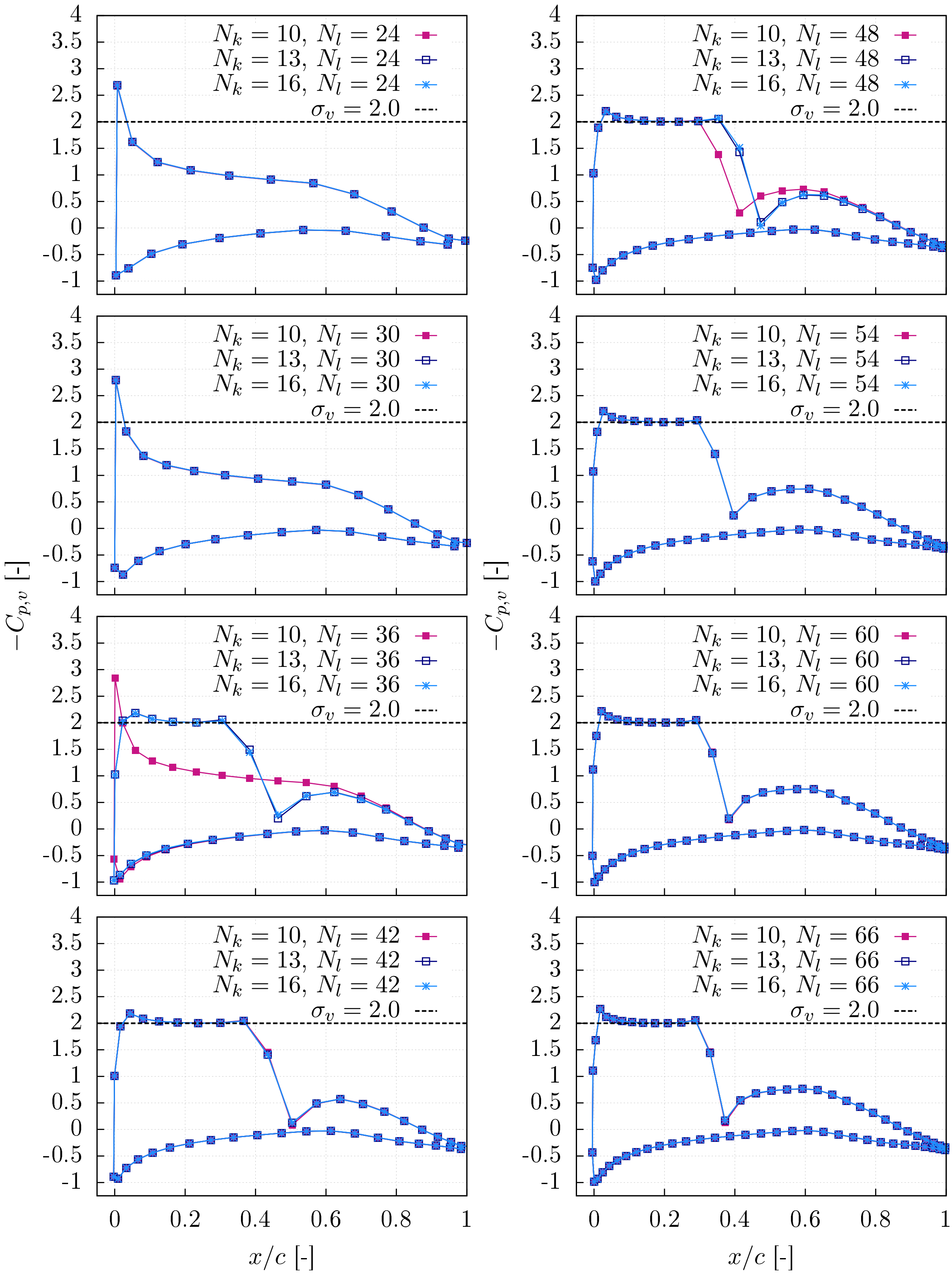

Figure 5.9: Comparison of the scaled pressure coefficients calculated by *pan*MARE with different grid resolutions for the simulation case 1 with $\sigma_v = 2.0$

ber $\sigma_v = 2.0$. One can explicitly see that the results computed with the grid resolutions $N_l = 54/60/66$ converge to the measured cavity length, namely $0.3c$. Grids with $N_l = 36/42/48$ panels lead to overestimated cavity shapes. By using a grid resolution with $N_l = 24/30$ panels no cavitation is detected. This can be explained by the fact that a coarse grid involves an imprecise pressure distribution at the leading edge. Indeed, the value of the pressure at the leading edge is very important for the sheet cavity detection and the grid there should be fine enough to calculate the pressure values accurately. The grid refinement in the span-wise direction has a relatively small influence on the calculated scaled pressure distributions and corresponding cavity shapes (s. Figures 5.9). Only the simulation results with $N_k = 10$ panels differ slightly from the results obtained with finer grid resolutions.

Figure 5.10: Sheet cavitation extent measured in experiment for the simulation case 2 and $\sigma = 3.0$ with air content of 80% (taken from Richter (2011, p. 4.10))

The following section concerns the discussion of the second simulation study. The flow around the hydrofoil is simulated at the angle of attack $\alpha + \alpha_0 = 18°$ (corresponds to $\alpha + \alpha_0 = 15°$ in experiments) for the cavitation number $\sigma_v = 3.0$. Figure 5.10 illustrates the sheet cavity extent measured by Richter (2011, p. 4.10) in experiments with the air content in water of 80%. The photograph shows that sheet cavitation extends until approximately 30% of the foil chord length. Figures 5.11-5.12 and D.9 present the calculated results in form of the scaled pressure distributions and sheet cavity extents for different grid resolutions. Independent of the surface grid resolution, the scaled pressure distribution $-C_{p,v}$ within the cavity sheet is equal to the cavitation number $\sigma_v = 3.0$. This observation verifies the implemented sheet cavitation model. The calculated sheet cavitation length and thickness strongly depend on the refinement of the surface grid in the circumferential direction. By using the grid resolutions $N_l = 24/30/36$, no cavitation is detected by the underlying numerical method (s. Figure 5.11). For $N_l = 48/54/60/66$ the calculated cavity lengths converge to the same value, namely 30% of the chord length, which coincides very well with the measured cavity length. According to Figure 5.12, the grid refinement in the span-wise direction does not influence the calculated results.

All simulated cases show that the calculated sheet cavitation lengths are in agreement with measurements and that the scaled pressure distribution within the cavitating area is

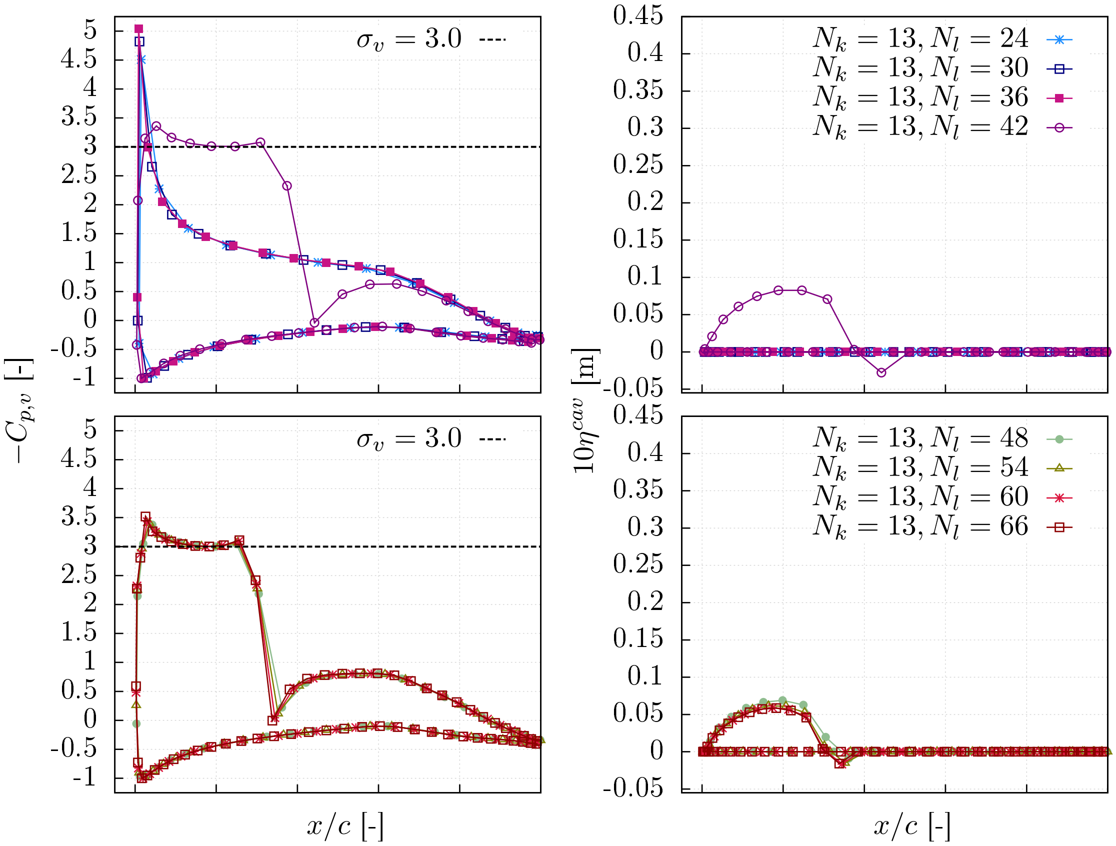

Figure 5.11: Scaled pressure coefficients and sheet cavitation extents calculated by *pan*MARE with different grid resolutions for the simulation case 2 with $\sigma_v = 3.0$

reproduced correctly. The present study points out that the choice of a suitable grid is a very important preparatory step to be taken before the computations. The employed sheet cavitation model delivers reliable results only for particular grid resolutions. The refinement of the hydrofoil grid in the span-wise direction should have at least 13 panels. The number of panels in the circumferential direction should be higher or equal to 54. The results with such grids were reliable and matched well with the measurements. The user of the program must find a compromise between the required level of accuracy and tolerable computation time. On the one hand, the hydrofoil grid should be fine enough to achieve grid-independent results. But on the other hand, the grid should be not too fine since the computational effort increases rapidly and the simulation results will not improve significantly.

In a final step, the influence of sheet cavitation on the hydrofoil flow characteristics is investigated. Figures 5.13 and 5.14 illustrate the relative lift and drag coefficients $^{C_l}/_{C_l^{noncav}}$ as well as $^{C_d}/_{C_d^{noncav}}$ as functions of the cavitation number $\sigma_v$. The results are presented for the surface grid resolution $13 \times 66$ for both simulation cases. It can be observed that a decrease of the cavitation number (which corresponds to a higher amount of sheet cavitation

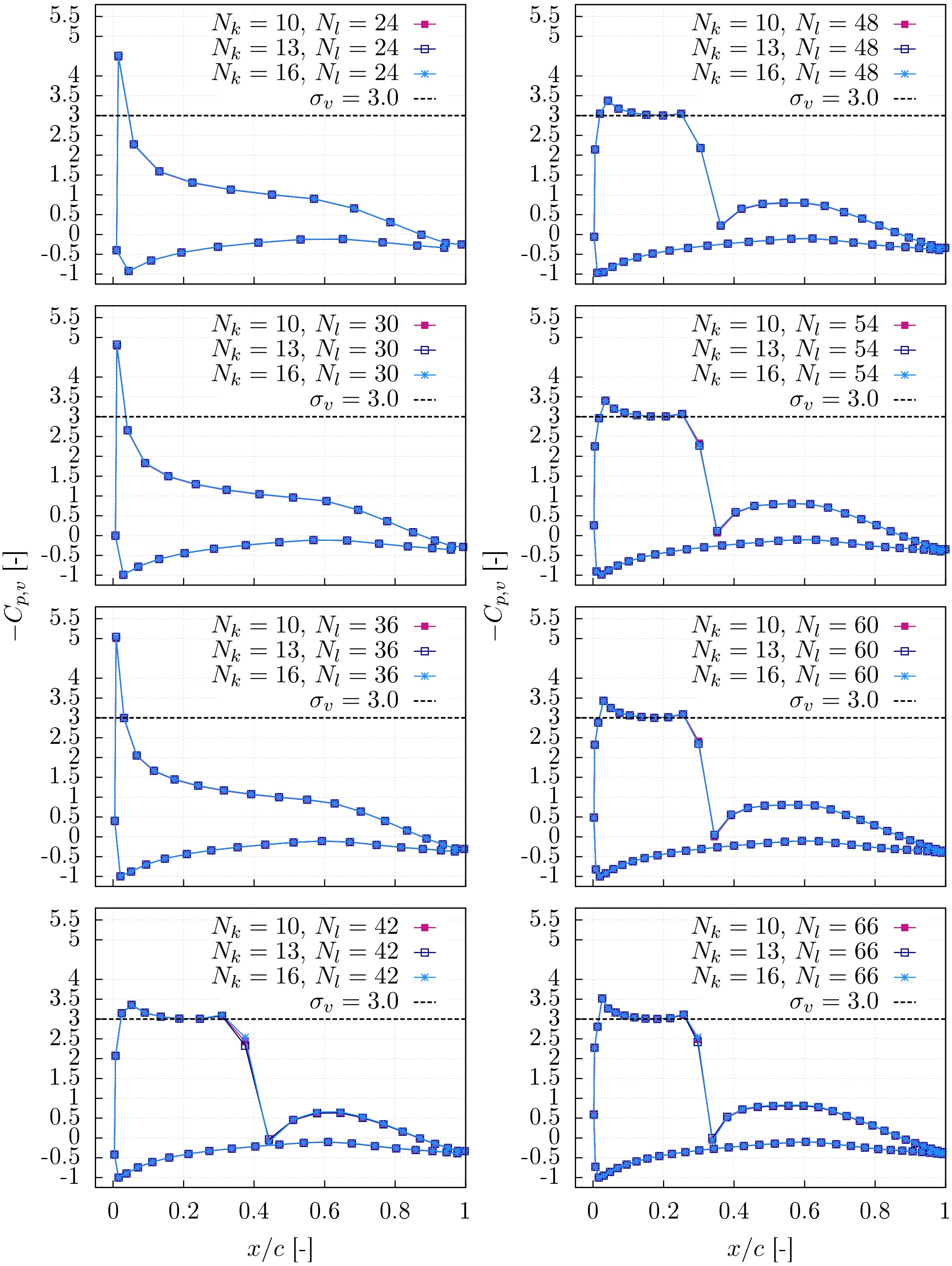

Figure 5.12: Comparison of the scaled pressure coefficients calculated by *pan*MARE with different grid resolutions for the simulation case 2 with $\sigma_v = 3.0$

on the foil) leads to an increase of the relative lift and drag coefficients. Phoemsapthawee et al. (2009, p. 2) report that partial sheet cavitation leads to a slight increase of the lift and drag coefficients. When the cavitation number is decreased so far that supercavitation

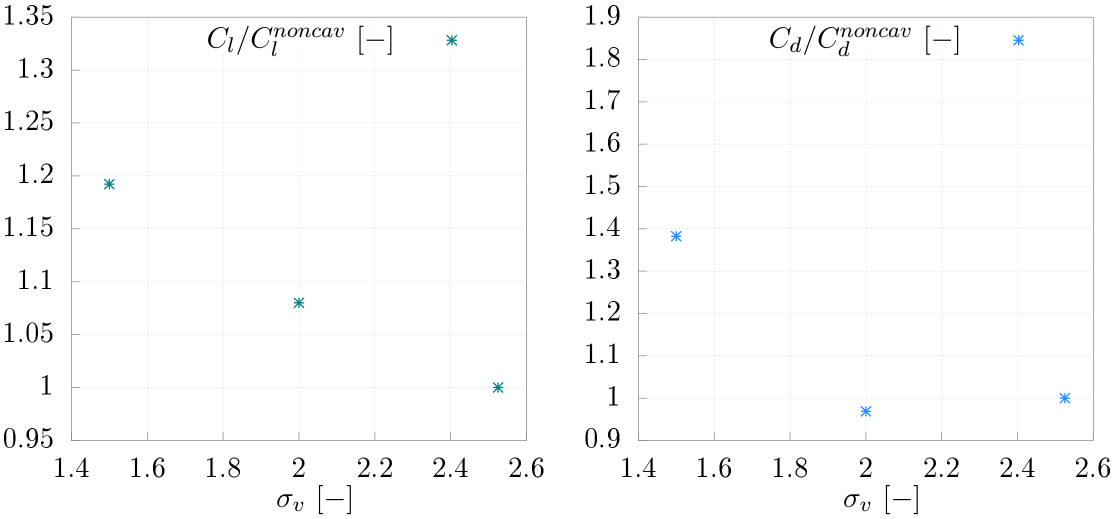

Figure 5.13: Relative lift and drag coefficients as functions of the cavitation number calculated by *pan*MARE for the simulation case 1

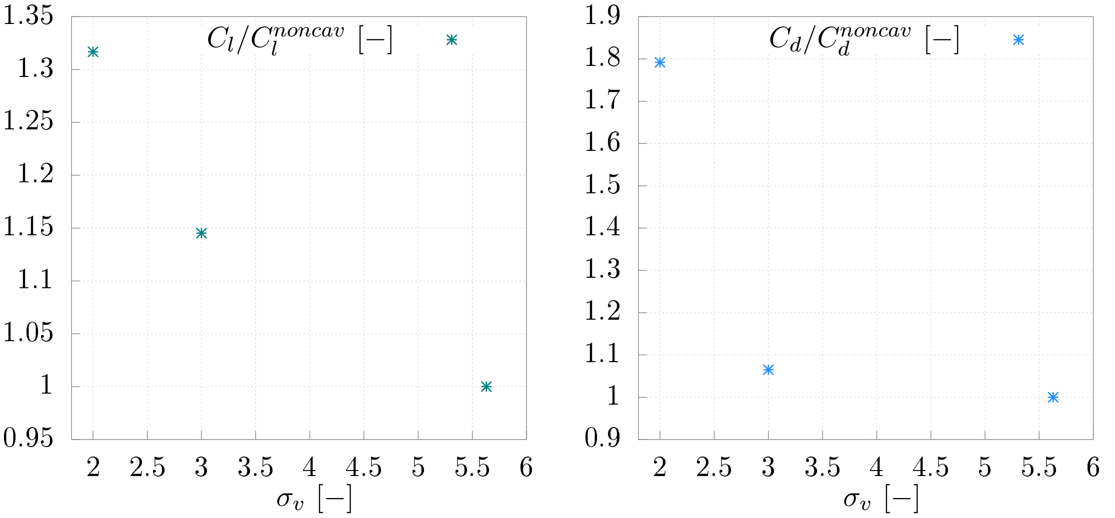

Figure 5.14: Relative lift and drag coefficients as functions of the cavitation number calculated by *pan*MARE for the simulation case 2

occurs on the hydrofoil, an abrupt decrease of the lift and drag coefficients is expected. In the underlying study no supercavitation was simulated and the calculated increase of the lift and drag coefficients in presence of partial sheet cavitation seems plausible.

### 5.1.2 NACA0010 rectangular hydrofoil

In the present study, the three-dimensional flow around the NACA0010 hydrofoil is analysed. The geometry of the foil is illustrated in Figure 5.15. All relevant geometrical configuration and input data are summarised in Table 5.6. The foil has a chord length of 0.2m and a span width of 0.3m. The grid used here consists of 13 panels in the span-wise direction and 66 panels in the cross-wise direction.

The aim of the study is to investigate the sheet cavitation behaviour of the NACA0010 hydrofoil with different cavitation numbers and to validate the implemented sheet cavitation model. The NACA0010 hydrofoil is examined in detail in the publication of Phoemsapthawee et al. (2009). According to this publication, the 3-D flow around the NAC0010 hydrofoil was measured by the Bulgarian Ship Hydrodynamic Centre in a cavitation tunnel. In the experiments the foil was attached to the upper tunnel wall, while a strut with the same section as the hydrofoil but with a zero angle of attack was installed between the hydrofoil and the tunnel wall. In order to simulate this experimental set-up in the present study, a strut and the mirror symmetry model were used in the software tool *pan*MARE in the simulations. The angle of attack is adjusted in order to match the lift coefficient measured in the experiments under non-cavitating conditions.

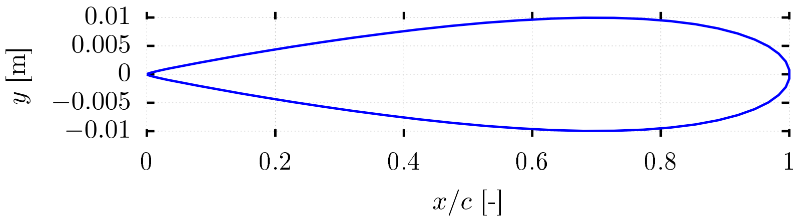

Figure 5.15: Geometry of the NACA0010 hydrofoil section

| **Characteristics** | **Notation** | **Value** | **Unit** |
|---|---|---|---|
| Span length | $b$ | 0.3 | m |
| Chord length | $c$ | 0.2 | m |
| Foil area | $A$ | 0.06 | $\mathrm{m}^2$ |
| Maximum thickness | $t_{max}$ | 0.10 | m |
| Aspect ratio | $\Lambda$ | 1.5 | - |
| Inflow velocity | $V_{inflow}$ | 6 | m/s |
| Angle of attack | $\alpha$ | 8.1 | ° |
| Non-cavitating lift coefficient | $C_l^{noncav}$ | 0.354 | - |
| Cavitation number | $\sigma_v$ | 0.893/0.9/0.992/1.001/1.1 | - |

Table 5.6: NACA0010 geometry and input data for the steady case study

In Figure 5.16 the sheet cavitation shapes measured in experiments and the results calculated by Phoemsapthawee et al. (2009) are demonstrated. The results obtained in the simulations by *pan*MARE are illustrated on Figure 5.17. It can be observed that the sheet cavity area decreases by increasing the cavitation number. For the cavitation number $\sigma_v = 1.1$ the cavity length is at its smallest and the cavity sheet covers approximately 25% of the foil's chord length. For the cavitation number $\sigma_v = 0.893$ the cavity sheet has the greatest length and thickness and extends to 45% of the chord length. The results

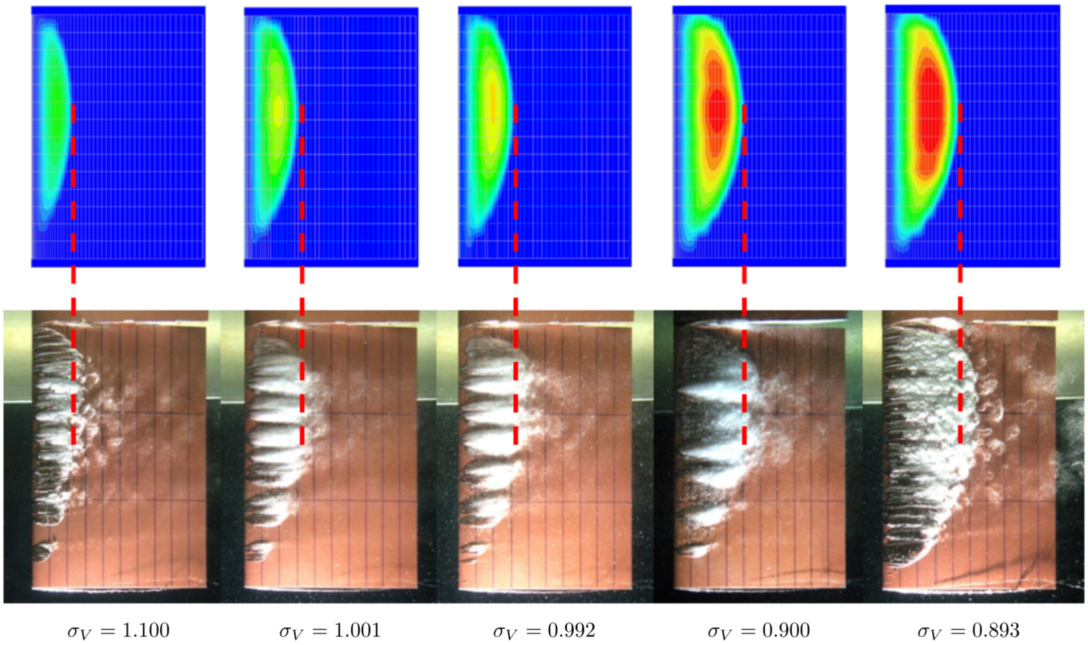

Figure 5.16: Sheet cavitation extents measured in experiment and calculated numerically by Phoemsapthawee et al. (2009, p. 15) for different cavitation numbers for the NACA0010 hydrofoil

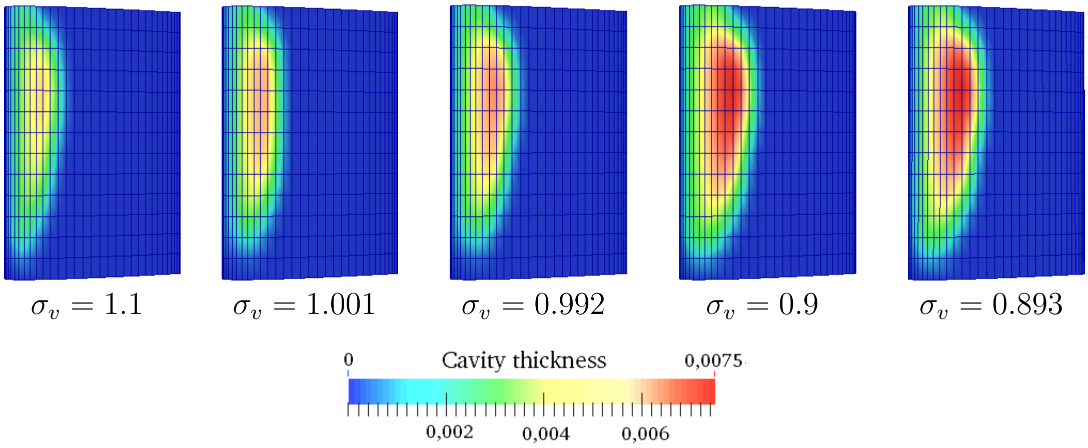

Figure 5.17: Sheet cavitation extents calculated by *pan*MARE for different cavitation numbers for the NACA0010 hydrofoil

calculated by *pan*MARE coincide very well with the results gained in experiments and numerical calculations of Phoemsapthawee et al. (2009). This example shows that the developed sheet cavitation model delivers accurate results for a steady three-dimensional hydrofoil flow with sheet cavitation and is able to reproduce the influence of the cavitation number on the sheet cavitation shape.

### 5.1.3 P1356 propeller

This section is dedicated to the study of the five-bladed propeller P1356 designed for the KRISO container ship (KCS). The propeller has a diameter of 7.9m in full scale and a skew angle of 31.83° and is used for diverse research studies (e.g. Richter and Heinke (2006), Heinke and Jaksic (2003), Heinke and Jaksic (2004)). The main parameters of the propeller are summarized in Table 5.7. The shape of the propeller is illustrated in Figure 5.18.

| **Characteristics** | **Notation** | **Value** | **Unit** |
|---|---|---|---|
| Propeller diameter in full scale | $D$ | 7.9 | m |
| Propeller diameter in model scale | $D_{model}$ | 0.25 | m |
| Pitch ratio | $P_{0.7}/D$ | 0.9967 | - |
| Mean pitch ratio | $P_{0.5}/D$ | 0.94 | - |
| Propeller area ratio | $A_E/A_0$ | 0.8 | - |
| Skew | $\theta$ | 31.83 | ° |
| Hub Ratio | $D_{hub}/D$ | 0.180 | - |
| Number of blades | $z$ | 5 | - |
| Blade section | | NACA66 | - |
| Scale factor | $\lambda$ | 31.6 | - |
| Propeller type | | fixed-pitch propeller | |
| Material | | brass | |
| Direction of rotation | | right-handed | |

Table 5.7: P1356 geometry data

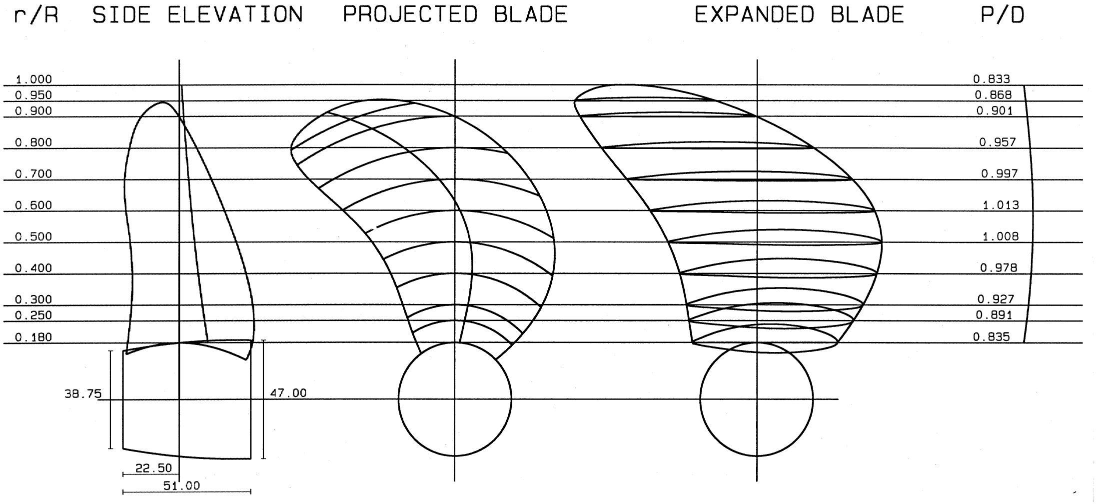

Figure 5.18: Geometry of the P1356 propeller (taken from Richter and Heinke (2006, p. 3.1))

In the first part of this section, the non-cavitating flow around the P1356 propeller is simulated and the open water characteristics are evaluated and validated against measured data of Richter and Heinke (2006). The second part of this section deals with the cavitating flow around the propeller. The calculated sheet cavitation shapes and scaled pressure distributions on selected radial sections of the propeller key blade are presented and compared with results obtained in measurements by Richter and Heinke (2006). Additionally, the thrust and torque coefficients are computed for several cavitation numbers in order to investigate their impact on the propeller flow characteristics. As detected in Section 5.1.1, the grid resolution has a significant influence on the simulation results for a hydrofoil flow. Consequently, this section also analysis the influence of the grid resolution on the flow characteristics and the sheet cavitation shape.

### Non-cavitating P1356 propeller flow

The input parameter for the simulations of the non-cavitating flow around the propeller are summarised in Table 5.8. The propeller is simulated in model scale with the rotational speed $n_{model} = 25{}^1\!/_s$ and different advance coefficients. The grid of the propeller blades is varied in the radial and circumferential direction. Altogether $4 \times 4 = 16$ grids are used (s. Table 5.9).

| **Characteristics** | **Notation** | **Value** | **Unit** |
|---|---|---|---|
| Rotation speed of model propeller | $n_{model}$ | 25 | 1/s |
| Advance coefficient | $J$ | 0.1325-1.0209 | - |
| Water density | $\rho$ | 998.238 | $kg/m^3$ |

Table 5.8: Input data for the non-cavitating case study (P1356 propeller)

| **Characteristics** | **Notation** | **Value** |
|---|---|---|
| Number of panels in span-wise direction | $N_k$ | 10/13/16/19 |
| Number of panels in cross-wise direction | $N_l$ | 16/24/32/40 |

Table 5.9: Grid resolutions of the P1356 propeller blades for the non-cavitating case study

Figures 5.19-5.20 and D.10-D.15 illustrate the open water characteristics calculated by *pan*MARE for various grid resolutions plotted against the measured values taken from Richter and Heinke (2006, p. 2.1). For very small advance coefficients, i.e. $J \leq 0.3$, the calculations do not converge for all grids. The values of the divergent calculations are extracted from the graphs. The calculated thrust coefficients are in good agreement with the measured values. The torque coefficients coincide very well with the measurements for $J \geq 0.5$. For lower advance coefficients the torque coefficients are slightly underestimated. For low advance coefficients, the abilities of a potential flow solver are limited since friction effects play a very important role. Nevertheless, the results calculated by

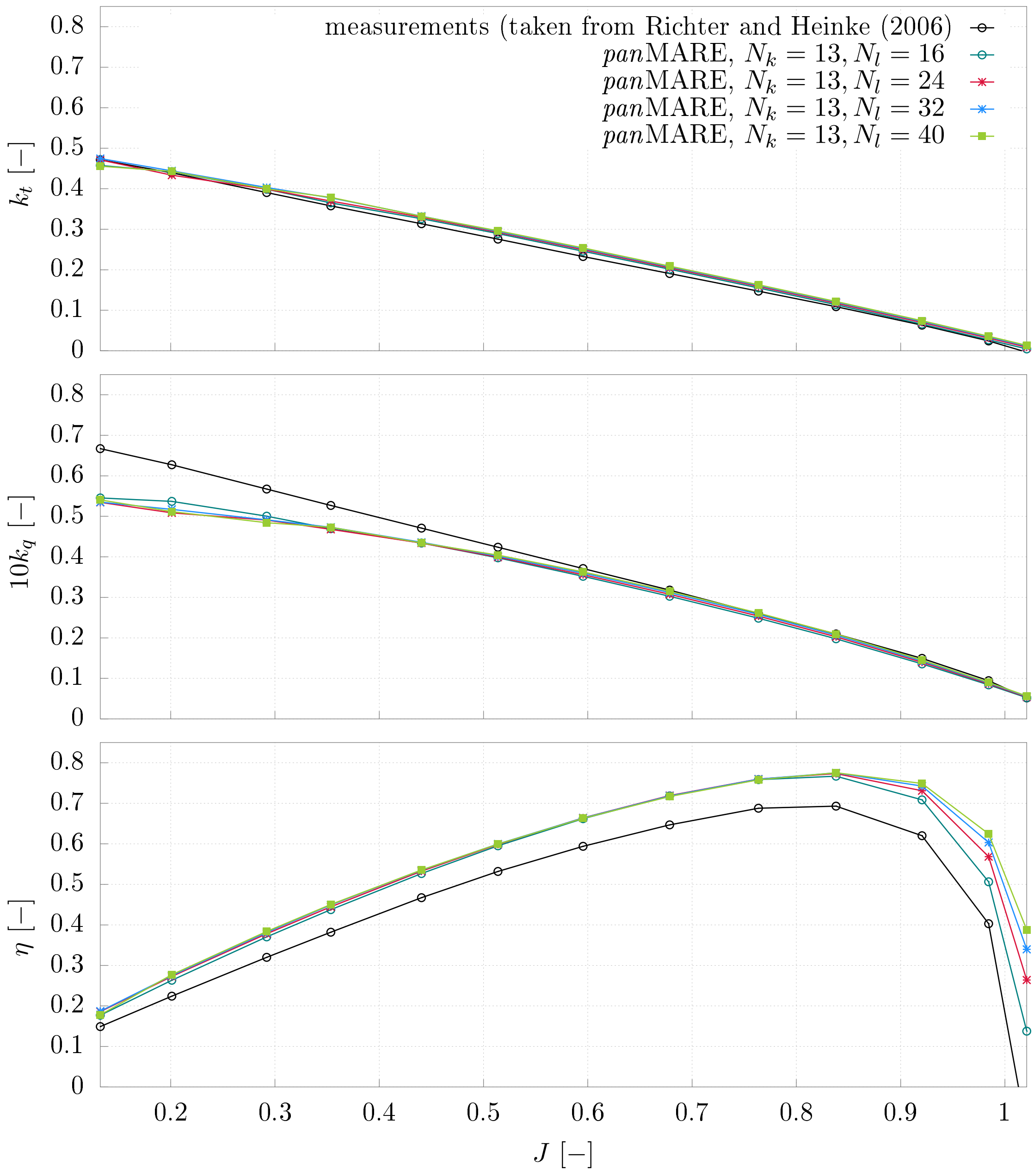

Figure 5.19: Influence of the grid resolution in the cross-wise direction on the calculated open water characteristics of the P1356 propeller

the underlying numerical method are satisfying, especially the results for the thrust coefficient. The calculated propeller efficiency is overestimated compared to the measured data, which is a consequence of the overestimated ratio $k_t/k_q$.

The grid refinement has little influence on the open water characteristics of the P1356 propeller. The greatest difference occurs for low advance coefficients, i.e. $J \leq 0.35$ (s. Figures 5.19 and 5.20). For $J \leq 0.35$ the meshes with $N_l \geq 24$ and $N_k \geq 13$ panels seem to deliver grid-independent results for the thrust and torque coefficients since they converge to the same value. For $J > 0.35$ the refinement in the circumferential and ra-

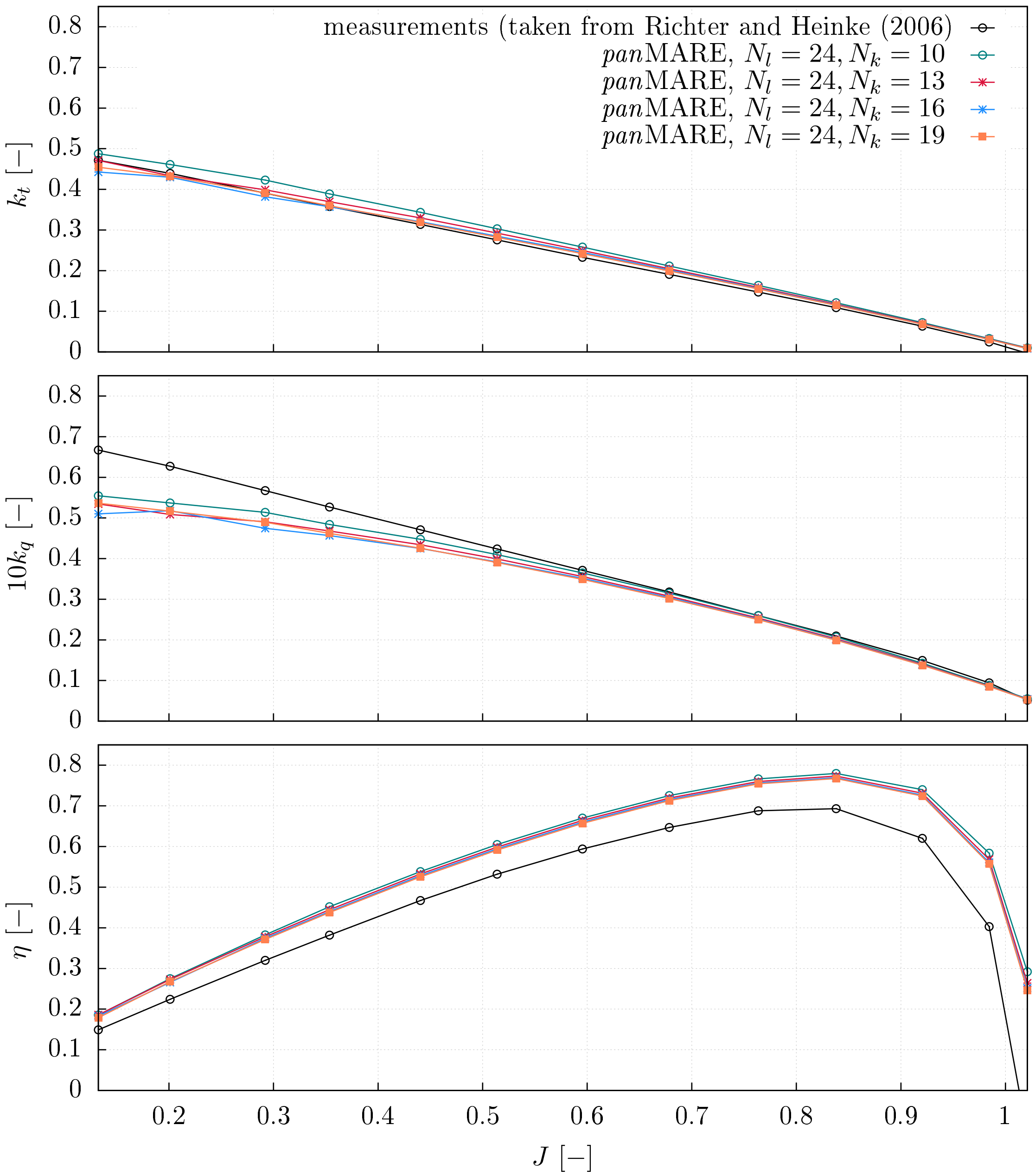

Figure 5.20: Influence of the grid resolution in the span-wise direction on the calculated open water characteristics of the P1356 propeller

dial direction has a negligible influence on the propeller flow characteristics. Hence, the grid resolution should be chosen depending on the considered advance coefficient. The smaller the advance coefficient, the finer the used grid should be.

### Cavitating P1356 propeller flow

This section analyses the cavitating flow around the propeller. The analysis includes a validation of the calculated sheet cavity extents and a verification of the scaled pressure distribution in the cavitating area. Moreover, the influence of the cavitation number on the calculated thrust and torque coefficients is investigated. The input parameters for this simulation case are outlined in Table 5.10. The rotational speed is $n_{model} = 25 ^1/_s$ and the advance coefficient is $J = 0.6$. The cavitation number based on the rotational speed is $\sigma_n = 2.312$, the corresponding cavitation number based on the inflow velocity is $\sigma_v = 6.422$. In line with the non-cavitating case study, different grid resolutions of the propeller blades are investigated (s. Table 5.11).

| **Characteristics** | **Notation** | **Value** | **Unit** |
|---|---|---|---|
| Rotation speed of model propeller | $n_{model}$ | 25 | 1/s |
| Advance coefficient | $J$ | 0.6 | - |
| Water density | $\rho$ | 998.238 | kg/m$^3$ |
| Cavitation number | $\sigma_n$ ($\sigma_v$) | 2.312 (6.422) | - |
| Thrust coefficient | $k_t^{noncav}$ | 0.22 | - |

Table 5.10: Input data for the cavitating case study (P1356 propeller)

| **Characteristics** | **Notation** | **Value** |
|---|---|---|
| Number of panels in span-wise direction | $N_k$ | 16/19/22/25 |
| Number of panels in cross-wise direction | $N_l$ | 44/56/68/80 |

Table 5.11: Grid resolutions of the P1356 propeller blades for the cavitating case study

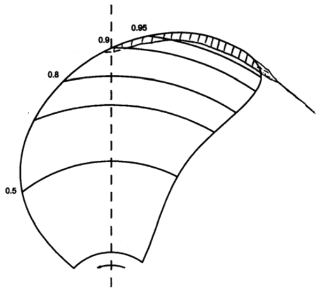

Figure 5.21: Sheet cavity extent on the P1356 propeller evaluated in experiment for $J = 0.6$ and $\sigma_n = 2.312$ (taken from Richter and Heinke (2006, p. 4.3))

Figure 5.21 shows the measured cavity extent for $J = 0.6$ and $\sigma_n = 2.312$ obtained in experiments by Richter and Heinke (2006, p. 4.3). The sheet cavity on the blade is relatively small and is restricted to the radial sections $r/R \in [0.89 : 1]$. At the tip of the blade vortex cavitation occurs. Figures 5.22a-5.22d illustrate the sheet cavity extents calculated by *pan*MARE for different grid resolutions. Tip vortex cavitation is not modelled by the underlying numerical method and is therefore not reproduced. The steady sheet cavitation model delivers accurate results for the sheet cavitation shape on the P356 propeller

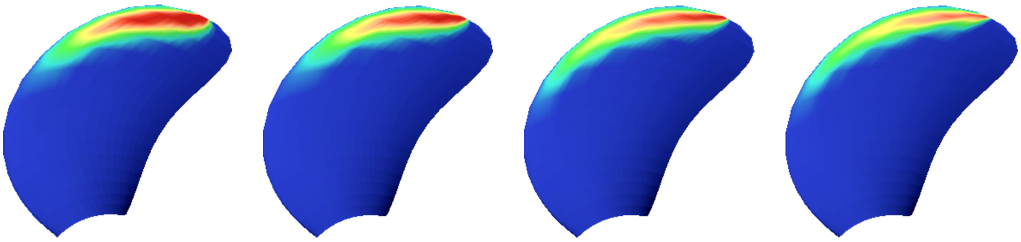

(a) $N_k = 16$ and $N_l = 44/56/68/80$

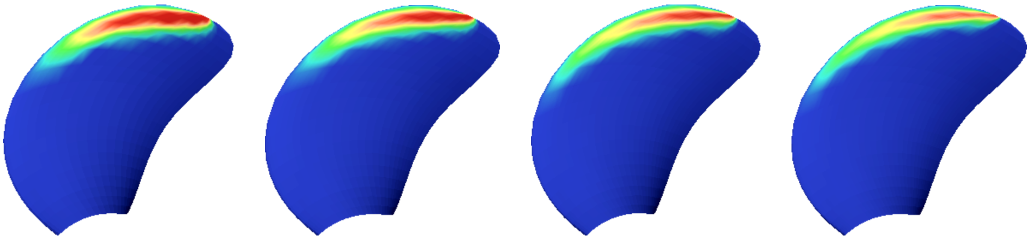

(b) $N_k = 19$ and $N_l = 44/56/68/80$

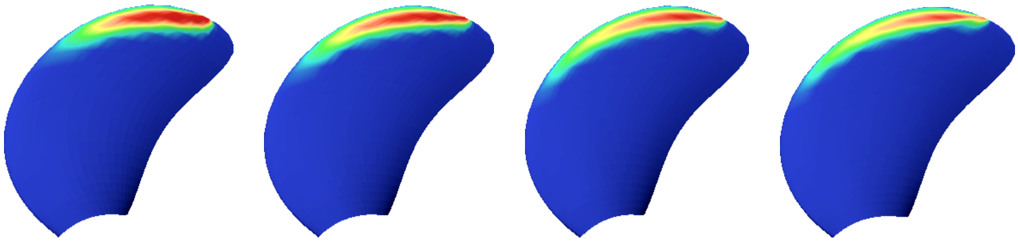

(c) $N_k = 22$ and $N_l = 44/56/68/80$

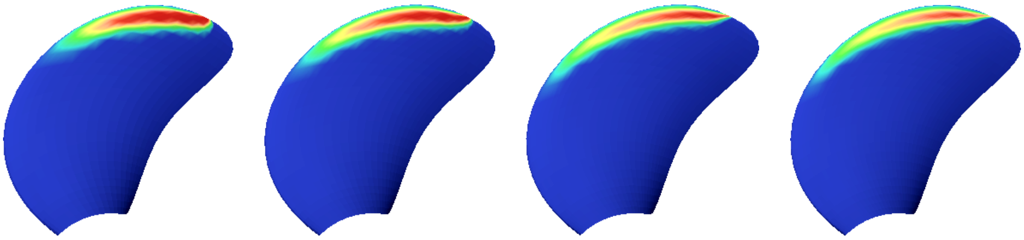

(d) $N_k = 25$ and $N_l = 44/56/68/80$

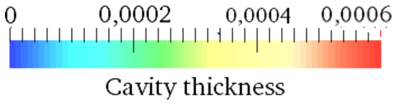

Figure 5.22: Sheet cavity extents on the P1356 propeller calculated by *pan*MARE for $J = 0.6$ and $\sigma_n = 2.312$ with different grid resolutions

for particular grids. For a propeller the grid refinement in the cross-wise direction has a considerable influence on the calculated sheet cavitation shapes, whereas the impact of the grid refinement in the radial direction is rather small. The cavity length and thickness decrease when the refinement of the grid is being increased. For $N_l = 44$ the cavity extents are overestimated for all radial refinements. For $N_l \geq 56$ and $N_k \geq 19$ the calculated results converge to the measured cavity shape. The refinement of the radial resolution can increase the computational time considerably since the wake panel grid depends on it.

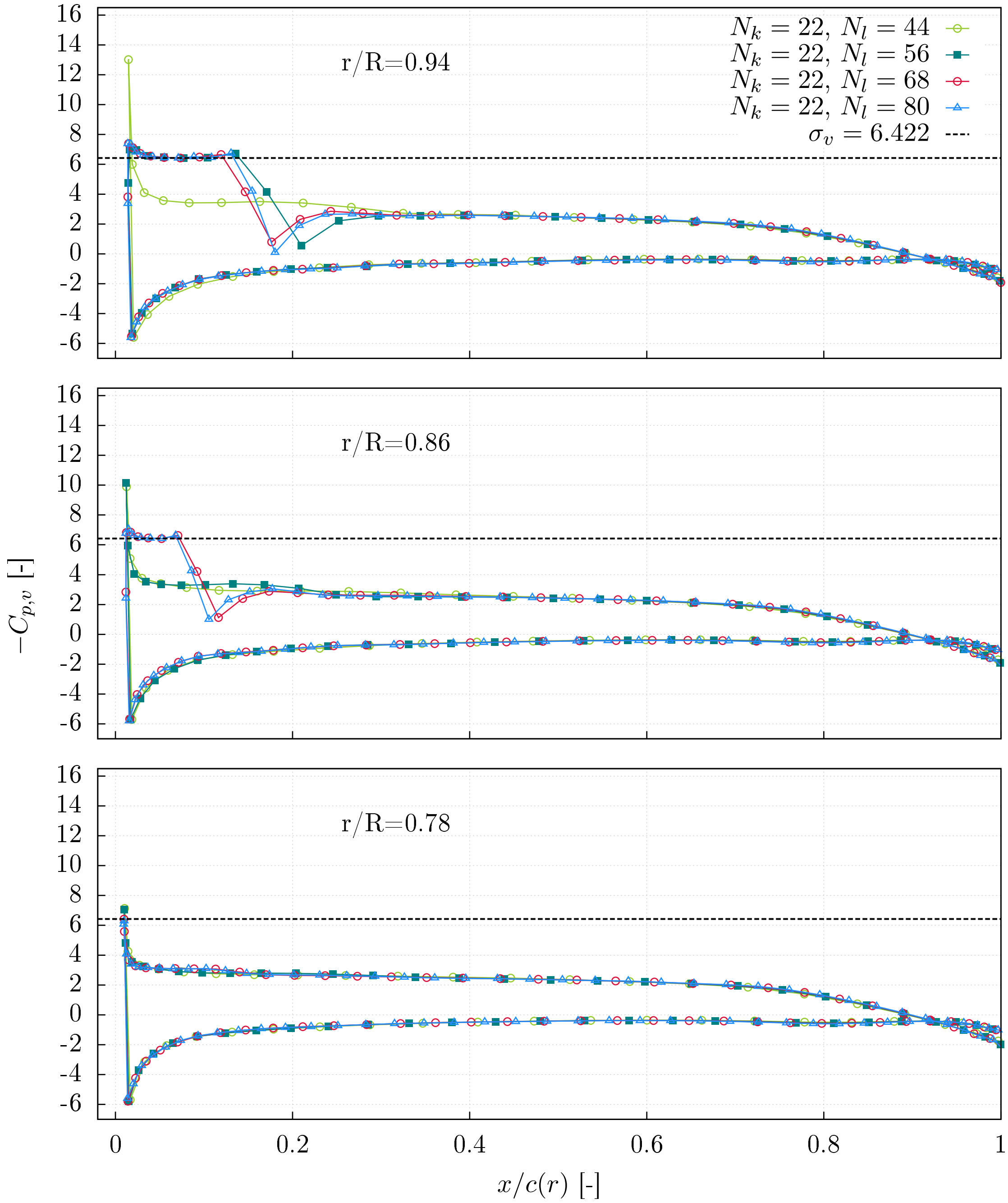

Figure 5.23: Pressure coefficients calculated by *pan*MARE for $J = 0.6$ and $\sigma_v = 6.422$ ($\sigma_n = 2.312$) with different grid resolutions in the cross-wise direction

Thus, the chosen grid resolution should not be too fine in order to limit the computational effort.

Additionally, Figures 5.23 and D.16-D.18 show the scaled pressure distribution on selected radial sections of the propeller key blade for all grid resolutions. The scaled pressure $-C_{p,v}$ is equal to the cavitation number $\sigma_v = 6.422$ within the cavity sheet, i.e. the numerical model reproduces the physics of the applied sheet cavitation model correctly.

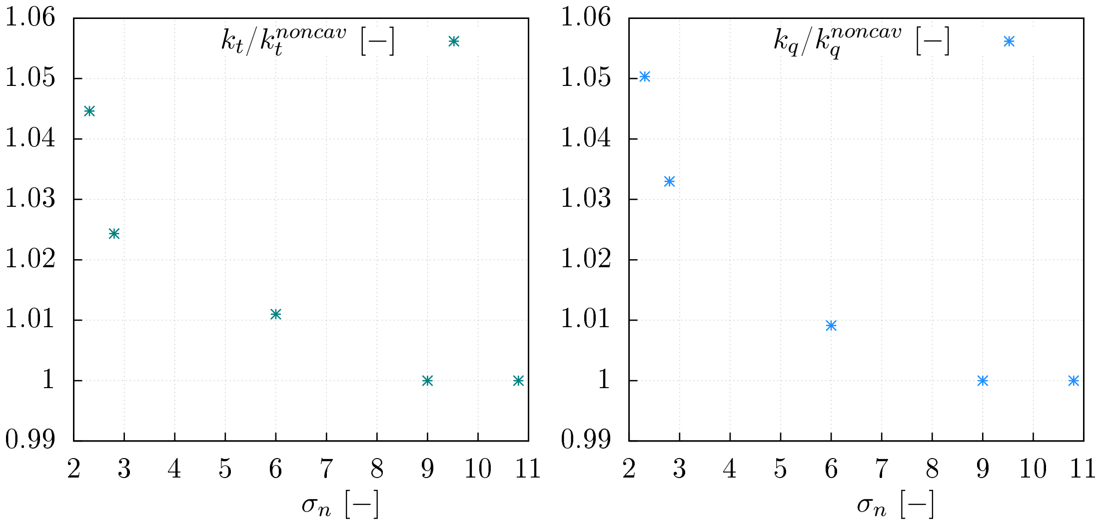

Figure 5.24: Relative thrust and torque coefficients as functions of the cavitation number calculated by *pan*MARE for $J = 0.6$ with different grid refinements in the circumferential direction

In Figure 5.24 the influence of sheet cavitation on the propeller flow characteristics is visualised. The relative thrust and torque coefficients of the propeller are calculated for different cavitation numbers and the blade surfaces are discretised into 22 × 68 panels. In presence of partial sheet cavitation the relative thrust and torque coefficients are slightly increased since the camber of the blade sections is increased by cavitation. The amount of partial sheet cavitation is small in the underlying simulations. In case of a high amount of sheet cavitation a decrease of the thrust and torque coefficients can be expected.

## 5.2 Unsteady sheet cavitation model

The focus of Section 5.2 is the validation and verification of the unsteady sheet cavitation model. Section 5.2.1 examines a verification case that analyses the unsteady flow past the three-dimensional NACA0010 hydrofoil. In Sections 5.2.2 and 5.2.3 the unsteady cavitating flows around two different propellers are investigated, namely the five-bladed P1356 propeller and the four-bladed P1380 propeller. The calculated results are compared with measured values and the influence of different ship wake fields on the computed sheet cavitation results is outlined.

### 5.2.1 NACA0010 rectangular hydrofoil in heave motion

This section investigates the flow around the NACA0010 hydrofoil in an oscillating pressure field. More precisely, the fluid is considered to be in a state of non-uniform motion. This kind of problem results in an unsteady interaction between the foil and the surrounding fluid. For the simulation of this case the inflow velocity component in the $z$-direction is defined as an oscillating function:

$$\mathbf{V}_\infty = (U_\infty, V_\infty, W_\infty(t)) \quad \text{and} \quad W_\infty(t) = W_0 \sin(\omega t), \tag{5.1}$$

where $W_0$ is the constant reference velocity and $\omega$ is the angular frequency. For a hydrofoil the oscillating velocity in the normal direction results in a change of the angle of attack. The reference velocity $W_0$ is chosen in such a way that the resulting angle of attack varies between $-5°$ and $5°$. By changing the angle of attack, the lift coefficient of the foil changes, i.e. the lift coefficient will be an oscillating function over the time period. Moreover, sheet cavitation is expected to occur on the back and face side of the hydrofoil. Thus, this example also serves as a verification case of the unsteady face and back sheet cavitation model.

| **Characteristics** | **Notation** | **Value** | **Unit** |
|---|---|---|---|
| Span length | $b$ | 1.2 | m |
| Chord length | $c$ | 0.2 | m |
| Foil area | $A_{ref}$ | 0.24 | $\mathrm{m}^2$ |
| Maximum thickness | $t_{max}$ | 0.10 | m |
| Aspect ratio | $\Lambda$ | 6 | - |
| Velocity in $x$-direction | $U_\infty$ | 1 | m/s |
| Velocity in $y$-direction | $V_\infty$ | 0 | m/s |
| Velocity in $z$-direction | $W_\infty(t)$ | $W_0 \sin(\omega t)$ | m/s |
| Reference velocity | $W_0$ | 0.0875 | m/s |
| Angular frequency | $\omega$ | $2\pi f$ | 1/s |
| Frequency | $f$ | 1.25 | 1/s |
| Time step | $\Delta t$ | 0.02 | s |
| Initial angle of attack | $\alpha$ | 0 | ° |
| Cavitation number | $\sigma_v$ | 0.65 | - |

Table 5.12: Geometry and input data of the NACA0010 hydrofoil in an oscillating velocity field

The surface grid used in these calculations is the same as in Section 5.1.2, namely $13 \times 66$. All relevant geometry and input data are presented in Table 5.12. The span length of the foil is 1.2m and the geometrical angle of attack is $0°$. The present simulation study is based on the numerical calculations performed by Phoemsapthawee et al. (2009). The angle of attack is varied during the simulations by varying the inflow velocity in the z-direction with the angular frequency $\omega = 2\pi f \, ^1\!/_s$, where $f = 1.25 \, ^1\!/_s$ is the frequency. The cavitation number used in the calculations is $\sigma_v = 0.65$. Altogether three different cases are simulated. In the first case the non-cavitating flow in an oscillating inflow velocity field is simulated. In the second simulation case the cavitating flow with the cavitation

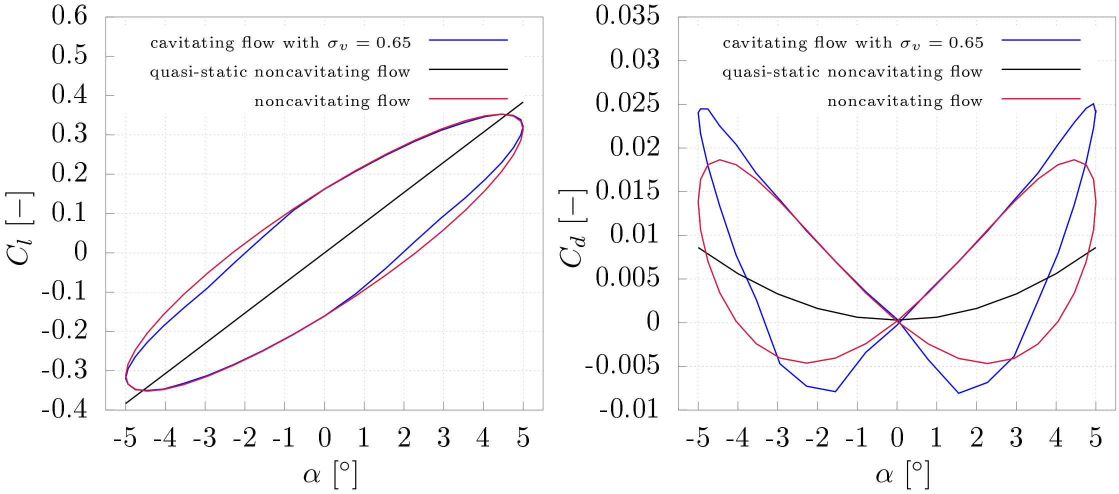

Figure 5.25: Lift and drag coefficients of the NACA0010 hydrofoil in an oscillating inflow velocity field

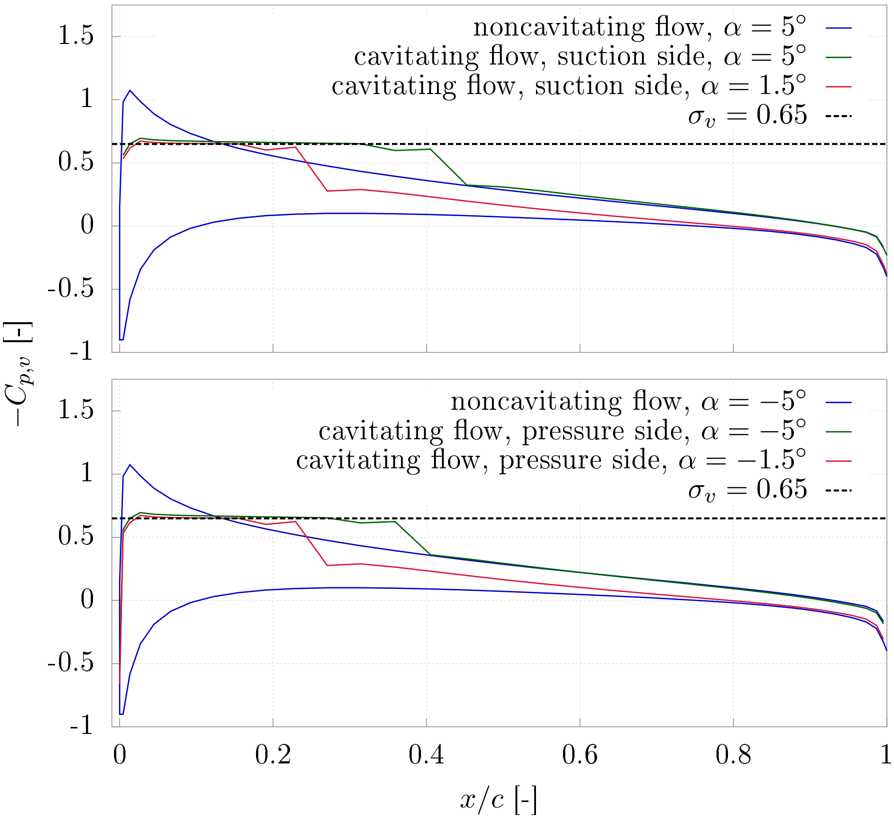

Figure 5.26: Verification of the pressure distribution on the mid-span of the NACA0010 hydrofoil for different angles of attack

number $\sigma_v = 0.65$ in an oscillating inflow velocity field is computed. In the third simulation case the quasi-static non-cavitating flow is calculated, where the inflow velocity is constant and the angle of attack is varied between $-5°$ and $5°$.

The calculated lift and drag coefficients for all simulated cases are plotted in Figure 5.25

as functions of the angle of attack. Sheet cavitation occurs for positive and for negative angles of attack. Sheet cavitation leads to an increase of the magnitude of the lift coefficient. The drag coefficient is decreased by sheet cavitation for the angles of attack between $-3°$ and $3°$. For the angles $\alpha \in [-5° : -3°]$ and $\alpha \in [3° : 5°]$ the drag coefficient increases and takes its maxima at $\alpha = 5°$ and $\alpha = -5°$, respectively. The occurrence of sheet cavitation obviously has little influence on the lift coefficient but a huge impact on the drag coefficient. The drag coefficient approximately increases by factor 1.6 for the maximal and minimal angle of attack of $5°$ and $-5°$.

In Figure 5.26 the scaled pressure distribution on the mid-span of the foil for different angles of attacks is verified. The value of the scaled pressure coefficient $-C_{p,v}$ is equal to the cavitation number on the cavitating part of the surface. Depending on the sign of the angle of attack, sheet cavitation occurs on the suction (positive angle) or on the pressure side (negative angle) of the foil. Furthermore, the scaled pressure is equal for face and back cavitation for an equal absolute value of the angle of attack. These observations together with the results obtained for the lift and drag coefficients verify the physics of the unsteady sheet cavitation model for a hydrofoil flow.

### 5.2.2 P1356 propeller in inhomogeneous inflow

Section 5.2.2 investigates the unsteady flow characteristics of the P1356 propeller in presence of sheet cavitation. The unsteady sheet cavitation patterns are analysed and compared with the results obtained in experiments of Heinke and Jaksic (2003, 2004). Heinke and Jaksic (2003) developed the dummy model DM40 of the KRISO containership in order to simulate the 3-D inflow to the propeller in the cavitation tunnel. The scale factor of the aft-ship in the measurements was $\lambda = 31.6$. According to Heinke and Jaksic (2003), the wake field was simulated for the Reynolds number of the model and for that of the full scale. The model ship wake field is denoted by DM40M and the predicted full scale wake field by DM40S. The wake fraction $w$ of both wake fields is illustrated in Figures 5.27a-5.27b. The wake peak of DM40M is wider than that of DM40S.

The calculations by *pan*MARE are performed with both ship wake fields, i.e. two simulation cases are investigated. The input data used in the simulations can be found in Table 5.13. The rotational speed is $n_{model} = 30{}^1\!/_s$ and the cavitation number is $\sigma_{n0.8R} = 1.489$ for DM40M and $\sigma_{n0.8R} = 1.487$ for DM40S. The ship velocity is chosen in such a way that the mean thrust coefficient $\bar{k}_t = 0.172$ for DM40M and $\bar{k}_t = 0.170$ for DM40S is achieved in the non-cavitating case by the underlying numerical method.

All five blades of the propeller are discretised in $22 \times 68$ panels. The trailing wake is aligned according to the axial wake alignment model. In the calculations with the ship wake field the wake alignment plays an important role. The use of the free alignment model often results in instabilities at the hub and tip of the propeller blades, that is why an alignment only in the axial direction is applied here. With the axial wake alignment model the results for the thrust and torque coefficients converge after 1.2 propeller rotations. Hence, in order to have convergent results, 2.2 rotations are performed and the results of the last rotation are evaluated.

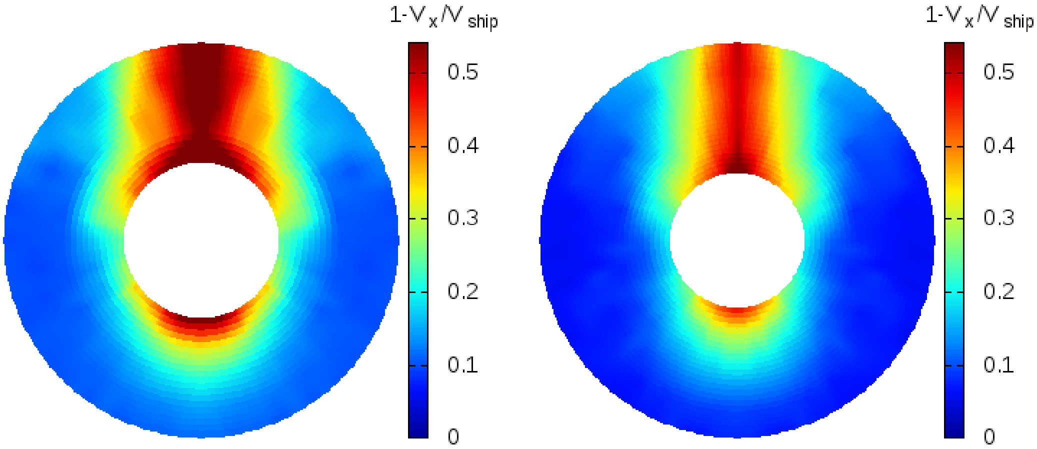

(a) Model wake field DM40M (b) Predicted full scale wake field DM40S

Figure 5.27: Model wake field DM40M and predicted full scale wake field DM40S

| **Characteristics** | **Notation** | **DM40M** | **DM40S** | **Unit** |
|---|---|---|---|---|
| Rotation speed | $n_{model}$ | 30 | 30 | $1/s$ |
| Thrust coefficient | $k_t$ | 0.172 | 0.170 | - |
| Cavitation number | $\sigma_{n0.8R}$ | 1.489 | 1.487 | - |

Table 5.13: Input data for the simulations of the unsteady P1356 propeller flow with sheet cavitation

Figures 5.28 and 5.29 show the calculated and measured sheet cavity shapes for the blade angular positions $\theta = 0/20/340°$ for the wake fields DM40M and DM40S, respectively. For the wake field DM40M sheet cavitation occurs in the experiment on the suction side for the blade angular positions $340° \leq \theta \leq 70°$ (s. Heinke and Jaksic, 2003, p. 1.33). For the wake field DM40S the measurements show an occurrence of sheet cavitation on the suction side for the blade angular positions $340° \leq \theta \leq 60°$ (s. Heinke and Jaksic, 2003, p. 1.33). According to the report by Heinke and Jaksic (2003, p. 5.1f.), the flow starts to cavitate as the blade enters the wake peak at the angular position $\theta = 340°$, reaching the maximal extent of sheet cavitation for the angles $10° \leq \theta \leq 30°$.

The results of the simulations illustrated in Figures 5.28 and 5.29 show that the cavity shape and thickness vary with the varying blade angular position. The calculated sheet cavity shapes are in good agreement with the measured results for both wake fields. Only for $\theta = 340°$ *pan*MARE detects a slightly higher amount of sheet cavitation at the inner

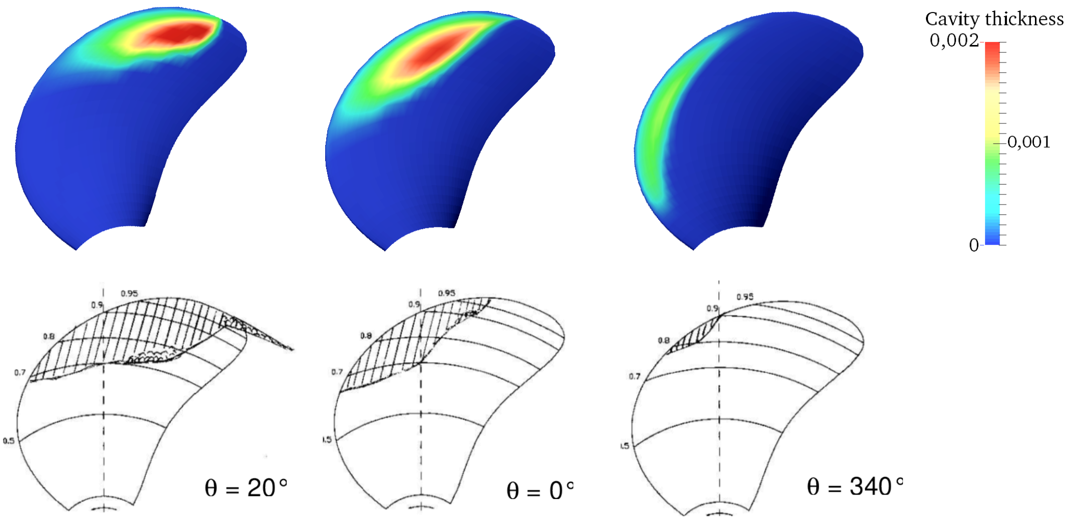

Figure 5.28: Sheet cavity extents on the P1356 propeller simulated by *pan*MARE and obtained in experiments (taken from the SVA Heinke and Jaksic (2003, p. 1.33)) with wake field DM40M in blade angular positions $\theta = 0/20/340°$

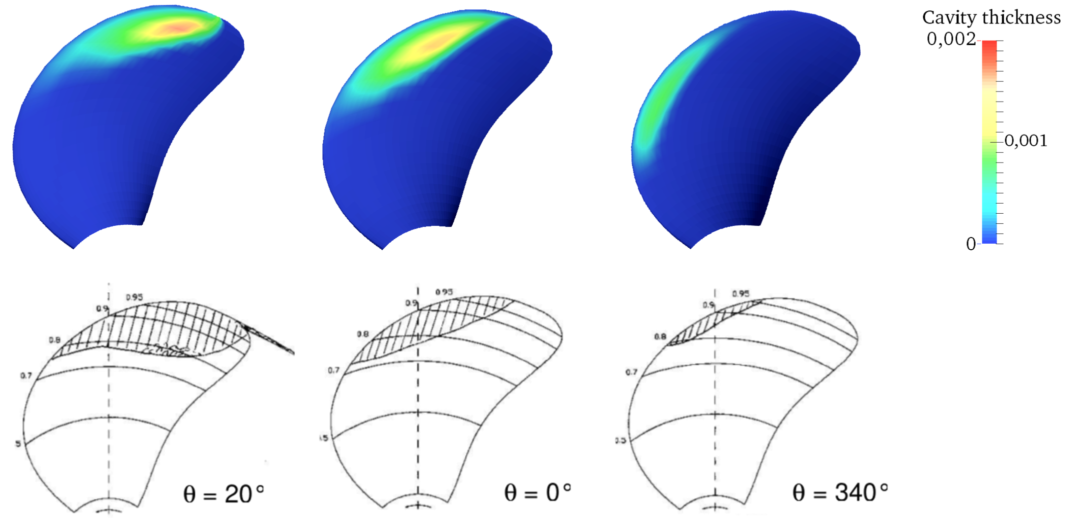

Figure 5.29: Sheet cavity extents on the P1356 propeller simulated by *pan*MARE and obtained in experiments (taken from the SVA Heinke and Jaksic (2003, p. 1.33)) with wake field DM40S for the blade angular positions $\theta = 0/20/340°$

radii of the propeller blade than the measurements show. The measurements and calculations with the model wake field DM40M feature a greater sheet cavity area and thickness compared to those for the full scale wake field. This observation can be explained by the wider wake peak of the model wake field.

Figures 5.30 and 5.31 present the unsteady flow characteristics and the cavitation behaviour of the P1356 propeller in the model and full scale wake field. The graphs in the figures visualise the relative thrust coefficient $k_t^{cav}/k_t^{noncav}$, the relative cavity area $A^{cav}/A_{ref}$ and the second derivative of the cavity volume $10^6 \partial^2 V^{cav}/\partial\theta^2$ as functions of the blade

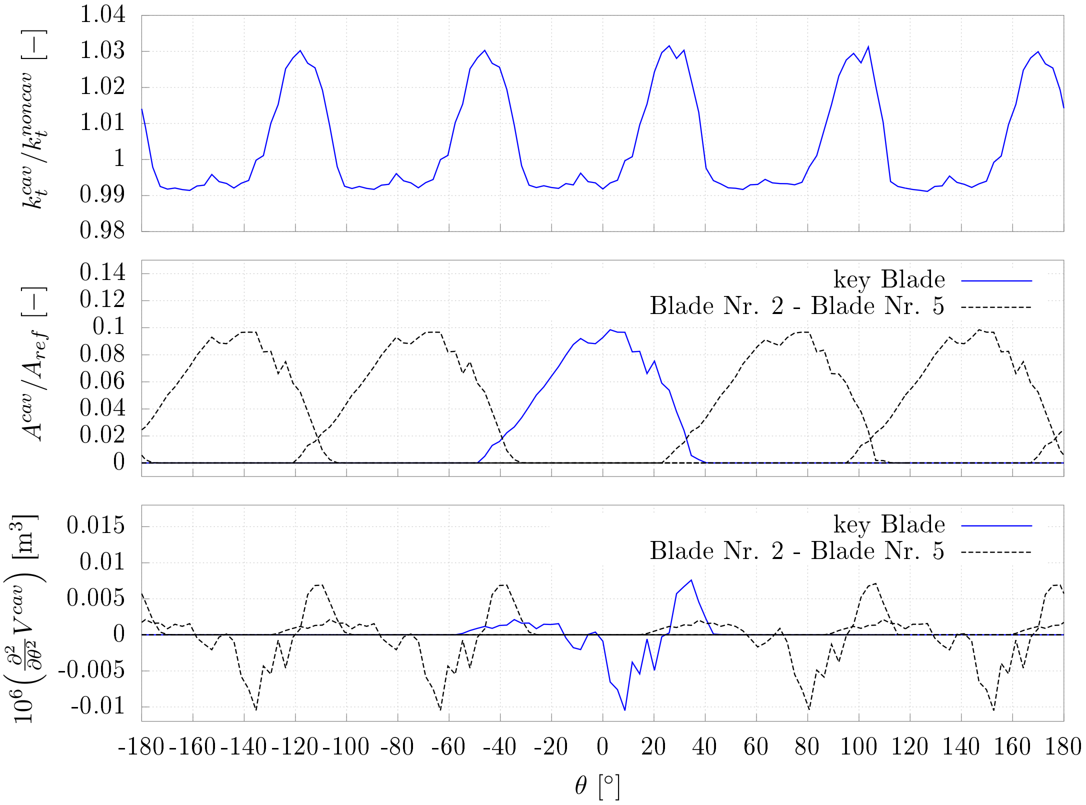

Figure 5.30: Unsteady flow characteristics of the P1356 propeller with ship wake field DM40M

angular position. For both wake fields a similar behaviour of the sheet cavitation characteristics is observed. The cavity area increases while the key blade enters the 310° position and takes its maximum at approximately 10°. At the same time the relative thrust coefficient decreases and takes its minimal value when the blade is covered with a high amount of sheet cavitation. While the key blade moves to the starboard towards the blade angular position of 30°, the relative thrust coefficient increases. At approximately 30° the cavity occurs on two blades, which can be observed on the graph of the cavity area and the relative thrust coefficient reaches its maximal value at this position. The second derivative of the cavity volume with respect to the angle step increases while the flow starts to cavitate and decreases while the cavity extent grows on the propeller blade. When sheet cavitation occurs simultaneously on two blades, the second derivative of the cavity volume increases again.

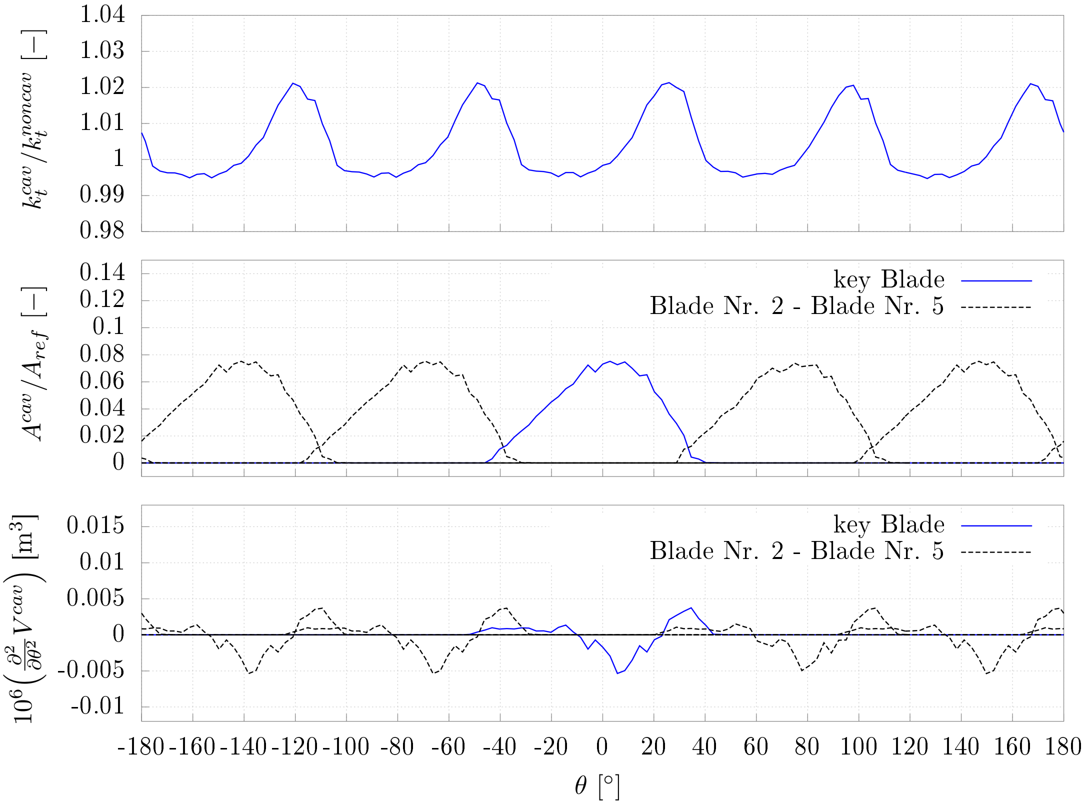

Figure 5.31: Unsteady flow characteristics of the P1356 propeller with ship wake field DM40S

### 5.2.3 P1380 propeller in inhomogeneous inflow

Section 5.2.3 investigates the unsteady cavitating flow around the four-bladed P1380 propeller. The propeller is illustrated in Figure 5.32a and its geometry data is summarised in Table 5.14. This propeller was experimentally investigated by Heinke and Jaksic (2004). In their experiments Heinke and Jaksic (2004) used a modified full scale wake field denoted by DM40S1 as the inflow to the propeller (s. Figure 5.32b). The wake field DM40S1 is a modification of the original full scale wake field DM40S introduced in Section 5.2.2.

The focus of the underlying study is to validate the unsteady cavitation patterns on the propeller P1380. For this purpose, the flow around the propeller is simulated subject to the DM40S1 wake field and the computed results are compared with measurements of Heinke and Jaksic (2004). The input data used in the simulations can be found in Table 5.15. The rotational speed of the propeller is $30\,{}^1\!/_s$ and the ship velocity is chosen in such a way that the mean thrust coefficient $\bar{k}_t = 0.184$ is achieved for the non-cavitating case. The blades of the P1380 propeller are discretised by $22 \times 68$ panels.

Figure 5.33 shows the photographs of the cavitating propeller flow in the wake field DM40S1 at the blade angular positions $\theta = 340/350/0/10/20/30°$ taken from the video

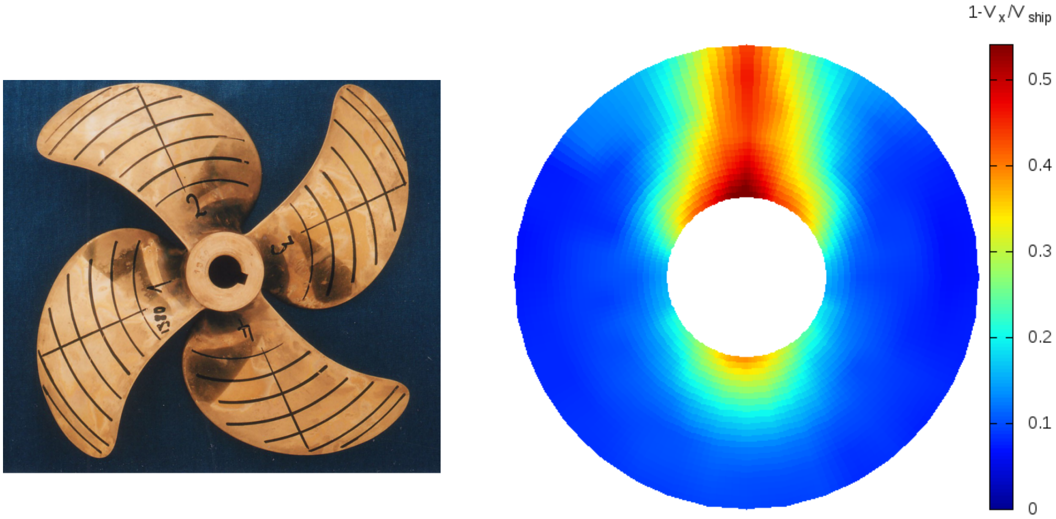

(a) Geometry of the P1380 propeller (b) Modified full scale wake field DM40S1

Figure 5.32: Geometry of the P1380 propeller (taken from Heinke and Jaksic (2004, p. 4.5)) and modified full scale wake field DM40S1

| **Characteristics** | **Notation** | **Value** | **Unit** |
|---|---|---|---|
| Propeller diameter in full scale | $D$ | 8.1 | m |
| Propeller diameter in model scale | $D_{model}$ | 0.2563 | m |
| Pitch ratio | $P_{0.7}/D$ | 1.04802 | - |
| Mean pitch ratio | $P_{0.5}/D$ | 1.02058 | - |
| Propeller area ratio | $A_E/A_0$ | 0.69 | - |
| Skew | $\theta$ | 36.99781 | ° |
| Hub Ratio | $D_{hub}/D$ | 0.1732 | - |
| Number of blades | $z$ | 4 | - |
| Scale factor | $\lambda$ | 31.6 | - |
| Propeller type | | fixed-pitch propeller | - |
| Material | | brass | - |
| Direction of rotation | | right-handed | - |

Table 5.14: P1380 geometry data

| **Characteristics** | **Notation** | **Value** | **Unit** |
|---|---|---|---|
| Rotation speed | $n_{model}$ | 30 | $1/s$ |
| Thrust coefficient | $k_t$ | 0.184 | - |
| Cavitation number | $\sigma_{n0.8R}$ | 1.56 | - |

Table 5.15: Input data for the simulations of the unsteady P1380 propeller flow with sheet cavitation

recordings of Heinke and Jaksic (2004, p. 5.10f.). It can be observed that sheet cavitation starts to develop at the blade angular position of 340° and reaches its maximum extent at $\theta = 10°$. Figure 5.34 illustrates the cavity extents calculated by *pan*MARE for the

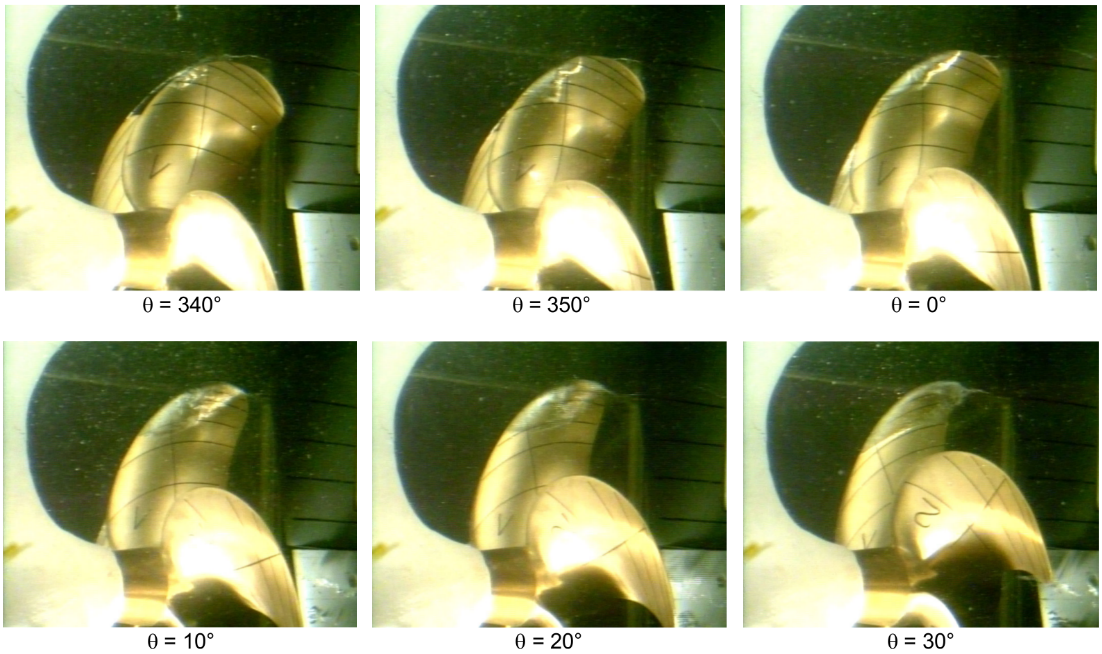

Figure 5.33: Sheet cavity extents on the P1356 propeller obtained in experiments (taken from the SVA Heinke and Jaksic (2004, p. 5.10f.)) with the wake field DM40S1 for the blade angular positions $\theta = 340/350/0/10/20/30°$

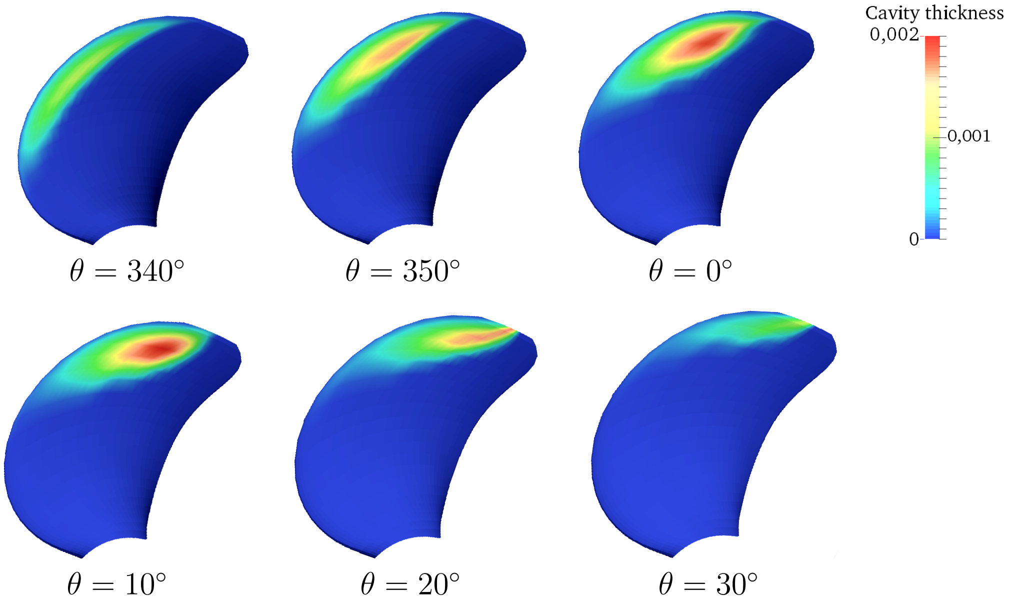

Figure 5.34: Sheet cavity extents on the P1356 propeller simulated by *pan*MARE with wake field DM40S1 for the blade angular positions $\theta = 340/350/0/10/20/30°$

wake field DM40S1. *pan*MARE calculates the maximum cavity extent for $\theta = 10°$ in agreement to the experiments. For all angular positions except of 340° the sheet cavity shapes coincide very well with the cavity shapes obtained in the measurements. For the angular position $\theta = 340°$ the cavity shape slightly differs from the measured one. The

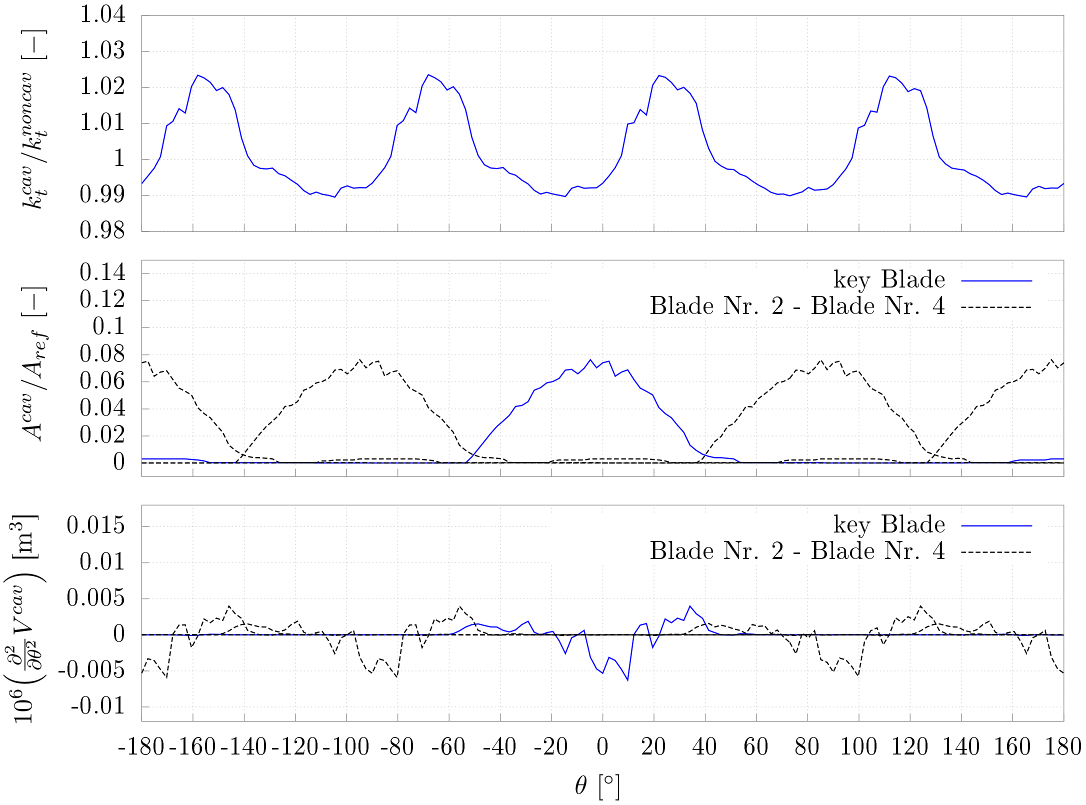

Figure 5.35: Flow characteristics of the P1380 propeller with wake field DM40S1

simulations detect sheet cavitation already appearing from the radius $r/R = 0.5$. The measured cavity shape shows no cavitation on the inner radii at this angular position of the key blade. The same problem was already faced for the P1356 propeller.

Additionally, in Figure 5.35 the time change of the relative thrust coefficient, the relative cavity area and the second derivative of the cavity volume over the angle step are plotted. The graphs show a similar behaviour as for the five-bladed P1356 propeller. The cavity area increases while the key blade enters the 310 degrees position and takes its maximum at approximately 10 degrees. The relative thrust coefficient decreases while the sheet cavitation area increases. While the key blade moves towards the blade angular position of 20 degrees, the relative thrust coefficient takes its maximum value. The value of the second derivative of the cavity volume with respect to the angle step slightly increases while the flow starts to cavitate and decreases while the cavity extent grows on the propeller blade.

The simulation studies for the P1356 and P1380 propeller validate the implemented unsteady sheet cavitation model. The numerical method is able to reproduce the unsteady sheet cavitation patterns on a propeller subject to a non-uniform inflow and to detect the influence of sheet cavitation on the propeller flow characteristics.

# Chapter 6

# Validation of propeller-induced pressure pulses on a ship hull

The present chapter focuses on the investigation of propeller-induced pressure pulses under consideration of partial sheet cavitation on propeller blades. Pressure fluctuations due to cavitating propellers can cause various problems for the operation of ships, e.g. excitation of the aft ship structure, generation of underwater noise and loss of propulsion efficiency. Hence, the prediction of propeller-generated operational loads attracted increasing academic interest in the recent years. According to Heinke and Jaksic (2003, p. 1.36), the following physical aspects are crucial for the determination of the amplitudes of pressure fluctuations induced by a cavitating propeller flow: the thickness of cavitation and the time change of the cavity volume. In Chapter 5 it was shown that the implemented sheet cavitation model is able to reliably predict both of these aspects. The objective of the present study is to investigate the impact of sheet cavitation on the magnitude of the pressure pulses. For this purpose the flow around the propeller P1356 is calculated with different inflow conditions. In the first section, Chapter 6.1, the propeller is simulated in a uniform inflow and the pressure pulses are evaluated on a flat plate located above the propeller. In the second section, Chapter 6.2, the propeller is simulated in a non-uniform inflow and the pressure pulses are monitored on a part of the ship hull located above the propeller. For both simulations the results computed by the numerical method *pan*MARE are validated with the measured data from experiments.

## 6.1 Pressure pulses induced by P1356 propeller in uniform inflow

In this section the propeller P1356 is simulated in a homogeneous inflow and the pressure pulses induced by the propeller flow are monitored on five points of a flat plate located above the propeller (s. Figure 6.1). The plate is discretised in $1000$ panels. The vertical distance of the plate to the propeller centre is $0.182$ m. The horizontal distance of the monitoring points to the propeller centre is $\pm 0.05$ m in x and y direction, respectively (s. Figure 6.1 and Table 6.1). The input data used in the simulations is summarised in Table

6.2. The flow is simulated in model scale for four different propeller loading conditions and cavitation numbers. The trailing wake of the propeller is not aligned in the simulations since the influence of wake deformation on the sheet cavitation shapes and pressure fluctuations is negligible for a propeller in homogeneous inflow.

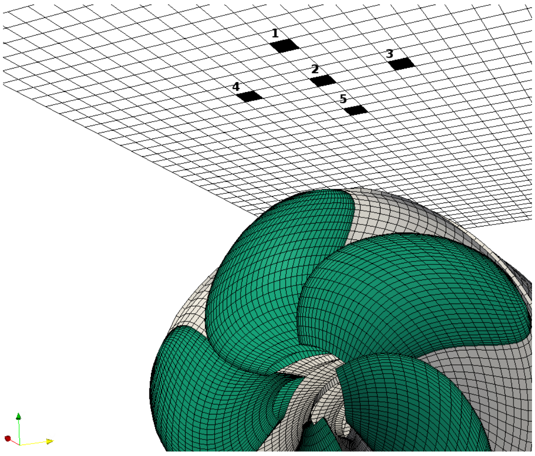

Figure 6.1: Location of the monitoring points on the plate

| Nr. | x [m] | y [m] | z [m] |
|---|---|---|---|
| 1 | 0.05 | 0 | 0.182 |
| 2 | 0.0 | 0 | 0.182 |
| 3 | 0.0 | 0.05 | 0.182 |
| 4 | 0.0 | -0.05 | 0.182 |
| 5 | -0.05 | 0 | 0.182 |

Table 6.1: Coordinates of the monitoring points on the plate

| Characteristics | Notation | Case 1 | Case 2 | Case 3 | Case 4 | Unit |
|---|---|---|---|---|---|---|
| Rotation speed | $n_{model}$ | 27.976 | 27.996 | 28.001 | 28.0 | $1/s$ |
| Advance coefficient | $J$ | 0.7115 | 0.6065 | 0.5998 | 0.5999 | - |
| Cavitation number | $\sigma_{n0.8R}$ | 1.822 | 1.821 | 1.601 | 2.0 | - |

Table 6.2: Input data for the pressure pulses calculations with P1356 propeller in uniform inflow

Figure 6.2 presents the sheet cavity shapes calculated by *pan*MARE for all simulated cases. For simulation case 1 there is a very small cavity extent. For the third simulation case *pan*MARE detects the greatest cavity extent. The cavity shapes of the second and fourth simulation case are almost equal and less than the shape of the third simulation case. The pressure values are evaluated on the monitoring points on the plate for one propeller rotation and then analysed by the Fourier transformation. The Fourier transforms of the calculated and measured pressure pulses are illustrated in Figures 6.3-6.6. The measured data is taken from the report of Richter and Heinke (2006). The bars in the graphs

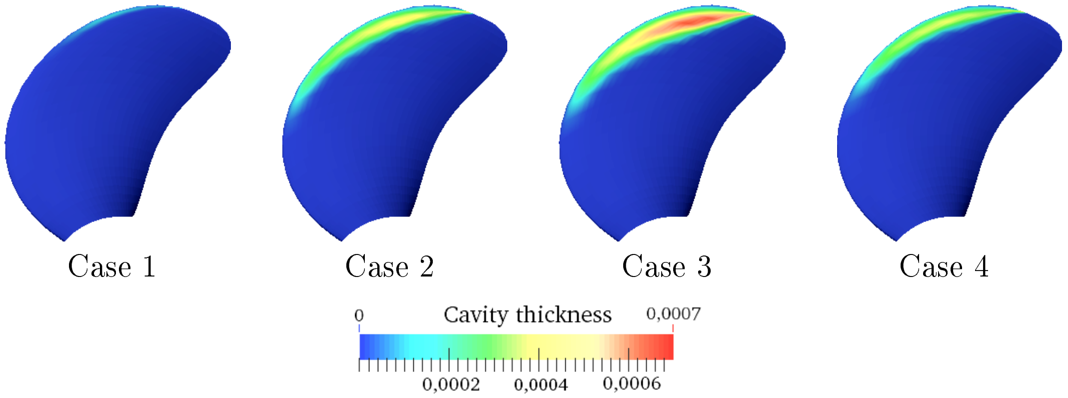

Figure 6.2: Sheet cavitation shapes calculated for different loading and cavitation conditions

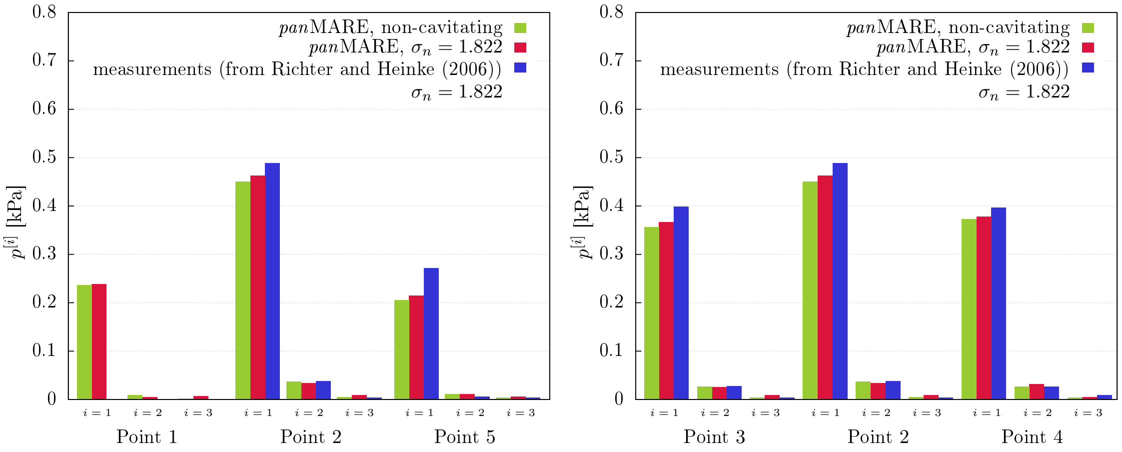

Figure 6.3: Pressure pulses calculated for simulation case 1

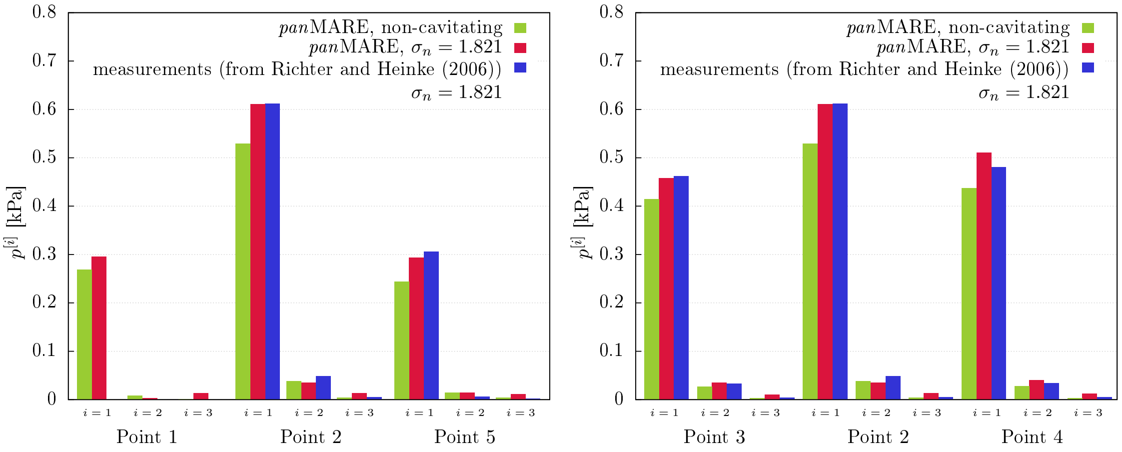

Figure 6.4: Pressure pulses calculated for simulation case 2

represent the first, second and third harmonics of the pressure pulses for the monitoring points 1 to 5. All values are presented in model scale. The amplitudes of the second and

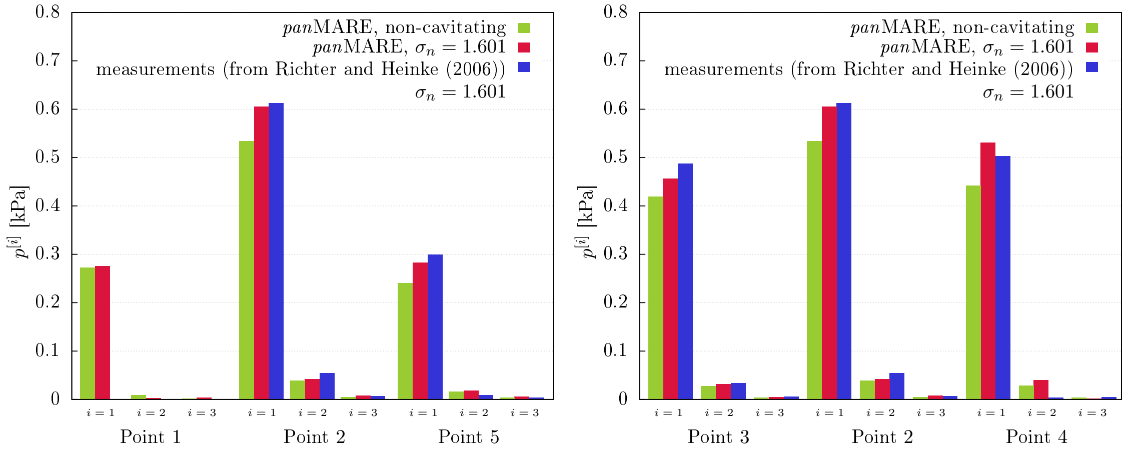

Figure 6.5: Pressure pulses calculated for simulation case 3

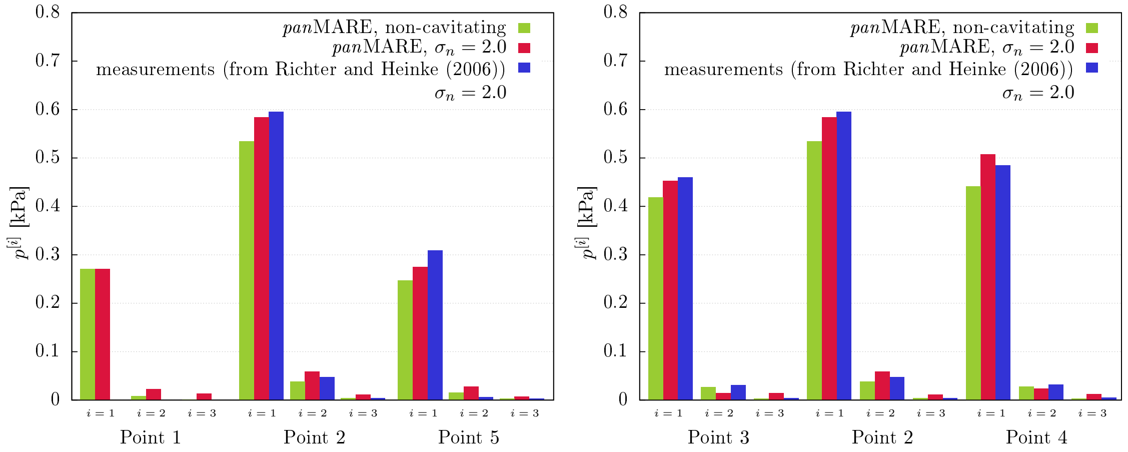

Figure 6.6: Pressure pulses calculated for for simulation case 4

third harmonics are very low compared to that of the first harmonic. The maximal amplitudes of the first order are located above the propeller (point 2), at the star board (point 4) and at the back board (point 3) for all simulated cases. For simulation case 1 the maximal amplitudes of the pressure pulses achieve $0.49$kPa (s. Figure 6.3). For the third simulation case the maximal amplitude is $0.61$kPa (s. Figure 6.5). The amplitudes of the harmonics calculated in the second and fourth simulation case do not differ significantly from those of the simulation case 3 (s. Figures 6.4 and 6.6).

All simulated cases show a rather small cavity extent, which has a minor influence on the magnitude of the pressure pulses. The results of the simulations are in good agreement with the results obtained in measurements for the monitoring points 2, 3, 4 and 5, for all orders (1, 2 and 3). For monitoring point 1 no measured data was available. This study shows that *pan*MARE delivers reliable results for the pressure pulses induced by a cavitating propeller flow in homogeneous inflow.

## 6.2 Pressure pulses induced by P1356 propeller in non-uniform inflow on a ship hull

In this section the pressure pulses induced by the propeller P1356 on a part of the ship hull located above the propeller are analysed. The propeller flow is simulated subject to a non-uniform inflow. For this two different ship wake fields are used, namely the model wake field DM40M and the full scale wake field DM40S (s. Figure 5.27). The different wake fields are used in order to detect their influence on the magnitude of the pressure pulses. The surface of the ship hull is discretised by 990 equilateral panels and the pressure pulses are evaluated on five monitoring points on the hull (s. Figure 6.7). The pressure values are observed on the panels of the hull that are arranged at the nearest position to the coordinates of the monitoring points in the experiments (s. Table 6.3). For points 1, 2 and 5 no panels are located directly on the centre line. Instead, the average value of the two nearest panels is calculated (s. Figure 6.7).

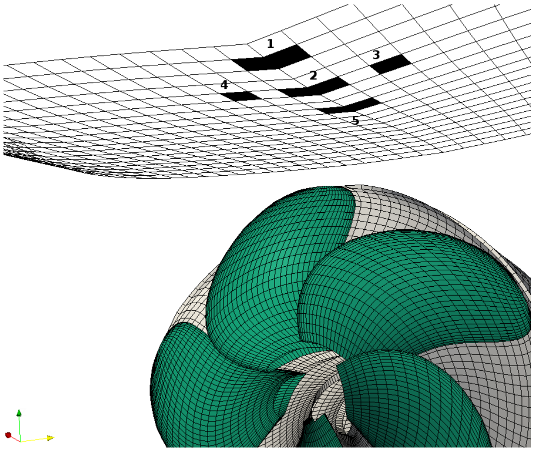

Figure 6.7: Location of the monitoring points on the ship hull

| Nr. | x [m] | y [m] | z [m] |
|---|---|---|---|
| 1 | 0.055 | 0 | 0.177 |
| 2 | 0.0 | 0 | 0.182 |
| 3 | 0.0 | 0.051 | 0.187 |
| 4 | 0.0 | -0.051 | 0.187 |
| 5 | -0.055 | 0 | 0.191 |

Table 6.3: Coordinates of the monitoring points on the ship hull

The input data used in the simulations is summarised in Table 6.4. The flow is simulated in model scale under non-cavitating and cavitating conditions. For both wake fields the same rotational speed and cavitation numbers are used. The ship speed $\mathbf{V}_{ship}$ is adjusted in the simulations in such a way that the mean thrust coefficient $\bar{k}_t$ measured in experiments for the non-cavitating case is obtained. The wake is aligned according to the axial wake alignment model since the wake deformation of a propeller subject to a non-uniform inflow has a significant influence on the magnitude of the pressure fluctuations.

| **Characteristics** | **Notation** | **DM40M** | **DM40S** | **Unit** |
|---|---|---|---|---|
| Rotation speed | $n_{model}$ | 30 | 30 | $1/s$ |
| Thrust coefficient | $\bar{k}_t$ | 0.170 | 0.168 | - |
| Cavitation number | $\sigma_{n0.8R}$ | 1.783/1.486/1.382 | 1.783/1.486/1.382 | - |

Table 6.4: Input data for the pressure pulses calculations with P1356 propeller in inhomogeneous inflow

Firstly, the results of the non-cavitating propeller flow are presented. Figures 6.8 and 6.9 show the first, second and third harmonics obtained by the Fourier analysis of the pressure pulses for the monitoring points 1 to 5. The $i$th harmonic of the pressure pulses is given in the unit kPa and is denoted by $p^{[i]}$. The bars in the graphs illustrate the measured data taken from the report (s. Heinke and Jaksic, 2003) and the results calculated by the numerical method *pan*MARE with the model and full scale wake field.

All values on the bar diagrams are presented in model scale. No significant influence of the different wake fields can be identified. Independent of the wake field, the amplitudes of the second and third harmonics are very low. The amplitude of the first harmonic reaches its maximal value in front and above the propeller centre (points 1 and 2) and achieve approximately 0.74kPa with the wake field DM40M and 0.68kPa with the wake field DM40S. The calculated results are in good agreement with the measured values for all orders. Only the amplitude obtained with the wake field DM40M for the fifth point is considerably underestimated by *pan*MARE compared to the measurements.

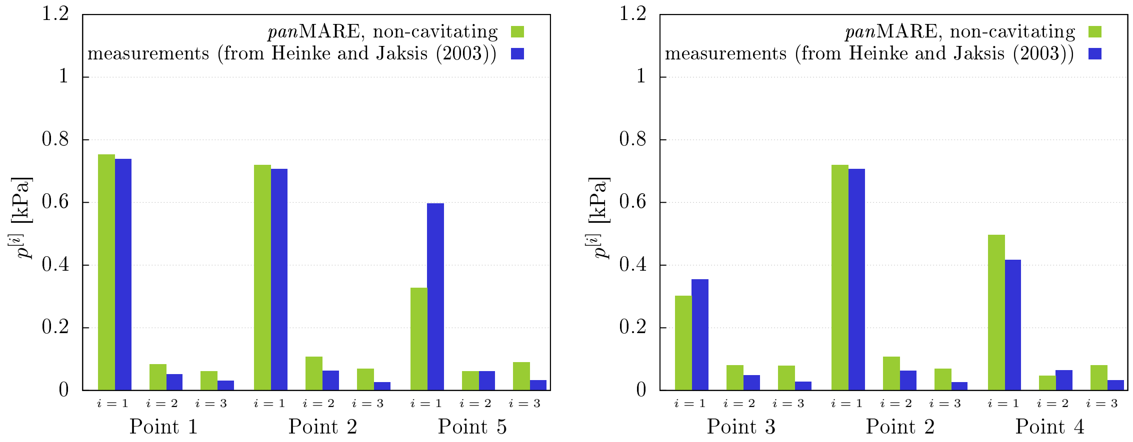

Figure 6.8: Pressure pulses calculated for the non-cavitating case with ship wake field DM40M

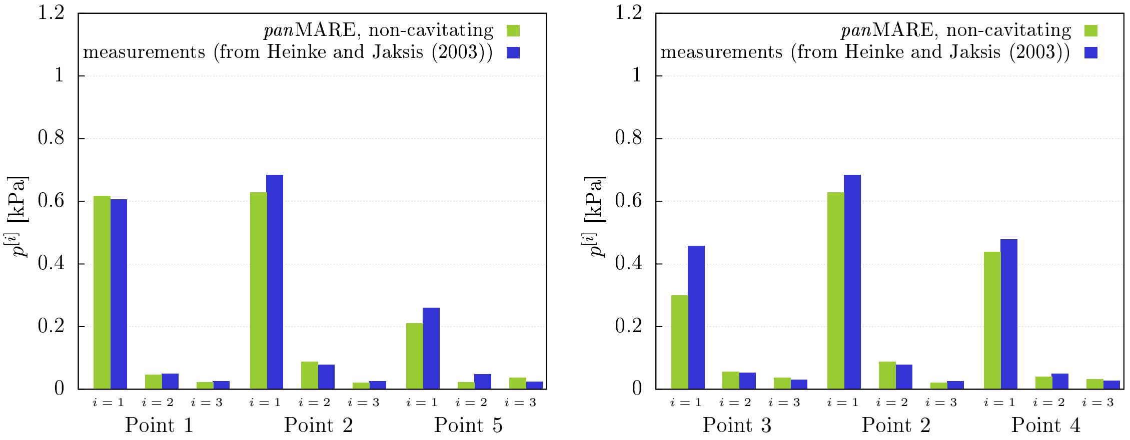

Figure 6.9: Pressure pulses calculated for the non-cavitating case with ship wake field DM40S

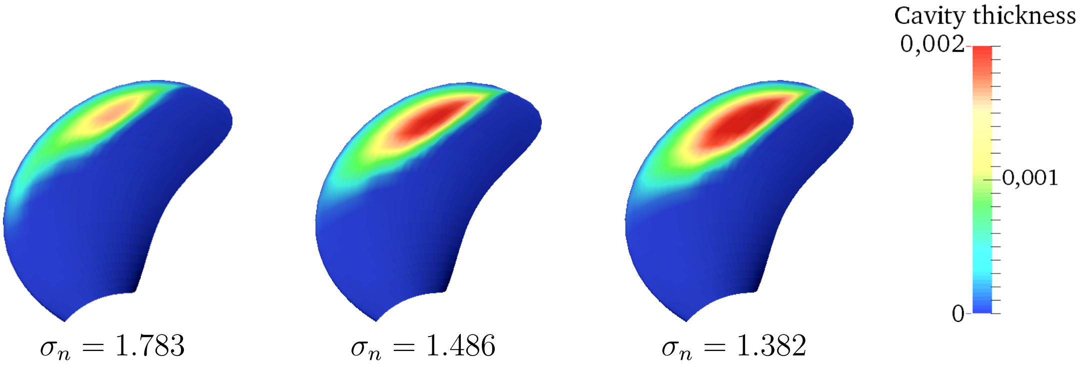

$\sigma_n = 1.783$ $\sigma_n = 1.486$ $\sigma_n = 1.382$

Figure 6.10: Sheet cavity extents at the angular position $\theta = 0°$ calculated by *pan*MARE with different cavitation numbers with the ship wake field DM40M

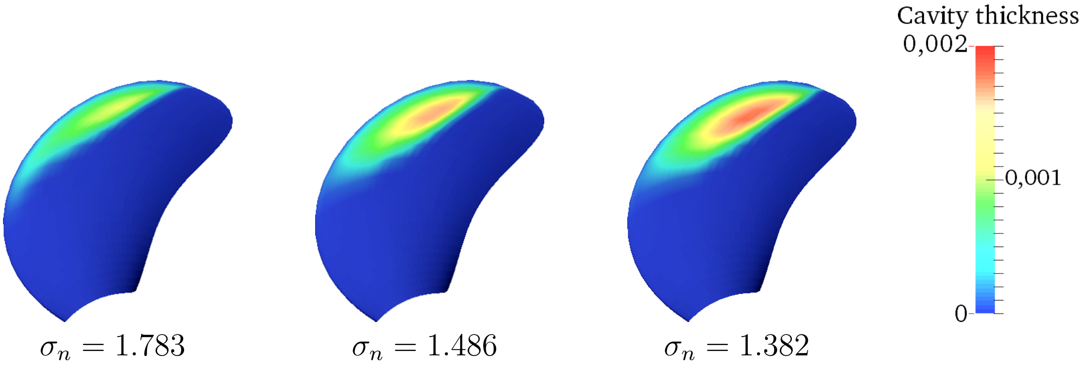

$\sigma_n = 1.783$ $\sigma_n = 1.486$ $\sigma_n = 1.382$

Figure 6.11: Sheet cavity extents at the angular position $\theta = 0°$ calculated by *pan*MARE with different cavitation numbers with the ship wake field DM40S

Now the results of the cavitating propeller flow with three different cavitation numbers are demonstrated. Figures 6.10 and 6.11 show the sheet cavity shapes on the key blade of the propeller calculated with the model and full scale wake field, respectively. The

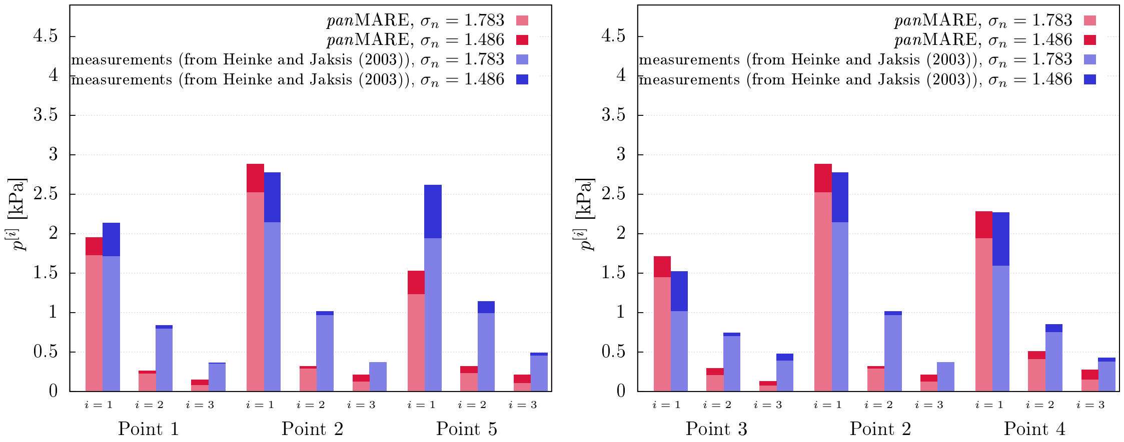

Figure 6.12: Pressure pulses calculated for the cavitation numbers $\sigma_{n0.8R} = 1.486$ and $\sigma_{n0.8R} = 1.783$ with the ship wake field DM40M

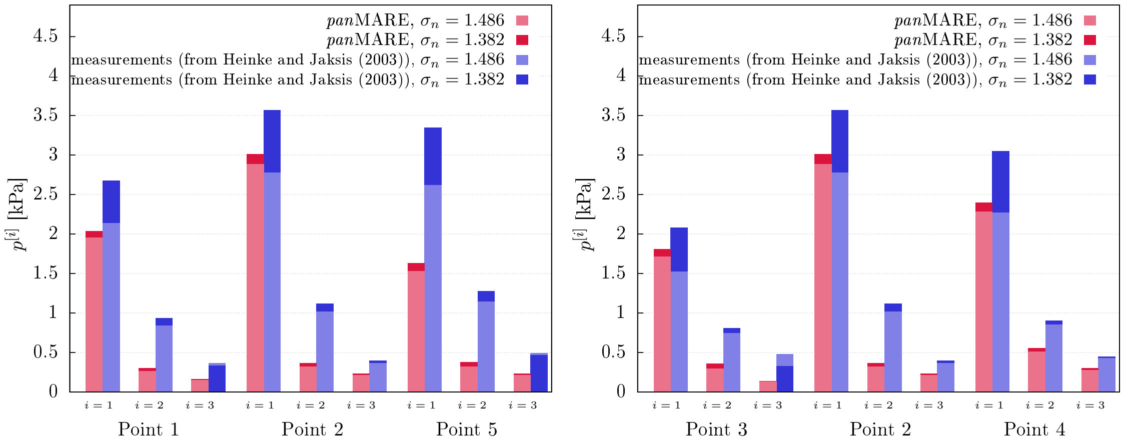

Figure 6.13: Pressure pulses calculated for the cavitation numbers $\sigma_{n0.8R} = 1.382$ and $\sigma_{n0.8R} = 1.486$ with the ship wake field DM40M

key blade is illustrated at the angular position of zero degree. It can be observed that the cavitation number has a significant impact on the sheet cavity extent and thickness on the blade. With the wake field DM40M a more extensive cavity thickness and length can be observed than with the wake field DM40S.

Figures 6.12 and 6.13 illustrate the first, second and third harmonics obtained by the Fourier analysis of the pressure pulses for the monitoring points 1 to 5 with the wake field DM40M. The values are presented in model scale and show the results for all three cavitation numbers. The pressure pulses rise significantly with the occurrence of sheet cavitation. For the cavitation number $\sigma_n = 1.382$ the first harmonic is 4.2 times higher than that obtained in the non-cavitating case. By reducing the cavitation number (which is equivalent to an increase of the cavity thickness and volume) the first harmonic increases.

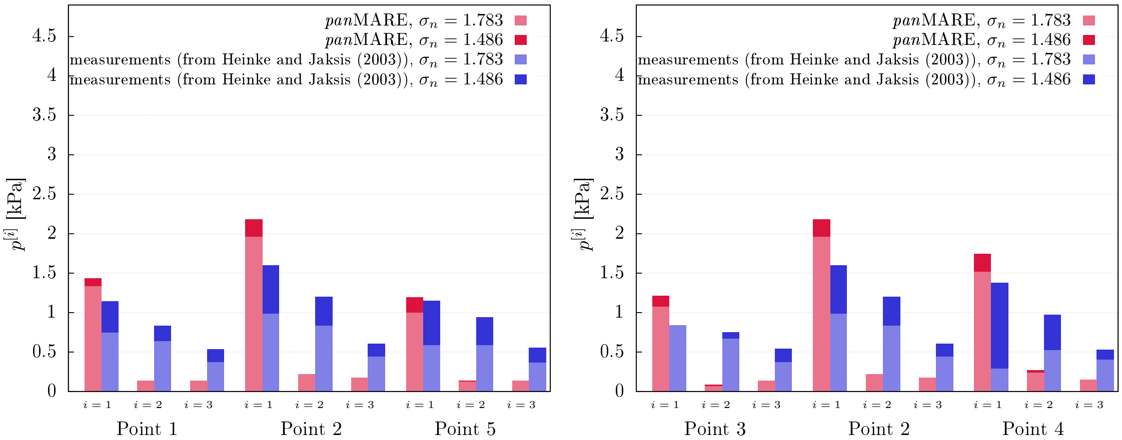

Figure 6.14: Pressure pulses calculated for the cavitation numbers $\sigma_{n0.8R} = 1.486$ and $\sigma_{n0.8R} = 1.783$ with the ship wake field DM40S

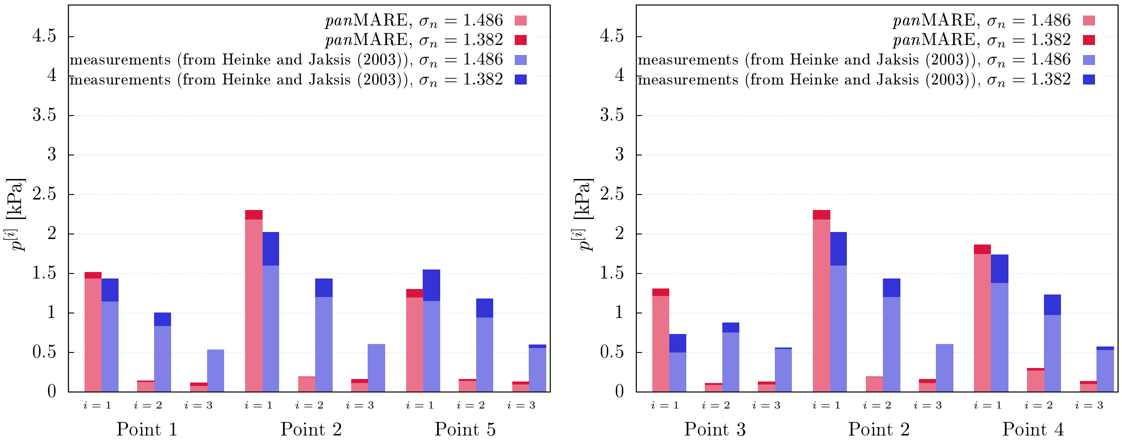

Figure 6.15: Pressure pulses calculated for the cavitation numbers $\sigma_{n0.8R} = 1.382$ and $\sigma_{n0.8R} = 1.486$ with the ship wake field DM40S

The measurements with the model wake field DM40M show a very high first harmonic. The maximal amplitudes occur above the propeller (point 2), at the star board side (point 4) and behind the propeller (point 5). The measured values show that cavitation also has a considerable influence on the second and third harmonics. In contrast to the first harmonics, a decrease of the cavitation number does not significantly increase the second and third harmonics. The simulation results coincide very well with the measured values for the first harmonic for the points 1-4. As for the non-cavitating case, the first harmonic calculated for the fifth point is underestimated. The influence of the cavitation number on the magnitude of the pressure pulses is well reproduced by the simulation tool. However, the calculated second and third harmonics are underestimated compared to the measurements. This can be explained by the fact that the tangential and radial velocity components of the wake fields were neglected in the simulations. Additionally, tip vortex cavitation is said to be relevant for the determination of the pressure pulses and is observed in experiments with both wake fields (s. Heinke and Jaksic, 2003, p. 1.36). In the simulations tip vortex cavitation was not calculated.

Figures 6.14 and 6.15 illustrate the calculated and measured first, second and third harmonics of the pressure fluctuations obtained with the full scale wake field DM40S. The measurements show very high second and third harmonics, which result from the strong unsteady cavitation patterns. According to Heinke and Jaksic (2003, p. 1.33), sheet cavitation is more extensive with the wake field DM40M but it fluctuates stronger with the wake field DM40S, which leads to higher second and third harmonics. The higher fluctuation of cavitation is a consequence of the tangential and radial velocity components of the wake field DM40S (s. Heinke and Jaksic, 2003, p. 1.33). In the simulations these velocity components were neglected. Thus, the second and third harmonics are underestimated by *pan*MARE. Nevertheless, the qualitative tendencies of the second and third harmonics are captured correctly. In presence of sheet cavitation the magnitude of the pressure fluctuations increases. For monitoring point 2 and cavitation numbers $\sigma_n = 1.783$ and $\sigma_n = 1.486$ the calculated first harmonics are overestimated. For the remaining points the agreement of the calculated and measured first harmonics is satisfying. The magnitude of the first harmonic with the wake field DM40M is higher than that obtained with the wake field DM40S. This observation applies to measured and calculated data. The higher amplitudes of the first order can be explained by the wider wake peak of the model wake field, which results in a higher sheet cavity thickness (s. Figures 6.10 and 6.11).

This simulation study indicates that the influence of the non-uniform inflow to the propeller is low when no cavitation occurs on the blades. When cavitation occurs, the influence of the non-uniform inflow increases. The pulsation of cavitation directly correlates with the heterogeneity of the wake field, which leads to higher pressure pulses. The first harmonic of the pressure pulses can be reproduced by the underlying numerical method with a satisfying level of accuracy. The second and third harmonics of the pressure pulses differ quantitatively from the experimental data, even though the qualitative tendencies are captured correctly. In future studies the effect of the tangential and radial velocity components of the wake field on the sheet cavitation patterns and on the magnitude of the second and higher harmonics should be examined. Additionally, the influence of tip vortex cavitation should be included in the analysis.

# Chapter 7

# Propeller-induced pressures and velocities on the harbour bed

In order to meet the increasing requirements on container traffic, bigger container ships with higher engine power are built nowadays. Container ships can be featured with one or more stern propellers and additionally, for manoeuvring purposes, with one or more bow thrusters. During the manoeuvring procedure the propulsion and manoeuvring devices operate close to the harbour bed and quay wall and generate water jets that can affect the harbour structures significantly. A rotating propeller, for instance, generates a slipstream that can lead to the scouring of the bed material (s. Figure 7.1). The present simulation study aims to calculate induced pressures and velocities on the harbour bed caused by a propeller flow during the manoeuvring process of a ship in the harbour basin. Induced velocities that exceed a critical value will put the bed material in motion (Schmidt, 1999, p. 27f.). The critical value of the induced velocities depends on several characteristics of the soil, such as grain size, grain shape and grain density (Schmidt, 1999, p. 27). Fluctuating pressure on the harbour bed can induce variations of the pore pressure within the marine sediments and lead to a deformation of the seabed skeleton (cf. Prescott, 2008, p. 113f.).

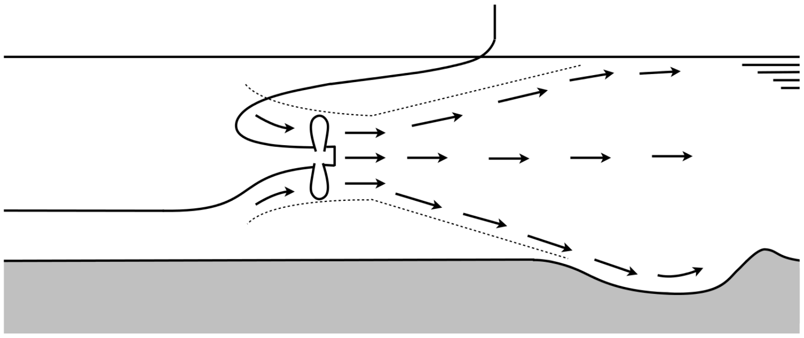

Figure 7.1: Propeller induced scour of the harbour bed (taken from Ulrich (2013, p. 5))

Due to the increasing dimensions of today's container ships, the loads on the harbour bed increase and the demand for fast and accurate numerical methods for their prediction is growing. To date there is only a limited number of numerical studies investigating this kind of application, providing enormous potential for further research. The most common approaches used to predict propeller flow induced velocities are based on the axial momentum theory. These approaches were introduced in the 1970s by Römisch (1975) and Blaauw and van de Kaa (1978) and are used in current practical guidelines and recommendations for coastal and harbour constructions (s. Bundesanstalt für Wasserbau (BAW), 2011). The axial momentum theory neglects the tangential and radial components of the velocity, only relying on the axial component. The propeller is idealised by an actuator disc and analytical expressions are formulated for the estimation of the induced velocities in the slipstream of the propeller and on the harbour bed. Since the slipstream of a propeller is a highly turbulent phenomenon, it is a very complex task to describe its influence on the harbour bed by analytical formulas. Theoretical approaches do not include the particular geometrical characteristics of a propeller, neglect the radial and tangential components of the velocity and are not able to corporate cavitation effects. But then again, relying on sophisticated numerical methods in order to investigate complex geometries and flows can be very time- and cost-consuming. The aim of the present chapter is to apply the panel method *pan*MARE to calculate propeller-induced loads in the harbour basin. On the one hand, the panel method is fast compared to model tests and very sophisticated numerical methods, such as the Smoothed Particle Hydrodynamics (SPH) method. On the other hand, it allows for a more detailed analysis of the propeller-induced loads on the harbour bed than the approaches based on axial momentum theory.

## 7.1 Simulation set-up

The focus of the present investigation lies in the numerical calculation of pressures and velocities induced by a stern propeller flow on the harbour bed. The simulations are performed by *pan*MARE in full scale with the well-investigated propeller P1356 (cf. Figure 5.18 and Table 5.7). The diameter of the propeller measures 7.9m. The geometrical set-up of the underlying application case is illustrated in Figure 7.2. The simulations are performed with a 12m draught (extreme loadcase). The water depth in the harbour basin measures $h_\text{w} = 13.5$m and the distance from the propeller centre line to the harbour bottom is $h_\text{d} = 5.6$m. Free water surface, aft ship body and rudder are not included in the simulations. The harbour bed is modelled as a flat plate with the grid resolution $60 \times 45$. On the plate the induced velocities and pressures are calculated by the following equations (cf. Chapter 3.2):

$$\begin{aligned} \mathbf{v}(x_j,t^n) &= \textstyle\sum_{i=1}^{N^{prop}} \mu_i^n A_{i,j} - \sum_{i=1}^{N^{prop}} \sigma_i^n B_{i,j} + \sum_{i=1}^{N_W^{prop}} \mu_{W,i}^n A_{i,j} - \sum_{i=1}^{N^{bed}} \sigma_i^n B_{i,j}, \\ p(x_j,t^n) &= p_\infty + \tfrac{\rho}{2}\Big(|\mathbf{V}_{\infty,j}(x_j,t^n)|^2 - |\mathbf{V}(x_j,t^n)|^2\Big) - \rho\tfrac{\partial\phi_j}{\partial t}(x_j,t^n) + \rho g(z_\infty - z_j), \end{aligned}$$

for all monitoring points, denoted by $x_j$, $j = 1, \ldots, N$, and time steps $t^n$, $n \in \mathbf{N}$.

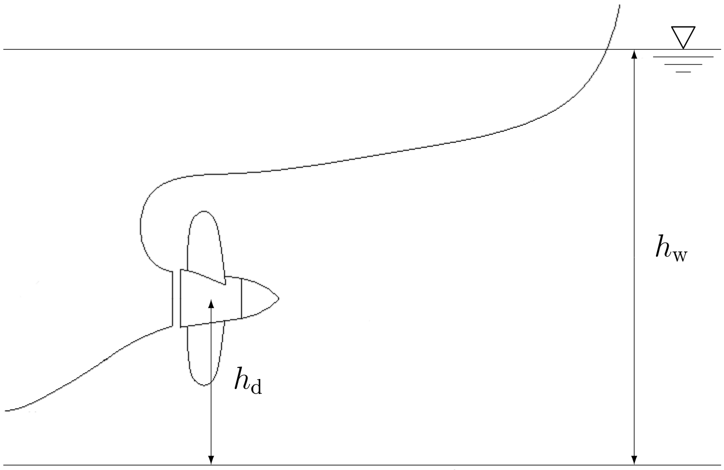

Figure 7.2: Geometrical set-up and monitoring points

The input parameters of the simulated test cases are summarised in Table 7.1. Altogether two cases are simulated: in case 1 no cavitation is considered and in case 2 the propeller flow is simulated by use of the sheet cavitation model. The cavitation number in the simulation case 2 is $\sigma_n = 1.24$. The rotation number and ship speed are $n = 2.135\,{}^{1}\!/_{s}$ and $V_{ship} = 1.686\,{}^{m}\!/_{s}$ in both test cases.

| **Characteristics** | **Notation** | **Case 1** | **Case 2** | **Unit** |
|---|---|---|---|---|
| Rotation speed | $n$ | 2.135 | 2.135 | $1/s$ |
| Ship speed | $V_{ship}$ | 1.686 | 1.686 | $m/s$ |
| Distance to the river bed | $z/D$ | 0.71 | 0.71 | - |
| Cavitation number | $\sigma_n$ | - | 1.24 | - |

Table 7.1: Simulation cases

When entering and leaving the port, the ship is manoeuvring with a low ship speed. The modelling of the slipstream of a propeller for such an operation condition (low advance coefficient) is a complex task for a panel method. For low advance coefficients the induced velocity gradients are very high and the alignment of the trailing wake causes problems. In order to simulate the present application case by means of the panel method *pan*MARE, the wake alignment model is modified. The modified wake model includes the influence of turbulent mixing with the surrounding fluid by approximating the increase of the slipstream radius according to the following formula (Brix, 1993, p. 84f.):

$$R_x = R + \Delta R(x), \tag{7.1}$$

where $x$ is the distance from the propeller centre and the additive term $\Delta R(x)$ is defined as follows (Brix, 1993, p. 85):

$$\Delta R(x) = 0.15x \frac{V_x - V_\infty}{V_x + V_\infty}. \tag{7.2}$$

This modified wake alignment model is applied by *pan*MARE in steady calculations to initialise the shape of the trailing wake. The wake is not deformed in unsteady computations.

## 7.2 Simulation results

This section presents the calculated results for pressures and induced velocities on the harbour bed. The velocity values are evaluated at three stripes of the plate with the coordinates $y_1 = y/D = -0.21$, $y_2 = y/D = 0$, $y_3 = y/D = 0.21$ and $x/D \in [-1.7 : 0.22]$ as shown in Figure 7.3a. The pressure values are evaluated at five points beneath the propeller as illustrated in Figure 7.3b. Their coordinates are summarised in Table 7.2.

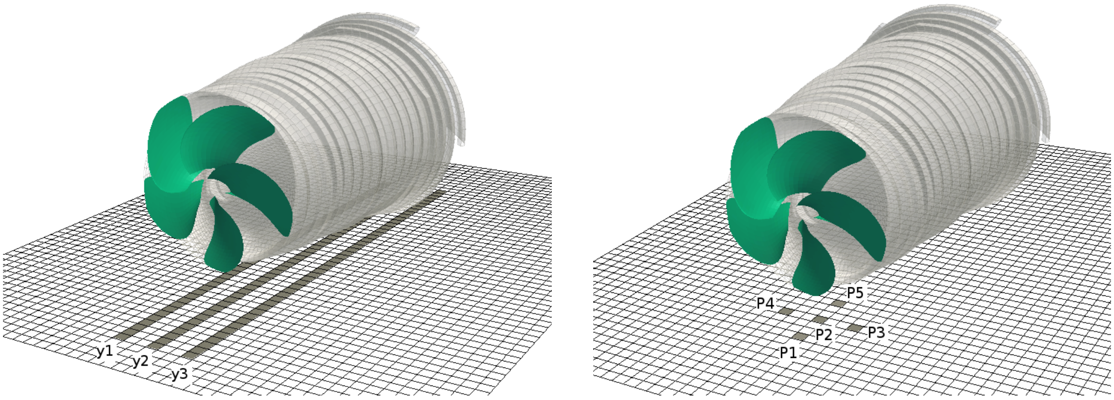

(a) Points for velocity evaluation (b) Points for pressure evaluation

Figure 7.3: Monitoring points on the harbour bed

| | $P_1$ | $P_2$ | $P_3$ | $P_4$ | $P_5$ |
|---|---|---|---|---|---|
| $x/D$ | 0.22 | 0 | 0 | 0 | -0.21 |
| $y/D$ | 0 | 0 | 0.21 | -0.21 | 0 |
| $z/D$ | 0.71 | 0.71 | 0.71 | 0.71 | 0.71 |

Table 7.2: Coordinates of the monitoring points on the plate

Figure 7.4 shows the magnitude of the induced velocity after one propeller rotation. The simulations show that the propeller flow leads to induced velocities on the harbour bottom that increase while the propeller slipstream expands in the radial direction. For a more detailed analysis of the results the maximal value of the velocity magnitude is plotted in

Figures 7.5a-7.5d as a function of $x/D$. The values are plotted for the cavitating and non-cavitating case. The magnitude of the induced velocity is at highest for the stripe $y_2$ that is located in the propeller centre plane. The velocity magnitude increases while the slipstream approaches the harbour bottom and reaches the maximum value $|v_{bed}^{max}| = 5.92\,{}^{m}/_{s}$ at $x = -1.7D$ (s. Figure 7.5). Sheet cavitation seems to only have a small influence on the magnitude of the induced velocities on the harbour bed. The amount of sheet cavitation computed in the simulation is shown in Figure 7.6.

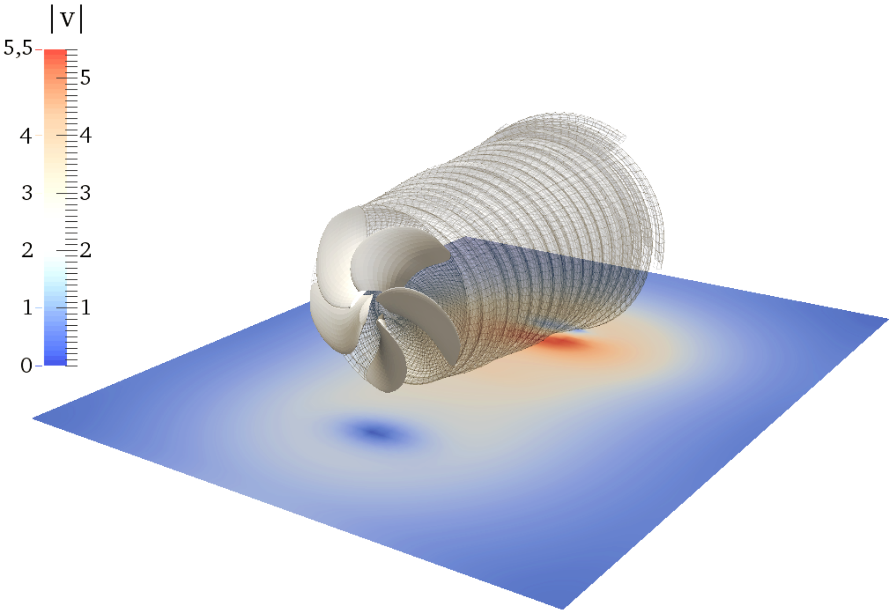

Figure 7.4: Calculated magnitude of the induced velocity on the harbour bottom after one propeller rotation

Figures 7.7a-7.7b illustrate the amplitudes of the first, second and third harmonics determined by the Fourier transformation of the pressure fluctuations induced by the propeller on the monitoring points 1 to 5. The amplitude of the first harmonic is at highest underneath the propeller centre at point $P_2$. In presence of sheet cavitation the amplitude of the pressure pulses increases noticeably at points $P_2$, $P_3$ and $P_5$ and achieves a maximal value of $6.3\,kPa$ at Point $P_2$. At the monitoring points $P_1$ and $P_4$ the first order amplitudes are slightly increased by sheet cavitation. The amplitudes of the second and third harmonics are very low compared to the amplitude of the first harmonic and sheet cavitation seems to have a small influence on their magnitude.

Supplementary the induced axial velocity on the harbour bed is calculated using the empirical approach based on the axial momentum theory as proposed by the Bundesanstalt für Wasserbau (BAW) (2011, p.89f.). The Bundesanstalt für Wasserbau (BAW) (2011) derived analytical expressions for the estimation of the maximal value of the induced axial velocity for ducted and unducted propellers and different rudder arrangements. In the present simulations the propeller is unducted and no rudder is arranged. For the case

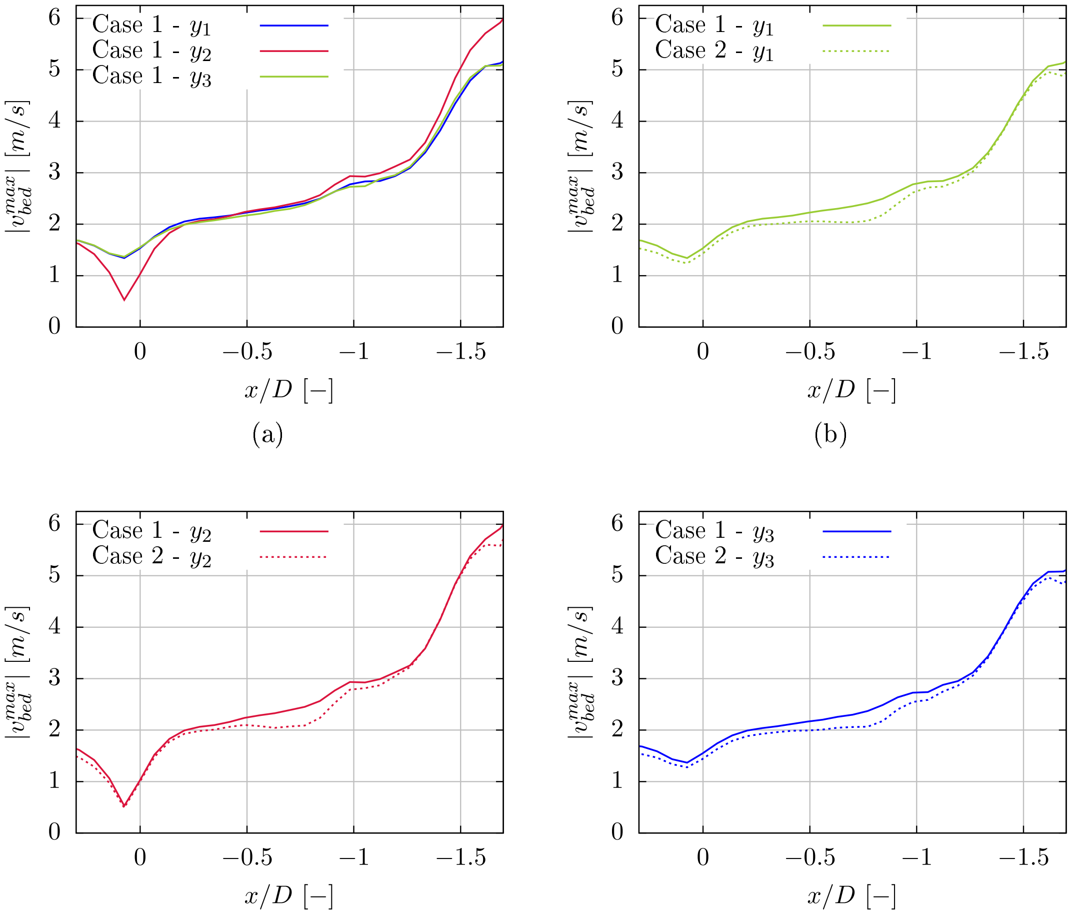

(a) (b) (c) (d)

Figure 7.5: Maximal induced velocity magnitude on the harbour bottom

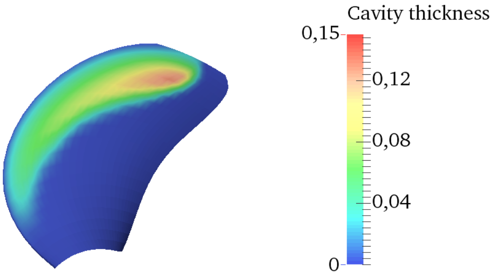

Figure 7.6: Sheet cavity thickness on the key blade for the simulation case 2 with $\sigma_n = 1.24$

$V_{ship} \neq 0$ the formula for the maximal induced velocity on the harbour bed reads as follows (s. Bundesanstalt für Wasserbau (BAW), 2011, p. 90):

$$v_{x,bed}^{max} = v_0 E\left(\frac{D}{h_d}\right)\left(1 - \frac{V_{ship}}{nD}\right), \tag{7.3}$$

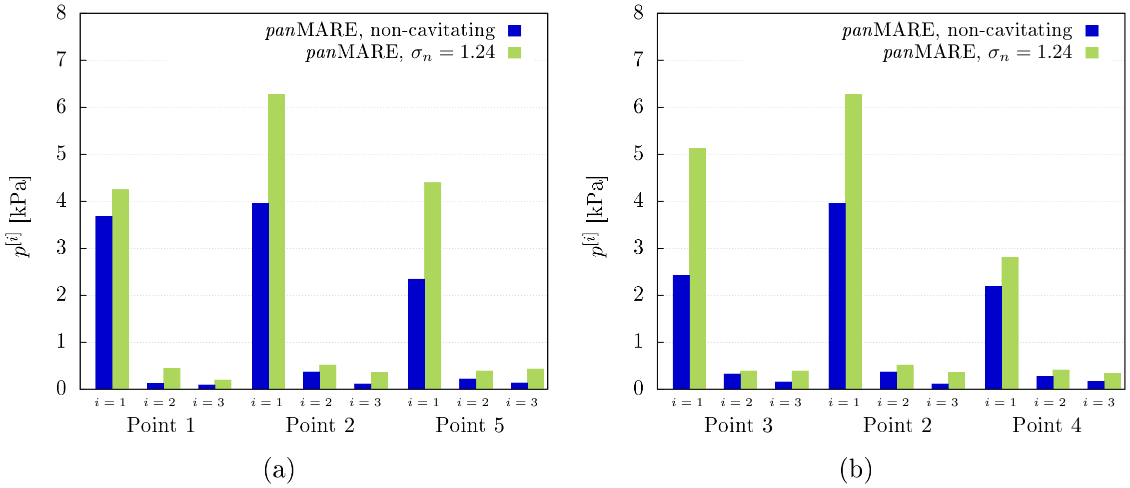

(a) (b)

Figure 7.7: Propeller-induced pressure pulses on five monitoring points on the harbour bottom

where $v_0$ is the maximal value of the initial induced velocity in the propeller slipstream for $V_{ship} = 0$ and $E$ is a factor that includes a characterisation of the stern form and rudder arrangement. For the underlying case the factor $E$ is equal to $0.42$ ($E = 0.71$ for a slender stern form with a central rudder and $E = 0.42$ for a slender stern form without central rudder). The maximum of the initial induced velocity in the slipstream is defined by the Bundesanstalt für Wasserbau (BAW) (s. 2011, p. 76) as follows:

$$v_0 = 1.6 f_N n D \sqrt{k_{t,0}}, \tag{7.4}$$

where $f_N = 0.75$ is a factor, $n$ the nominal rotational speed and $k_{t,0}$ the thrust coefficient for the ship speed $V_{ship} = 0$. The nominal rotational speed of the P1356 propeller is $n = 101.4\,rmp$ and the thrust coefficient is $k_{t,0} = 0.5178$ (s. Günther, 2002, p. 2.5). By applying the formulas (7.3) and (7.4), one obtains: $v_{x,bed}^{max} = 5.48\,{}^{m}\!/\!{}_{s}$. For comparison, the maximal induced axial velocity obtained in the simulations measures: $v_{x,bed}^{max} = 5.92\,{}^{m}\!/\!{}_{s}$. The additional value of the simulations is to be found in the detailed description of the spatial distribution of the induced loads on the harbour bed. Aside from that, all three velocity components, particular geometrical characteristics of a propeller and the influence of sheet cavitation can be included. Although the results presented here have demonstrated the great abilities of the simulation tool, there are still some limitations of the implemented method. First, the propeller slipstream is modelled by a simplified procedure such that the highly unsteady character of the wake deformation is excluded. Second, the soil deformation due to the propeller-induced loads is not simulated, i.e. the intensity of the soil erosion and development of scours in the soil are not predicted. On account of this, there is still room for further development of the numerical method.

# Chapter 8

# Conclusions and perspectives

In the present work a three-dimensional inviscid boundary element method for the simulation of partial sheet cavitation on marine propellers was introduced. In the first step, the approach used to modelling propeller flows and the applied numerical method were presented. The modelling approach is based on potential flow theory with the assumptions that the fluid is incompressible and the flow is irrotational and non-viscous. For a potential flow the fundamental fluid dynamic equations for mass and momentum simplify to the Laplace and Bernoulli equation. The solution of the Laplace equation for the velocity potential was obtained by distributing dipoles and sources on the problem boundaries and by applying suitable boundary conditions. The consequent boundary value problem was then reduced to a set of algebraic equations by using the three-dimensional low-order panel method. The panel method is based on the idea that the body and wake surfaces of a lifting body are discretised into small two-dimensional elements, called panels. In the present work quadrilateral elements were used as panels and the strengths of the dipoles and sources, describing the lifting and displacement effect of each panel, were assumed to have a constant distribution. The solution of the implemented panel method consisted of finding the strengths of the dipoles and sources for each panel of the body and wake surface. In the second step, the mathematical model describing steady and unsteady partial sheet cavitation was derived and implemented in the panel method. Sheet cavitation occurs in the form of an attached vapour sheet on the solid body surface and is very common on marine propulsion organs. Its numerical prediction is important for the optimisation of propeller geometries and for the prediction of propeller-induced hydrodynamic forces. Partial sheet cavitation is a type of cavitation that does not exceed the trailing edge of the blade profiles and can be located on the pressure and/or on the suction side of the propeller blades. In the present work a model was derived that allows for sheet cavitation occurrence on both sides of the blades. The physics of sheet cavitation were described by the dynamic and kinematic boundary conditions. The dynamic boundary condition defines the velocity potential on the cavity surface, while the kinematic boundary condition determines the thickness of the cavity sheet. The governing equations of the cavitating propeller flow were formulated for the steady and unsteady case and the treatment of the unsteady terms in the boundary conditions was outlined. The boundary value problem was formulated using the potential-based integral equations and the boundary conditions were implemented by the partially non-linear approach without grid re-meshing. The partially non-linear approach is characterised in a way that the boundary conditions are not applied directly on the cavity surface but on an auxiliary surface underneath the cavity sheet. Since the extent of sheet cavitation is not known a priori, its determination is a part of the solution process. For the prediction of the unknown cavity extent an iterative procedure for steady and unsteady flow calculations was derived.

In the third and last step, the accuracy and robustness of the developed numerical method were proved in various examples. In the first example study the method was verified and validated for the steady flow problem. For this purpose, the flow around two different hydrofoils and a propeller was simulated. The results of the calculations were verified by comparing the scaled pressure distribution within the cavitating area of the body with the cavitation number. It was found that the physics of sheet cavitation are reproduced correctly. In order to validate the calculated results, the sheet cavitation lengths on three different geometries were computed and compared with measurements. The simulations delivered reliable results for all considered flows and cavitation conditions. Furthermore, the influence of the grid resolution on the computed sheet cavitation shape was studied by using different surface grid discretisation levels. It was detected that the choice of a suitable grid is very important in the run-up to the computations. The employed sheet cavitation model delivers reliable results only for particular grid resolutions. The grid refinement in the cross-wise direction has a considerable influence on the calculated sheet cavitation shapes, whereas the impact of the grid refinement in the radial direction is relatively small.

In the second example study the numerical method was verified and validated for the unsteady flow problem. The verification was done by simulating the flow around a hydrofoil in an oscillating inflow velocity field. The time change of the inflow velocity and the resulting change of the angle of attack of the hydrofoil lead to a varying sheet cavitation extent. Sheet cavitation appeared periodically on the pressure and on the suction side of the hydrofoil. Hence, the functionality of the implemented face and back cavitation model was proven by this example. Subsequently, the method was validated with regards to the unsteady sheet cavitation model by simulating the flow around two different propeller geometries subject to an inhomogeneous inflow. The calculated sheet cavitation extents were shown to be in agreement with the measurements obtained in cavitation tunnel experiments. It was illustrated that the cavity shape and thickness vary with the varying blade angular position, i.e. the numerical method is able to reproduce the unsteady sheet cavitation patterns for a propeller subject to a non-uniform inflow. In addition, the influence of the ship wake shape on the extent of sheet cavitation was studied by using the original and a modified ship wake fields. The simulations displayed that a wider wake peak of the wake field leads to a greater amount of sheet cavitation, which is in accordance with the observations made in measurements.

In the third example study the numerical method was validated regarding the calculation of propeller-induced hull pressure fluctuations with and without partial sheet cavitation. First, the propeller was simulated in a uniform inflow and the pressures were evaluated on a flat plate located above the propeller. Second, the propeller was simulated subject to a non-uniform inflow and the pressures were monitored on a part of the ship hull located above the propeller. In both studies the computed results were analysed by the Fourier transformation and compared with measured data. Furthermore, the impact of sheet cavitation on the magnitude of the pressure pulses was analysed. The computed results indicate that the influence of the non-uniform inflow to the propeller is small when no cavitation occurs on the blades. When cavitation occurs, the influence of the non-uniform inflow increases. The pulsation of cavitation directly correlates to the heterogeneity of the wake field, which leads to higher pressure pulses. The underlying numerical method calculates the first frequency of the pressures induced by a cavitating propeller with a high degree of accuracy. The second and third harmonics of the pressures are underestimated compared to the measured data. This can be explained by the absence of tip vortex cavitation that is found to highly influence the magnitude of the second and higher harmonics.

After an in-depth verification and validation of the developed numerical method, the simulation tool was then applied to the prediction of the hydrodynamic loads induced by a marine propeller on the harbour bed in the port area. During the manoeuvring of a ship the rotating propeller generates a slipstream that can radiate an immense force on the harbour bottom and lead to harbour bed erosion. In the present work the induced pressures and velocities due to a rotating propeller were calculated for the non-cavitating and cavitating test case. The simulations delivered relevant information about the spatial distribution of propeller-induced loads on the harbour bed and highlighted the influence of sheet cavitation. It was shown that sheet cavitation significantly increases the amplitudes of the oscillating pressures underneath the propeller center. Downstream of the propeller centre, where the slipstream of the propeller approaches the harbour bed, the induced axial velocities are high and sheet cavitation has a negligible influence.

The validation and application examples presented in this work emphasise the wide range of applications and the advantages of the implemented numerical method. The method is able to reliably predict the extent and thickness of sheet cavitation in steady and unsteady flows. Furthermore, the effects of unsteady sheet cavitation and the cavity volume variations can be accurately reproduced on the magnitude of the propeller-induced pressures. It was shown that the accuracy of the numerical results is comparable with the experimental results of cavitation tunnel measurements. But compared to model tests, the developed numerical method is much more time-efficient, which allows parameter studies and the computation of propeller-induced pressure fluctuations in an acceptable time frame. In addition, the developed sheet cavitation model is flexible so that other common forms of cavitation on propellers such as supercavitation and tip vortex cavitation can easily be added as an extension to the partial sheet cavitation model. However, the analysed examples also revealed that there is still potential for the expansion of the numerical method. There are three major issues which are recommended for future research:

- The accuracy of the implemented partially non-linear sheet cavitation model without re-meshing of the grid strongly depends on the surface grid resolution. The non-re-meshing of the grid simplifies the implementation of the model but it also involves difficulties concerning the choice of a suitable grid discretisation level. Alternatively, the approach with re-meshing of the cavity surface grid can be used. This approach is for example applied by Kanemaru and Ando (2009). The implementation of a grid re-meshing procedure is more sophisticated and can increase the computation time. But the method is expected to be less dependent on the grid discretisation level.
- The validation of the propeller-induced hull pressures showed that the second and higher frequencies of the pressures are underestimated by the numerical method. According to ITTC (1999), tip vortex cavitation is essential in the prediction of the second and higher harmonics of hull pressure fluctuations. Hence, the inclusion of a tip vortex model in the current numerical method is expected to significantly improve the simulation results.
- A promising enhancement of the current method with regards to the port hydrodynamic problems is expected by implementing a model for the simulation of the soil deformation due to the propeller induced flow. Such a model will allow to predict the intensity of the soil erosion and simulate the scouring of the harbour bottom.

# Bibliography

Abbott, I. and von Doenhoff, A. E. (1959). *Theory of Wing Sections*. Dover Books on Aeronautical Engineering.

Achkanadze, A. S. and Krasilnikov, V. I. (2001). A Velocity Based Boundary Element Method with Modified Trailing Edge for Prediction of the Partial Cavities on the Wings and Propeller Blades. In *CAV2001, 4th International Symposium on Cavitation*.

Ando, J. and Nakatake, K. (2001). Calculation of three-dimensional unsteady sheet cavitation by a simple surface panel method "SQCM". In *CAV2001, 4th International Symposium on Cavitation*.

Bal, S. and Kinnas, S. A. (2002). A BEM for the prediction of free surface effects on cavitating hydrofoils. *Computational Mechanics*, 28:260–274.

Blaauw, H. G. and van de Kaa, E. J. (1978). Erosion of bottom and sloping banks caused by the screw of manoeuvring ships. *7th International Harbour Congress, Antwerp*, (202).

Breslin, J. P., Houten, R. J. V., Kerwin, J. E., and Johnsson, C. A. (1982). Theoretical and experimental propeller-induced hull pressures arising from intermittent blade cavitation, loading, and thickness. *Transactions of SNAME*, 90:111–151.

Brix, J. (1993). *Manoeuvring Technical Manual*. Seehafen Verlag Hamburg.

Bundesanstalt für Wasserbau (BAW) (2011). Grundlagen zur Bemessung von Böschungs- und Sohlensicherungen an Binnenwasserstraßen. Bundesanstalt für Wasserbau.

Carlton, J. (2007). *Marine Propellers and Propulsion*. Elsevier Ltd, 2nd edition.

Dang, J. (2001). *Numerical Simulation of Unsteady Partial Cavity Flows*. PhD thesis, Delft University of Technology, The Netherlands.

Falcão de Campos, J. A. C., Vaz, G., and Bosschers, J. (2006). Influence of the reduced frequency on the 2-D partial sheet cavitation behaviour for a foil in a gust. In *Sixth International Symposium on Cavitation CAV2006, Wageningen, The Netherlands*.

Fine, N. E. (1992). *Nonlinear Analysis of Cavitating Propellers in Nonuniform Flow*. PhD thesis, Massachusetts Institute of Technology, USA.

Gans, H. J. D. K. (1994). *Numerical Time Dependent Sheet Cavitation Simulations using a Higher Order Panel Method*. PhD thesis, Delft University, Netherlands.

Gent, W. V. (1994). Pressure Field Analysis of a Propeller with Unsteady Loading and Sheet Cavitation. *Proceedings of the 20th Symposium on Naval Hydrodynamics*, page 355–367.

Grabe, J. (2011). *Ports for Container Ships of Future Generations, 2nd Workshop*. Technische Universität Hamburg, Institut für Geotechnik und Baubetrieb, Hamburg, Germany.

Günther, B. (2002). Widerstands- und Propulsionsversuch sowie Nachstrommessung am Modell eines Containerschiffes, Modell Nr. 1111 S 001. Technical Report 2808, Schiffbau-Versuchsanstalt Potsdam GmbH, Potsdam, Germany.

Heinke, H.-J. and Jaksic, D. (2003). Untersuchung des Einflusses des Nachstromfeldes (Modell- oder Großausführungsnachstrom) auf die Kavitation und Druckschwankungen am KRISO Containerschiff KS621. Technical Report 2852, Schiffbau-Versuchsanstalt Potsdam GmbH, Potsdam, Germany.

Heinke, H.-J. and Jaksic, D. (2004). Kavitationsuntersuchungen und Druckschwankungsmessungen mit fünf Propellern am Dummymodell des KRISO Containerschiffs KS 621. Technical Report 3036, Schiffbau-Versuchsanstalt Potsdam GmbH, Potsdam, Germany.

Hsin, C.-Y. (1990). *Development and Analysis of Panel Methods for Propellers in Unsteady Flow*. PhD thesis, Massachusetts Institute of Technology, USA.

Hundemer, J. (2013). *Entwicklung eines Verfahrens zur Berechnung der instationären potenzialtheoretischen Propellerumströmung*. PhD thesis, Technische Universität Hamburg-Harburg, Hamburg, Germany.

Hundemer, J. and Abdel-Maksoud, M. (2009). Prediction of tip vortex cavitation inception on marine propellers at an early design stage. In *Proceedings of the 7th International Symposium on Cavitation*, number 143, Ann Arbor, Michigan, USA.

Iben, H. K. (1995). *Tensorrechnung*. B.G. Teubner.

ITTC (1999). The specialist committee on cavitation induced pressure fluctuation. In *Final Report and Recommendations to the 22nd ITTC*. International Towing Tank

Conference. `http://ittc.info/download/proceedings/22nd%20Conference%20(SeoulShanghai%201999)/index.pdf` (Accessed on: 04.12.2014).

Kanemaru, T. and Ando, J. (2009). A Numerical Analysis of Steady and Unsteady Sheet Cavitation on a Marine Propeller Using a Simple Surface Panel Method "SQCM". In *First International Symposium on Marine Propulsors SMP'09, Trondheim, Norway*, pages 372–379.

Kanemaru, T. and Ando, J. (2011). Numerical Analysis of Pressure Fluctuation on Ship Stern Induced by Cavitating Propeller Using a Simple Surface Panel Method "SQCM". In *Second International Symposium on Marine Propulsors, SMP'11, Hamburg, Germany*, pages 372–379.

Katz, J. and Plotkin, A. (2001). *Low-Speed Aerodynamics*. Cambridge University Press, Cambridge, 2nd edition.

Kerwin, J. E., Kinnas, S. A., Lee, J.-T., and Shih, W.-Z. (1987). A surface panel method for the hydrodynamic analysis of ducted propellers. In *In Transactions of Society of Naval Architects and Marine Engineers*, volume 95, Teddington, England.

Kerwin, J. E., Kinnas, S. A., Wilson, M. B., and McHugh, J. (1986). Experimental and analytical techniques for the study of unsteady propeller sheet cavitation. *Proceedings of the 16th Symposium on Naval Hydrodynamics, Berkeley*, page 387–414.

Kerwin, J. E. and Lee, C. S. (1978). Prediction of steady and unsteady marine propeller performance by numerical lifting-surface theory. (86):247–8.

Kinnas, S. A. (1992). Inversion of the source and vorticity equations for supercavitating hydrofoils. *Journal of Engineering Mathematics*, 26:349–361.

Kinnas, S. A. and Fine, N. E. (1992). A Nonlinear Boundary Element Method for the Analysis of Unsteady Propeller Sheet Cavitation. *Proceedings of the 19th Symposium on Naval Hydrodynamics, Seoul, Korea*, page 717–737.

Kinnas, S. A. and Fine, N. E. (1993). A Numerical Nonlinear Analysis of the Flow Around 2-D and 3-D Partially Cavitating Hydrofoils. *Journal of Fluid Mechanics*, 254:151–181.

Kinnas, S. A. and Young, Y. L. (2003). Modeling of cavitating or ventilated flows using BEM. *International Journal of Numerical Methods for Heat & Fluid Flow*, 13:672–697.

Kornev, N. (2009). Propellertheorie. Vorlesungsskript, Universität Rostock, Fakultät für Maschinenbau und Schiffstechnik.

Krishnaswamy, P. (2000). *Flow Modelling for Partially Cavitating Hydrofoils*. PhD thesis, Department of Naval Architecture and Offshore Engineering, Technical University of Denmark.

KRISO Container Ship (KCS). http://www.nmri.go.jp/cfd/cfdws05/Detail/KCS/container.html. [Online; accessed November 2011].

Kuiper, G. (1981). *Cavitation Inception on Ship Propeller Models*. PhD thesis, TU Delft, Delft, Netherlands.

Lee, C.-S. (1979). *Prediction of Steady and Unsteady Performance of Marine Propellers with or without Cavitation by Numerical Lifting-Surface Theory*. PhD thesis, Massachusetts Institute of Technology, USA.

Lee, H. and Kinnas, S. A. (2004). Application of a Boundary Element Method in the Prediction of Unsteady Blade Sheet and Developed Tip Vortex Cavitation on Marine Propellers. *Journal of Ship Research*, 48(1):15–30.

Lee, H. S. and Kinnas, S. A. (2005). A BEM for the modeling of unsteady propeller sheet cavitation inside of a cavitation tunnel. *Computational Mechanics*, 37:41–51.

Lee, J.-T. (1987). *A Potential Based Panel Method for the Analysis of Marine Propellers in Steady Flow*. PhD thesis, Massachusetts Institute of Technology, USA.

Mueller, A. C. and Kinnas, S. A. (1999). Propeller Sheet Cavitation Predictions Using a Panel Method. *Journal of Fluids Engineering*, 121:282–288.

Nakamura, N. (1985). Estimation of Propeller Open-Water Characteristics Based on Quasi-Continuous Method. *Journal of the Society of Naval Architects of Japan*, 157:95–107.

Natarajan, S. (2003). *Computational Modeling of Rudder Cavitation and Propeller/Rudder Interaction*. PhD thesis, The University of Texas at Austin, Austin, USA.

Pan, Y. (2009). *A viscous/inviscid interactive approach and its application to hydrofoils and propellers with non-zero trailing edge thickness*. PhD thesis, The University of Texas at Austin, Austin, USA.

Phoemsapthawee, S., Leroux, J.-B., Laurens, J.-M., and Deniset, F. (2009). A Transpiration Velocities Based Sheet Cavitation Model. *Ship Technology Reasearch*, 56.

Polhamus, E. C. (1968). Application of the leading-edge-suction analogy of vortex lift to the drag due to lift of sharp-edge delta wings. Technical report, NASA, Washington, D.C.

Prescott, A. I., editor (2008). *Ocean Engineering Research Advances*. Nova Science Publishers, Inc.

Richter, H. (2011). Kraftmessungen und Kavitationsbeobachtungen an einem 2D-Profil NACA$66_2 - 415$ im Kavitaionstunnel. Technical Report 3770, Schiffbau-Versuchsanstalt Potsdam GmbH, Potsdam, Germany.

Richter, H. and Heinke, H.-J. (2006). Freifahrt- und Kavitationsversuche sowie Druckschwankungsmessungen mit dem Propeller P 1356 in homogener Zuströmung. Technical Report 3213, Schiffbau-Versuchsanstalt Potsdam GmbH, Potsdam, Germany.

Römisch, K. (1975). Der Propellerstrahl als erodierendes Element bei An- und Ablegemanövern im Hafenbecken. *Seewirtschaft*, 7(7):431–434.

Salvatore, F. and Esposito, P. G. (2001). An improved boundary element analysis of cavitating three-dimensional hydrofoils. In *CAV2001, 4th International Symposium on Cavitation*.

Salvatore, F., Greco, L., and Calcagni, D. (2011). Computational analysis of marine propeller performance and cavitation by using an inviscid-flow BEM model. In *Second International Symposium on Marine Propulsors, SMP'11, Hamburg, Germany*.

Salvatore, F. and Ianniello, S. (2002). Preliminary Results on Acoustic Modelling of Cavitating Propellers. In *IABEM 2002, International Association for Boundary Element Methods*, Austin, USA.

Salvatore, F., Testa, C., and Greco, L. (2003). A viscous/inviscid coupled formulation for unsteady sheet cavitation modelling of marine propellers. In *Fifth International Symposium on Cavitation (Cav2003), Osaka, Japan*.

Schmidt, E. (1999). *Ausbreitungsverhalten und Erosionswirkung eines Bugpropellerstrahles vor einer Kaimauer*. PhD thesis, Technische Universität Carolo-Wilhelmina zu Braunschweig, Germany.

Sun, H. and Kinnas, S. A. (2006). Simulation of sheet cavitation on propulsor blades using a viscous/inviscid interactive method. In *Sixth International Symposium on Cavitation CAV2006, Wageningen, The Netherlands*.

Szantyr, J. A. (1994). A method for analysis of cavitating marine propellers in non-uniform flow. *Int. Shipbuild. Progr.*, 41(427):223–242.

Ulrich, C. (2013). *Smoothed-Particle-Hydrodynamics Simulation of Port Hydrodynamic Problems*. PhD thesis, Technische Universität Hamburg-Harburg, Hamburg, Germany. Schriftenreihe Schiffbau der Technischen Universität Hamburg-Harburg, Bericht Nr. 671.

Vaz, G., Bosschers, J., and Falcão de Campos, J. (2003). Two-dimensional Modelling of Partial Cavitation with BEM. Analysis of Several Models. In *Fifth International Symposium on Cavitation (Cav2003), Osaka, Japan.*

Vaz, G. N. V. B. (2005). *Modelling of Sheet Cavitation on Hydrofoils and Marine Propellers using Boundary Element Methods*. PhD thesis, Universidade Técnica de Lisboa, Instituto Superior Técnico, Lisbon, Portugal.

Young, Y. L. (2002). *Numerical Modeling of Supercavitating and Surface-Piercing Propellers*. PhD thesis, Environmental and water resources engineering department of civil engineering, University of Texas at Austin, Austin, USA.

Young, Y. L. and Kinnas, S. A. (2001). A BEM for the Prediction of Unsteady Midchord Face and/or Back Propeller Cavitation. *Journal of Fluids Engineering*, 123:311–319.

Young, Y. L. and Kinnas, S. A. (2003a). Analysis of supercavitating and surface-piercing propeller flows via BEM. *Computational Mechanics*, 32:269–280.

Young, Y. L. and Kinnas, S. A. (2003b). Fluid and structural modelling of cavitating propeller flows. In *Fifth International Symposium on Cavitation (Cav2003), Osaka, Japan*.

# Chapter A

# Description of the propeller geometry

This chapter deals with the description of propeller design parameters. The first part, Chapter A.1, introduces the geometry parameters of a circular blade section. Afterwards, in Chapter A.2, the geometry parameters that apply to the overall propeller are presented. The chapter gives only a brief overview of the most important geometrical characteristics of a propeller. For a more detailed view on propeller geometries the reader is kindly referred to the publications Abbott and von Doenhoff (1959) and Carlton (2007).

## A.1 Nomenclature for a blade profile

A circular arc section of a propeller blade at some radius looks like a foil profile and the shape of the profiles changes across the blade radius. The shape of a profile can be characterized by the coordinates of the upper and lower surface. An example of a blade section is pictured in Figure A.1. In the following, all relevant geometry parameters for a profile are explained and listed in Table A.1.

| **Characteristics** | **Notation** | **Units** |
|---|---|---|
| Thickness | $t$ | m |
| Maximal thickness | $t_{max}$ | m |
| Camber | $\eta$ | m |
| Maximal camber | $\eta_{max}$ | m |
| Chord | $c$ | m |
| Angle of attack | $\alpha$ | degree |
| Span width | $b$ | m |
| Reference area | $A_{ref}$ | $m^2$ |
| Aspect ratio | $\Lambda$ | - |

Table A.1: Geometrical parameters of a blade profile

**Pressure and suction side:** The side of the profile where a high pressure is generated is called pressure side ($PS$) and the side where a low pressure is produced is called suction side ($SS$) (s. Figure A.1).

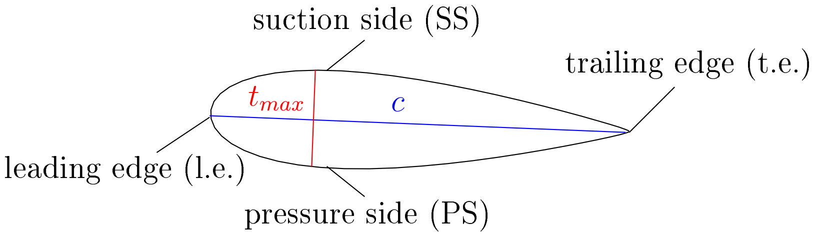

Figure A.1: Circular arc section of a blade

**Leading and trailing edge:** The edge at the nose of the profile that cuts through the fluid is called leading edge ($l.e.$). The edge downstream of the foil is called trailing edge ($t.e.$) (s. Figure A.1).

**Chord line/length:** The straight line between the trailing and the leading edge of a profile is called the chord line **c** and its arc length is defined as chord length $c$ (s. Figure A.1).

**Camber line:** The camber line $a$ describes the mean profile of the foil as a function of the chordwise position. The camber height $\eta$ is obtained by:

$$\eta = \frac{y_{SS} + y_{PS}}{2}, \tag{A.1}$$

where $SS$ denotes the suction side and $PS$ the pressure side of the profile and $y = y(x)$ is the contour curve of the profile. Camber is the measure of the curvature of the profile, e.g. symmetric profiles have no camber.

**Maximum camber:** The maximum of the camber height $\eta_{max}$ is computed by the following formula:

$$\eta_{max} = \max_{i=t.e.}^{l.e.} \left( \frac{y_{SS,i} + y_{PS,i}}{2} \right). \tag{A.2}$$

**Thickness:** The thickness $t$ of a foil is defined as the distance between the upper and the lower side of the foil orthogonal to the camber line and is calculated by:

$$t = |y_{SS} - y_{PS}|. \tag{A.3}$$

**Maximum thickness:** The maximum thickness of a foil is denoted by $t_{max}$ and is defined by (s. Figure A.1):

$$t_{max} = \max_{i=t.e.}^{l.e.} |y_{SS,i} - y_{PS,i}|. \tag{A.4}$$

**Span:** The span $b$ of a foil is the distance from one tip of the foil to another normal to the cross-section.

**Angle of attack:** The angle between the inflow velocity vector and the chord line **c** is called the angle of attack $\alpha$.

**Reference area:** The reference area is the product of the span width $b$ and the chord length $c$: $A_{ref} = bc$.

**Aspect ratio:** Since the numerical calculations are performed for a profile with a finite span, the calculated results must be adjusted by a factor which is called the aspect ratio $\Lambda$. The aspect ratio describes the relation between the span width $b$ and the reference area $A_{ref}$:

$$\Lambda = \frac{b^2}{A_{ref}}. \tag{A.5}$$

## A.2 Nomenclature for a propeller

This section describes the geometry parameters that apply to the overall propeller geometry. Table A.2 shows a summary of these parameters and their nomenclature.

| **Characteristics** | **Notation** | **Units** |
|---|---|---|
| Number of blades | $z$ | - |
| Propeller diameter | $D$ | m |
| Propeller radius | $R$ | m |
| Hub diameter | $D_{hub}$ | m |
| Hub ratio | $D_{hub}/D$ | - |
| Skew angle | $\theta$ | degree |
| Pitch angle | $\psi$ | degree |
| Pitch ratio | $P_{0.7}/D$ | - |
| Mean pitch ratio | $P_m/D$ | - |
| Propeller area | $A_0$ | - |
| Propeller area ratio | $A_E/A_0$ | - |
| Rotational speed of propeller | $n$ | 1/s |

Table A.2: Geometrical parameters of a propeller

**Reference line:** The line that is orthogonal to the shaft axis is called propeller reference line.

**Generator line:** The line generated by the intersection of the pitch helices and the plane containing the shaft axis and the reference line is called generator line.

**Number of blades:** The choice of the number of blades, denoted by $z$, depends on two main criteria. A low number of blades improves propeller efficiency. A high number of blades reduces the pressure fluctuations induced by the propeller blades on the ship hull.

Thus, a propeller designer must decide whether it is more important to avoid vibrations on the ship hull or to achieve a preferably high efficiency coefficient.

**Blade tip and root:** The tip of a blade is defined as the furthest point on the blade measured from the propeller shaft. The root of the blade is the region where the blade attaches to the hub of the propeller.

**Radius and diameter:** The distance between propeller shaft centre and propeller tip is the radius of the propeller. Propeller diameter $D = 2R$ is one of the most significant propeller parameters. For the optimal propeller efficiency it should be chosen as high as possible. But on the other hand, the propeller should not emerge in case of a ballast voyage and it should not induce high pressure pulses, which are associated with high diameters.

**Hub diameter:** The hub diameter $D_{hub}$ is twice the hub radius. There is a tradeoff between size and strength of the hub. A small diameter results in a higher thrust, but in less strength.

**Hub ratio:** The ratio between the hub diameter and propeller diameter ${}^{D_{hub}}\!/_{D}$ is defined as the hub ratio.

**Left-handed or right-handed:** The right-handed propellers rotate clockwise, whereas the left-handed ones rotate counter-clockwise.

**Propeller area:** Propeller area is defined as: $A_0 = {}^{\pi D^2}\!/_{4}$.

**Propeller area ratio:** Propeller area ratio, denoted by ${}^{A_E}\!/_{A_0}$, is defined as the ratio between the propeller area $A_0$ and the projected area $A_E$, where the projected area is given by the formula:

$$A_E = z \int_{r_{hub}}^{r_{tip}} c(r)dr, \tag{A.6}$$

where $c(r)$ is the chord length at radius $r$.

**Pitch/Pitch angle:** The distance moved forward by the helical line during one propeller revolution is called the pitch and is denoted by $P$. The angle of the helix is the pitch angle $\psi$ and is given by:

$$\psi = \tan^{-1}({}^{P}\!/_{2\pi R}). \tag{A.7}$$

**Pitch ratio/Mean pitch ratio:** The pitch of a propeller varies with the radius. As a characteristic value for the pitch of a propeller the pitch ratio $P_{0.7}/D$ at the relative radius $r/R = 0.7$ is often used. The mean pitch ratio describes the pitch ratio $P_{0.5}/D$ at $r/R = 0.5$.

**Skew/Skew angle:** Skew describes the shifting of the blade tip relative to the blade root at a certain skew angle $\theta$ along the chord direction and at a certain pitch along the shaft axis. The skew angle is the greatest angle measured from the shaft axis between two lines passing through the mid-chord of any two propeller sections.

**Rake:** The movement of the propeller plane to the generator line is defined as the rake of the propeller.

**Rotational speed:** The rotational speed of a propeller, denoted by $n$, is the number of revolutions of a propeller in a time unit. In the present work seconds are used as the base unit of time for the measurement of the number of revolutions.

# Chapter B

# Transformation of the coordinate systems

This chapter deals with the transformation of different coordinate systems. In Chapter B.1 the formulas for the transformation of a vector from the global Cartesian coordinate system to a local orthogonal or non-orthogonal coordinate system are described. In Chapter B.2 and B.3 the vice-versa transformations are formulated.

## B.1 Transformation from the global Cartesian coordinate system to a local coordinate system

The following paragraphs describe a procedure for the transformation of a vector from the global Cartesian coordinate system to a local coordinate system. The base unit vectors of the Cartesian coordinate system are denoted by $\mathbf{e}_i$, $i = 1, 2, 3$. The base unit vectors of the local orthogonal and non-orthogonal coordinate system are denoted by $\tau_i$ and $\mathbf{t}_i$, $i = 1, 2, 3$, respectively. Let a vector $\mathbf{a}$ be given in the global Cartesian coordinates: $\mathbf{a} = a_x\mathbf{e_1} + a_y\mathbf{e_2} + a_z\mathbf{e_3}$. Its components in the Cartesian system are computed by:

$$a_x = \mathbf{a}\cdot\mathbf{e_1}, \quad a_y = \mathbf{a}\cdot\mathbf{e_2}, \quad a_z = \mathbf{a}\cdot\mathbf{e_3}.$$

For the transformation of the Cartesian coordinates to the local coordinates, the global coordinate system must be transformed to the origin of the local coordinate system, denoted by $\mathbf{c}_0$. The displacement of the system's origin is called translation and the translated coordinates are given by:

$$\bar{\mathbf{a}} = \mathbf{a} - \mathbf{c}_0.$$

The components of the local orthogonal and non-orthogonal coordinate systems are then obtained by:

$$\begin{aligned} a_\xi &= \bar{\mathbf{a}}\cdot\tau_1 = (\mathbf{a}-\mathbf{c}_0)\cdot\tau_1, \qquad & a_{s_1} &= \bar{\mathbf{a}}\cdot\mathbf{t}_1 = (\mathbf{a}-\mathbf{c}_0)\cdot\mathbf{t}_1,\\ a_\eta &= \bar{\mathbf{a}}\cdot\tau_2 = (\mathbf{a}-\mathbf{c}_0)\cdot\tau_2, \qquad & a_{s_2} &= \bar{\mathbf{a}}\cdot\mathbf{t}_2 = (\mathbf{a}-\mathbf{c}_0)\cdot\mathbf{t}_2,\\ a_\zeta &= \bar{\mathbf{a}}\cdot\tau_3 = (\mathbf{a}-\mathbf{c}_0)\cdot\tau_3, \qquad & a_{s_3} &= \bar{\mathbf{a}}\cdot\mathbf{t}_3 = (\mathbf{a}-\mathbf{c}_0)\cdot\mathbf{t}_3. \end{aligned} \tag{B.1}$$

## B.2 Transformation from the local orthogonal coordinate system to the global Cartesian coordinate system

This section presents the transformation of a vector defined in a local orthogonal coordinate system to a vector in global Cartesian coordinates. Let a vector $\mathbf{a}$ be given in the local orthogonal coordinates, its components are denoted by $a_\xi$, $a_\eta$ and $a_\zeta$. The transformation of the local orthogonal coordinates into the global Cartesian coordinates is performed by the following formula (s. Iben, 1995, p. 45):

$$\begin{pmatrix} a_x \\ a_y \\ a_z \end{pmatrix} = a_\xi \tau^1 + a_\eta \tau^2 + a_\zeta \tau^3 + \mathbf{c}_0. \tag{B.2}$$

The vectors $\tau^i$ are the so-called contra-variant vectors of the curvilinear coordinate system (s. Iben, 1995, p. 38), whereas $\tau_i$ for $i = 1, 2, 3$ are the covariant vectors. The contra-variant vectors can be calculated by means of the covariant vectors by the following equation (s. Iben, 1995, p. 38):

$$\tau^i = \frac{\tau_j \times \tau_k}{(\tau_1 \times \tau_2) \cdot \tau_3}, \qquad i, j, k = 1, 2, 3 \quad \text{cyclic.}$$

According to Iben (1995, p. 45) it holds:

$$\begin{pmatrix} a_x \\ a_y \\ a_z \end{pmatrix} = a_\xi \tau^1 + a_\eta \tau^2 + a_\zeta \tau^3 + \mathbf{c}_0 = a^\xi \tau_1 + a^\eta \tau_2 + a^\zeta \tau_3 + \mathbf{c}_0, \quad \text{where} \quad a^i = \mathbf{T}^{ij} a_j.$$

The matrix $\mathbf{T}^{ij}$ is defined as $\mathbf{T}^{ij} = (\mathbf{T}_{ij})^{-1}$ and $\mathbf{T}_{ij} = \tau_i \cdot \tau_j$ (s. Iben, 1995, p. 42). Since all vectors of the orthogonal coordinate system are perpendicular, it follows $\tau_i \cdot \tau_j = 0$ for $i \neq j$. Thus, for the matrix $\mathbf{T}_{ij}$ one obtains:

$$\mathbf{T}_{ij} = \begin{pmatrix} |\tau_1|^2 & 0 & 0 \\ 0 & |\tau_2|^2 & 0 \\ 0 & 0 & |\tau_3|^2 \end{pmatrix} = \begin{pmatrix} 1 & 0 & 0 \\ 0 & 1 & 0 \\ 0 & 0 & 1 \end{pmatrix}.$$

The inverse of the matrix $\mathbf{T}_{ij}$ is the identity matrix: $\mathbf{T}^{ij} = (\mathbf{T}_{ij})^{-1} = \mathbf{I}$. Subsequently, one obtains the Cartesian components of the vector $\mathbf{a}$ as follows:

$$a_x = (a^{\xi}\tau_1 + a^{\eta}\tau_2 + a^{\zeta}\tau_3 + \mathbf{c}_0) \cdot \mathbf{e_1} = a_{\xi}\tau_{11} + a_{\eta}\tau_{21} + a_{\zeta}\tau_{31} + \mathbf{c}_0 \cdot \mathbf{e}_1,$$
$$a_y = (a^{\xi}\tau_1 + a^{\eta}\tau_2 + a^{\zeta}\tau_3 + \mathbf{c}_0) \cdot \mathbf{e_2} = a_{\xi}\tau_{12} + a_{\eta}\tau_{22} + a_{\zeta}\tau_{32} + \mathbf{c}_0 \cdot \mathbf{e}_2,$$
$$a_z = (a^{\xi}\tau_1 + a^{\eta}\tau_2 + a^{\zeta}\tau_3 + \mathbf{c}_0) \cdot \mathbf{e_3} = a_{\xi}\tau_{13} + a_{\eta}\tau_{23} + a_{\zeta}\tau_{33} + \mathbf{c}_0 \cdot \mathbf{e}_3.$$

## B.3 Transformation from the local non-orthogonal coordinate system to the global Cartesian coordinate system

This section describes the transformation of a vector defined in a local non-orthogonal coordinate system to a vector in global Cartesian coordinates. Let a vector $\mathbf{a}$ be given in the local non-orthogonal coordinates, its components are denoted by $a_{s_1}$, $a_{s_2}$ and $a_{s_3}$. The transformation of the local non-orthogonal coordinates into the global Cartesian coordinates is performed analogous to the formula introduced in Equation (B.2):

$$\begin{pmatrix} a_x \\ a_y \\ a_z \end{pmatrix} = a_{s_1}\mathbf{t}^1 + a_{s_2}\mathbf{t}^2 + a_{s_3}\mathbf{t}^3 + \mathbf{c}_0 = a^{s_1}\mathbf{t}_1 + a^{s_2}\mathbf{t}_2 + a^{s_3}\mathbf{t}_3 + \mathbf{c}_0, \text{ where } a^i = \mathbf{T}^{ij}a_j.$$

The matrix $\mathbf{T}^{ij}$ is defined as $\mathbf{T}^{ij} = (\mathbf{T}_{ij})^{-1}$ and $\mathbf{T}_{ij} = \mathbf{t}_i \cdot \mathbf{t}_j$. The normal vector is perpendicular to the axial and tangential vector and it holds $\mathbf{t}_1 \cdot \mathbf{t}_3 = 0$, $\mathbf{t}_2 \cdot \mathbf{t}_3 = 0$. Now the matrix $\mathbf{T}_{ij}$ is computed:

$$\mathbf{T}_{ij} = \begin{pmatrix} |\mathbf{t}_1|^2 & \mathbf{t}_1 \cdot \mathbf{t}_2 & 0 \\ \mathbf{t}_1 \cdot \mathbf{t}_2 & |\mathbf{t}_2|^2 & 0 \\ 0 & 0 & |\mathbf{t}_3|^2 \end{pmatrix} = \begin{pmatrix} 1 & \mathbf{t}_1 \cdot \mathbf{t}_2 & 0 \\ \mathbf{t}_1 \cdot \mathbf{t}_2 & 1 & 0 \\ 0 & 0 & 1 \end{pmatrix}.$$

The inverse of the matrix $\mathbf{T}_{ij}$ is given by:

$$\mathbf{T}^{ij} = (\mathbf{T}_{ij})^{-1} = \frac{1}{1-(\mathbf{t}_1 \cdot \mathbf{t}_2)^2} \begin{pmatrix} 1 & -\mathbf{t}_1 \cdot \mathbf{t}_2 & 0 \\ -\mathbf{t}_1 \cdot \mathbf{t}_2 & 1 & 0 \\ 0 & 0 & 1-(\mathbf{t}_1 \cdot \mathbf{t}_2)^2 \end{pmatrix}.$$

Subsequently, the Cartesian components of the vector $\mathbf{a}$ can be computed:

$$\begin{aligned}
a_x &= (a^{s_1}\mathbf{t}_1 + a^{s_2}\mathbf{t}_2 + a^{s_3}\mathbf{t}_3 + \mathbf{c}_0) \cdot \mathbf{e}_1 = \frac{t_{11}}{1-(\mathbf{t}_1 \cdot \mathbf{t}_2)^2}(a_{s_1} - (\mathbf{t}_1 \cdot \mathbf{t}_2)a_{s_2}) \\
&+ \frac{t_{21}}{1-(\mathbf{t}_1 \cdot \mathbf{t}_2)^2}(a_{s_2} - (\mathbf{t}_1 \cdot \mathbf{t}_2)a_{s_1}) + t_{31}a_{s_3} + \mathbf{c}_0 \cdot \mathbf{e}_1, \\
a_y &= (a^{s_1}\mathbf{t}_1 + a^{s_2}\mathbf{t}_2 + a^{s_3}\mathbf{t}_3 + \mathbf{c}_0) \cdot \mathbf{e}_2 = \frac{t_{12}}{1-(\mathbf{t}_1 \cdot \mathbf{t}_2)^2}(a_{s_1} - (\mathbf{t}_1 \cdot \mathbf{t}_2)a_{s_2}) \\
&+ \frac{t_{22}}{1-(\mathbf{t}_1 \cdot \mathbf{t}_2)^2}(a_{s_2} - (\mathbf{t}_1 \cdot \mathbf{t}_2)a_{s_1}) + t_{32}a_{s_3} + \mathbf{c}_0 \cdot \mathbf{e}_2, \\
a_z &= (a^{s_1}\mathbf{t}_1 + a^{s_2}\mathbf{t}_2 + a^{s_3}\mathbf{t}_3 + \mathbf{c}_0) \cdot \mathbf{e}_3 = \frac{t_{13}}{1-(\mathbf{t}_1 \cdot \mathbf{t}_2)^2}(a_{s_1} - (\mathbf{t}_1 \cdot \mathbf{t}_2)a_{s_2}) \\
&+ \frac{t_{23}}{1-(\mathbf{t}_1 \cdot \mathbf{t}_2)^2}(a_{s_2} - (\mathbf{t}_1 \cdot \mathbf{t}_2)a_{s_1}) + t_{33}a_{s_3} + \mathbf{c}_0 \cdot \mathbf{e}_3.
\end{aligned}$$

# Chapter C

# Computation of the influence functions

This chapter discusses the computation of the influence functions introduced in Equation $(3.5)$. The value of the influence functions depends on the shape of the panels as well as on the distribution of the singularities. The shape of the panels can be approximated by polynomials of an arbitrary order, e.g.:

- Approximation of first order: $\zeta = a_0 + b_1\xi + b_2\eta$.
- Approximation of second order: $\zeta = a_0 + b_1\xi + b_2\eta + c_1\xi^2 + c_2\eta^2 + c_3\xi\eta$.

where $\xi, \eta$ and $\zeta$ are the local coordinates of the panel. The panels considered in this work are approximated by first order polynomials.
In the same way, the singularity strength distribution can be approximated by piecewise polynomial functions of different orders:

- Approximation of zero order: $\mu = \mu_0 = const$, $\sigma = \sigma_0 = const$.
- Approximation of first order: $\mu = \mu_0 + \mu_1\xi + \mu_2\eta$, $\sigma = \sigma_0 + \sigma_1\xi + \sigma_2\eta$.
- Approximation of second order: $\mu = \mu_0 + \mu_1\xi + \mu_2\eta + \mu_3\xi^2 + \mu_4\eta^2 + \mu_6\xi\eta$, $\sigma = \sigma_0 + \sigma_1\xi + \sigma_2\eta + \sigma_3\xi^2 + \sigma_4\eta^2 + \sigma_6\xi\eta$.

In the present work the singularity distribution is approximated by piecewise polynomials of zero order, i.e. the strengths of the sources and dipoles are assumed to be constant.
Assuming that the discretised body surface consists of flat quadrilateral panels that are bounded by four straight edges and that the singularities are piecewise constant functions, the influence functions can be computed analytically. The potential in an arbitrary point $\mathbf{P} = (\xi, \eta, \zeta)$ of the flow domain induced by a panel with the centre point $\mathbf{P}_i = (\xi_0, \eta_0, 0)$ and a constant source or dipole distribution of strength $\sigma$ or $\mu$, respectively, is given by:

$$\phi_S(\xi, \eta, \zeta) = -\frac{\sigma}{\epsilon}\int_{\eta_0}\int_{\xi_0} \frac{1}{\sqrt{(\xi-\xi_0)^2 + (\eta-\eta_0)^2 + \zeta^2}} d\xi_0 d\eta_0 = -\frac{\sigma}{\epsilon}B_{i,j},$$
$$\phi_D(\xi, \eta, \zeta) = -\frac{\mu}{\epsilon}\int_{\eta_0}\int_{\xi_0} \frac{\zeta}{((\xi-\xi_0)^2 + (\eta-\eta_0)^2 + \zeta^2)^{3/2}} d\xi_0 d\eta_0 = \frac{\mu}{\epsilon}A_{i,j}.$$

The velocity components are obtained by differentiating $\phi_S$ and $\phi_D$, respectively:

$$v_S(\xi,\eta,\zeta) = \begin{pmatrix} \frac{\partial \phi_S}{\partial \xi} \\ \frac{\partial \phi_S}{\partial \eta} \\ \frac{\partial \phi_S}{\partial \zeta} \end{pmatrix} = -\frac{\sigma}{\epsilon}\int_{\eta_0}\int_{\xi_0} \nabla\Big[\frac{1}{\sqrt{(\xi-\xi_0)^2+(\eta-\eta_0)^2+\zeta^2}}\Big]\, d\xi_0 d\eta_0$$

$$= -\frac{\sigma}{\epsilon}\nabla B_{i,j},$$

$$v_D(\xi,\eta,\zeta) = \begin{pmatrix} \frac{\partial \phi_D}{\partial \xi} \\ \frac{\partial \phi_D}{\partial \eta} \\ \frac{\partial \phi_D}{\partial \zeta} \end{pmatrix} = -\frac{\mu}{\epsilon}\int_{\eta_0}\int_{\xi_0} \nabla\Big[\frac{\zeta}{((\xi-\xi_0)^2+(\eta-\eta_0)^2+\zeta^2)^{3/2}}\Big]\, d\xi_0 d\eta_0$$

$$= \frac{\mu}{\epsilon}\nabla A_{i,j}.$$

According to Katz and Plotkin (2001, p. 246f.), the functions $B_{i,j}$ and $A_{i,j}$ can be calculated analytically by the following formulas:

$$\begin{aligned} B_{i,j} &= \sum_{i=1,\,\text{modulo}\,4}^{4} \Big[|\zeta|\Big(\tan^{-1}(\frac{m_{i,i+1}e_i-h_i}{\zeta r_i}) - \tan^{-1}(\frac{m_{i,i+1}e_{i+1}-h_{i+1}}{\zeta r_{i+1}})\Big) \\ &+ \frac{(\xi-x_i)(y_{i+1}-y_i)-(\eta-y_i)(x_{i+1}-x_i)}{d_{i,i+1}}\ln\Big(\frac{r_i+r_{i+1}+d_{i,i+1}}{r_i+r_{i+1}-d_{i,i+1}}\Big)\Big], \quad \text{(C.1)} \\ A_{i,j} &= \sum_{i=1,\,\text{modulo}\,4}^{4} \Big[\tan^{-1}(\frac{m_{i,i+1}e_i-h_i}{\zeta r_i}) - \tan^{-1}(\frac{m_{i,i+1}e_{i+1}-h_{i+1}}{\zeta r_{i+1}})\Big]. \end{aligned}$$

The constants $d_{i,i+1}$, $m_{i,i+1}$, $r_i$, $e_i$ and $h_i$ are defined as:

$$\begin{aligned} d_{i,i+1} &= \sqrt{(x_{i+1}-x_i)^2+(y_{i+1}-y_i)^2}, \\ m_{i,i+1} &= \frac{y_{i+1}-y_i}{x_{i+1}-x_i}, \\ r_i &= \sqrt{(\xi-x_i)^2+(\eta-y_i)^2+\zeta^2}, \\ e_i &= (\xi-x_i)^2+\zeta^2, \\ h_i &= (\xi-x_i)(\eta-y_i), \end{aligned}$$

for $i = 1,2,3,4$, where $i$ is calculated modulo $4$ and $(x_i, y_i, 0)$ are the coordinates of the corner points of the point $\mathbf{P}_i$.

For the corresponding velocities one obtains (s. Katz and Plotkin (2001), S. 246f.):

$$
\begin{aligned}
(\nabla B_{i,j})_\xi &= -\sum_{i=1,modulo4}^{4} \frac{(y_{i+1}-y_i)}{d_{i,i+1}} \ln\Big(\frac{r_i + r_{i+1} - d_{i,i+1}}{r_i + r_{i+1} + d_{i,i+1}}\Big),\\
(\nabla B_{i,j})_\eta &= -\sum_{i=1,modulo4}^{4} \frac{(x_i - x_{i+1})}{d_{i,i+1}} \ln\Big(\frac{r_i + r_{i+1} - d_{i,i+1}}{r_i + r_{i+1} + d_{i,i+1}}\Big),\\
(\nabla B_{i,j})_\zeta &= -\sum_{i=1,modulo4}^{4} \Big(\tan^{-1}(\frac{m_{i,i+1}e_i - h_i}{\zeta r_i}) - \tan^{-1}(\frac{m_{i,i+1}e_{i+1} - h_{i+1}}{\zeta r_{i+1}})\Big) = -A_{i,j},\\
(\nabla A_{i,j})_\xi &= \sum_{i=1,modulo4}^{4} \frac{\zeta(y_i - y_{i+1})(r_{i+1}+r_i)}{r_i r_{i+1}[r_i r_{i+1} - (\xi - x_i)(\xi - x_{i+1}) - (\eta - y_i)(\eta - y_{i+1}) - \zeta^2]},\\
(\nabla A_{i,j})_\eta &= \sum_{i=1,modulo4}^{4} \frac{\zeta(x_{i+1} - x_i)(r_{i+1}+r_i)}{r_i r_{i+1}[r_i r_{i+1} - (\xi - x_i)(\xi - x_{i+1}) - (\eta - y_i)(\eta - y_{i+1}) - \zeta^2]},\\
(\nabla A_{i,j})_\zeta &= \sum_{i=1,modulo4}^{4} \frac{[(\xi - x_{i+1})(\eta - y_i) - (\xi - x_i)(\eta - y_{i+1})](r_{i+1}+r_i)}{r_i r_{i+1}[r_i r_{i+1} - (\xi - x_i)(\xi - x_{i+1}) - (\eta - y_i)(\eta - y_{i+1}) - \zeta^2]}.
\end{aligned}
$$

Now two problems can occur while evaluating the influence functions:

- The edges of the panels become too small such that the source potential $B_{i,j}$ and the velocity components $(\nabla B_{i,j})_\xi$ and $(\nabla B_{i,j})_\eta$ become infinite.
- The $\zeta$-coordinate of the point $\mathbf{P}$ approaches zero. In this case the dipole potential $A_{i,j}$ and the normal velocity component $(\nabla B_{i,j})_\zeta$ become infinite.

In case of the first problem, the source influences must be suppressed in order to avoid instabilities. For this purpose, the following criterion for the minimum edge length can be used: $d_{i,i+1} \geq$ const. If $d_{i,i+1} <$ const, the influence of the edge $i$ should be suppressed. In case of the second problem, the formulas for $A_{i,j}$ and $(\nabla B_{i,j})_\zeta$ change and it holds for $\zeta \to 0\pm$ (s. Katz and Plotkin, 2001, p. 209):

$$
A_{i,j} = \mp\frac{1}{2}, \quad (\nabla B_{i,j})_\zeta = \pm\frac{1}{2}.
$$

The influence functions are functions of the geometry of the body or wake. For a body the influence functions do not change in time, i.e. they remain the same for all time steps. The wake geometry changes in time, thus the influences of the wake panels must be recalculated for each time step in the unsteady computations.

# Chapter D
# Simulation results

This chapter presents a part of the results obtained in the simulations of Chapters 5.1.1 and 5.1.3. For more information on the considered geometries and the simulation background the reader is kindly referred to the respective Chapters.

## D.1 $\text{NACA}66_2 - 415$ hydrofoil

The present section displays the simulation results obtained for the non-cavitating and cavitating flow around the $\text{NACA}66_2 - 415$ hydrofoil. Figures D.1-D.6 illustrate the results for the non-cavitating flow. The calculated and measured lift coefficients are plotted as functions of the angle of attack. On Figures D.7-D.9 the computed results for the scaled pressure distributions and the corresponding cavity shapes are visualised for the simulation cases 1 and 2 with different surface grid resolutions (s. Section 5.1.1).

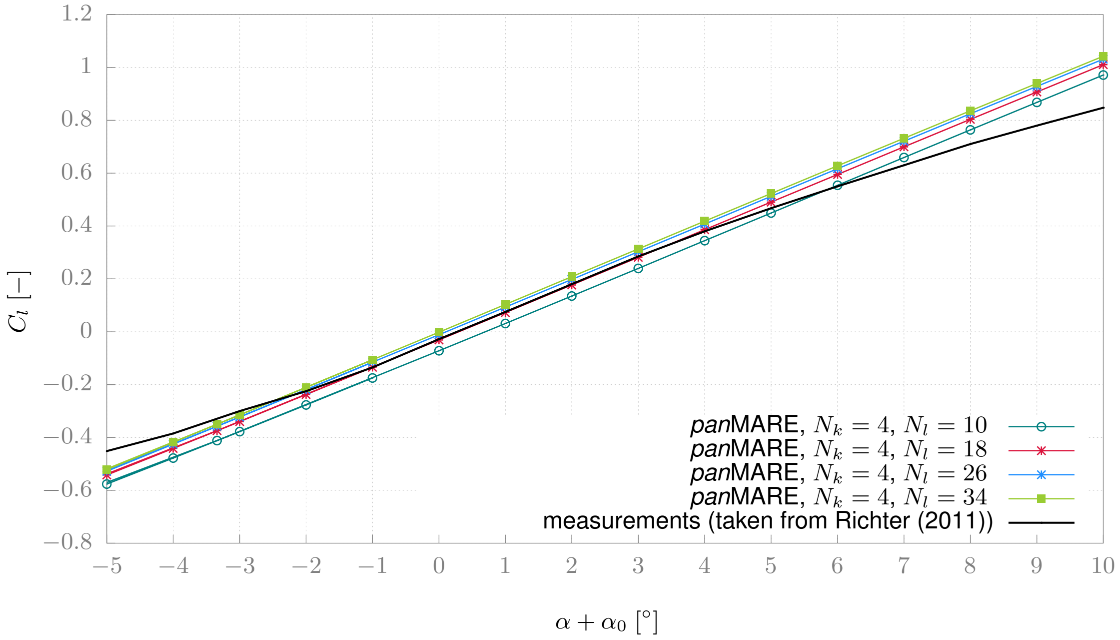

Figure D.1: Influence of the grid resolution in the cross-wise direction on the calculated lift coefficients of the $\text{NACA}66_2$-415 hydrofoil ($N_k = 4$)

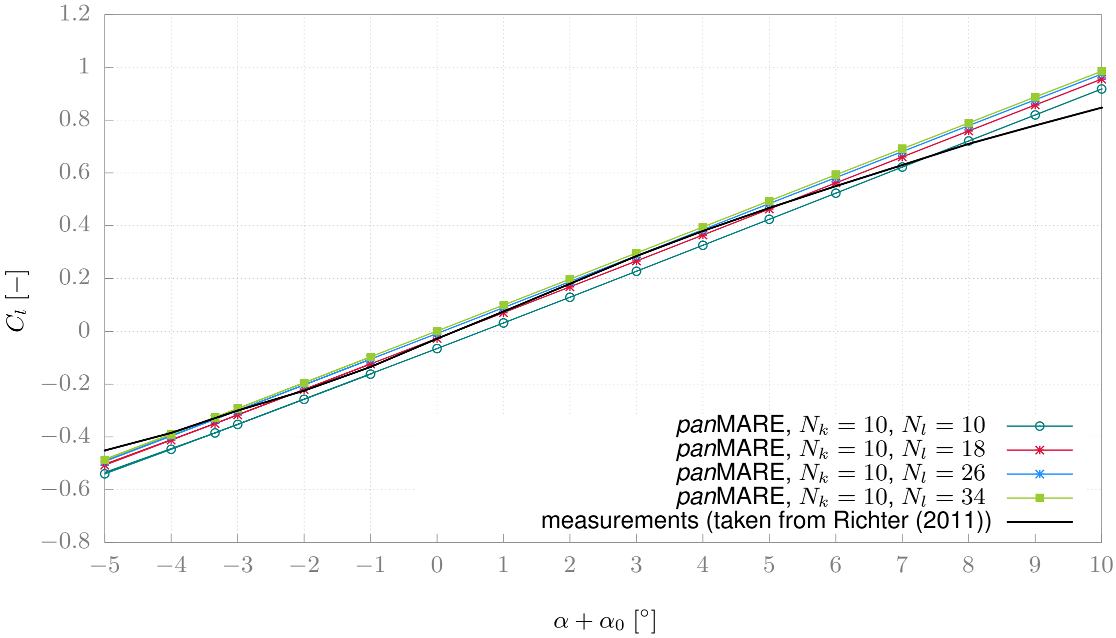

Figure D.2: Influence of the grid resolution in the cross-wise direction on the calculated lift coefficients of the NACA66$_2$-415 hydrofoil ($N_k = 10$)

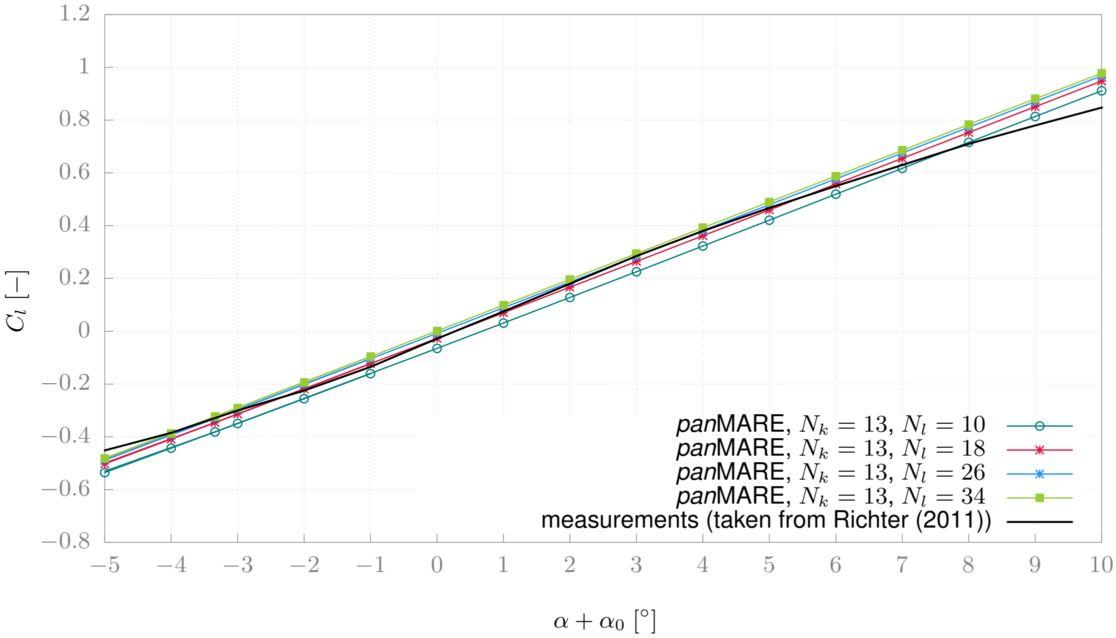

Figure D.3: Influence of the grid resolution in the cross-wise direction on the calculated lift coefficients of the NACA66$_2$-415 hydrofoil ($N_k = 13$)

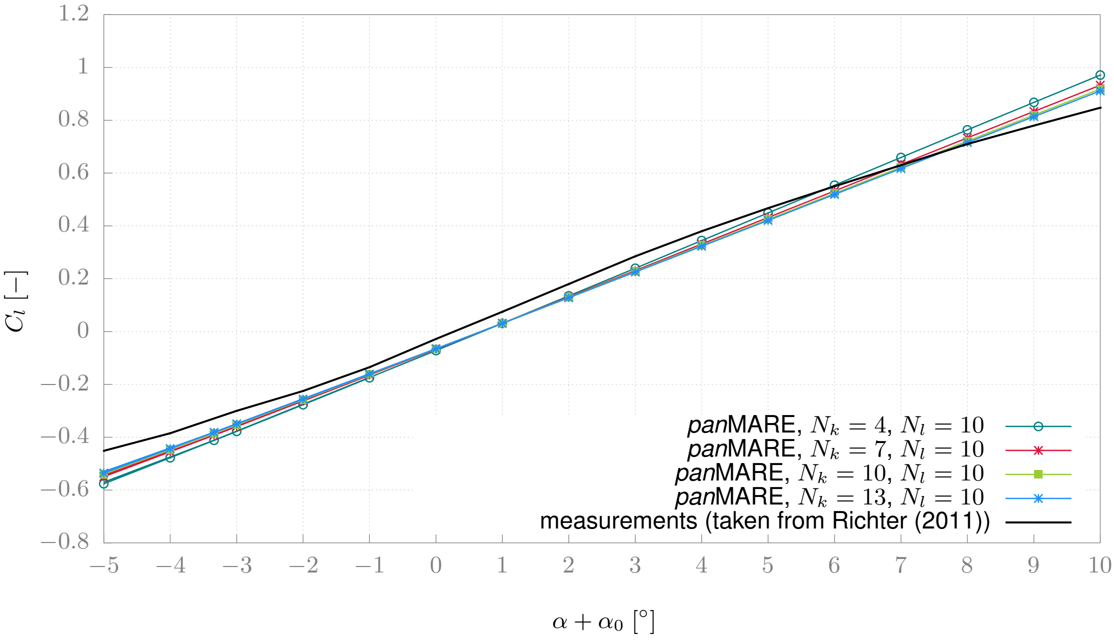

Figure D.4: Influence of the grid resolution in the span-wise direction on the calculated lift coefficients of the NACA$66_2$-415 hydrofoil ($N_l = 10$)

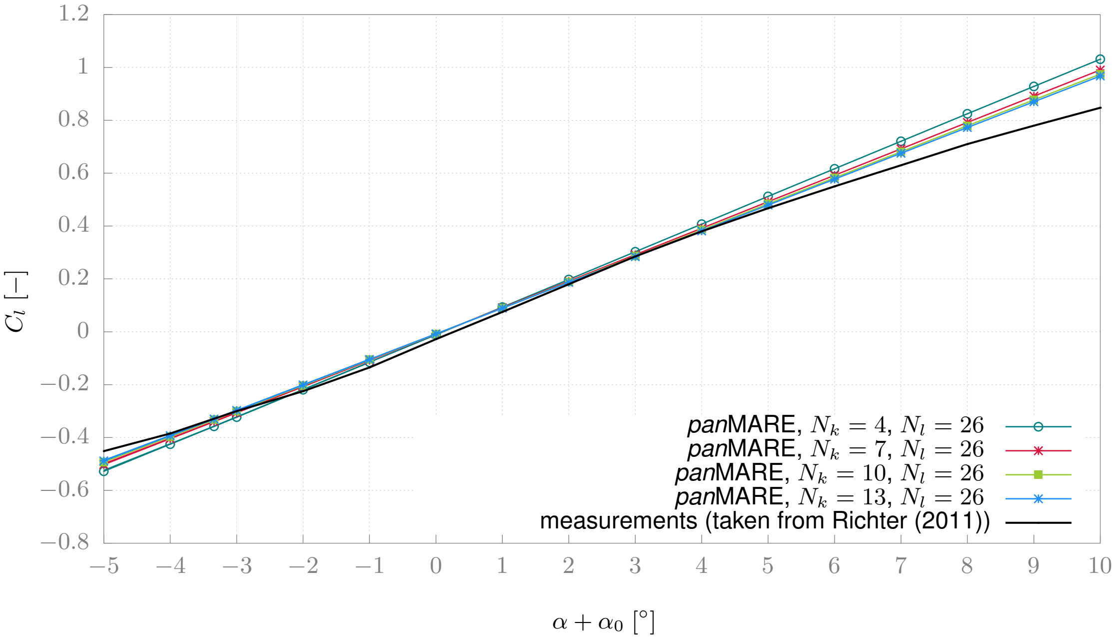

Figure D.5: Influence of the grid resolution in the span-wise direction on the calculated lift coefficients of the NACA$66_2$-415 hydrofoil ($N_l = 26$)

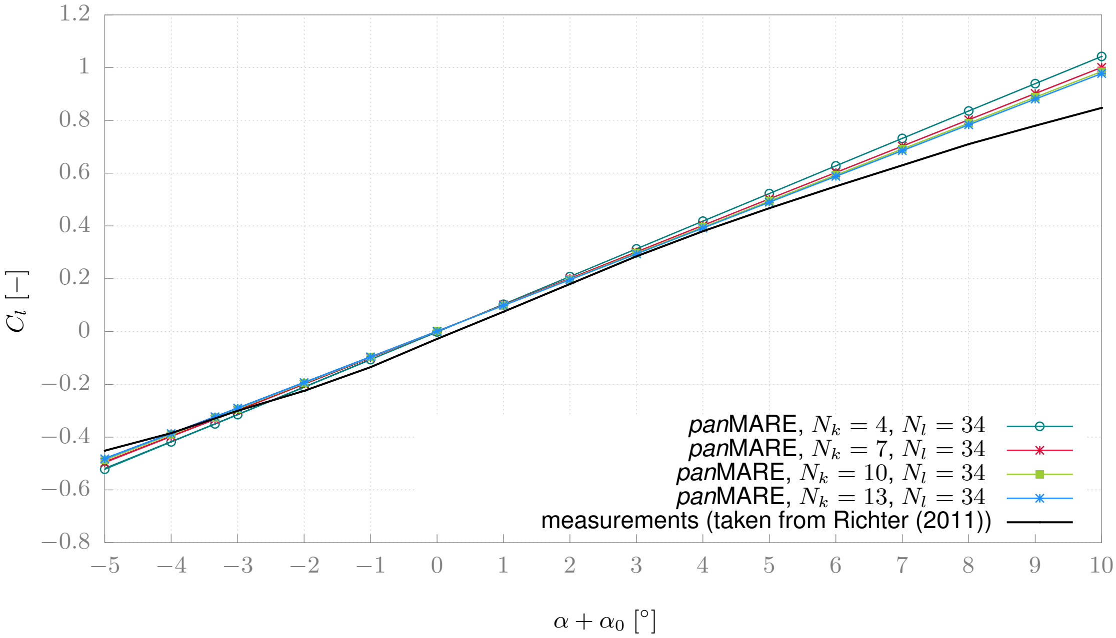

Figure D.6: Influence of the grid resolution in the span-wise direction on the calculated lift coefficients of the NACA66$_2$-415 hydrofoil ($N_l = 34$)

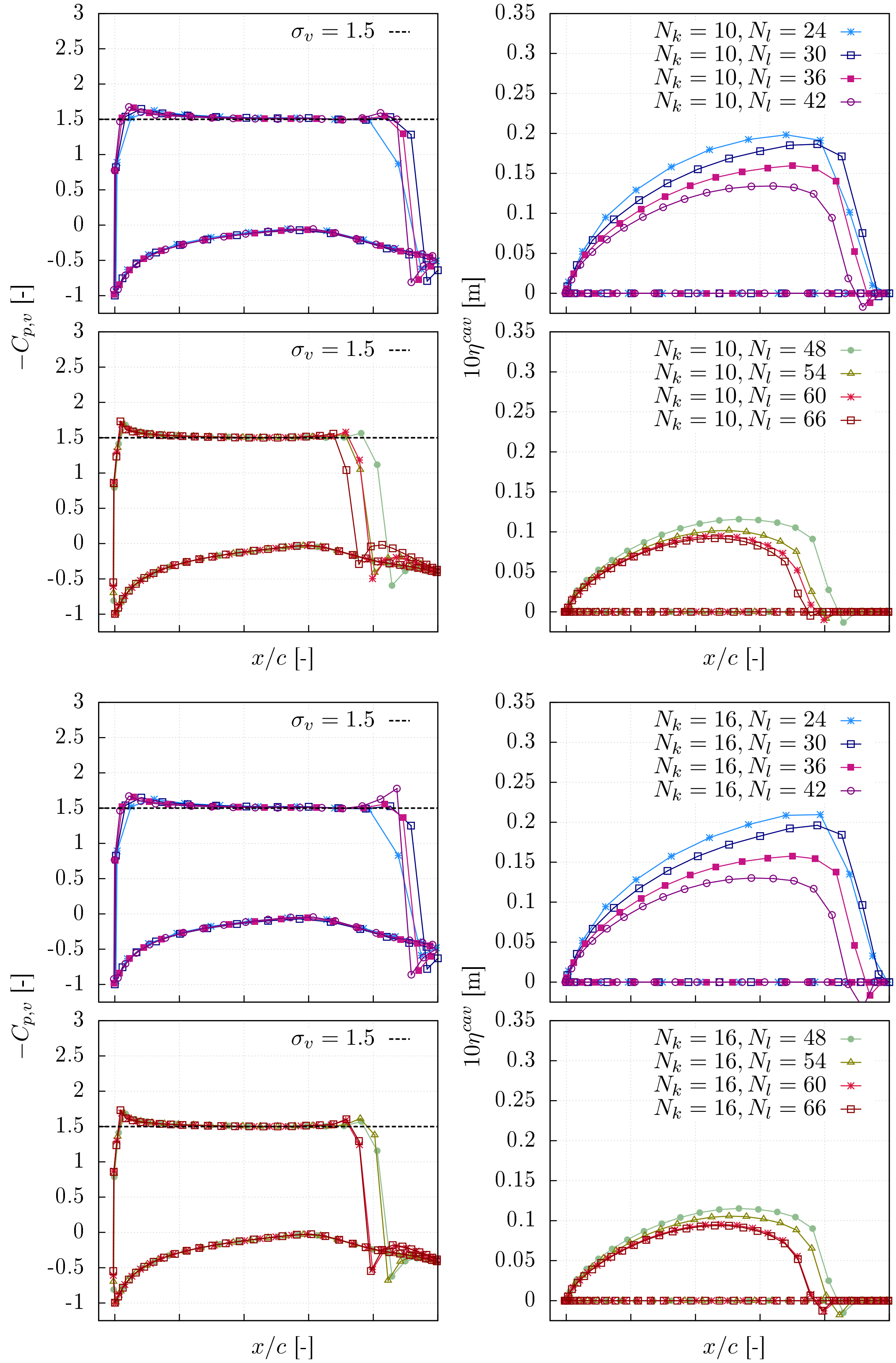

Figure D.7: Scaled pressure coefficients and sheet cavitation extents calculated by *pan*MARE with different grid resolutions for the simulation case 1 with $\sigma_v = 1.5$

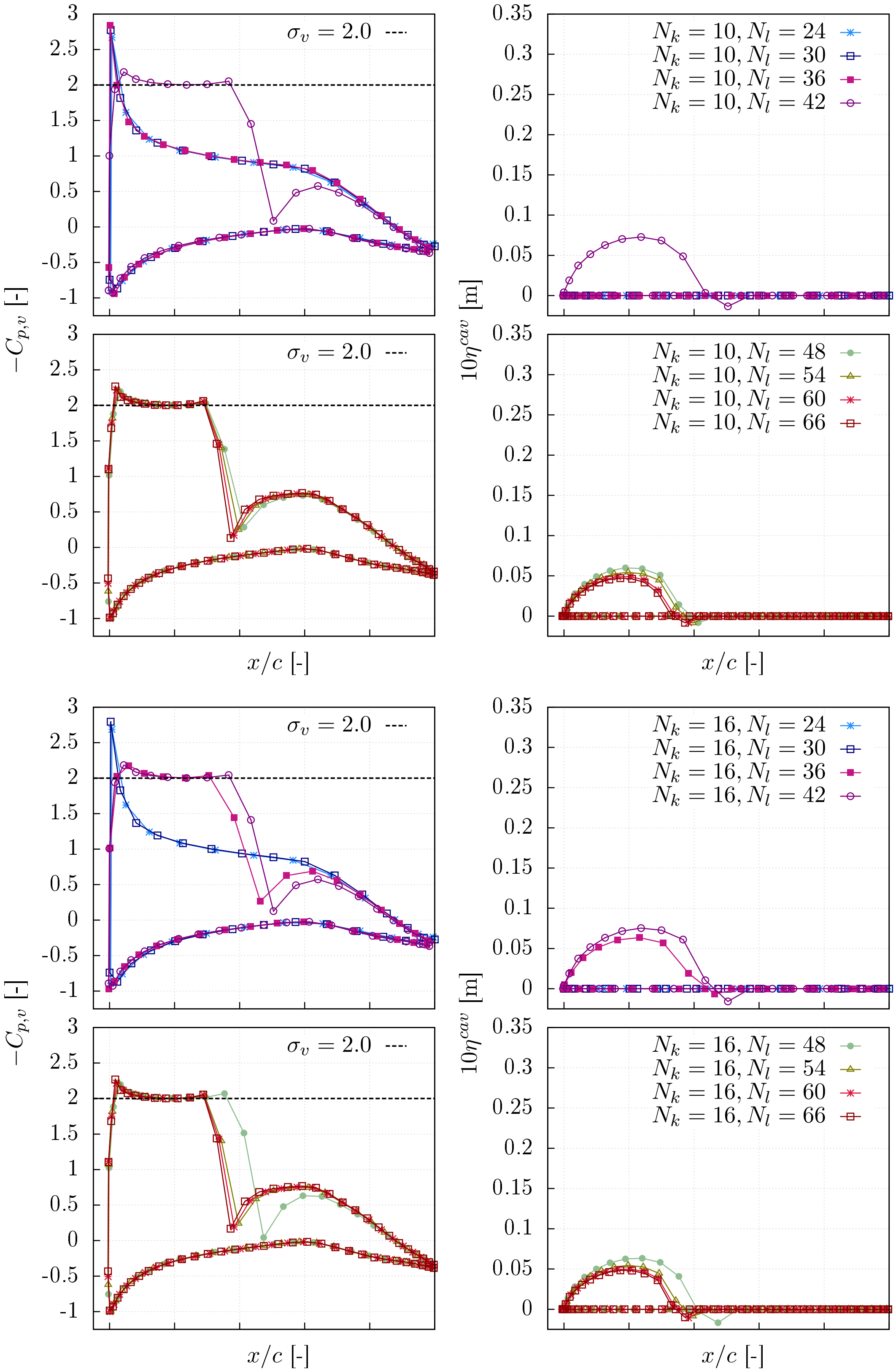

Figure D.8: Scaled pressure coefficients and sheet cavitation extents calculated by *pan*MARE with different grid resolutions for the simulation case 1 with $\sigma_v = 2.0$

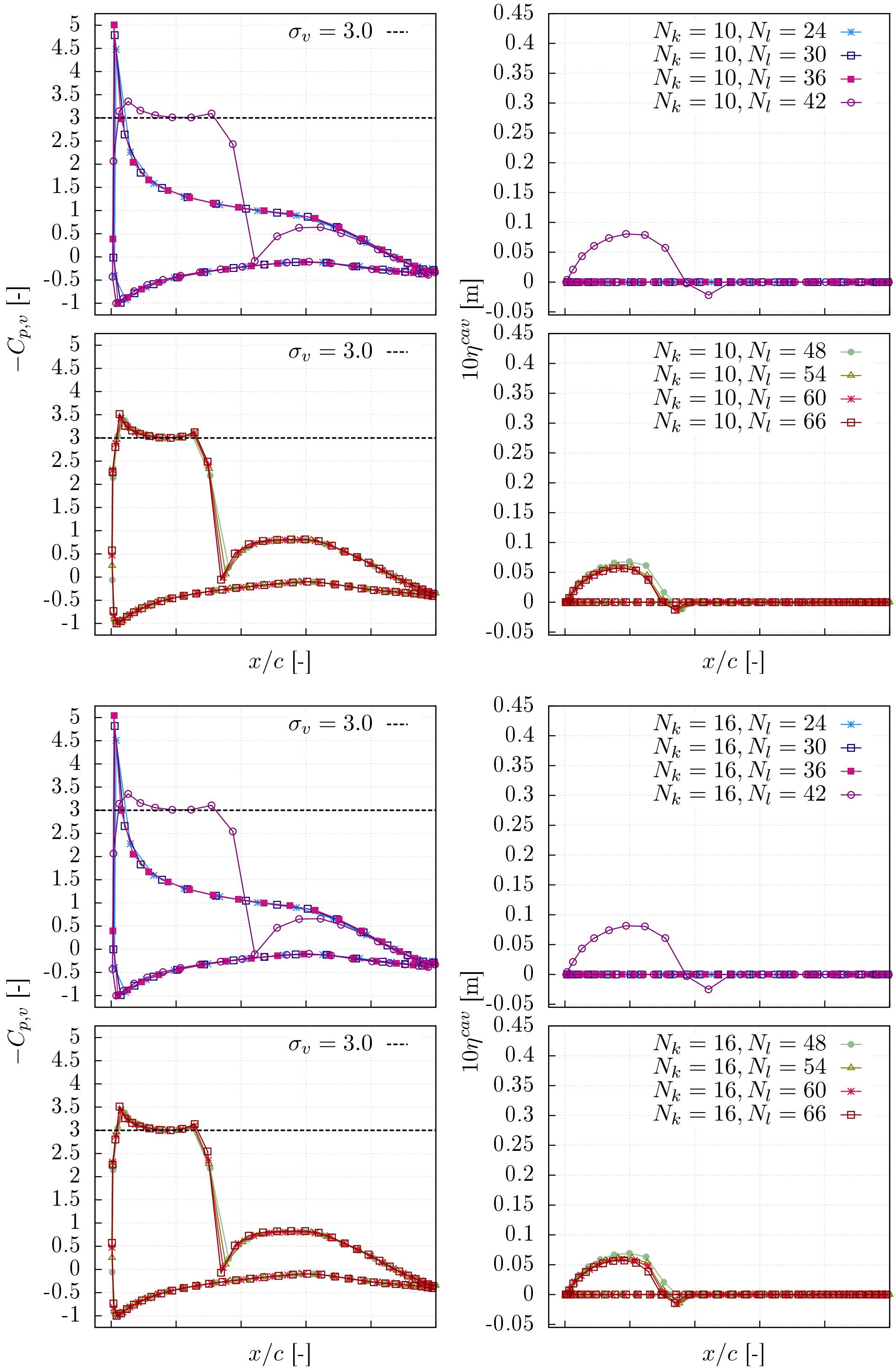

Figure D.9: Scaled pressure coefficients and sheet cavitation extents calculated by *pan*MARE with different grid resolutions for the simulation case 2 with $\sigma_v = 3.0$

## D.2 P1356 propeller

This section displays the simulation results obtained for the non-cavitating and cavitating flow around the P1356 propeller. Figures D.10-D.15 illustrate the calculated and measured open water characteristics of the non-cavitating propeller flow. On Figures D.16-D.18 the computed results for the cavitating flow around the P1356 propeller are visualised. The Figures show the scaled pressure distributions obtained with different surface grid resolutions.

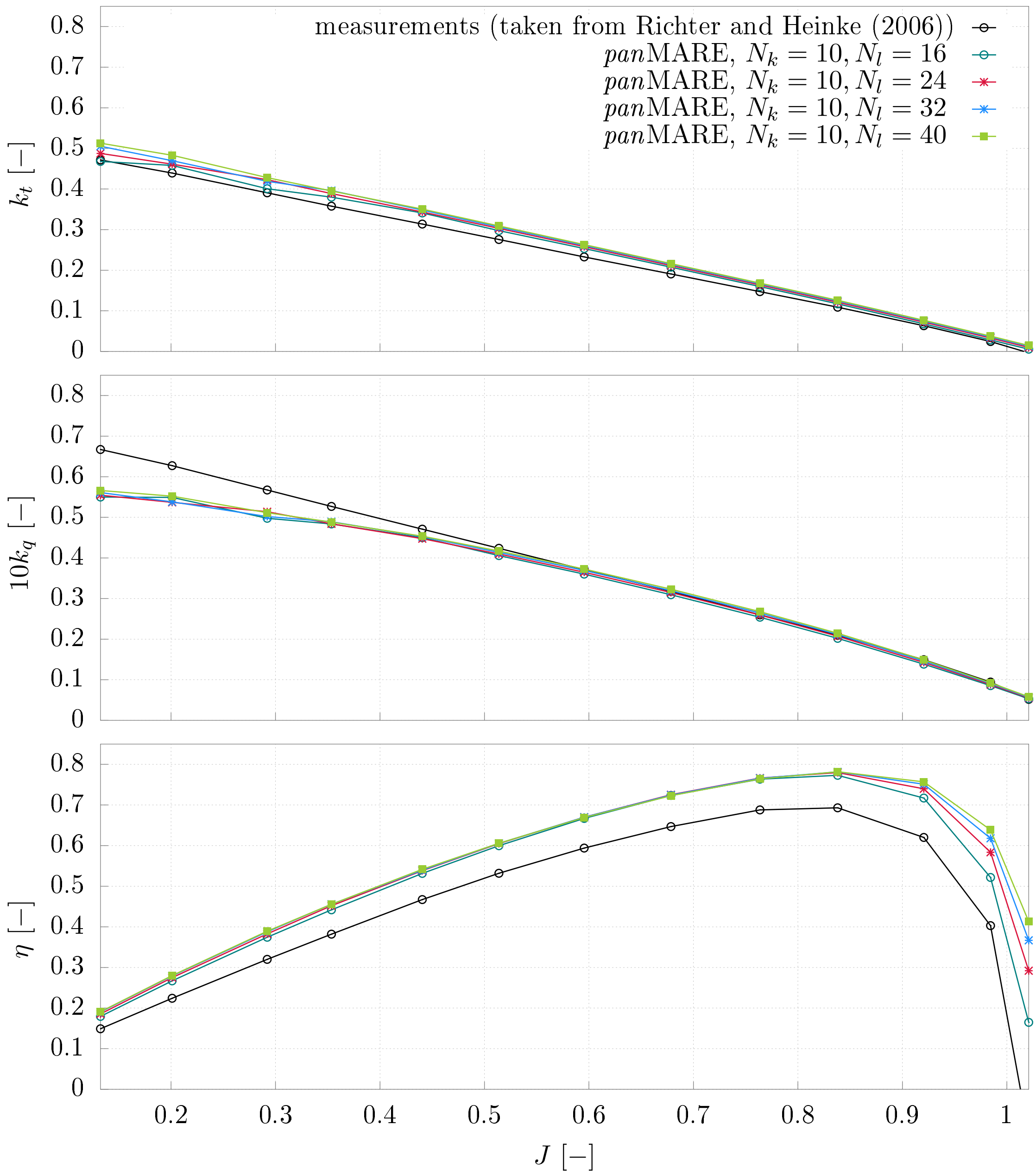

Figure D.10: Influence of the grid refinement in the cross-wise direction on the calculated open water characteristics of the P1356 propeller ($N_k = 10$)

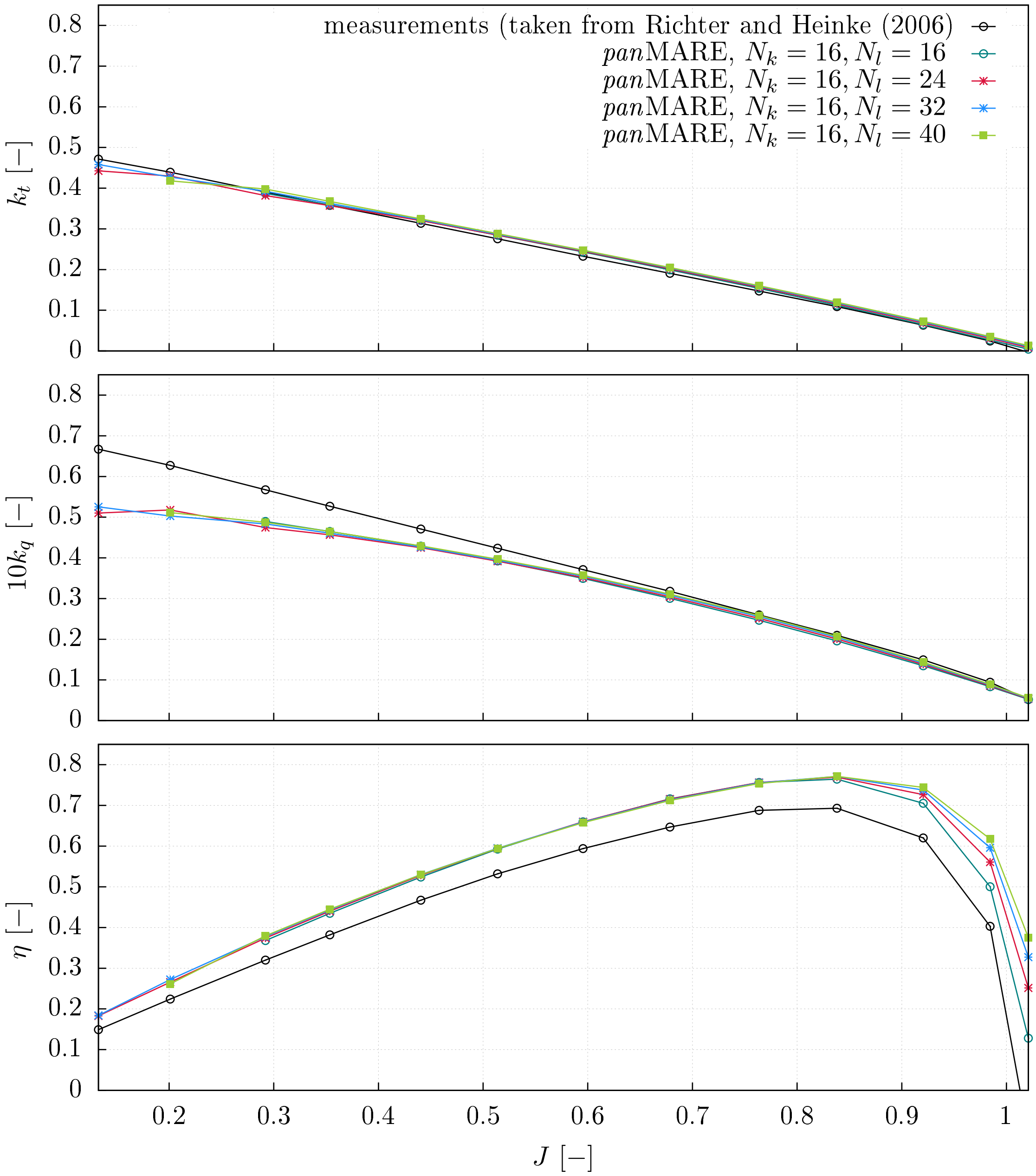

Figure D.11: Influence of the grid refinement in the cross-wise direction on the calculated open water characteristics of the P1356 propeller ($N_k = 16$)

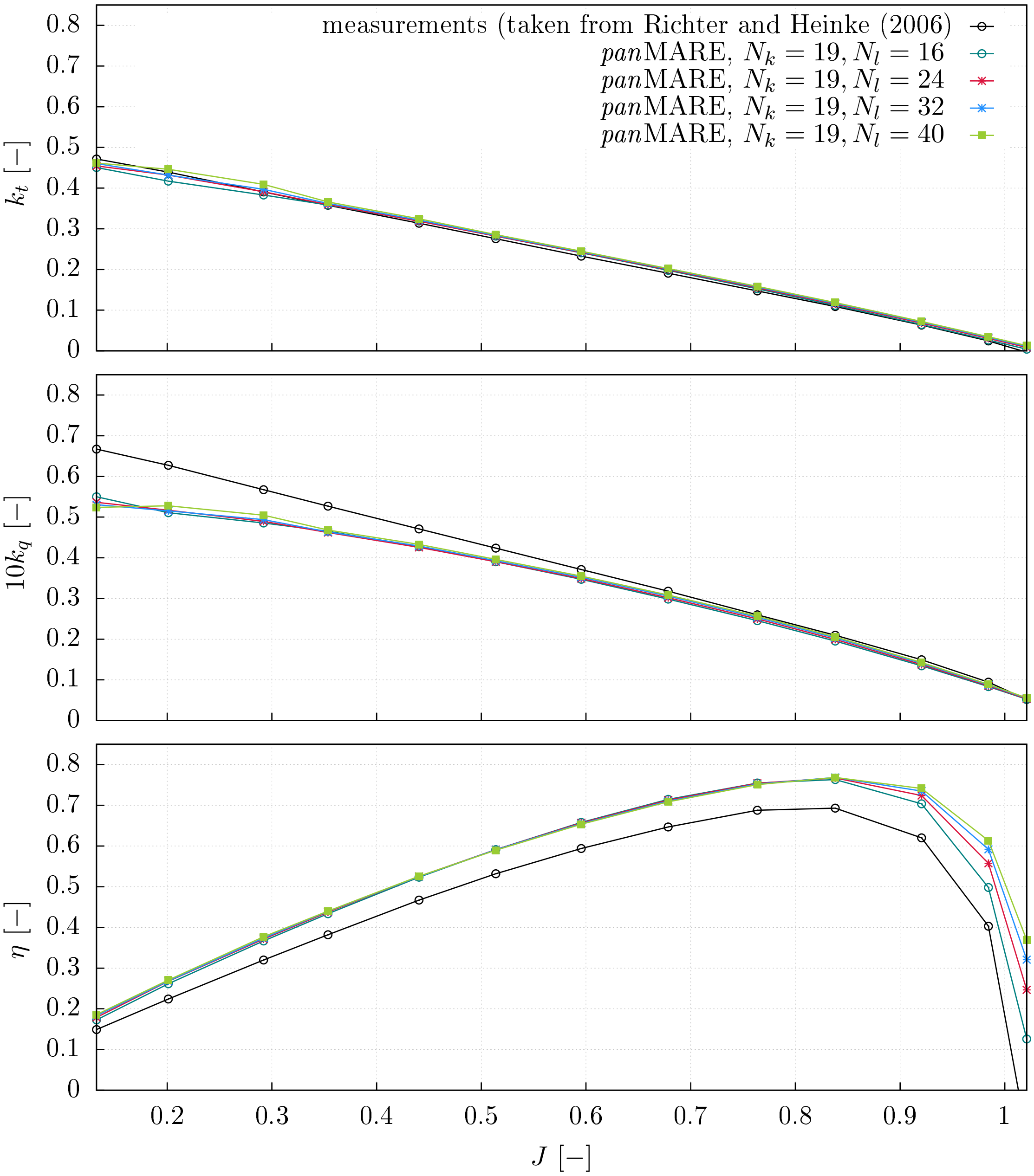

Figure D.12: Influence of the grid refinement in the cross-wise direction on the calculated open water characteristics of the P1356 propeller ($N_k = 19$)

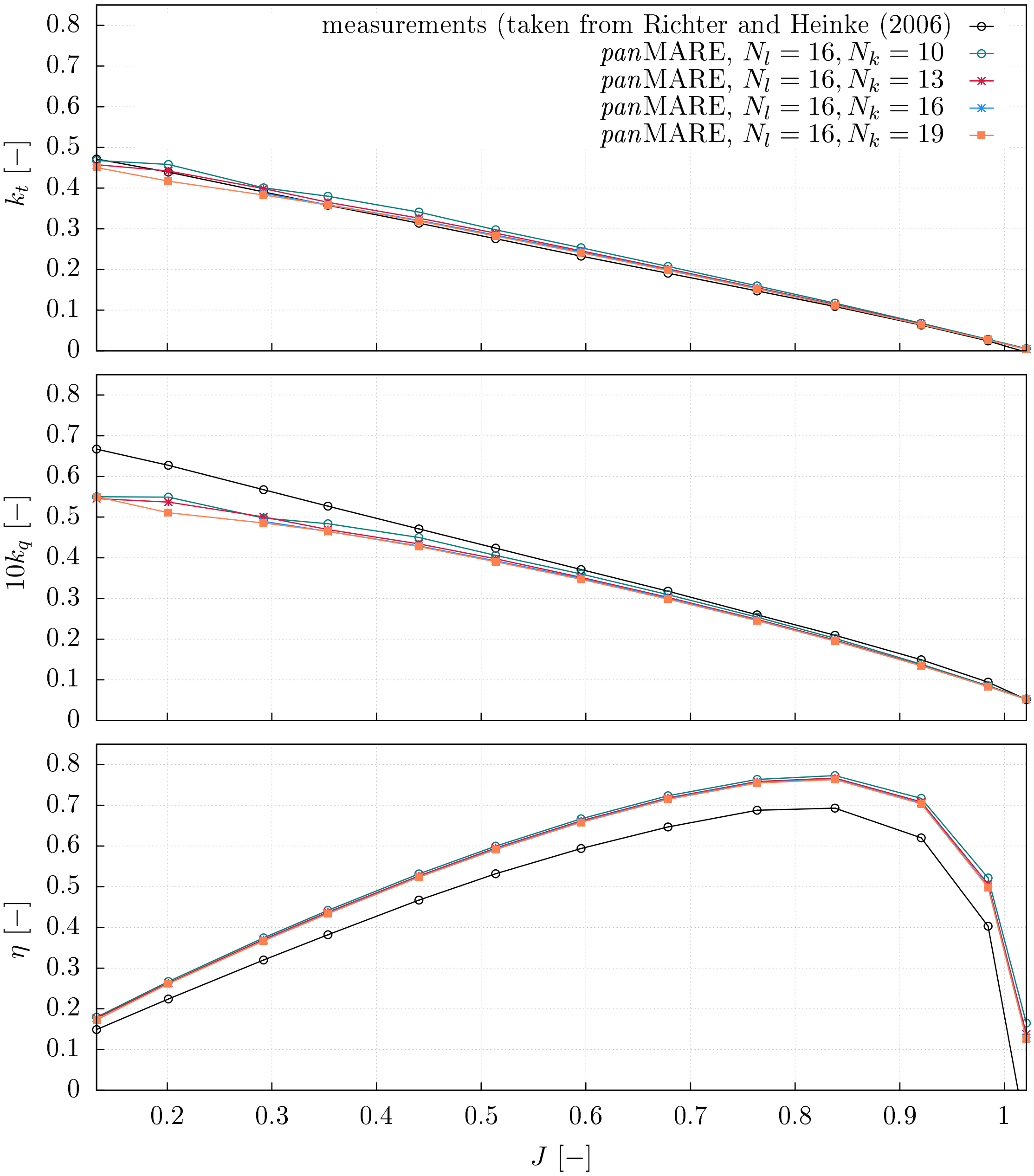

Figure D.13: Influence of the grid refinement in the span-wise direction on the calculated open water characteristics of the P1356 propeller ($N_l = 16$)

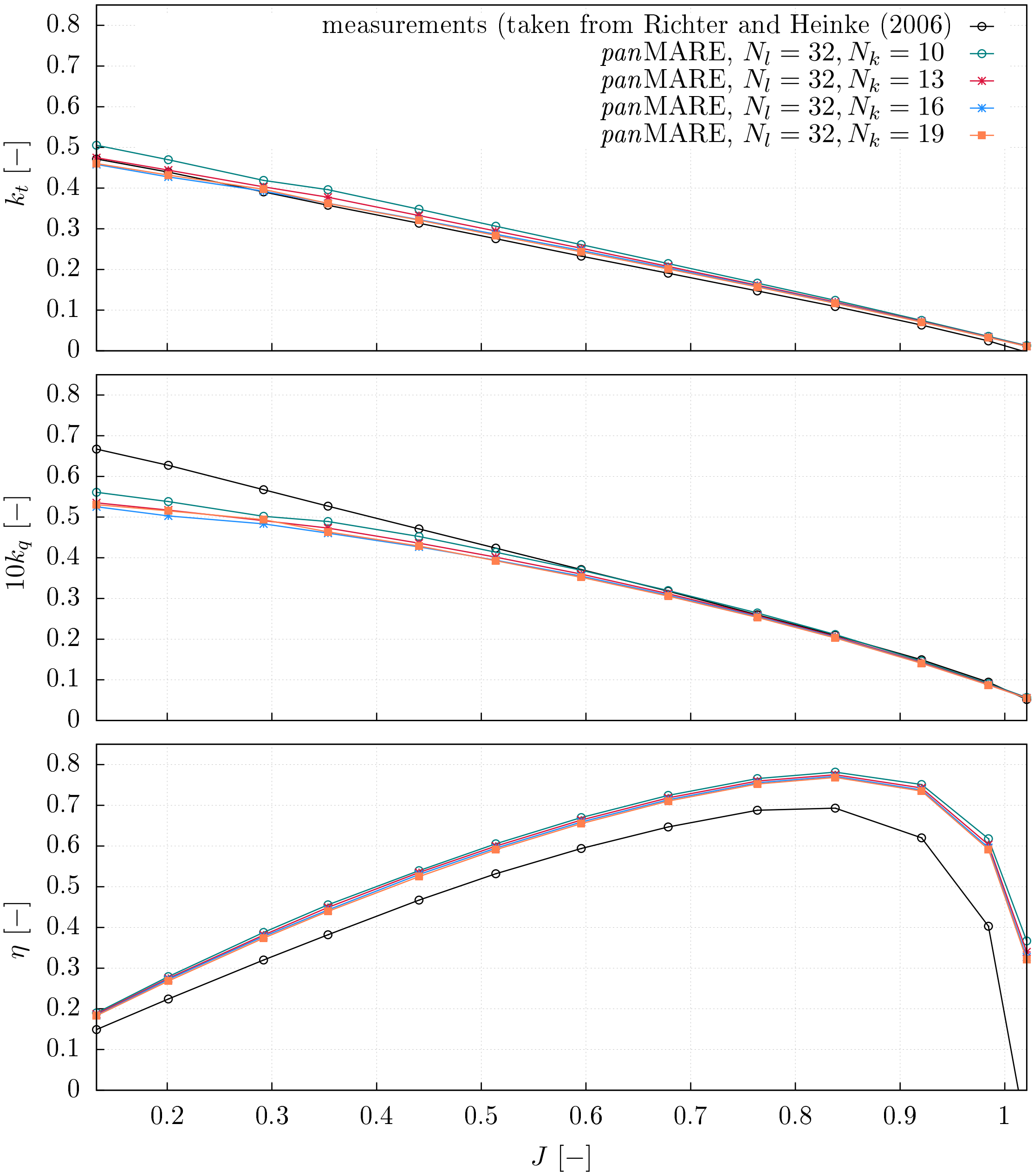

Figure D.14: Influence of the grid refinement in the span-wise direction on the calculated open water characteristics of the P1356 propeller ($N_l = 32$)

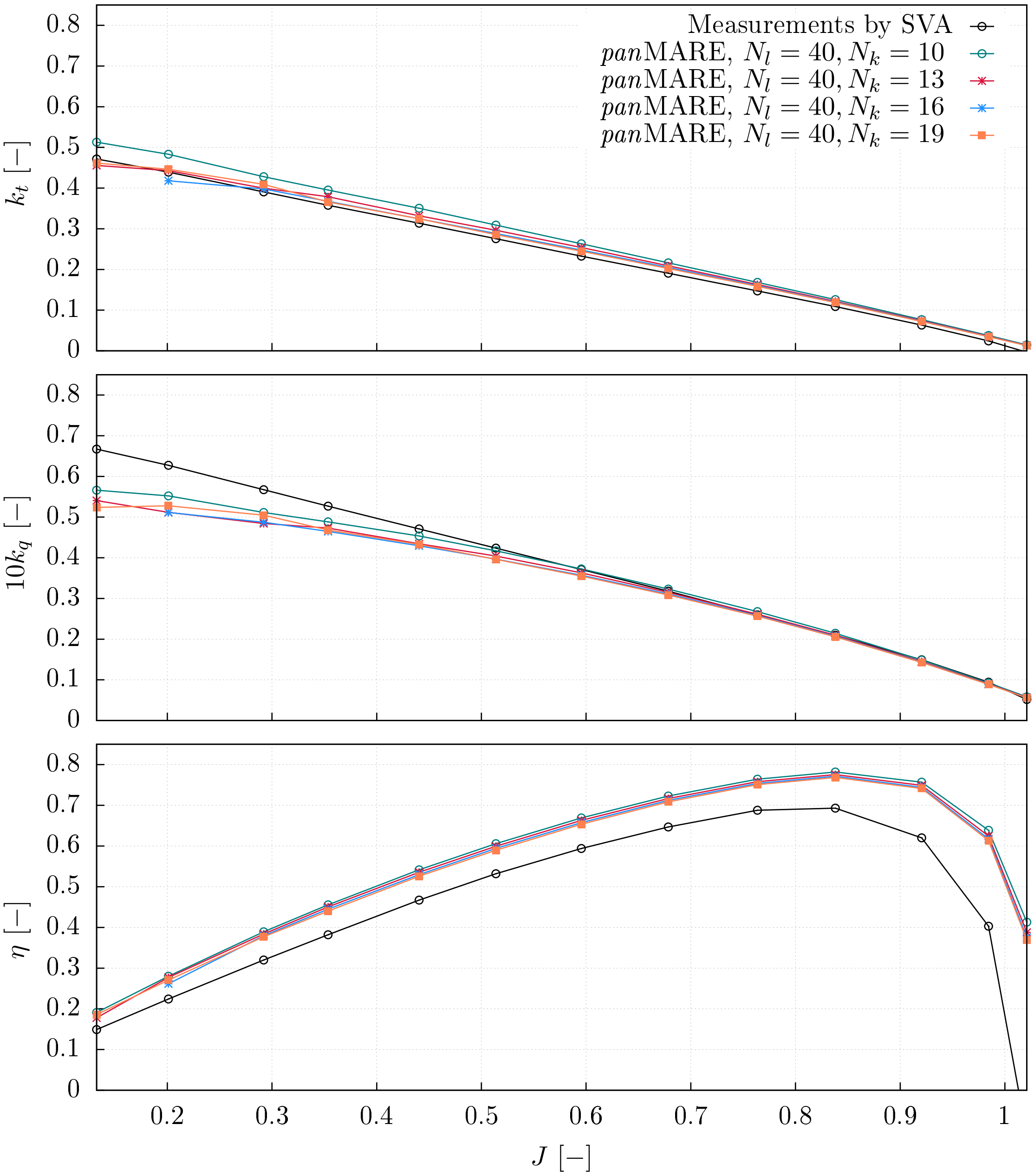

Figure D.15: Influence of the grid refinement in the span-wise direction on the calculated open water characteristics of the P1356 propeller ($N_l = 40$)

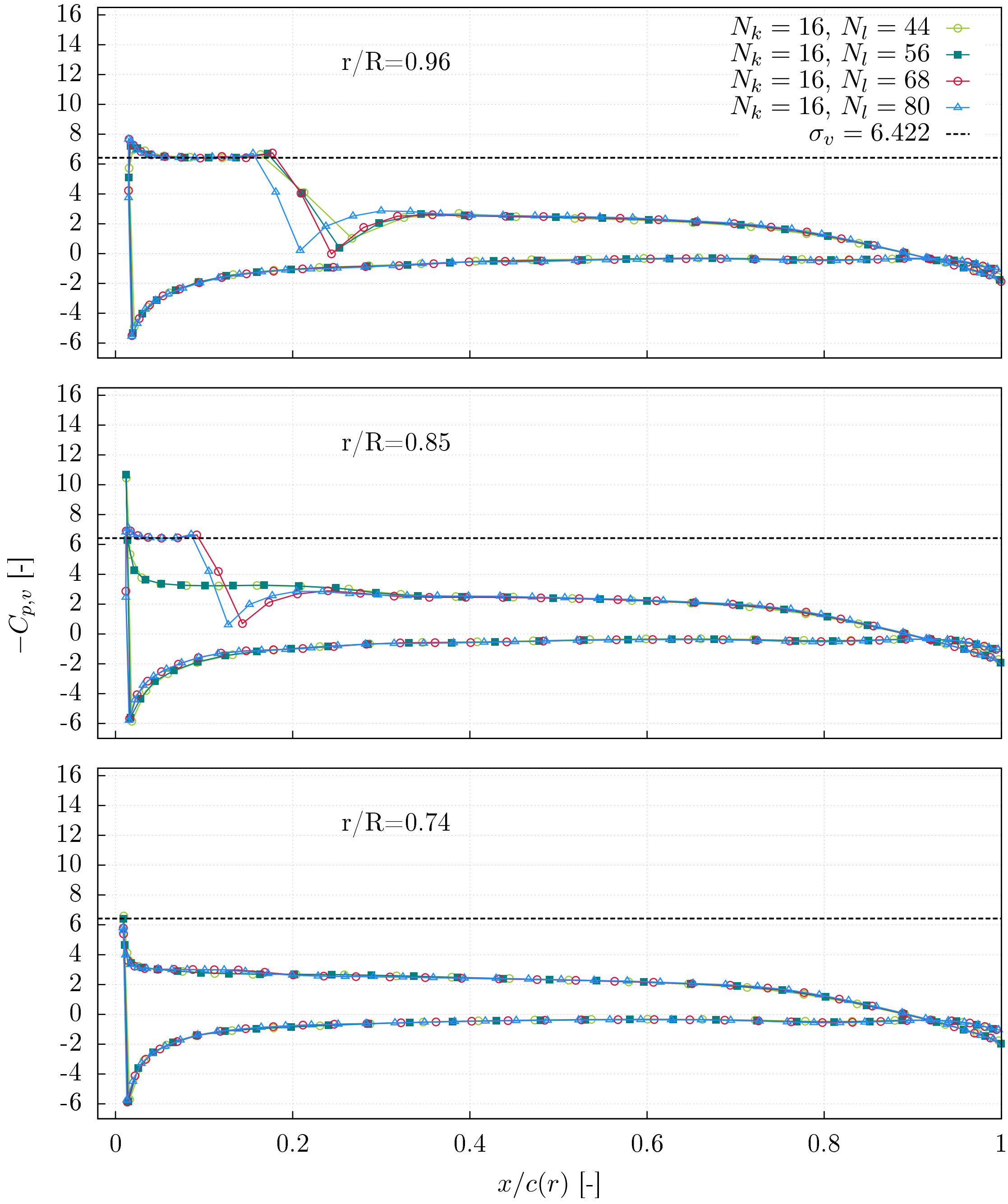

Figure D.16: Pressure coefficients calculated by *pan*MARE for $J = 0.6$ and $\sigma_v = 6.422$ ($\sigma_n = 2.312$) with different grid resolutions in the cross-wise direction ($N_k = 16$)

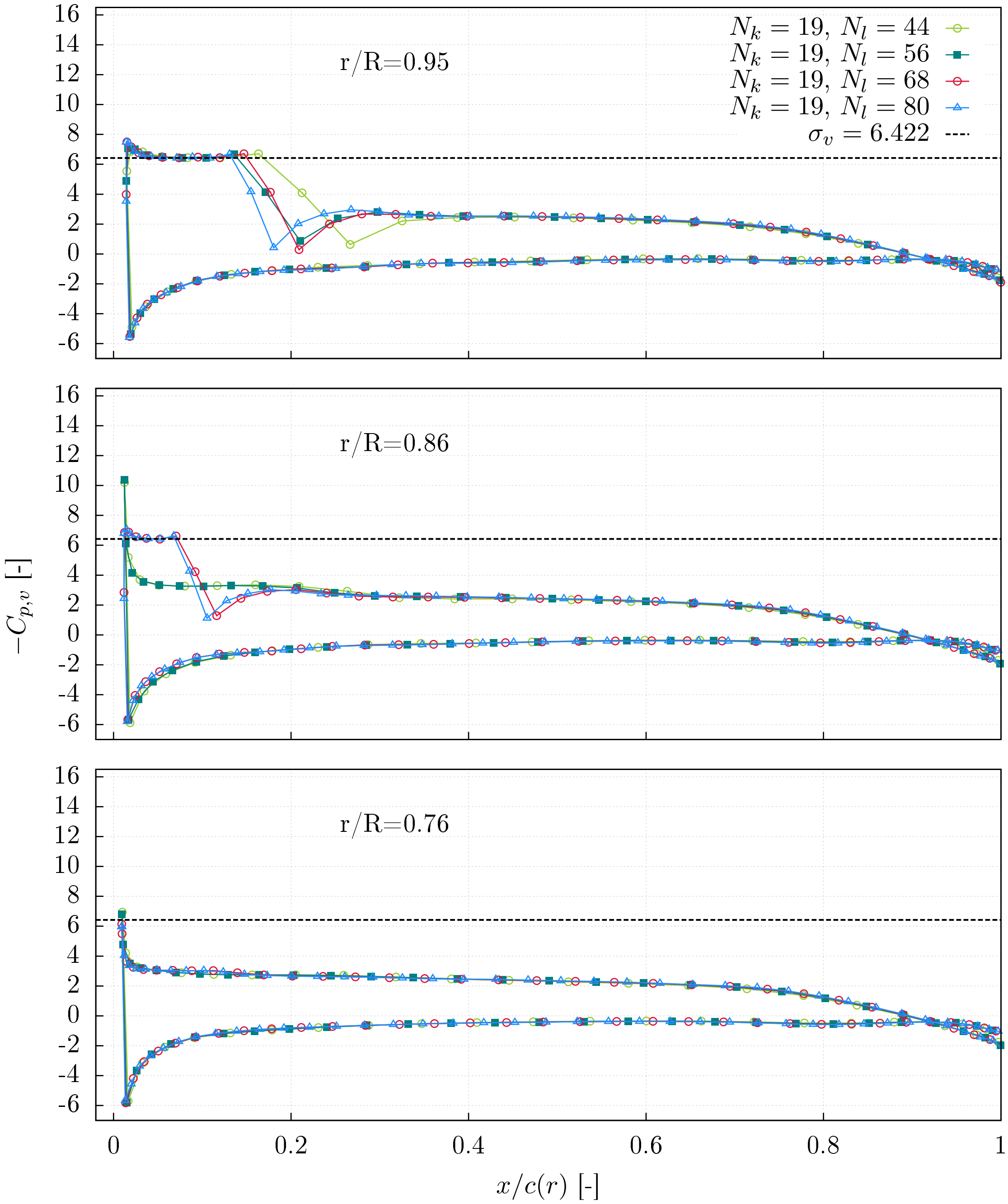

Figure D.17: Pressure coefficients calculated by *pan*MARE for $J = 0.6$ and $\sigma_v = 6.422$ ($\sigma_n = 2.312$) with different grid resolutions in the cross-wise direction ($N_k = 19$)

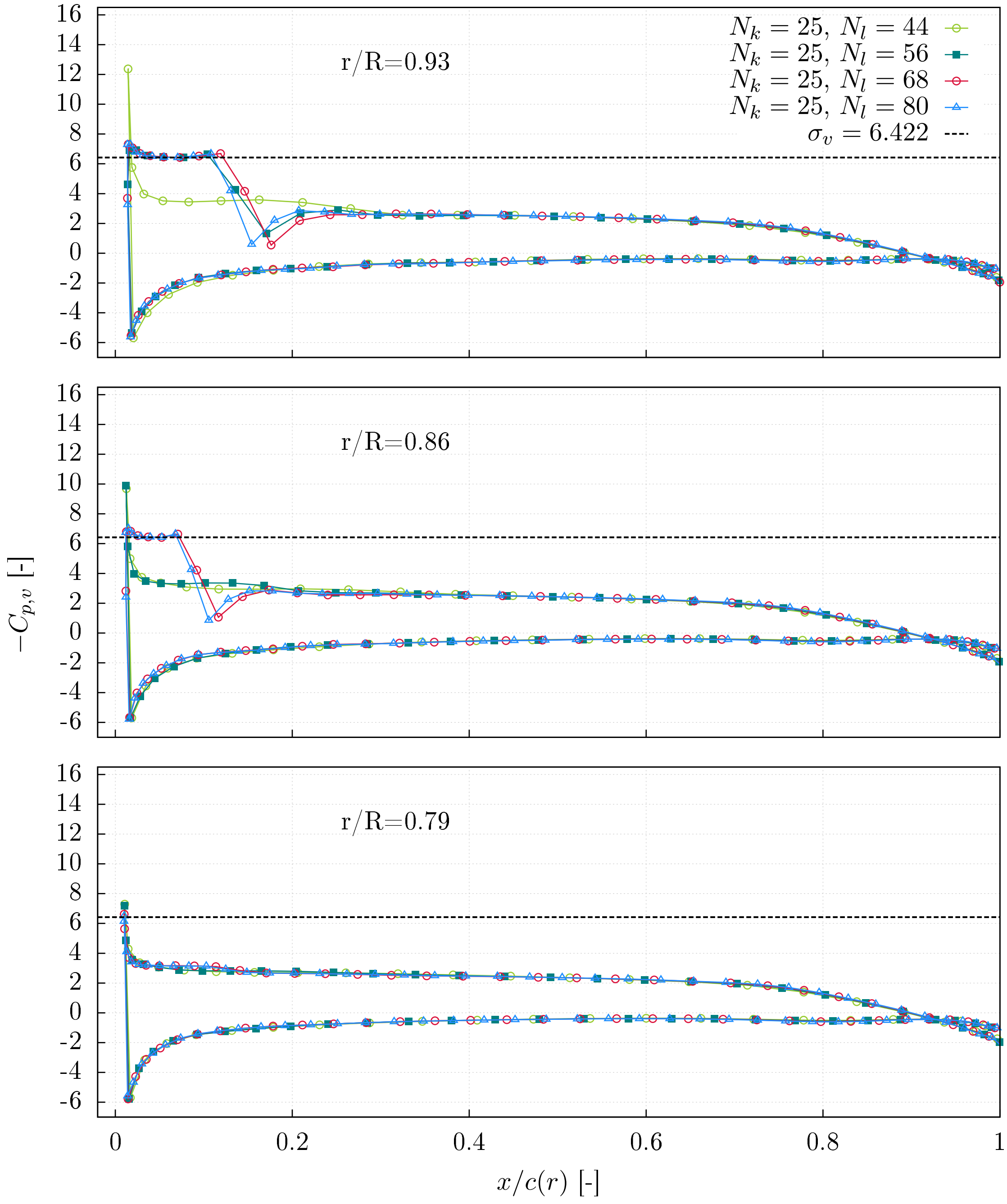

Figure D.18: Pressure coefficients calculated by *pan*MARE for $J = 0.6$ and $\sigma_v = 6.422$ ($\sigma_n = 2.312$) with different grid resolutions in the cross-wise direction ($N_k = 25$)